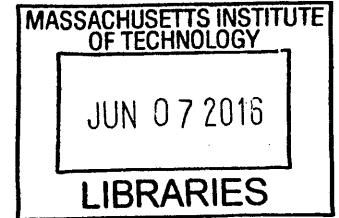# From Clay Slurries to Mudrocks: A Cryo-SEM Investigation of the Development of the Porosity and Microstructure

by

Amer Deirieh

B. Eng., Civil Engineering
Birziet University, West Bank, Palestine (2008)

S.M., Civil and Environmental Engineering
Massachusetts Institute of Technology (2011)

Submitted to the Department of Civil and Environmental Engineering
in Partial Fulfillment of the Requirements for the Degree of

Doctor of Philosophy in Geotechnical and Geoenvironmental Engineering

at the

MASSACHUSSETTS INSTITUTE OF TECHNOLOGY

February 2016

Signature redacted

Signature of Author: ....
Department of Civil and Environmental Engineering
October 1, 2015

Signature redacted

Certified by: ....
√
John T. Germaine
Research Professor in Civil and Environmental Engineering, Tufts University
Thesis Supervisor

Signature redacted

Accepted by: ....
Heidi Nepf
Donald and Martha Harleman Professor of Civil and Environmental Engineering
Chair, Departmental Committee for Graduate Students

From Clay Slurries to Mudrocks: A Cryo-SEM Investigation of the Development of the Porosity and Microstructure

by

Amer Deirieh

Submitted to the Department of Civil and Environmental Engineering on October 1, 2015
in Partial Fulfillment of the Requirements for the Degree of
Doctor of Philosophy in Geotechnical and Geoenvironmental Engineering

ABSTRACT

This thesis investigates the microstructure of smectitic and illitic rich mudrocks that are resedimented in the laboratory from the Gulf of Mexico and Boston Blue clay natural sediments. The resedimentation technique consists of mixing clay sediments with saline water to form a slurry, which is then subjected to a wide range of effective stresses. Cryo-SEM and conventional SEM techniques are used to investigate the microstructure of the clay slurry and resedimented mudrocks. Cryo-SEM enables the imaging of samples in their in-situ conditions, while conventional SEM is used to image oven-dried samples.

Two techniques are used to prepare the slurry samples for cryo-SEM imaging: high-pressure freezing and plunge freezing. The microstructure of high-pressure frozen clay slurries consists of individual clay particles and clay aggregates randomly distributed in water. These results demonstrate that one of the widely accepted models for clay slurries, the honeycomb structure, is an artifact of the plunge-freezing method and does not reflect the in-situ structure. In the field of geological sciences, this contrasts a fundamental view of fabric evolution that has inferred the presence of honeycomb structures that gradually evolve to an oriented fabric.

Furthermore, we developed a method to obtain representative information about the heterogeneous pore space of mudrocks. This method combines information obtained from SEM images at different magnifications to represent the porosity of mudrocks. High magnification images provide high resolution and are used to sample small pores, while low magnification images provide low resolution and are used to sample large pores. The developed method provides a practical alternative to the current method that stitches together hundreds of images to obtain large representative mosaics.

We show that SEM imaging detects only a fraction (~30%) of the total porosity of mudrocks, neglecting the significant amount of pores below the resolution of SEM. Furthermore, we show that oven drying, which is a prerequisite for most characterization methods, leads to a dramatic shrinkage (~50%) in the nanometer-sized clay pores, and does not influence the pore space visible in SEM images. Finally, we show that the application of stress on mudrocks leads to a simultaneous compression of inter-particle and intra-particle pores.

Thesis Supervisor: John T. Germaine

Title: Research Professor, Tufts University

ACKNOWLEDGEMENTS

TABLE OF CONTENTS

LIST OF TABLES

LIST OF FIGURES

13

16

17

19

1 INTRODUCTION

1.1 Problem Statement

Mudrocks- composed of clay particles, silt inclusions, and pore space- constitute 75 percent of the section in most sedimentary basins. The focus on mudrocks has increased drastically in the past two decades as several formations have been identified as, not only the sealing formations to many conventional oil and gas plays, but also gas and oil reservoirs. Despite their ubiquitous presence and importance, mudrocks are the least understood compared to other sedimentary rocks.

One of the research efforts to understand mudrocks focuses on the use of microfabric information to predict the macroscopic behavior. In particular, Scanning Electron Microscopy (SEM) has been the most widely used technique to obtain information about the microfabric of mudrocks. For example, in an attempt to investigate the processes that lead to the formation of mudrocks, several authors used plunge-freezing and SEM imaging and showed the existence of a honeycomb structure in clay slurries (O'Brien, 1971; Osipov and Sokolov, 1978; Stawinsk et al., 1990; Zbik et al., 2008, 2010; Du et al., 2009, 2010; Morris and Żbik, 2009). These results were used to infer that the fabric evolution of mudrocks consists of a honeycomb structures that gradually evolve to an oriented fabric (Bennett et al., 1991; O'Brien and Pietraszek-Mattner, 1998; Slatt and O'Brien, 2011). Furthermore, several studies utilized Mercury Porosimetry Intrusion (MIP) and SEM to investigate the evolution of the pore space of mudrocks as a function of the consolidation stress (Delage and Lefebvre, 1984; Griffiths and Joshi, 1989; Al-Mukhtar et al., 1996; Qi et al., 1996). These studies showed that an increase in the applied stress leads to the collapse of large macro pores, while very little to no effect on the small micro pores. The above studies assumed that the used preparation method, mainly plunge freezing, preserves the microstructure of mudrocks.

The purpose of this research is twofold: to assess the influence of preparation techniques such as oven drying and plunge on the microstructure of mudrocks, and to evaluate the validity of results obtained using these preparation methods. In particular, we quantify the influence of the preparation methods in terms of the measured porosity. We utilized state-of-the-art cryo-preparation and imaging techniques to investigate the microstructure of mudrocks in their in-situ

conditions. We used conventional SEM imaging and conventional milling techniques to prepare oven-dried samples. For wet samples, we utilized-high pressure freezing to cryoimmobilize the water in the pore space. Then we used a cryo-polisher to prepare artifact-free flat surfaces for imaging.

1.2 Thesis Scope and Objectives

The aim of this thesis is to establish the link between the microstructure of fine-grained resedimented mudrocks and the applied effective stress. The research approach pursued consists of using Scanning Electron Microscopy (SEM) to image the microstructure of mudrocks over a wide range of effective stresses. The research conducted in this study has three main objectives. The first objective is to establish the microstructure of clay slurries utilizing cryo-SEM technique and cryo-preparation methods. Clay slurries represent a mixture of clay minerals and saline water with a porosity of approximately 0.75. Two methods are used to prepare clay slurries for imaging: plunge freezing and high-pressure freezing. These methods allow the imaging of samples in their in-situ conditions.

The second objective of this study consists of developing a method to obtain representative information from SEM images about the pore space of mudrocks. Mudrocks are highly heterogeneous sedimentary rocks that contain pores and particles that range in size from nanometers to microns. As a consequence of this wide-scale and heterogeneous nature, it is not possible to use one SEM image at a specific magnification to obtain representative porosity information. The developed method combines porosity information obtained from images acquired at different magnifications to represent the entire pore space of mudrocks. High magnification images provide high resolution and small field of view, while low magnification images provide low resolution and large field of view. Therefore, high magnification images are used to sample the nanometer-sized pores, while low magnification images are used to sample the large pores. The new methodology will circumvent the need to stitch together hundreds of images to provide representative information about mudrocks.

The third objective of this study is to investigate the influence of oven drying on the microstructure of mudrocks. Oven drying is a prerequisite for most material characterization methods including SEM imaging. Mudrocks undergo dramatic shrinkage upon drying, and hence

it is necessary to understand the influence of drying shrinkage on the microstructure to obtain meaningful conclusions from SEM imaging. This task can be achieved by comparing the microstructure of oven-dried samples to that of wet samples. Conventional SEM is used to image oven-dried samples, while cryo-SEM is used to image wet samples. High pressure freezing is used to preserve the microstructure of wet samples for cryo-SEM imaging. Finally, the microstructure of mudrocks samples is investigated over a wide range of effective stresses. In particular, the development of the pore space of mudrocks as a function of stress is established.

1.3 Organization of the Thesis

This thesis is organized into seven chapters that provide a complete picture about the research performed.

Chapter 2 presents a literature review of important research performed in areas relevant to this thesis. In particular, this chapter aims to establish an overall idea of the current knowledge regarding the utilization of SEM technique to investigate the microstructure of mudrocks. The chapter begins by discussing the research conducted to provide a qualitative description of the microstructure of mudrocks and shale rocks. This is followed by the use of large mosaics of SEM images to obtain representative information about mudrocks. The large mosaics were used mainly to calculate the porosity of mudrock samples, as well as the pore size distributions. The influence of drying shrinkage on the microstructure of mudrocks was discussed based on MIP studies and SEM studies. The final section of this chapter discusses the development of the microstructure of mudrocks as a function of the applied stress.

Chapter 3 presents the origin and index properties of the soils tested in this investigation including Gulf of Mexico-Eugene Island (GOM-EI) and Boston Blue Clay (BBC). Chapter 4 describes the equipment and procedures used to image mudrock samples. This chapter begins with a brief description of the SEM technique, followed by a discussion of the influence of critical imaging parameters on the quality of images. The process of resedimentation is then described including the procedure and equipment. The preparation of samples for imaging is also discussed and divided into two parts: sample preparation of resedimented mudrock samples and sample preparation of slurry samples. The preparation of resedimented mudrock samples begins with a detailed description of the procedures and equipment used in the ion-milling and imaging

of oven-dried samples. This is followed by a discussion of the methods used to prepare wet mudrock samples for imaging. These methods include high-pressure freezing, plunge freezing, and cryo cross-section polishing. The final section of this Chapter discusses the preparation of slurry samples for cryo-SEM imaging. These methods include high-pressure freezing and plunge freezing.

Chapter 5 describes the analysis of SEM images to obtain information about the microstructure of mudrocks. The chapter begins with a brief discussion of the basic steps used in image analysis, as well as the resolution of SEM technique. The next section introduces the Integration of Magnifications (IOM) method, developed in this investigation to obtain representative information about the pore space of mudrocks. This method combines information obtained from images at different magnification to represent the entire length scale of mudrock porosity. The new method will circumvent the need to stitch together hundreds of images to provide representative information about mudrocks. The IOM method was first validated using 2-D simulations, which consists of using a synthetic microstructure to simulate the process of imaging. The last section shows an example application of the IOM method on mudrock samples to obtain porosity and pore size distribution information.

Chapter 6 presents the results obtained about the microstructure of GOM-EI and BBC clay slurries. The first section summarizes the experimental program performed to investigate the microstructure of clay slurries. The next section presents the result obtained for plunge-frozen clay slurries. In particular, the influence of the plunge-freezing method on the microstructure of GOM-EI slurries is discussed in detail, including the influence of parameters such as the cooling rate, ice segregation, and sublimation. The microstructure of plunge-frozen GOM-EI and BBC clay slurries is then presented. The last section discusses the results and provides interpretations for the observed behavior.

Chapter 7 presents the imaging results of resedimented mudrock samples. The Chapter begins with a summary of the experiments performed to investigate the microstructure of oven-dried and wet mudrock samples. The next section presents a qualitative description of the microstructure of oven-dried and wet mudrock samples. The porosity measurements performed in this investigation are then presented. These measurements include SEM imaging porosity, MIP porosity, wet lab porosity, and oven-dried lab porosity. The influence of drying shrinkage

on the microstructure is then discussed. Finally, the influence of consolidation stress on the pore space of mudrocks is presented.

Chapter 7 summarizes the main conclusions which can be drawn from the results of the research. Lastly, recommendations for future work are discussed.

2 BACKGROUND

2.1 Introduction

This chapter briefly summarizes the published work related to the topics covered in this investigation. Section 2.2 discusses the utilization of SEM to characterize the microstructure of mudrocks. The first part of this section describes the use of SEM to provide qualitative information about the microstructure of mudrocks, while the second part describes the use of large mosaics of SEM images to obtain representative and quantitative information about the microstructure of mudrocks. Section 2.3 discusses the use of MIP technique to address the influence of the consolidation stress on the evolution of the pore space of mudrocks. Finally, Section 2.4 discusses the use MIP and SEM techniques to investigate the influence of drying shrinkage on the microstructure mudrocks.

2.2 SEM Imaging of the Microstructure of Mudrocks

Scanning Electron Microscopy (SEM) has been widely used to investigate the microstructure of mudrocks. The utilization of SEM to investigate the microstructure of mudrocks gained popularity after the development of milling techniques such Broad Ion Beam (BIB) milling and Focused Ion beam (FIB) milling. These techniques provide flat surfaces for imaging, and enable the detection of features on the order of nanometers. The detection of these features was previously limited by sample preparation techniques such as mechanical polishing and fractured surfaces. SEM investigations of mudrocks focused mainly on describing the microstructure in terms of the spatial distribution of minerals and pore morphology at the micro scale (Desbois et al., 2009; Loucks et al., 2009, 2012; Schieber, 2010; Sondergeld et al., 2010; Keller et al., 2011; Slatt and O'Brien, 2011; Chalmers et al., 2012; Curtis et al., 2012). These studies used SEM images acquired for relatively small areas, and hence they provided a qualitative description of the microstructure of mudrocks. Small fields of view are not considered representative because mudrocks are very heterogeneous and contain pores and particles that range in size from nanometers to microns. A few studies used mosaics of hundreds of images to obtain representative information about the microstructure of mudrocks (Klaver et al., 2012, 2015; Giffin et al., 2013; Hemes et al., 2013, 2015; Houben et al., 2013, 2014). This technique

28

was used to obtain information such as porosity, pore size distribution, and mineralogy. Hemes et al., (2015) combined BIB representative mosaics with FIB-SEM and X-ray μ-CT 3D volumes to investigate the pore space of Boom Clay across several length scales. Furthermore, because the BIB SEM mosaics provided representative results about mudrocks, it was possible to compare these results with other techniques such as Mercury Porosimetry Intrusion (MIP). The following sections provide details about these studies.

2.2.1 Qualitative Description of the Microstructure

The qualitative utilization of SEM to describe the microstructure of mudrocks focused mainly on spatial distribution of minerals and pore morphology and types. For example, several studies provided classification schemes for the pores based on their occurrence and location within the mineral matrix (Desbois et al., 2009; Loucks et al., 2009; Milner et al., 2010; Schieber, 2010; Heath et al., 2011; Slatt and O'Brien, 2011; Curtis et al., 2012). Loucks et al. (2012) compiled data published in the literature for variety of shale formations, and provided a general pore classification that categorized pores into three types: interparticle pores (interP), intraparticle pores (intraP), and organic matter pores (OM). The definition of these pores is summarized in a schematic in Figure 2-1. They also concluded that the pore network for each mudrock consists of a combination of different pore types, which in turn depends on mineralogy and texture. Furthermore, SEM imaging of flat milled surfaces was used to investigate the texture of kerogen (organic matter) in shale rocks (Loucks et al., 2009; Milner et al., 2010; Schieber, 2010; Sondergeld et al., 2010; Curtis et al., 2012). These studies revealed the porous nature of kerogen and showed that its texture is complex, and a function of maturity (e.g., see Figure 2-2, Figure 2-3, and Figure 2-4). Several authors used FIB-SEM serial cross-sectioning technique to construct 3D volumes on the order of 10 μm^3 of shale and mudrock samples (Desbois et al., 2009; Curtis et al., 2010; Holzer et al., 2010; Keller et al., 2011). For example, Keller et al., (2011) utilized FIB-SEM to investigate the 3D structure of three Opalinus clay samples. They used the constructed 3D volumes to determine parameters such as orientation of the pore space, length of pore paths and tortuosity. Because the volumes used were small (~10 μm^3), these investigations provided qualitative conclusions about mudrocks.

2.2.2 Representative Elementary Area (REA)

A few studies used large mosaics of SEM images to obtain representative information about the microstructure of mudrocks (Klaver et al., 2012, 2015; Hemes et al., 2013, 2015; Houben et al., 2013, 2014) and the microstructure of coal (Giffin et al., 2013). These studies used large BIB milled surfaces to acquire hundreds of images and stitch them together to obtain large areas. Mosaics of relatively low magnification Backscattered SEM images (BSE) were used to calculate the volume fractions of different minerals. On the other hand, mosaics of high magnification Secondary Electron (SE) images were used to characterize the pore space down to the resolution of SEM. In these mosaics, the obtained resolution is a function of the chosen magnification and the practical pore resolution (PPR). PPR refers to the minimum number of pixels required to properly quantify pores. For example, Klaver et al., (2012) and Hemes et al. (2013) used a PPR value of 10 pixels at a magnification of 30 KX, which resulted in a resolution of 36 nm. See Table 2 in Giffin et al. (2013) and Hemes et al. (2013) for more examples of the relationship between the chosen magnification and the obtained resolution. The magnification used to form the mosaics is usually chosen based on practical considerations such as the number of images required to obtain a large area. For example, Houben et al., (2013) showed that the number of images required for one REA is 3, 200, and 800 for magnifications of 3 KX, 25 KX, and 50 KX, respectively. The author also considered 500 images to be a realistic number for one mosaic.

Once the mosaic has been obtained, the REA was then determined using the box counting method based on porosity and mineralogy (Kameda et al., 2006). In this method, a stepwise growing box is placed on the mosaic to perform porosity and mineralogy calculations (see Figure 2-5). The REA represents the area above which the area fraction of minerals and pores does not vary significantly. The obtained REA in the above studies ranged from 61x61 μm^2 to 250x250 μm^2 depending on the studied samples (Table 2-1). The REA was then used to calculate information of interest such as mineralogy and porosity. The pore size distribution was described using the concept of fractal geometry (Desbois et al., 2009). The following discussion is based on Klaver et al., (2012). In this technique, pore area is presented as a function of the normalized discrete frequency as follows:

$$\frac{N_i}{b_i S_{mosaic}} = CS_{pore}^{-D} \qquad (2\text{--}1)$$

where N_i is the number of pores with pore area S_{pore} within bin b_i. S_{mosaic} is the area of the mosaic, C is a constant and D is a power law exponent. Equation (1-1) can rewritten in the form:

$$\log\left(\frac{N_i}{b_i S_{mosaic}}\right) = -DLog\left(S_{pore}\right) + LogC \qquad (2\text{--}2)$$

The parameters C and D can be calculated by fitting a line to the pore size distribution data between the largest pore visible in the SEM mosaics and PPR (Figure 2-6). This method can be used to compare pore distributions of different samples and mosaics. Furthermore, it can be used to extrapolate the pore space to account of pores below the resolution of SEM by assuming that the non-visible pores follow the same power-law distribution.

The above method was used to calculate information of interest from representative BIB mosaics. In particular, porosity was calculated for several samples from different origins (Table 2-1). In these studies, the porosity was calculated for the different mineral phases present in the sample such as clay minerals, quartz, and fossils. See Table 2 in Hemes et al. (2013) for an example of the different porous phases identified in different samples. In these studies, clay porosity was found to be the dominant type of porosity in almost all samples (Table 2-1). Furthermore, because the method provides representative information, it was possible to compare the calculated porosity from BIB mosaics to other methods such as Mercury Porosimetry Intrusion (MIP). In the MIP measurements, pores larger than the maximum diameter observed in SEM mosaics were removed, and assumed to be associated with surface roughness and cracks. In all of these studies, the visible SEM porosity was found to be less than MIP (Table 2-1). This discrepancy was attributed to the resolution differences between the two techniques. While the minimum pore diameter measured in BIB mosaics is a function of the used magnification and PPR, the minimum pore diameter measured by MIP is approximately 3 nm. To account for this difference, the pore size distribution power-law calculated from the BIB mosaics was used to extrapolate pore sizes down to 3 nm (Figure 2-6) (Table 2-1). Studying different shale samples, Klaver et al., (2015) found that the extrapolated SEM porosity is in general agreement with MIP porosity for shale samples. In contrast, Klaver et al., (2012) found that the extrapolated porosity is higher than MIP porosity, and attributed the discrepancy to the

31

unconnected part of the porosity resolvable by MIP. Houben et al., (2014) found that the extrapolated SEM porosity is in agreement with water content porosity, but higher than MIP porosity (Table 2-1). Hemes et al. (2013) calculated MIP porosity within the pore sizes visible in BIB mosaics. They found that the calculated MIP porosity is higher than SEM porosity, and attributed the discrepancy to larger pores and cracks due to sample drying, and concluded that BIB SEM porosity is not representative of larger pores and cracks.

In summary, the above studies revealed important trends regarding the porosity obtained using SEM imaging (see Table 2-1). The visible SEM porosity is less than the porosity calculated from other methods such as MIP and water-loss measurements. The porosity associated with the clay matrix was found to be the most dominant type of porosity in almost all studied mudrock and shale samples. Furthermore, the calculated REA differed significantly form one sample to another, and there was no attempt to relate the REA to sample properties such as clay mineralogy and particle sizes. Most importantly, these studies attributed the discrepancy between SEM porosity and MIP porosity to differences in resolution between the two methods. They used a power-law distribution to extrapolate the pore size distribution down to a pore size of 3 nm to account for the missing pores due to SEM resolution. The extrapolated porosity was then compared with MIP porosity and water-loss porosity. In some cases, the extrapolated porosity was less than the MIP porosity, and in other cases it was more than the MIP porosity. These differences were used to infer information about the microstructure of mudrocks, such as pore connectivity and the amount of cracks in the studied samples.

2.3 Influence of the Consolidation Stress on the Microstructure of Mudrocks

Several studies investigated the influence of the consolidation stress on the microstructure of mudrocks. The microstructure of mudrocks was described mainly in terms of the pore space characteristics measured using MIP. The application of SEM technique to address the influence of the consolidation stress on the microstructure was limited by the available sample preparation techniques such as broken surfaces. These techniques limited the resolution and the quality of SEM images, and as a consequence the quality of information that can be extracted from these images. Therefore, MIP has been the main technique used to investigate the development of the microstructure of mudrocks with stress. Furthermore, MIP was performed on freeze-dried samples, and the authors assumed that freeze drying preserves the microstructure.

The following paragraphs summarize the main studies that addressed the influence of the applied stress on the microstructure of mudrocks.

Delage et al., (1984) utilized MIP and SEM to investigate the influence of different consolidation stresses on the evolution of the pore space of sensitive Champlain clay under consolidation stresses that ranged from 23 to 1452 KPa. They concluded that only the largest macro pores collapse under a given stress, while the small intra-aggregate pores are not affected until all macro pores have been collapsed (Figure 2-7a). Al-Mukhtar et al., (1996) investigated the development of the pore space of Boom clay (62% clay fraction) under different consolidation stresses of: 1 MPa, 5 MPa, and 15 MPa. The authors showed that the applied stress reduced larger pores before reducing the smaller pores (Figure 2-7b). Qi et al., (1996) used MIP and BET nitrogen adsorption techniques to study the influence of consolidation on the pore space of Na-laponite clay. They showed that for consolidation stresses that ranged from 1 to 10 MPa, the applied stresses reduced macro pores larger than 50 nm, while pores smaller than 50 nm remain unchanged (Figure 2-7c). Griffiths et al., (1989) studied the fabric evolution under consolidation stress of four different soils of different mineralogy and liquid limits. Each soil was consolidated to 0.03, 0.12, 0.45, and 1.5 MPa. They showed that an increase in stress reduced the total porosity of samples, which was due to the reduction of the volume of the largest pores. Intra-aggregate pore space or pore space between clay minerals did not change with increasing consolidation stress. Dewhurst et al., (1998) studied two London clay samples with different clay fractions (67% and 40%). Samples were subjected to consolidation stresses that ranged from 1 to 33 MPa. Similar to other studies, the authors showed that as the consolidation stress increases larger pores collapse and small pores remain unaffected.

In summary, studies that addressed the influence of the applied stress on the microstructure of mudrocks utilized MIP as the main technique to describe the evolution of the pore space. The MIP measurements were performed on freeze-dried samples, and the authors assumed that freeze drying preserves the microstructure of mudrock samples. Furthermore, all of these studies showed that an increase in the applied stress leads to the collapse of large macro pores, with very little to no effect on the small micro pores. The separation between macro and micro pores differed from one study to another. In general, macro pores usually refer to inter-aggregate pores while micro pores refer to intra-aggregate pores or pores between clay particles.

2.4 Influence of Drying Shrinkage on the Microstructure of Mudrocks

Drying shrinkage is an important phenomena in geotechnical engineering and soil science. Fine-grained rocks and soils undergo dramatic volume changes due to drying shrinkage. Studies related to drying shrinkage in soil science can be divided into three main categories. First, studies that focused on the understanding of shrinkage driving forces and the resulting desiccation cracks under various boundary conditions (Scherer, 1990; Peron et al., 2009; Shin and Santamarina, 2011; Tang et al., 2011; Hu et al., 2013a, 2013b). Second, studies that utilized MIP to investigate the evolution of the pore space as a result of shrinkage at specific suction values (Simms and Yanful, 2001, 2002; Cuisinier and Laloui, 2004; Koliji et al., 2006; Romero, 2013; Wei et al., 2013). Third, studies that addressed the influence of drying shrinkage on the microstructure of mudrocks and soils in the context of sample preparation methods. This topic is of particular importance to this study because samples have to be oven-dried for SEM imaging. Understanding the influence of drying shrinkage is thus crucial for obtaining meaningful results from SEM images. Studies that addressed the influence of drying shrinkage on the microstructure of mudrocks and soils utilized two techniques: MIP and SEM. The following sections summarize the main conclusions of these studies.

Several drying methods can be used to prepare samples for MIP and SEM measurements. These methods include oven drying, air drying, and freeze drying. Oven drying involves drying the sample in an oven at a specified temperature. For example, several studies use 110°C for 24 hours as their drying procedures. Air dying involves leaving the sample at room temperature for a specified period of time, which ranges from days to weeks. On the other hand, freeze drying involves first plunging the sample in liquid cryogen such as liquid nitrogen to freeze the water in the pore space. The frozen samples are then sublimated under controlled temperature and pressure. Studies that use freeze dying assume that the freezing step vitrifies the water in the pore space and prevents ice crystallization and associated volume changes that may alter the microstructure.

2.4.1 MIP Studies

Delage et al., (1984) showed that the natural water content of two intact sensitive Champlain clay samples obtained using phase relations (83.3%, 76.9%) is similar to the volume

of intruded mercury (84.4 mm3/g, 75.1 mm3/g). The same agreement was obtained for remolded samples. They also presented SEM images of freeze-dried samples and concluded that freeze drying preserves the microstructure of clay samples (Figure 2-8a, b). Furthermore, to investigate the influence of oven drying on the microstructure, they compared the Pore Size Distributions (PSD) of freeze-dried intact clay samples with the PSDs of oven-dried intact and remolded clay samples (Figure 2-8c). They showed that samples undergo dramatic shrinkage upon drying. This shrinkage results mainly from the disappearance of large pores, and a slight change to the size of small pores.

Sasanian et al., (2013) investigated the influence of air drying on the microstructure of clay slurry samples at different moisture contents. Two types of clay samples were investigated: EPK Kaolin and Nanticoke clay. The former is a commercially available pulverized Kaolin clay, while the latter contains 48% clay fraction of illite and chlorite. To prepare samples with moisture content higher than the plastic limit, clay powder was mixed with water at the target water content. For samples with a moisture content less than the plastic limit, the moisture content was reduced in accordance with ASTM D2216-05. The authors assumed that freeze drying preserves the microstructure of clay samples based on previous studies, and they used the results obtained on freeze-dried samples as a reference. The Nanticoke clay sample with high moisture content (98%) exhibited a dramatic reduction of pore volume after air drying, which resulted from the collapse of all pores above 160 nm (Figure 2-9a, b). EPK Kaolin clay samples collapsed to the same total pore volume regardless of the initial moisture content. This pore volume reduction resulted from the collapse of pores larger than 400 nm. Furthermore, they concluded that MIP of freeze-dried samples accurately measures the moisture content of samples for moisture content values less than 50%.

Burton et al., (2015) investigated the influence of air drying and oven drying on the microstructure of undisturbed and consolidated Maryland clay samples. They compared PSD obtained using MIP of freeze-dried samples and air-dried samples. The total pore volume of the undisturbed samples was reduced due to drying, and the pore volume reduction appeared as a shift in the dominant pore diameter from 0.07 to 0.04 μm. The consolidated samples exhibited a dramatic reduction in the pore volume, which was caused by a shrinkage of the dominant pore diameter from 3 μm to 0.08 μm. These results show that drying shrinkage lead to the collapse of large pores of the undisturbed and the consolidated samples.

Simms et al., (2002) investigated the evolution of the pore space of a compacted Regina clay sample and an undisturbed Sarnia clay sample at different suction pressures. Furthermore, the authors investigated the influence of oven drying and air drying on the microstructure of the clay samples. They showed that all air-dried and oven-dried samples have identical PSDs regardless of the initial water content (Figure 2-10). For Sarnia clay, the dried PSDs were identical to those measured after a suction pressure of 2.5 MPa (Figure 2-10b). In contrast, the PSD of Regina clay changed dramatically after a suction pressure of 2 MPa, and after air and oven drying (Figure 2-10a). This difference in behavior was attributed to the high smectite content of Regina clay (28%) compared to that of Sarnia clay (1%). In both samples, the shrinkage was caused by the collapse of large pores.

Thompson et al., (1985) investigated the effect of drying on the microstructure of three different soil samples with different clay fractions. The samples were investigated in two conditions: undisturbed and compacted. The authors utilized MIP and measured the porosity of samples dried in three different ways: freeze-dried, acetone-dried, and oven-dried. The initial porosity was calculated using water content measurements, and considered as the reference porosity (Figure 2-11a, b). They showed that the relative decrease in porosity of freeze-dried samples range from 3% to 17% for the compacted samples (Figure 2-11b), and from 17% to 22% for the undisturbed samples (Figure 2-11a). On the other hand, the relative decrease in porosity of the oven-dried samples ranged from 19% to 25% for the compacted samples, and from 38% to 52% for the undisturbed samples. Furthermore, PSD measurements showed that the dominant pore size interval in freeze-dried samples (0.2-2 μm) is significantly reduced upon drying, and the small pores are unaffected. The authors did not rule out the possibility of ice formation during freezing of samples, and pointed out that the process of freezing might have changed the PSD of freeze-dried samples.

Al-Mukhtar et al., (1996) reported the porosity of Boom clay samples at three different consolidation stresses obtained using MIP of freeze-dried samples, as well as the porosity obtained using water content measurements. The porosity of freeze-dried samples was approximately 40% less than the porosity obtained using water content measurements (Figure 2-11c). The authors did not explain the discrepancy between the two measurements. Dewhurst et al., (1998) studied two London clay samples, a clay-rich sample and a silt-rich sample, at different consolidation stresses (1 to 33 MPa). The authors showed that the water-content

36

porosity of the silt-rich sample is identical to that measured using MIP of freeze dried samples. On the other hand, the water-content porosity of the clay-rich sample (0.43-0.26, with effective stress) is higher than the MIP porosity of freeze-dried samples (0.34-0.21). This discrepancy was attributed to the pores smaller than 4 nm that are not measured in MIP.

In summary, studies that utilized MIP to address the influence of drying on the microstructure resulted in contradictory conclusions. While some studies showed that the porosity of freeze-dried samples measured using MIP is identical to that obtained using water content measurements, other studies showed that the porosity of freeze-dried samples obtained using MIP is significantly less than that obtained using water content measurements. Despite these differences, all of the above studies assumed that freeze drying preserves the microstructure of clay samples. Furthermore, all of the above studies showed that oven drying and air drying cause a dramatic reduction in pore volume. The reduction in pore volume results from the collapse of large pores, while small pores remain unchanged. Comparing the influence of the applied stress and shrinkage on the microstructure of mudrocks, the above studies show that the response of the microstructure to these conditions is similar. Also, these studies used MIP as the main technique to investigate the microstructure of mudrock samples.

2.4.2 SEM Studies

Although SEM might seem the suitable technique to address the influence of drying on the microstructure of mudrocks, only a few studies utilized SEM for this purpose. This is because sample preparation techniques to prepare artifact-free flat surfaces became available only recently. In particular, the use of BIB and FIB ion milling techniques has enabled the preparation of such surfaces. The following paragraphs provide a summary of the studies that used SEM to investigate the influence of drying on the microstructure.

Desbois et al., (2009) compared SEM images of oven-dried and plunge-frozen Boom clay samples. The frozen samples were plunged in liquid nitrogen, and the freezing procedure was assumed to preserve the microstructure and prevent ice crystallization. The authors used BIB milling to prepare flat surfaces for the oven-dried samples, and cryo-FIB to prepare flat surfaces for the plunge-frozen samples. The frozen samples were sublimated inside a cryo-SEM to remove surface ice for imaging. Although a shrinkage of approximately 10% was reported, the authors concluded that there is no difference in pore morphology between the frozen and oven-

dried samples. Holzer et al., (2010) investigated the suitability of preparation methods for SEM imaging on a Bentonite slurry sample with a water content of 220%. The volume of free water in this sample was estimated to be around 75%. After oven drying and freeze drying, the samples were impregnated with epoxy and mechanically polished for SEM imaging. The calculated SEM porosity of the oven-dried samples was approximately 25%, which lead the authors to conclude that the material underwent dramatic drying shrinkage due to oven drying. Furthermore, the authors showed that the microstructure of the freeze-dried sample is highly porous. The porous structure was attributed to crystallization during freezing. The authors then concluded that freeze drying is unsuitable for material preparation. It is worth mentioning that this conclusion is only applicable for similar samples with high water content. The formation of ice crystals during freezing is strongly dependent on water content, and crystals may not form in samples with low water content (Moor, 1987).

Houben et al., (2013) investigated the influence of drying method on the microstructure of Opalinus clay samples. The authors compared the microstructure of samples prepared using three different methods: air drying, oven-drying, and freeze-drying. The air-dried samples were slowly dried at room temperature at a relative humidity of 35% for a month. The oven-dried sample was dried at 60°C for a week. The freeze-dried sample was first plunge-frozen in liquid nitrogen and freeze-dried for 24 hours at a pressure of 0.1 mbar and a temperature of -40°C. The authors concluded that the three drying methods do not show differences in the visible damage measured as the amount of cracks in the samples (Figure 2-12)

Desbois et al., (2014) utilized BIB-cryo-SEM to investigate the influence of sublimation drying on the microstructure of Boom clay samples. The clay samples were first plunge-frozen in nitrogen slush to fix the water in the pore space, before milling the samples using the BIB-cryo-SEM technique. This technique allows the milling of large flat surfaces inside an SEM at cryogenic conditions. The milled samples were heated from -160°C to 20°C inside the SEM to sublimate the water. Selected areas of the samples were imaged before and after sublimation to assess potential changes in the microstructure. The authors concluded that the microstructure revealed in the cryo-SEM images is comparable to similar samples prepared using BIB milling of oven-dried samples in other studies. Four types of damage mechanisms were identified due to sublimation drying. These mechanisms include breaks of clay-clay particle interfaces,

38

detachments at clay-clast interface, formation of cracks wider than 1 μm, and a slight increase of pore area. Statistical analysis of pore sizes and pore morphology before and after sublimation showed no difference. The authors then concluded that drying does not influence the microstructure of clay samples, and characterization of oven-dried samples is representative of the microstructure. Furthermore, the authors attributed the observed four types of damage to the swelling and shrinkage behavior of clay minerals. While the results of this study are interesting, the sublimation drying is not representative of oven drying and air drying. Surface tension forces are responsible for the shrinkage behavior of clay-dominated mudrocks. These forces result from interfaces between air and water, which in turn develop during the drying process. The main purpose of sublimation is to prevent the development of the air-water interface, and hence prevent the formation of surface tension forces. The results of this study are representative of the freeze drying technique, which uses sublimation to evaporate water from the pore space of mudrock samples.

In summary, the above studies concluded that drying shrinkage does not affect the microstructure of mudrock samples. These studies used plunge freezing in liquid nitrogen or nitrogen slush to preserve the microstructure of wet samples. These samples were then freeze-dried and imaged in a conventional SEM or sublimated and imaged inside a cryo-SEM. The conclusions of these studies contradict the conclusions of the studies that utilized MIP to investigate the influence of drying on the microstructure of mudrocks. While the SEM studies showed that there is no difference in the visible SEM porosity, MIP studies reported that large pores in the range of visible SEM porosity collapse upon drying. These contradicting conclusions will be discussed in detail in Chapter 7.

2.5 Structure of Clay Slurries

In this investigation, the studied mudrock samples are made in the lab using the resedimentation technique (e.g., Abdulhadi, 2009; Adams, 2014; Casey, 2014). This technique consists of subjecting clay slurries to 1-D compression until the desired stress state is reached. Understanding the structure of clay slurries will provide valuable insight about the processes that govern the development of the microstructure of mudrocks. Furthermore, several studies used clay slurries to understand the initial structure of clay minerals, and to infer the structure of clay minerals at early stages of deposition. This section provides a brief summary of these studies.

The interaction of clay particles in clay slurries is governed by repulsive electrostatic double layer forces and attractive van der Waals forces. The electrostatic double layer forms when negatively charged clay particles attract ions of the opposite sign, while van der Waals forces result from interactions between atoms and molecules in particles. Electrostatic double layer repulsion is a strong function of electrolyte concentration. The addition of electrolytes compresses the double layer and reduces repulsion (Van Olphen, 1977), which leads to the formation of clusters of particles due to flocculation and aggregation. Flocculation refers to the formation of edge-face, and edge-edge contacts between clay particles. Aggregation, on the other hand, refers to the formation of face-face contacts between clay particles (van Olphen, 1964). An increase in particle concentration leads to the formation of a continuous gel structure. The mechanisms responsible for the development of gel structure in clay slurries has been the topic of much debate with three main competing ideas: a cardhouse structure that favors the formation of edge-edge and face-edge contacts (Goldschmidt, 1926; Lambe, 1953; van Olphen, 1964; Khandal and Tadros, 1988), a band-type or honeycomb structure that postulates the formation of face-face contacts between clay particles to form a continuous 3D structure (Terzaghi, 1925; Casagrande, 1932; Weiss and Frank, 1961), and the stabilization of the gel structure due to electrostatic repulsion between clay particles. (Norrish, 1954; Callaghan and Ottewill, 1974). Studying Na^+-montmorillonite suspensions, Abend and Lagaly (2000) proposed the formation of repulsive gel at low salt concentration in which the gel structure is maintained by double layer repulsion between particles. At high salt concentrations, the repulsive gel transforms into an attractive gel in which the gel structure is dominated by attractive van der Waals forces. These models have been formulated based on rheological observations of clay suspensions.

Direct imaging of the microstructure of clay suspensions has not been successful due to sample preparation limitations. Conventional electron microscopy requires the removal of water from samples, which changes the native state of the material. The development of cryo electron microscopy has provided an attractive alternative to investigating clay suspensions in their native state. In this technique, the water is first cryoimmobilized using various freezing methods, with the main aim of achieving vitrification to prevent ice crystallization and, hence, preserve the microstructure. Plunge freezing has been one of the most widely utilized cryo techniques to immobilize aqueous samples and preserve the microstructure (see Dubochet et al., 1988 for a review). Several authors used this technique to investigate the structure of clay slurries and

40

showed the existence of a honeycomb structure at various conditions. Plunge freezing was followed by either freeze drying to remove water for conventional SEM imaging (O'Brien, 1971; Osipov and Sokolov, 1978; Stawinsk et al., 1990), or directly imaged using the cryo SEM technology (Zbik et al., 2008, 2010; Du et al., 2009, 2010; Morris and Żbik, 2009). See Figure 2-13 for examples of the imaged honeycomb structure. The results of these studies were used to postulate models for the fabric evolution of mudrocks. These studies postulated that the fabric of mudrocks starts with a honeycomb structure that gets deposited and compressed to form oriented fabric (Bennett et al., 1991; O'Brien and Pietraszek-Mattner, 1998; Slatt and O'Brien, 2011). Figure 2-14 presents a schematic of these proposed models.

These studies assumed that plunge freezing prevents ice crystallization and, hence, preserves the microstructure of clay slurries. The critical cooling rate required to prevent ice crystallization in plunge freezing is more than 100000 Ks^{-1} for cells and tissues (Bald, 1986; Bachmann and Mayer, 1987; Moor, 1987). Several researchers showed that it is only possible to immobilize 10 μm thick layer of the sample surface at atmospheric pressure (Dubochet et al., 1987; Moor, 1987; Studer et al., 1989). Vali and Bachmann (1988) used spray freezing and jet freezing to check the suitability of plunge freezing as well as the gelation mechanism of clay suspensions. They used jet freezing to prepare 100 μm thick clay samples, and spray freezing to prepare 10-50 μm clay droplets. The results of this study are questionable because spray freezing and jet freezing are only capable of preserving 20-30 μm and 10 μm thick samples, respectively (Echlin, 1992, p. 77). Holzer et al. (2010) showed that plunge freezing in liquid nitrogen produces segregation patterns in bentonite suspensions in comparison to high pressure freezing.

High pressure freezing has been extensively used to characterize aqueous biological samples because of its efficiency in suppressing ice crystallization (Dahl and Staehelin, 1989). In this technique, it is possible to preserve samples of 200 μm thickness (Studer et al., 1995, 2001, 2008). The application of high pressure before freezing lowers the freezing point of water, nucleation rate, and ice crystal growth. This in turn reduces the heat produced by crystallization, and as a consequence the heat removed from the sample (Moor, 1987). These changes reduce the cooling rate required for vitrification to a few 1000 Ks^{-1} (Studer et al., 1995, 2001). Despite its development in the past two decades, high pressure freezing has not been utilized to investigate the gel structure of clay suspensions.

41

Table 2-1: Summary of the investigations that used representative BIB mosaics to obtain information about the microstructure of mudrocks and their main conclusions.

Reference	Source of Samples	Samples	Total Clay Fraction [%]	REA [μm^2]	SEM Visible Porosity [%]	Corrected MIP Porosity [%]	Water content Porosity [%]	Extrapolated porosity [%]	Clay Porosity Contribution [%]
(Klaver et al., 2012)	Posidonia Shale	RWEP06	23	140x140	2.75	3.4-3.7		4.8	
		RWEP08	14		2.74	3.3-3.6		6.45	
(Hemes et al., 2013)	Boom clay	EZE52	34	125x125	16.9		36-39	Discrepancy of 40 %	33.3
		EZE54	61	61x61	10.4	26.4			88.1
		EZE55	51	91x91	12	26.6			85.4
		EZE64	28	125x125	19.9	32.1			8.7
(Houben et al., 2013)	Opalinus clay	BCS-2/1		100x100	1	13.3		13.4-28.9	70
		BCS-2/3			2.1				47
		BCS-2/5			2.69				51
(Houben et al., 2014)	Opalinus clay	Sandy facies clay	56	250x250	0.67-3.1	8.84-9.9	6.1-17.2	9.3-14.1	53-95
		Sandy facies carbonates	8.4						
		Sandy facies sand	14.4						
		shaly facies clay 1	57.2	180x180	0.9-2.35	11.56-13.01	12.6-24.7	15.5	49-62.5
		shaly facies clay 2	57.2						
(Klaver et al., 2015)	Haynesville shale	SBI 9-4	33	200x200	1.71	9.2		In the range of MIP data	
		SBI 8-2	35		1.36	7.5			
		SOM 4-4	28		1.58	9.2			
		SOM 9-2	44		0.75	8.3			
		SHSI 6-2	55		0.28	4.4			
	Bossier shale	SHSI 1-6	60		0.11	3.9			
		SCN 3-6	28		0.51	6.9			
		SMY 4-2	10		0.54	2.2			
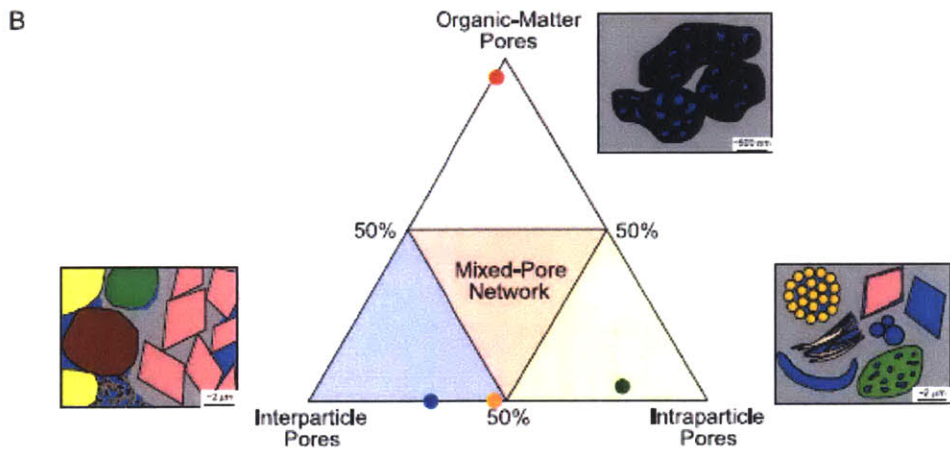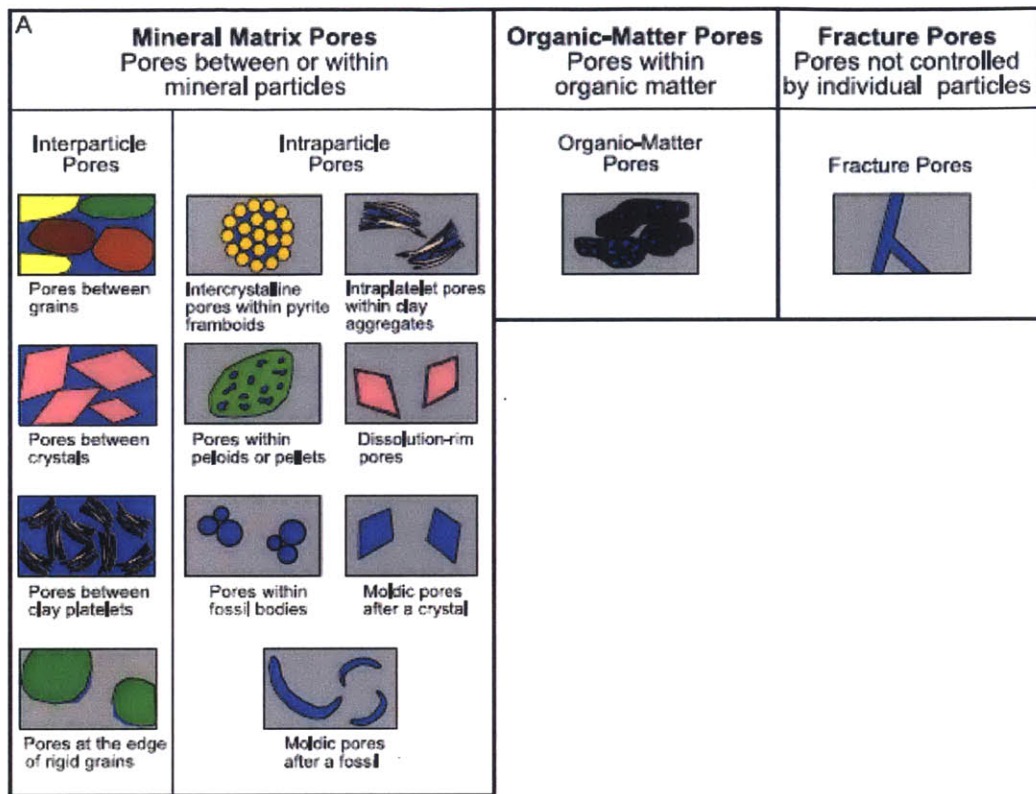
Figure 2-1: Summary of pore classification scheme proposed by Loucks et al. (2012).
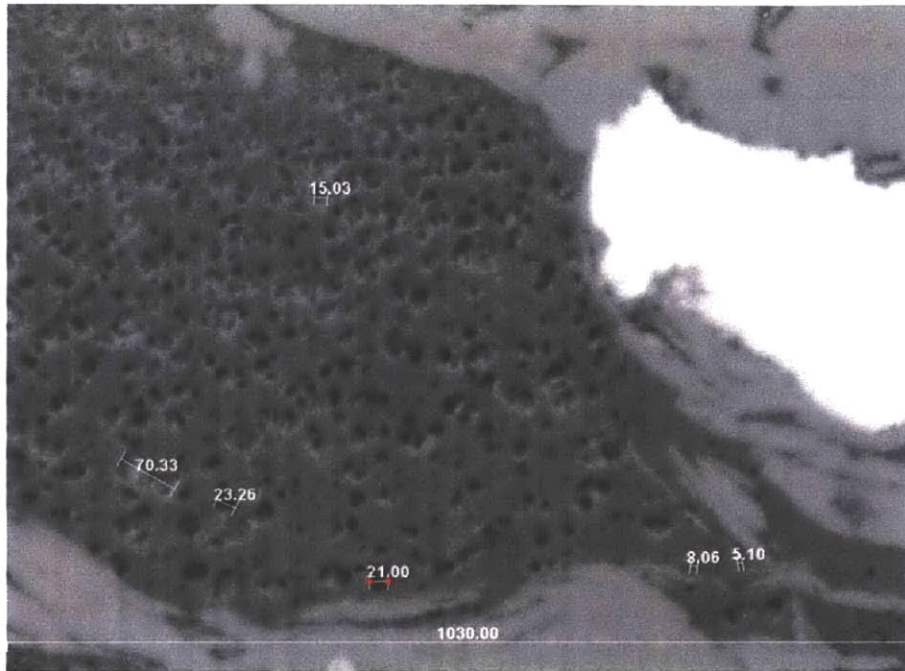
Figure 2-2: Backscattered SEM image (BSE) reveals the porous nature of kerogen (dark gray) in shale (Sondergeld et al., 2010).
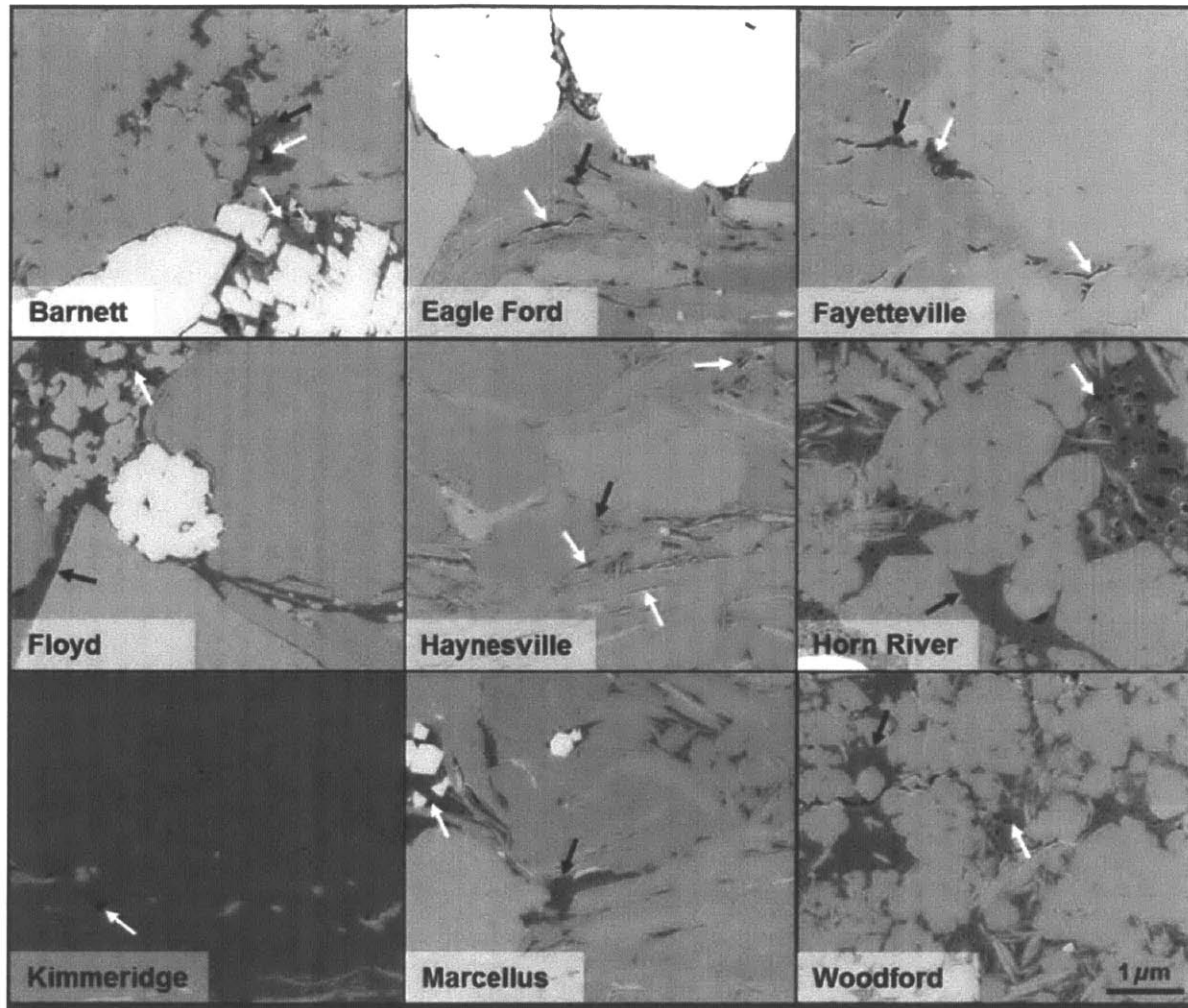
Figure 2-3: Backscattered SEM images of shale samples from different formations reveals the complex texture of kerogen (dark gray) (Curtis et al., 2012).
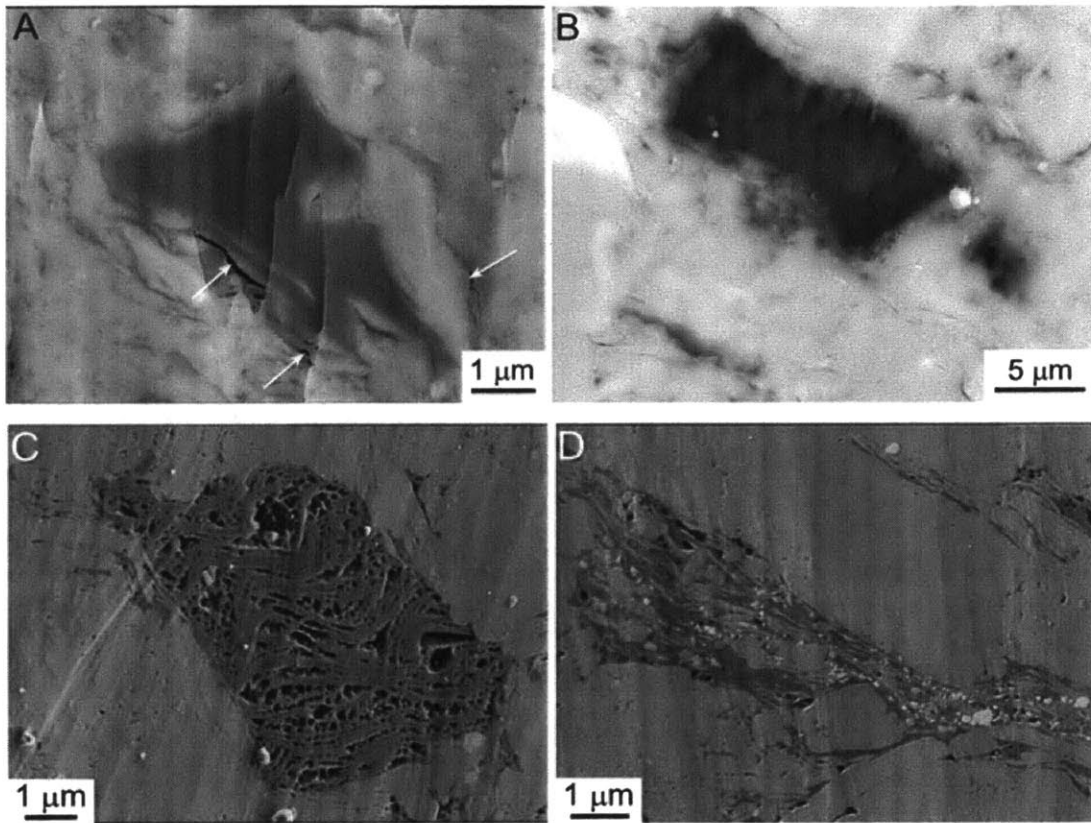
Figure 2-4: Backscattered SEM images that show the microstructure of kerogen as a function of maturity (Loucks et al., 2009).
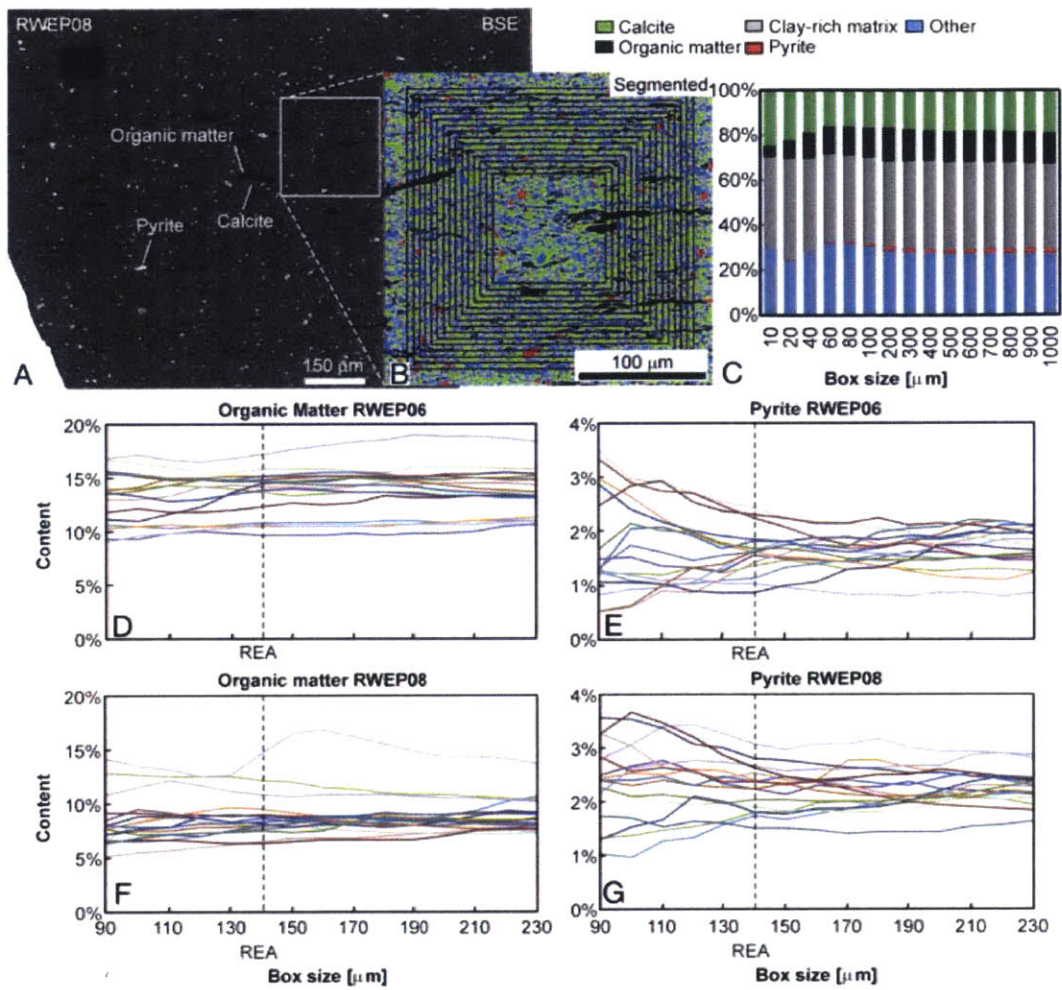
Figure 2-5: Calculation of Representative Elementary Area (REA) using box counting method (Klaver et al., 2012).
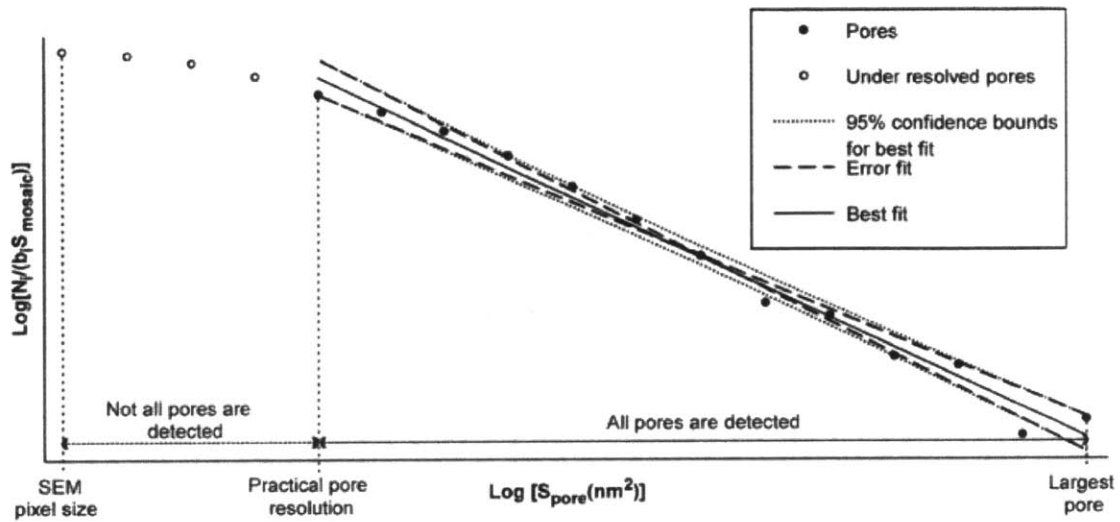
Figure 2-6: Illustration of the power law pore size distribution obtained using equation (1-2). Black-filled circles represent visible SEM pores above PPR, whereas empty circles represent extrapolated pores below the resolution of SEM. Lines represent best fit lines used to determine C and D parameters in equation (2-2) (Klaver et al., 2012).
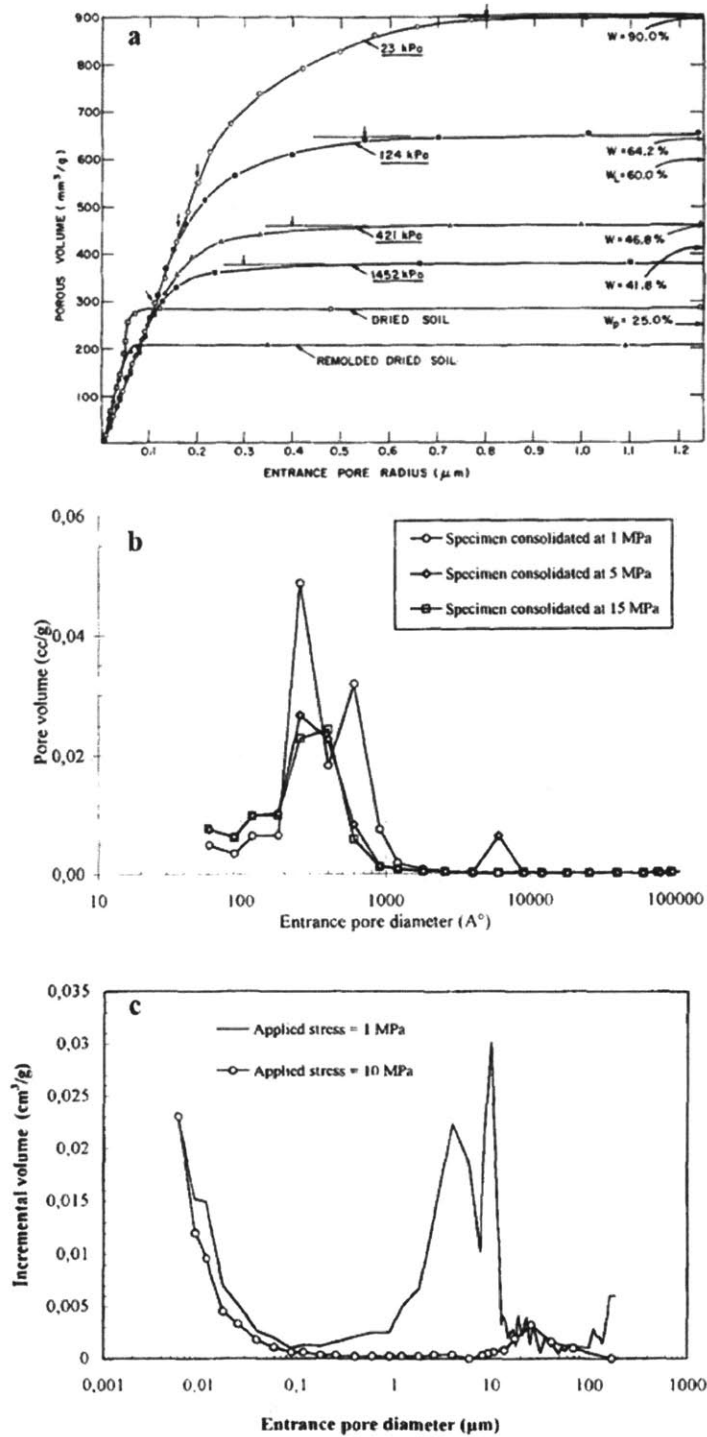
Figure 2-7: Consolidation influence on the MIP pore size distribution for: a) sensitive Champlain clay (Delage and Lefebvre, 1984), b) Boom clay (Al-Mukhtar et al., 1996), and c) Na-laponite clay (Qi et al., 1996).
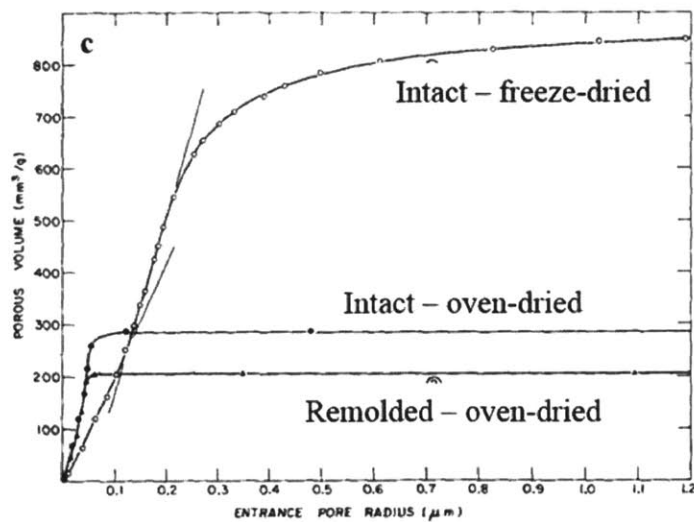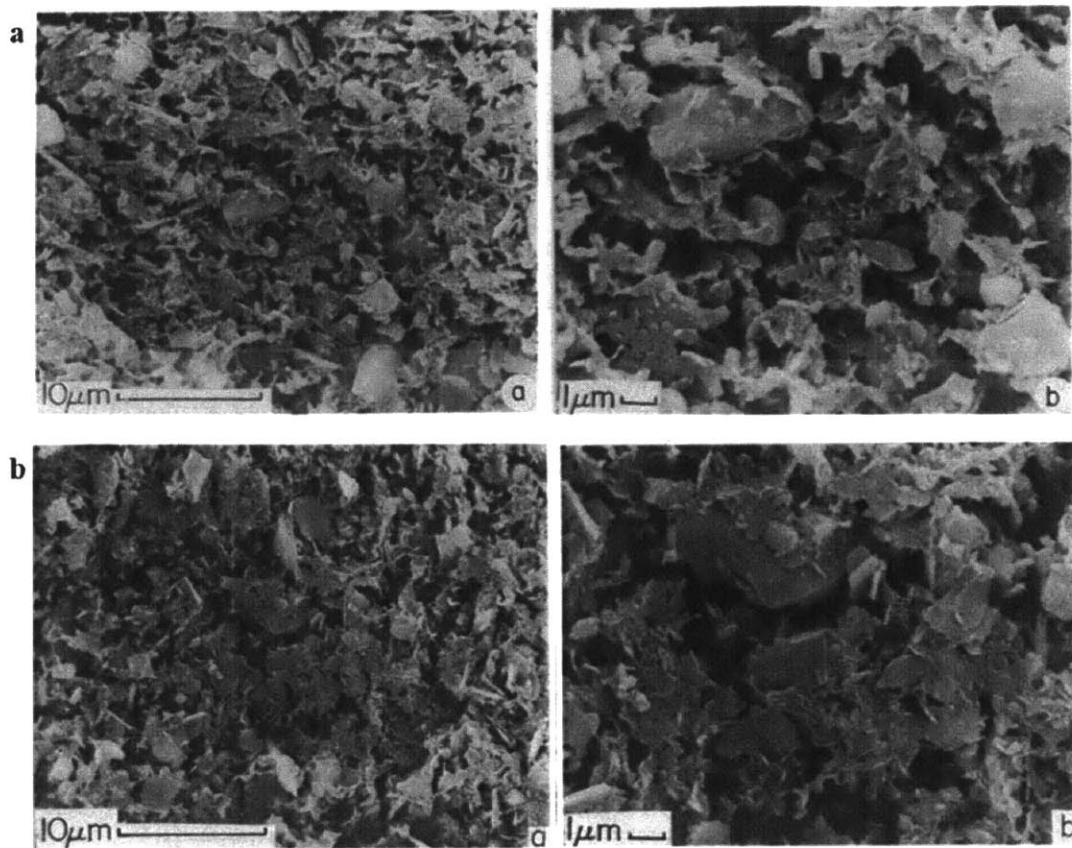
Figure 2-8: a) freeze-dried SEM images of an intact sensitive Champlain clay samples, b) freeze-dried SEM images of a remolded Champlain clay sample, and c) PSD obtained using MIP for

intact freeze-dried sample, intact oven-dried sample, and remolded oven-dried sample (Delage and Lefebvre, 1984).
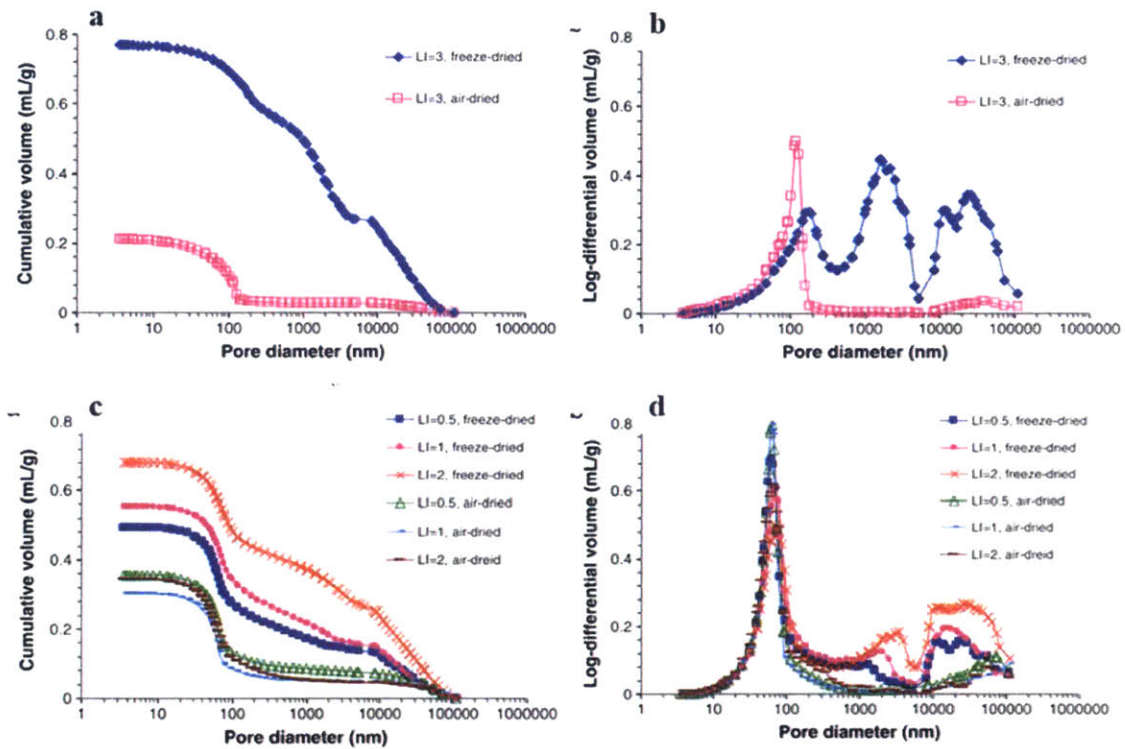
Figure 2-9: a, b) PSD obtained using MIP for freeze-dried and air-dried Nanticoke clay sample with a moisture content of 98% (LI=3). c, d)) PSD obtained using MIP for freeze-dried and air-dried EPK clay samples with different moisture contents of 48.5% (LI=0.5), 61% (LI=1), and 86% (LI=86) (Sasanian and Newson, 2013).
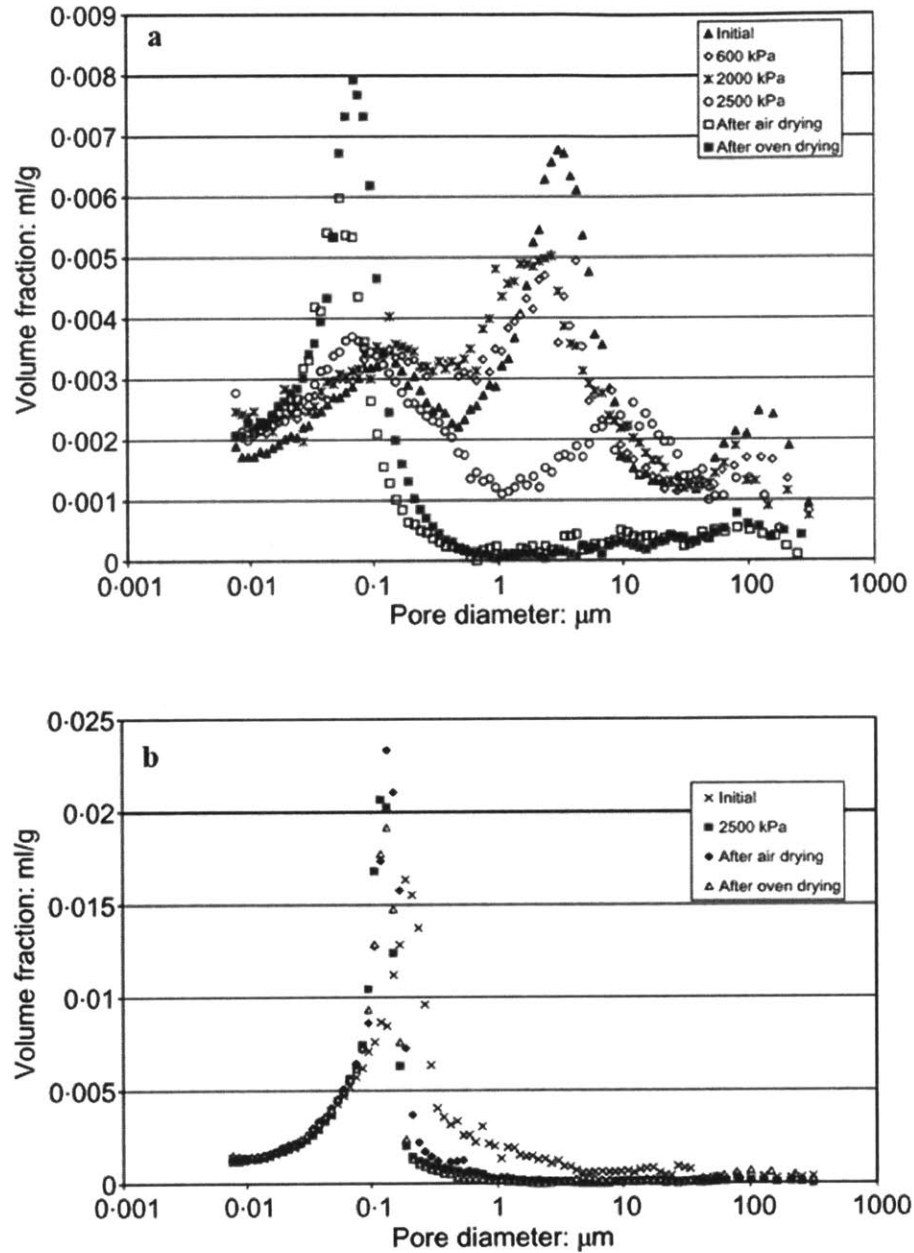
Figure 2-10: Pore size distribution obtained using MIP at different suction pressures of a) a compacted Regina clay sample from Canada, and b) and an undisturbed Sarnia clay from Canada. Regina clay contains 46% clay size while Sarnia clay contains 45% clay size (Simms and Yanful, 2002).
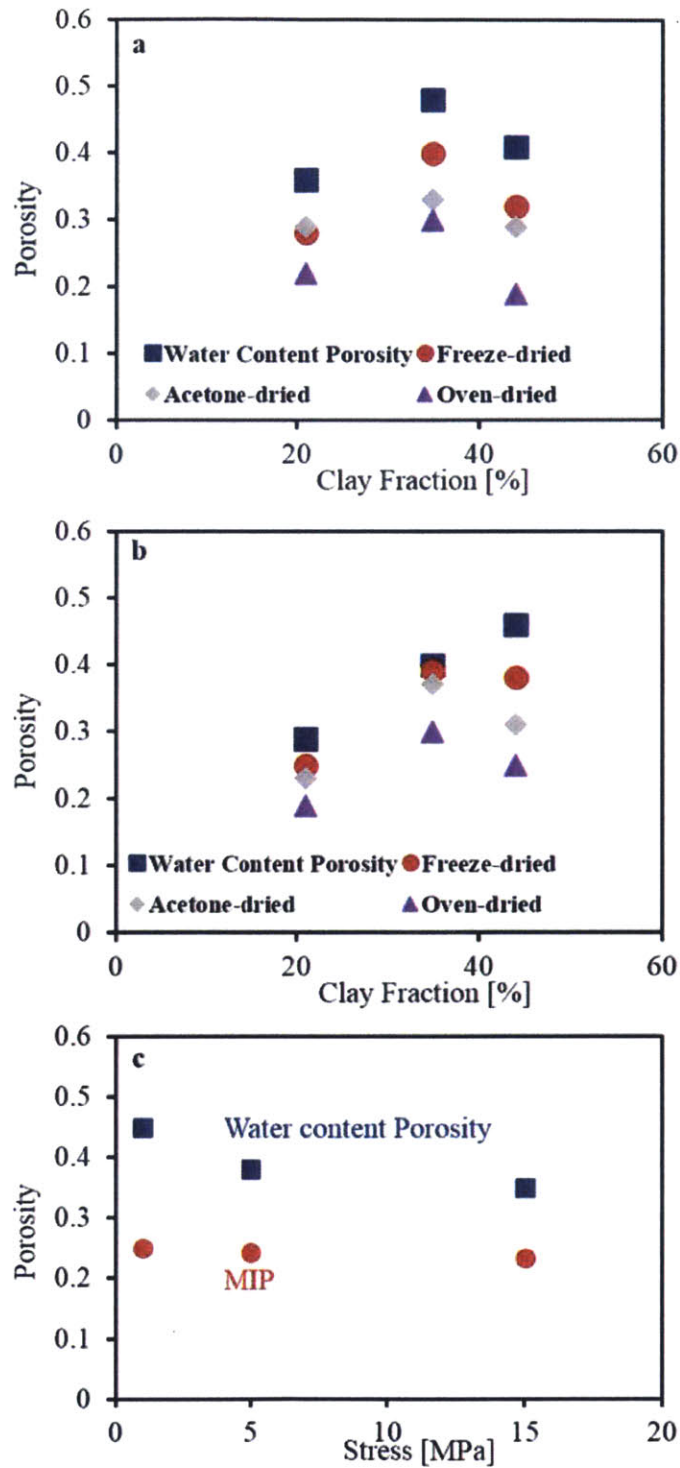
Figure 2-11: Porosity values obtained using different methods published by (Thompson et al., 1985) for three clay samples at different conditions a) undisturbed and b) compacted. c) Summary of porosity values obtained for Boom clay by (Al-Mukhtar et al., 1996) using water content measurements and MIP test.
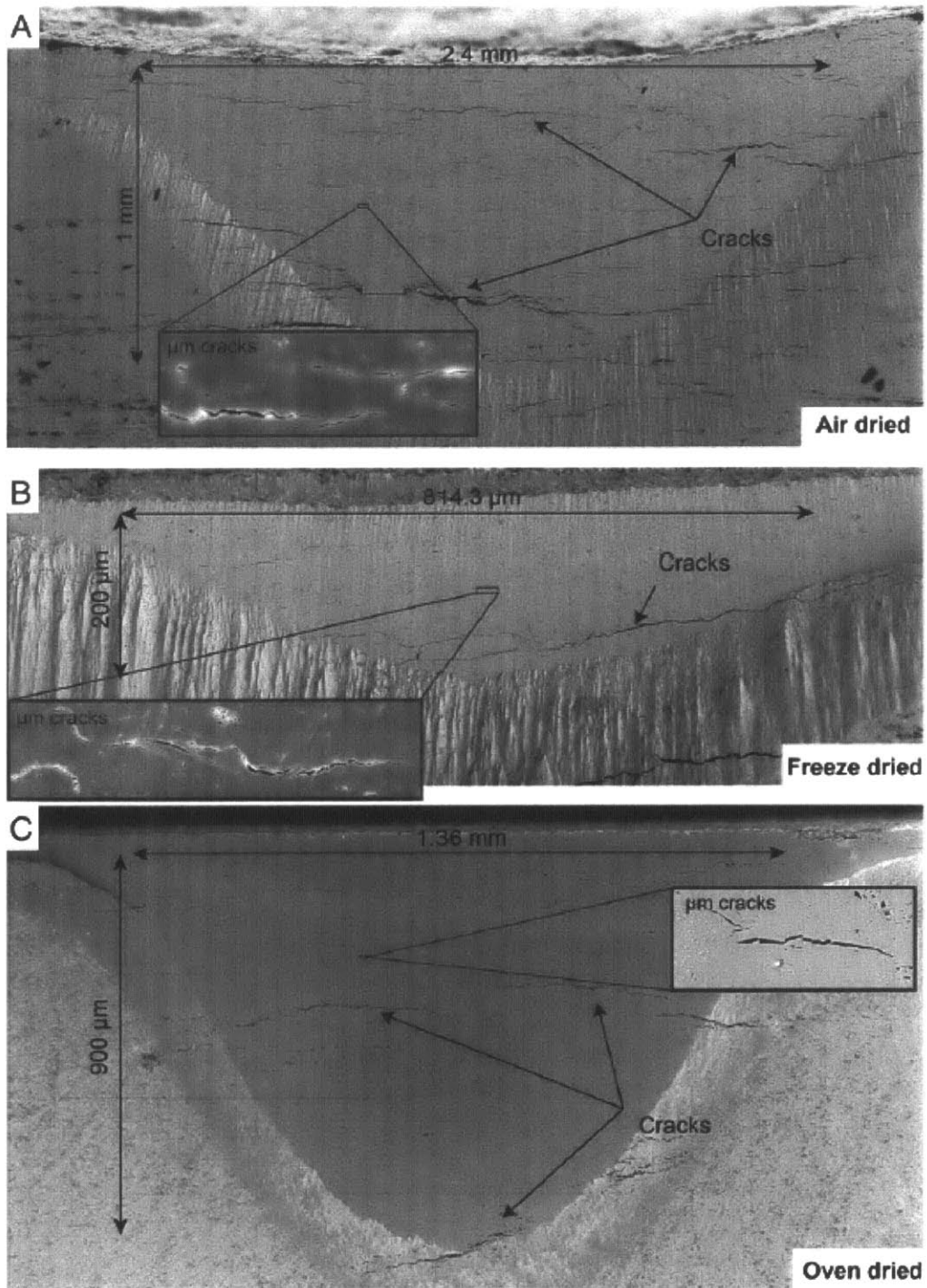
Figure 2-12: Milled surfaces of Opalnius clay samples dried using three different methods (Houben et al., 2013).
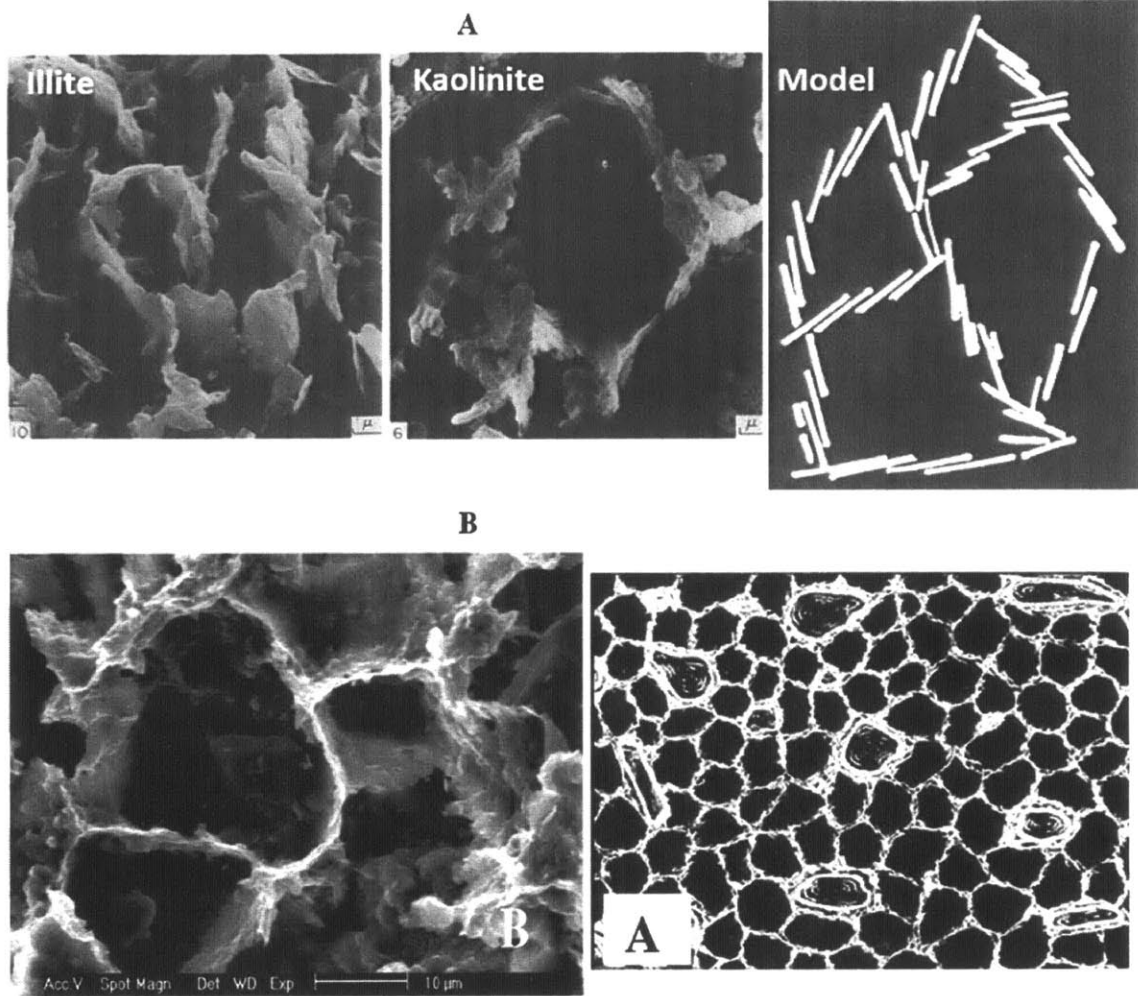
Figure 2-13: A) Microstructure of illite and kaolinite slurries determined using freeze drying and conventional SEM imaging (O'Brien, 1971), and B) Microstructure of kaolinite-smectite slurry determined using plunge freezing and cryo-SEM imaging (Zbik et al., 2010).

a

FLOCCULATED

DISPERSED

Model 1

Model 2

b

A

B

gas
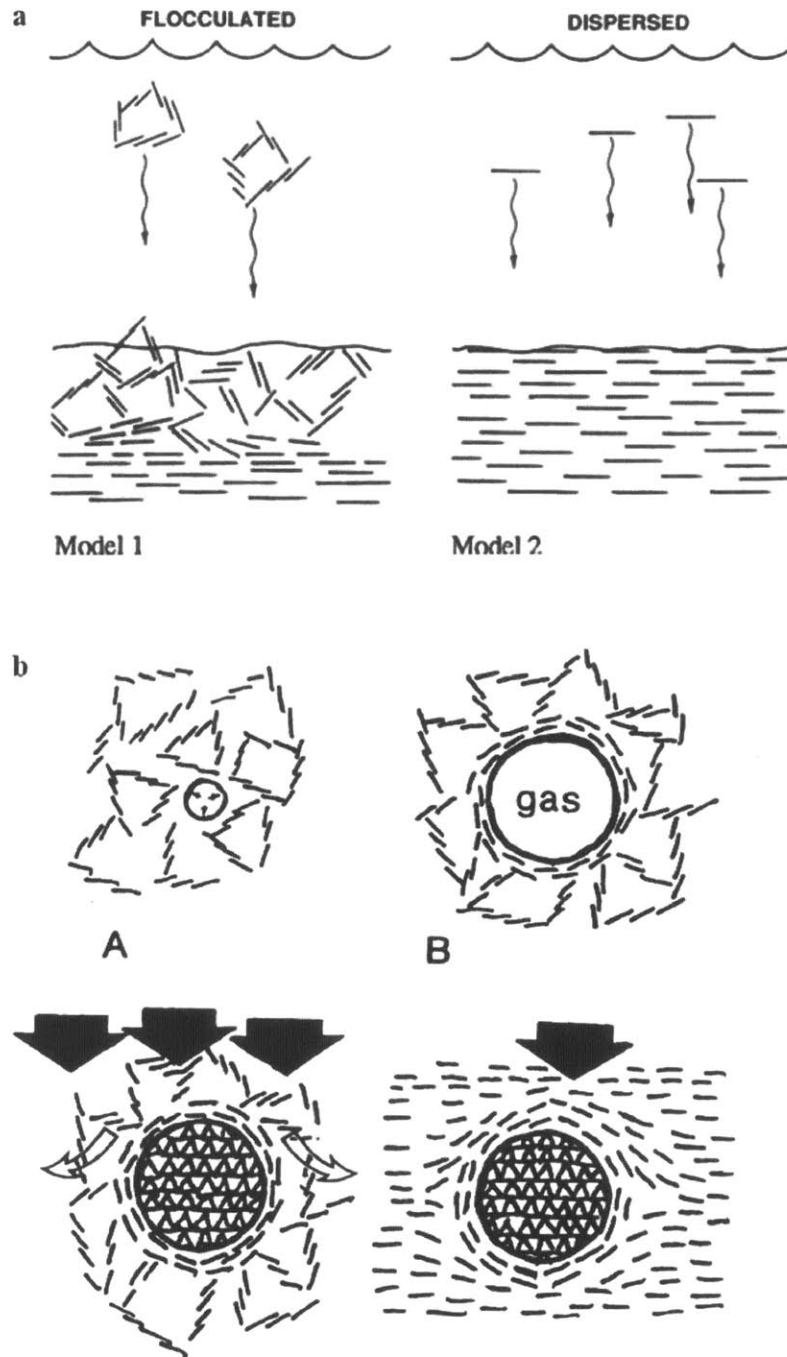
Figure 2-14: Proposed models of the evolution of mudrocks fabric published by a) (O'Brien and Slatt, 1990), and b) (O'Brien, 1995).

3 MATERIALS

3.1 INTRODUCTION

This chapter describes the soils tested in this investigation. The chapter starts with a detailed description of Gulf of Mexico- Eugene Island (GOM-EI) soil in Section 3.2.1, followed by a description of Boston Blue Clay (BBC) in Section 3.2.2. This description includes the depth and location from which the soils were obtained, as well as the processing of the soil to prepare it for the resedimentation technique. Finally, Section 3.2.3 summarizes the soil properties gathered in our lab and external labs. These properties include index properties, size distribution, and mineralogy.

3.2 TEST MATERIALS

3.2.1 Gulf of Mexico – Eugene Island (GOM-EI)

This high plasticity clay comes from the Eugene Island block located approximately 160 km off the coast of Louisiana at a water depth of ~ 77m. In this area, the basin consists of over 4 km of Pliocene and Pleistocene sedimentary fill deposited over a salt-weld. The soil was extracted from two cores drilled in July 1997, namely, A-20 in Block 330 and A-12 in Block 316. The soil existed at a depth below seabed between 6690' (2039m) and 7550' (2301m) (see Figure 3-1). The soil deposit was found to have an in-situ vertical effective stress ranging between 7.1 and 7.4 MPa, and an in-situ porosity of 0.23. In-situ measurements of the lateral stress ratio made during leak-off tests indicate that the lateral stress ratio $K_0 = 0.84 - 0.91$. K_0 represents the ratio of the horizontal effective stress over the vertical effective stress (Stump and Flemings, 2001). A total of 485' (148m) of 4" diameter core was extracted from both wells. The soil was later extracted from the cores, air-dried, then roller ground to a fine powder with 100% passing the #100 sieve (<0.15mm), and finally homogenized. The natural salt content was found to be 8g of salt (NaCl) per kg of soil. Based on the in situ water content of GOM-EI soil, this value is equivalent to approximately 80g of salt per liter of pore fluid. The processing of GOM-EI soil was conducted at the University of Texas at Austin. A detailed description of the geologic origin, processing and consolidation behavior of GOM-EI is given in Betts (2014). The results of several triaxial tests performed on resedimented GOM-EI samples (RGOM-EI) are provided in Fahy (2014).

3.2.2 Boston Blue Clay (BBC)

The BBC soil used in this investigation is from Series IV, which was obtained in 1992 from the base of an excavation for MIT's Biology Building. Approximately 2500 kg of BBC was excavated at a depth of about 12 m, where the OCR of the clay varied from 1.3 to 4.3 (Berman, 1993). The natural material obtained from the ground was first softened with tap water and mixed into a thick slurry. The slurry was then passed through a #10 sieve (nominal diameter of 2 mm) to remove all non-natural material, gravel, coarse sand, and large shell fragments before being oven-dried at 60°C. This oven-dried material was then ground to 95% passing through a #100 sieve (nominal diameter of 0.15 mm) by the Sturtevant Company using a roller mill. Finally, the material was manually blended to produce a homogenous powder before being stored in 40 gallon drums (Cauble, 1996).

The pore fluid of natural BBC contains salt that varies in concentration as a function of both location and depth. The salt content of BBC Series IV powder used for resedimentation was measured using the conductivity method and calibrated against a KCL standard. The salt content was found to be 2.68±0.05 g per kg of dry powder. At an in-situ water content of 40 %, this value corresponds to 6.70±0.12 grams per liter of pore fluid. Cauble (1996) determined the organic content of Series IV powder to be 4.4% by the loss-on-ignition method (ASTM D2974),although Horan (2012) later measured a much lower value of just 1.4 %. More information about the mechanical properties of BBC soil can be found in Adams (2014) and Casey (2014).

3.2.3 Soil Properties

Table 3-1 presents index properties of GOM-EI and BBC soils. Index properties include liquid limit, plasticity index, specific gravity, and clay fraction. Clay fraction is defined as the percentage of particles with an equivalent diameter less than 2 μm, which is determined by the hydrometer test (ASTM D422). **Error! Reference source not found.** shows the particle size distributions of the GOM-EI and BBC soils determined by the hydrometer test. The clay fraction (< 2 μm) was determined to be approximately 63% for GOM-EI soil and 56 % for BBC soil. The Atterberg limits were determined using distilled water and in accordance with ASTM D4318 (Betts, 2014; Casey, 2014; Fahy, 2014). The liquid limit (w_L) was found to be 87% for GOM-EI soil and 47 % for BBC soil. The plasticity index (I_P) is 63% and 23 % for GOM-EI soil and BBC

soil, respectively. According to the Unified Soil Classification System (USCS), GOM-EI soil is classified as a high-plasticity clay (CH), while BBC soil is classified as a low-plasticity clay (CL). The cation exchange capacity (CEC) was measured by copper adsorption by the SUNY lab at the University of Buffalo. The CEC is 10.7 meq/100 g for BBC soil and 32.4 meq/100 g for GOM-EI soil. The specific gravity, Gs, of the soil was determined in accordance with ASTM D854. The average Gs values for GOM-EI and BBC soils were found to be 2.779 and 2.775, respectively. These values were used in the phase relation calculations to estimate porosity of samples in this investigation.

The mineralogy analyses of GOM-EI and BBC soils were obtained using X-ray powder diffraction (XRPD) technique performed on bulk samples, as well as on the clay fraction (< 2 μm) of the soils. The mineralogy tests were carried out by Macaulay Scientific Consulting Ltd. of Aberdeen, U.K. Table 3-2 presents the bulk mineralogy of each sample, while Table 3-3 presents the relative proportions of clay minerals in the < 2 μm fraction of each sample. The samples primarily contain quartz, plagioclase, K-feldspar and clay minerals in varying proportions, as well as several other minerals at trace levels (Table 3-2). GOM-EI soil is predominantly smectitic with 87% of the clay fraction composed of a mixed layer illite-smectite with 70-80% expandability. BBC soil, on the other hand, is predominantly illitic with 65 % of the clay fraction composed of illite, and a 28 % mixed layer illite-smectite with 5-10 % expandability (Table 3-3). The remainder of the clay fraction of the two soils is made up of kaolinite and chlorite.

Table 3-1: Index properties and USCS classification of BBC and GOM-EI soils

Soil	Liquid Limit, W_L (%)	Plasticity Index, I_P (%)	Clay Fraction (%)	Specific Gravity	Cation Exchange Capacity (meq/100 g)	USCS Classification
BBC	47	22.7	56	2.779	10.7	CL
GOM-EI	87	62.9	65	2.775	32.4 ± 1.7	CH

Table 3-2: Bulk mineralogy in weight percent of the soils tested in this thesis

Soil	Quartz (%)	Plagioclase (%)	K-Feldspar (%)	Muscovite (%)	Total Clay (%)	Other minerals* (%)
BBC	21.3	20.5	8.2	13.8	16.4	19.9
GOM-EI	27.8	5.3	4.0	1.9	53.9	3.9

* Other minerals include minerals that exist in trace levels (~ 1 %) such as calcite, dolomite, siderite, pyrite, halite, amphibole. BBC soil also includes tri-mica (9.2 %) and hydrobiotite (5.4%).

Table 3-3: Relative percentage of clay minerals in the less than 2 μm soil fraction

Soil	Illite (%)	Illite-Smectite (%)	Kaolinite (%)	Chlorite (%)	Expandability (%)
BBC	65	28	2	5	5-10
GOM-EI	8	87	4	1	70-80
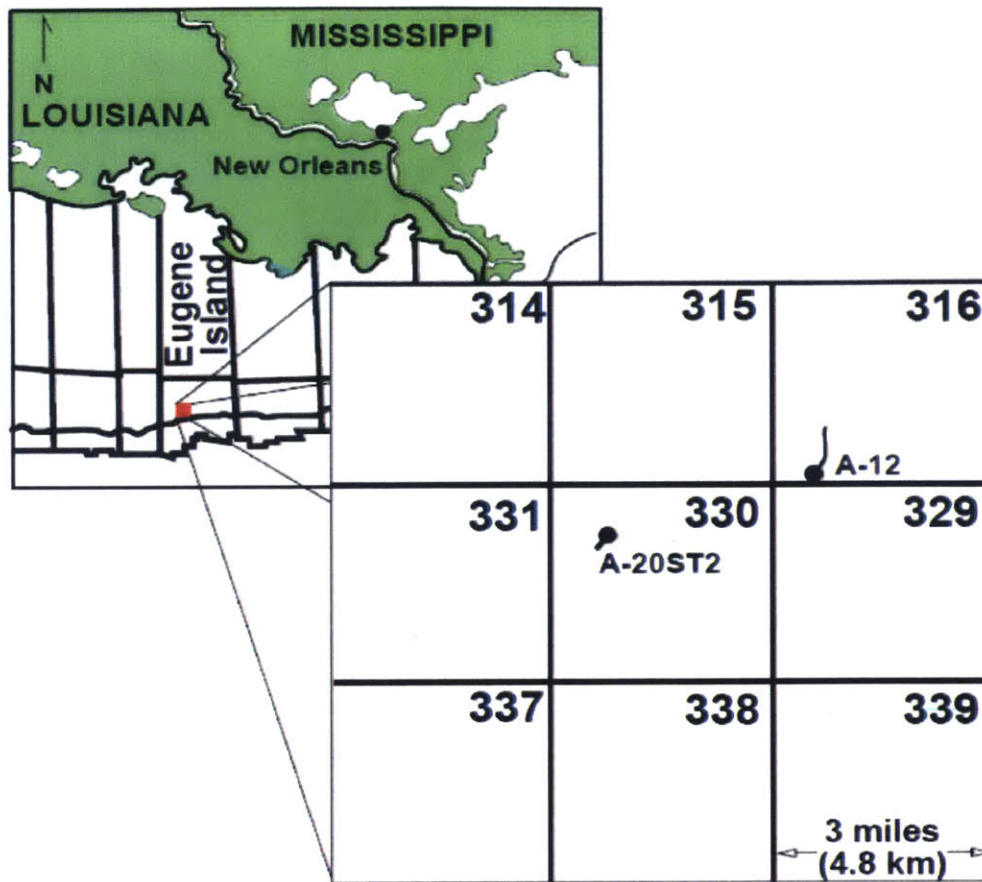
Figure 3-1: A map that shows the location from which the Gulf of Mexico- Eugene Island material was obtained (Betts, 2014).
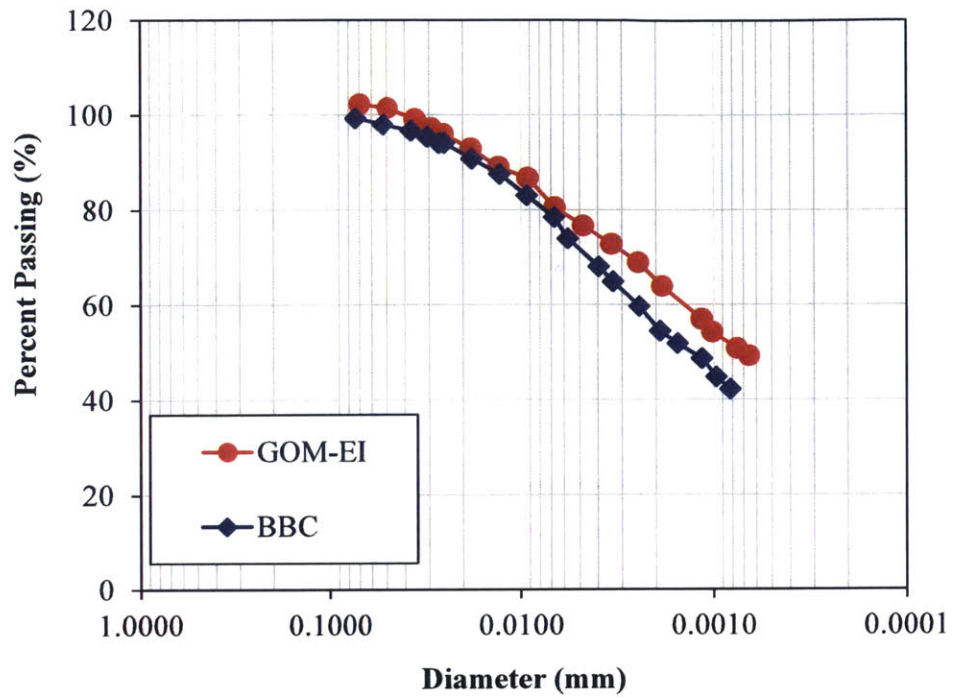
Figure 3-2: GOM-EI and BBC soils particle size distribution obtained using hydrometer test

4 METHODS AND PROCEDURES

4.1 Introduction

This chapter describes the methods used in this investigation, as well as the procedures followed for the preparation and imaging of mudrock samples. Section 4.2 introduces the Scanning Electron Microscopy (SEM) technique used to investigate the microstructure of mudrock samples. This section briefly describes the main parts of SEMs, the different types of emissions that can be used to extract information about materials, and the imaging parameters. Section 4.3 briefly introduces the resedimentation technique used in our lab to prepare mudrock samples for various tests, one of which is SEM imaging. Section 4.4 discusses in detail the preparation and imaging procedures of oven-dried mudrock samples. The first part describes the preparation of samples for ion milling, followed by descriptions of the ion milling and SEM imaging procedures. Section 4.5 describes in detail the preparation of wet mudrock samples for cryo-SEM imaging. Two different methods were used to prepare wet mudrock samples: high pressure freezing and plunge freezing. Furthermore, the use of the Leica TIC3X cryo-ion-polisher tool to prepare flat surfaces for imaging is discussed. Section 4.6 describes the methods we used to prepare clay slurry samples for cryo-SEM imaging. Two methods were used for this purpose: high pressure freezing and plunge freezing.

4.2 Scanning Electron Microscopy

SEM is used to determine the topography and composition of exposed surfaces in a sample. The basic components of an SEM are: electron gun, lenses, electron detectors, and vacuum chamber. The electron gun emits a beam of electrons with high energy (0.1-30 kV), and the lenses focus the beam onto the specimen as a spot with a size on the order of 10 nm. The beam interacts with the specimen surface to produce electron and X-ray emissions. Emitted electrons are collected by various detectors to produce images of the surface of interest. X-rays are characteristic of the elements from which they are emitted, and provide qualitative and quantitative measurements of the elements present in the sample. Most SEMs are equipped with X-ray detectors that enable the collection and analysis of X-rays of selected elements. The wide use of SEM stems from the relatively easy sample preparation, high resolution, and non-destructive nature of the technique

4.2.1 Specimen-Beam Interactions

In SEM experiments, a beam of electrons is accelerated to the sample surface to excite radiations that are a function of the topography and composition of the sample. These interactions cause three main types of emissions: secondary electrons, backscattered electrons, and x-ray emissions (Reed, 2005).

As the beam of electrons interacts with the specimen, secondary electrons are produced from the emitted valence electrons of atoms in the specimen. This kind of electron scattering is referred to as inelastic scattering because it involves dissipation of energy through interactions with bound electrons. Secondary electrons, by convention, possess energy less than 50 eV (Reed, 2005). As a result of their low energy, secondary electrons that are generated within a few nanometers of the surface are able to leave, whereas secondary electrons that are generated at a deep region are absorbed by the specimen. Consequently, secondary electrons provide information about the topography of a specimen surface.

Backscattered electrons represent the fraction of the beam of electrons that are reflected due to interactions with the atoms of the specimen. These interactions are referred to as elastic scattering because the total kinetic energy of the collision of electrons is conserved. Backscattered electrons are, by convention, electrons with energies greater than 50 eV (Reed, 2005). The fraction of the beam of electrons that are deflected through angles greater than 90° represents the backscattering coefficient, and it is strongly dependent on the atomic number, Z, as shown in Figure 4-1 (Reed, 2005). Hence, backscattered electrons provide information about the composition of the sample.

X-ray emissions, produced as a result of the interactions between the beam of electrons and sample, are characteristic of the elements from which they are emitted. X-ray emissions are produced by electron transition between the bound orbits, which possess energy governed by the quantum number (n). These orbits are usually designated as K (n=1), L (n=2), and M (n=3). Each of these orbits contain subshells with slight energy differences as shown in Figure 4-2 (Reed, 2005). For an x-ray to be produced, the incident beam energy must exceed the critical excitation energy required to ionize the sample. The energy of the x-ray is equal to the difference between the initial and final energy in the transition process. The lines are designated as K, L, and M based on the energy level from which the electron is ejected (Reed, 2005). X-ray emissions can

be used to identify the composition of a specimen because they are characteristic of the elements from which they are emitted. Most SEMs are equipped with energy dispersive spectrometers (EDS), which characterize the emitted X-rays based on their energy. One detector is usually sufficient to measure all chemical elements within scanned region that generate detectable radiations.

4.2.2 Imaging Parameters

Image quality controls the information that can be extracted from SEM micrographs. Image quality is a function of two factors: signal to noise ratio and resolution. Signal to noise ratio is a function of beam current and scan speed, while resolution is a function of the accelerating voltage and working distance. The beam current used in this study was chosen to provide a good balance between the generated signal and sample charging. Charging represents the accumulation of negative charge from the electrons on the surface of nonconductive samples, which affects the image quality. In Zeiss Supra55VP SEMs, the beam current can be modified by changing an aperture size. In this study we used a standard aperture size of 30 um. Scan speed is a critical parameter that controls the noise level in SEM images. Slow scan speeds reduce noise levels and hence improve image quality. Very slow scan rates might lead to poor image quality if there is mechanical drift or charging. The term charging refers to the accumulation of static electric charge on the sample surface, which leads to the deterioration of image quality. While mechanical drift can be minimized in most cases, charging is an inherent problem in mudrock imaging. A balance between scan speed and noise level is thus critical to the quality of SEM images of mudrocks. We found that for images with a size of 1024 pixels x 768 pixels, a scan speed of 8-9 frames per second (~ 20 seconds per image) is sufficient to obtain high-quality images suitable for image analysis. This scan speed might be increased or reduced depending on the condition of SEM during imaging.

Two parameters control the resolution of SEM images: the accelerating voltage and working distance. The working distance represents the distance between the final condenser lens and the specimen. Decreasing the working distance increases the resolution of the SEM images. In this study, we used a working distance of 3-5 mm, which provided a good resolution and contrast in the SEM images. Accelerating voltage is the most important parameter that affects the resolution of SEM images. In general, increasing the accelerating voltage increases the imaging

resolution. Higher accelerating voltages will penetrate deeper into the specimen. The deep beam penetration will increase the electron yield from deeper parts of the sample. This increase in electron yield will reduce the edge effect and hence obscure surface details (see Figure 4-3). Low accelerating voltages, therefore, have the advantage of providing sharp surface details while at the same time reduce charging. In this study, we found that an accelerating voltage of 1-2 kV produces images with sharp surface details. For EDS analysis, the accelerating voltage is limited by the critical excitation energy of elements in the sample, and must be high enough to excite the characteristic X-rays of the elements of interest. To satisfy this condition, an accelerating voltage of around two times the critical excitation energy is recommended (Reed, 2005). For example, iron with a critical excitation energy of 7.1 keV for the $K\alpha$ shell requires an accelerating voltage of approximately 15 kV (Reed, 2005). In this investigation, the accelerating voltage for EDS analysis was chosen based on the elements of interest.

4.3 Resedimentation

Resedimentation is the technique used in our lab to prepare mudrock samples by consolidating a dilute clay slurry in a rigid-walled cylindrical container referred to as a consolidometer. Germaine (1982) substantially improved this technique to produce fully saturated and uniform samples of RBBC with salt concentration of 16 g/l. Further modifications were later introduced by Seah (1990), who improved productivity and sample uniformity. Recently, Abdulhadi (2009) introduced a different approach for preparing individual resedimented samples for each test. The new procedure dramatically reduces the load required to achieve a particular preconsolidation stress, a critical issue for samples that need to be consolidated to high stresses. The basic procedure of the resedimentation technique consists of four main stages: processing, deposition, consolidation, and sample extrusions. This section briefly describes these stages. The interested reader is referred to the work of Abdulhadi (2009), Adams (2014), and Casey (2014) for more details.

In the first stage, the natural material obtained from the field is broken down, dried, and ground into a powder. The powder is then homogenized and stored in buckets or drums to be used for resedimentation as needed. In the second stage, the dry soil powder is thoroughly mixed with water using an electric blender to produce a homogeneous slurry (Figure 4-4a). The water added is usually mixed with sea salt to achieve a desired pore fluid salinity in the resedimented

sample. In this investigation, GOM-EI soil was mixed at a pore fluid salinity of 80 g/l, while BBC soil was mixed at a pore fluid salinity of 16 g/l of saltwater. The mixing water content is approximately twice the liquid limit of soil, which results in a workable slurry with no free water. The slurry is then vacuumed to remove any entrapped air as shown in Figure 4-4b. In the third stage, the de-aired slurry is slowly poured in a consolidometer using a funnel to avoid entrapment of air bubbles (Figure 4-4c). The slurry is then loaded incrementally using a load increment ratio of one. Each load increment is maintained until the end of primary consolidation as determined by the root time method (Figure 4-4d). Once the desired maximum stress has been reached, the resedimented sample is rebounded to an overconsolidation ratio (OCR) of 4. At this ratio, the soil is close to isotropic conditions, and therefore, the shear strains due to sample extrusion are minimal. In the final stage, after the resedimentation in the consolidometer is completed, the sample is removed and trimmed to the desired dimensions for various tests (Figure 4-4e).

4.4 Oven-Dried Sample Preparation and Imaging

Preparation of oven-dried mudrock samples for imaging consisted of three stages. In the first stage, wet samples were trimmed with a razor blade to create specimens that fit the ion milling instrument (~1 cm x 1 cm x 0.5 cm). The mudrock samples were cut in the wet state for ease of handling and to minimize sample disturbance. These samples were oven-dried for 24 hours at a temperature of 105 °C. The oven-dried samples did break and disintegrate before the desired dimensions are obtained. In case wet samples were not available, the samples were first cut using a saw to the smallest possible dimensions without causing the samples to break (~ 2 cm^3). Then, sand paper with a grit size of 220 (~66 μm) was used to polish the samples to the desired dimensions. Finally, the small oven-dried samples were further polished using sand paper with decreasing abrasive grain sizes (e.g., 9 μm and 3 μm). Two surfaces had to be polished: the surface to be ion milled and the surface perpendicular to it (see Figure 4-5). This step is critical to reduce ion milling curtaining artifacts and produce flat surfaces for imaging. Also, fine polishing reduces the depth of the disturbed surface due to razor blade cutting and coarse polishing to a few microns.

In the second stage, mudrock samples were ion milled using a JEOL cross-section polisher to produce flat surfaces for imaging. Ion milling preserves fine microstructural details such as porosity and particle texture, which may be destroyed using conventional mechanical polishing. The cross-section polisher consists of a sample chamber, vacuum system, microscope for positioning the sample, and a stationary ion beam (Erdman et al., 2006). Heated epoxy was used to glue mudrock samples onto the holder. The epoxy was heated using a hot plate at 100°C. This temperature was chosen to be compatible with the oven drying process used in our lab and to prevent further water loss. The mounted mudrock samples were then inserted into the cross-section polisher. The polisher microscope was used to choose an area of interest and position the mask such that a maximum of 50-100 μm of the sample edge is exposed to the ion beam (see Figure 4-6). The removal of 50-100 μm ensures that the milled surface is free of mechanical polishing artifacts as well as the smearing due to razor blade cutting. Furthermore, the removal of 50-100 μm provides a good compromise between the milling depth and the time required to produce large-enough cross sections for imaging. Removal of material more than 50-100 μm requires significantly longer time to mill a large surface. Once the mask had been aligned and properly positioned, the specimen chamber was evacuated and the sample was bombarded with a broad argon ion beam. We used an accelerating voltage of 5-6 kV and a milling time of 6-8 hours. The argon ion beam flow is usually optimized to obtain maximum current. The area of the milled section produced using these parameters was approximately 1 mm^2 (see Figure 4-6). The milled samples were then imaged in a Zeiss Supra55VP SEM. The samples were imaged in the secondary electron mode (SE) at an accelerating voltage of 1-2 kV and a working distance of 3-5 mm. All oven-dried imaging of resedimented mudrock samples was performed at the Center for Nanoscale Systems (CNS) at Harvard University (see Table 4-1).

4.5 Cryo-Preparation and Imaging of Wet Samples

Preparation of wet mudrock samples for cryo-SEM imaging is particularly challenging due to the high water content of the samples. Furthermore, wet mudrock samples are soft, which makes the handling of these samples very difficult. The preparation protocol of wet mudrock samples consisted of three stages. First, the samples were cryo-fixed using either high pressure freezing or plunge freezing. Second, the frozen samples were ion milled to produce flat surfaces for imaging. Finally, the milled samples were sublimated and coated before SEM imaging.

4.5.1 High Pressure Freezing

High pressure freezing requires very thin samples to prevent ice crystallization and associated volume changes that may alter the microstructure. Wet mudrock samples were thin-sliced using a sharp razor blade to roughly 300 μm. The sliced samples were then punched out to generate discs 4 mm in diameter using a razor sharp Harris Uni-Core cutter (https://www.tedpella.com/histo_html/unicore.htm). Each disc was transferred to a gold specimen carrier (d = 6 mm, t = 300 μm, Leica Microsystems, Vienna) roughened with a needle to improve sample adhesion to the carrier (see Figure 4-10). To further strengthen the sample-substrate bonding, a small amount of clay slurry was added to the sides of the specimen carrier. This step was necessary as some of the mudrock samples detached from the specimen carrier after freezing. The high water content of the added clay slurry improved bonding between the sample-carrier system. The free space in the specimen carrier had to be filled with a liquid to prevent the collapse of the sandwich under high pressure. We used 1-hexadecene to fill the void space left in the carriers after placing the thin sample and the clay slurry. 1-hexadecene has been successfully used as a filler in several studies as a result of its properties such as being chemically inert, hydrophobic, and of low surface tension (Studer et al., 1989) . Once the mudrock slice had been properly placed in the carrier with clay slurry and 1-hexadecene, a second carrier that was pre-coated with a 2% lecithin solution in chloroform to facilitate its removal after freezing was laid on top of the first carrier, with its flat side facing down. The assembled carrier sandwiches were immediately placed in a cartridge holder and cryo-fixed using a EM HPM100 high pressure freezer (Leica Microsystems, Vienna).

High-pressure-frozen carrier sandwiches were trimmed under liquid nitrogen using a custom-built cryo-saw (see Figure 4-7, Leica Microsystems, Vienna). The cryo-saw consists of a compartment for cutting samples using a rotary diamond saw under liquid nitrogen, a liquid nitrogen bath, and a dock for a vacuum-cryo-transfer system (VCT, Leica Microsystems, Vienna). Carrier sandwiches were opened under liquid nitrogen in the sample compartment. The bottom carrier containing the sample was clamped to a sample stage and cut along the midline under liquid nitrogen, using a diamond blade (grain size 30 μm) at a speed of ~900 rpm. The trimmed carrier was transferred under liquid nitrogen to a sample holder that positioned the trimmed edge of the sample in contact with a milling mask (tungsten carbide, 2-3° bevel). The sample holder was then retrieved from the liquid nitrogen bath using a pre-cooled VCT shuttle

and transferred to the Leica TIC3X tool for ion milling. The pre-cooling of the VCT shuttle involves adding nitrogen to the system a few minutes before use (see Figure 4-8).

The Leica TIC3X tool is a cyro ion milling system equipped with a cryostage and retrofitted with a VCT docking station for transfer of frozen-hydrated samples without breaking vacuum in the pre-cooled milling chamber (see Figure 4-9). Cryo-trimmed samples were loaded into the VCT shuttle at ambient pressure. The shuttle was then attached to the VCT docking station in the Leica TIC3X system and pumped down. The gate valve of the VCT station was then opened and the sample transferred to the cryostage of the Leica TIC3X. The ion milling process uses slope-cutter geometry, in which three broad, horizontal argon ion beams (1-10 kV) spaced regularly over an arc of 100° are aimed at the sample over a sloped mask (2-3° bevel, tungsten carbide). Milling was conducted at -150°C and ~6 x 10^{-4} mbar, an acceleration voltage of 8.0 kV, and a current of 3.5 mA per gun for ~8 hours. This process produced a flat milled surface with an area of a few mm^2 (see Figure 4-9).

After ion milling, the holder containing the sample was retrieved with a pre-cooled VCT shuttle and transferred under vacuum to a Leica ACE 600 (Leica Microsystems, Vienna) coater equipped with a cryostage and a VCT docking station. The temperature of the sample stage was set to -120°C, and the pressure was ~1 x 10^{-6} mbar. For sublimation, the stage temperature was raised to -100°C and held at this temperature for 60 minutes, before being cooled back down to -120°C. At this point, the sample stage was tilted by 25°, such that the surface of the specimen became normal to the platinum target. Approximately 4 nm of Pt/C was deposited onto the sample at roughly 0.10 nm/sec and ~5 x 10^{-6} mbar. Finally, samples were transferred under vacuum from the Leica ACE 600 using a pre-cooled VCT shuttle to a Hitachi S4800 FE-SEM equipped with a Leica VCT docking station and a cold stage. The base temperature of the stage was maintained at -120°C. Imaging was performed at a working distance of 8-9 mm, using an acceleration voltage of 2.0 kV, a current of 10 μA, and using the secondary electron detector. The high-pressure-freezing sample preparation and imaging were performed at Nuance Center at North Western University (see Table 4-1).

4.5.2 Plunge Freezing

For plunge freezing, wet mudrock samples were trimmed with a razor blade to create samples that fit the sample holder of the Leica TIC3X system (~ 10 mm x 7 mm x 2 mm). The

trimmed samples were then plunge-frozen in liquid nitrogen to cryo-fix the water in the pore space. The frozen samples were attached to a sample holder and cut under liquid nitrogen using a custom-built cryo-saw (see Figure 4-7, Leica Microsystems, Vienna). The cutting was performed using a diamond blade (grain size 30 μm) at a speed of ~900 rpm. The cutting was done such that around 50-100 μm of the sample was left sticking above the mask. Similar to oven-dried samples, the removal of 50-100 μm ensures that the milled surface is free of cutting and handling artifacts. Furthermore, the removal of 50-100 μm provides a good compromise between milling depth and the time required to produce large-enough cross sections for imaging. The sample holder was then retrieved from the liquid nitrogen bath using a pre-cooled VCT shuttle and transferred to the Leica TIC3X tool for ion milling. The ion milling process uses slope-cutter geometry, in which three broad, horizontal argon ion beams (1-10 kV) spaced regularly over an arc of 100° are aimed at the sample over a sloped mask (2-3° bevel, tungsten carbide). Milling was conducted at -150°C and ~6 x 10^{-4} mbar, an acceleration voltage of 8.0 kV, and a current of 3.5 mA per gun for ~8 hours. This process produced a flat milled surface with an area of a few mm^2 (see Figure 4-9).

The sample holder containing the sample was then retrieved with a pre-cooled VCT shuttle and transferred under vacuum to a Leica MED-020 sputter coater and freeze-fracture system (Leica Microsystems, Vienna). The temperature of the sample stage was set to -120°C, and the vacuum was ~1 x 10^{-7} mbar. For sublimation, the stage temperature was raised to -95°C and held at this temperature for 60 min, before being cooled back down to -120°C. At this point, 4 nm of platinum was deposited onto the sample at roughly 0.10 nm/sec and ~5 x 10^{-2} mbar. Finally, samples were transferred under vacuum from the Leica MED-020 using a pre-cooled VCT shuttle to a Zeiss Supra55VP SEM equipped with a Leica VCT docking station and a cold stage. The base temperature of the stage was maintained at -120°C. The samples were imaged in the secondary electron mode (SE) at an accelerating voltage of 1-2 kV and a working distance of 3-5 mm. All plunge freezing experiments of resedimented mudrock samples were performed at the Center for Nanoscale Systems (CNS) at Harvard University.

4.6 Slurry Samples Cryo-Imaging

Preparation of slurry samples for imaging consisted of three stages. First, slurry samples were cryo-fixed using high-pressure freezing and plunge freezing. Second, frozen slurry samples were freeze-fractured and sublimated to reveal fresh surface details for imaging. Finally, fractured slurry samples were coated to prevent sample charging during imaging.

4.6.1 High Pressure Freezing

For high pressure freezing, 0.6 μl of a slurry sample was transferred into two aluminum carriers ($d = 2\ mm, t = 100\ \mu m$, see Figure 4-10). One carrier was then placed inverted on the other, effectively sandwiching the sample volume. The assembled carrier sandwich was immediately placed in a cartridge holder and cryo-fixed using an EM HPM100 high pressure freezer (Leica Microsystems, Vienna). Frozen sample sandwiches were mechanically separated under liquid nitrogen using tweezers. This process created a fractured surface that reveals fresh surface details for imaging (see Figure 4-10). One carrier was loaded into a sample holder for sublimation. The sample holder containing the sample was retrieved with a pre-cooled VCT shuttle and transferred to a Leica ACE 600 coater (Leica Microsystems, Vienna). The temperature of the sample stage was set to -120°C, and the pressure was ~1 x 10^{-6} mbar. For sublimation, the stage temperature was raised to -100°C, and held at this temperature for 40 min, before being cooled back down to -120°C. At this point, the sample stage was tilted by 25°, such that the surface of the specimen became normal to the platinum target. Approximately 4 nm of Pt/C was deposited onto the sample at roughly 0.10 nm/sec and ~5 x 10^{-6} mbar.

Finally, samples were transferred under vacuum from the Leica ACE 600 using a pre-cooled VCT shuttle to a Hitachi S4800 FE-SEM equipped with a Leica VCT docking station and a cold stage. The base temperature of the stage was maintained at -120°C. Imaging was performed at a working distance of 8-9 mm, using an acceleration voltage of 2.0 kV, a current of 10 μA, and using the secondary electron detector. The high pressure freezing sample preparation and imaging was performed at Nuance Center at North Western University (see Table 4-1).

4.6.2 Plunge Freezing

In plunge freezing, a small volume of clay slurry was mounted on a 3 mm copper planchette (see Figure 4-11). The sample was then hand-plunged into a bath of liquid cryogen

using tweezers. The frozen sample was then transferred to a liquid nitrogen bath (see Figure 4-7) and attached to a sample holder. The sample holder was retrieved with a pre-cooled vacuum-cryo-transfer shuttle (VCT, Leica Microsystems, Vienna) and transferred to a Leica MED-020 sputter coater and freeze-fracture system (Leica Microsystems, Vienna). The sample was fractured using a cold knife and sublimated to reveal fresh surface details for imaging (see Figure 4-11). The sublimation process was performed by warming the sample surface to -90°C and held at this temperature for 5 minutes, before being cooled back to -120°C. Finally the sample was coated with 5-6 nm of platinum at ~5 x 10^{-2} mbar before being transferred to a cryo-SEM for imaging, which was performed at -120 C. Imaging was performed using a Zeiss Supra55VP SEM equipped with a Leica VCT docking station and a cold stage. The samples were imaged in the secondary electron mode (SE) at an accelerating voltage of 1-2 kV and a working distance of 3-5 mm. All plunge freezing experiments of slurry samples were performed at the Center for Nanoscale Systems (CNS) at Harvard University (see Table 4-1).

4.7 Porosity Measurements

One of the main goals of this investigation is the characterization of the development of the pore space of mudrocks under different conditions such as drying shrinkage and the resedimentation stress. In this thesis, we used several methods to measure the porosity of mudrock samples including water-content wet lab porosity, oven-dried lab porosity, Mercury Porosimetry Intrusion (MIP), and SEM imaging porosity. This section briefly describes these methods and the procedures used to perform the experiments.

4.7.1 Oven-Dried and Wet Macroscopic Porosity

This section describes the water-content wet lab porosity and the oven-dried lab porosity used to measure the porosity of mudrock samples. The water-content lab porosity is used to measure the porosity of saturated wet samples, while the oven-dried lab porosity is used to measure the porosity of dried samples. The difference in porosity between these two methods provides a measure of the drying shrinkage that mudrock samples undergo upon drying. For simplicity, the water-content lab porosity is referred to as the wet lab porosity.

Wet macroscopic lab porosity represents the porosity of mudrock samples in their wet state. This porosity is also referred to in the literature as water-loss porosity or saturation

73

porosity. The wet lab porosity is measured at the end of the resedimentation process, after the desired stress level has been reached. A piece of the sample is oven-dried at 110°C for 24 hours. The wet lab porosity is then calculated using the following formula:

$$n_w = \frac{M_w - M_d}{V_T} \tag{4-1}$$

Where n_w is the wet lab porosity, M_w is the mass of the sample before oven-drying, and M_d is the mass of the sample after oven drying at 110°C for 24 hours. Equation (4-1) provides an accurate measure of the wet lab porosity of the resedimented mudrock samples for two reasons. First, the resedimented samples are fully saturated, and hence the measured water content accurately represent the pore space. Second, the measurements were performed immediately after the samples have been extruded. Therefore, there is no water loss due to air drying that may result from long-term storage or transportation of samples.

The oven-dried lab porosity is calculated using the phase relations of the dry state of the samples. First, the wet samples are oven-dried at 110°C for 24 hours, and the dry weight of these sample, M_d, is recorded. Next, the volume of the dry samples is measured using the water displacement method carried out in accordance with ASTM D4943. In this method, the sample is coated with paraffin wax to prevent dry clay from absorbing water during the immersion in water. The density of paraffin wax used in the calculations is $0.92 g/cm^3$. The oven-dried porosity is then calculated using the following formula:

$$n_d = \frac{V_T - V_s}{V_T} \tag{4-2}$$

Where V_T is the total volume of the sample as determined by the water-displacement method, and V_s is the volume of the solid fraction of the sample, and is given by:

$$V_s = \frac{M_d}{G_s} \tag{4-3}$$

where G_s is the specific gravity of the soil. The specific gravity was determined in accordance with ASTM D854. The average G_s value for GOM-EI and BBC soils was found to be 2.779 and 2.775, respectively (see Chapter 3).

4.7.2 Mercury Porosimetry Intrusion (MIP)

MIP is one of the most widely used methods to calculate the porosity and pore size distribution of porous materials. In this method, the sample is intruded with mercury at increasing incremental pressure steps. The total intruded volume is then used to calculate the porosity and pore size distribution. The MIP method is based on the fact that mercury, a non-wetting fluid, intrudes the pore space by capillary action. The higher the applied pressure the smaller the pores that can be intruded and filled with mercury. The intruded volume of mercury at each pressure step can be used to calculate the pore size distribution of mudrocks using the Washburn equation (Washburn, 1921):

$$d = \frac{-4\gamma \cos \theta}{P} \qquad (4\text{--}4)$$

where d is the pore diameter, γ is the surface tension of mercury, θ is the contact angle of mercury, and p is the applied pressure. This method assumes that the pore space is composed of a set of cylindrical pores that are accessible to mercury. In this thesis, the MIP experiments were performed by Peter Polito from the University of Austin Texas as part of the UT GeoFluids consortium. The mudrock samples are first dried at 110°C for 24 hours. Samples of known weight are transferred to a chamber, which is then evacuated. The mercury is introduced and the applied pressure is incrementally increased. The maximum applied pressure used in this study is 39,000 psi, which reveals a minimum pore diameter of 3 nm.

4.7.3 SEM Imaging Porosity

SEM imaging was used in this investigation to calculate the porosity and pore size distributions of mudrock samples. SEM imaging of oven-dried samples was used to calculate the porosity and pore size distributions of oven-dried mudrock samples, while cryo-SEM imaging of wet samples was used to measure the porosity and pore size distributions of wet mudrock samples. The preparation procedure of the oven-dried and wet samples for imaging is described above. We used the Integration of Magnifications (IOM) method, developed in this study, to calculate the porosity and pore size distributions of mudrock samples (see Chapter 5). In this investigation, the resolution of SEM is controlled by the highest magnification used and the number of pixels required to properly quantify pores. As discussed in Chapter 5, the highest magnification used to image the pore space of mudrocks in this investigation is 30 KX. This

75

magnification results in a resolution of 35 nm. The SEM imaging porosity is the main topic of Chapter 5.

Table 4-1: A summary of the equipment used to prepare different samples in this thesis

Sample state	Cryo-Fixation	Ion Milling	Imaging	Lab
Oven-dried Mudrocks	NA	JEOL cross section polisher	Zeiss Supra55VP SEM	CNS, Harvard University
Plunge Frozen Mudrocks	Liquid nitrogen or nitrogen slush	Leica TIC3X polisher	Zeiss Supra55VP SEM	CNS, Harvard University
High-Pressure Frozen Mudrocks	EM HPM100	Leica TIC3X polisher	Hitachi S4800 FE SEM	Nuance Center, North Western University
Plunge Frozen Slurry Samples	Liquid nitrogen or nitrogen slush	NA	Zeiss Supra55VP SEM	CNS, Harvard University
High Pressure Frozen Slury Samples	EM HPM100	NA	Hitachi S4800 FE SEM	Nuance Center, North Western University
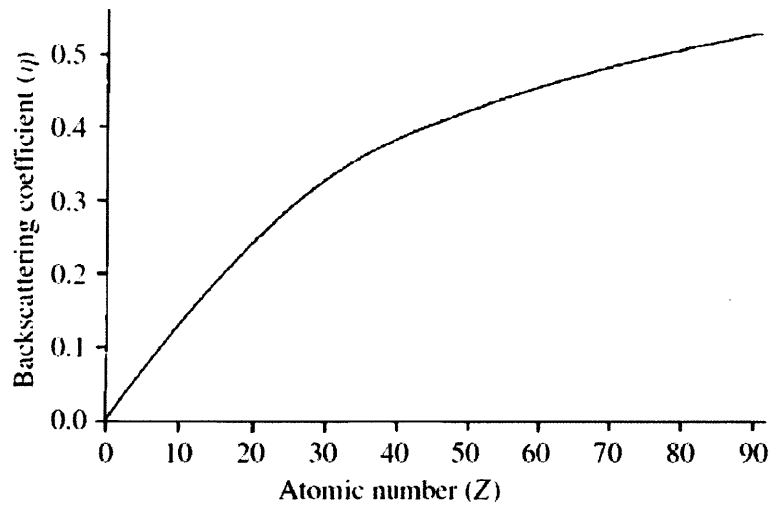
Figure 4-1: Backscattering coefficient versus atomic number. The figure shows the strong dependence of the backscattering coefficient on the atomic number (Reed, 2005).
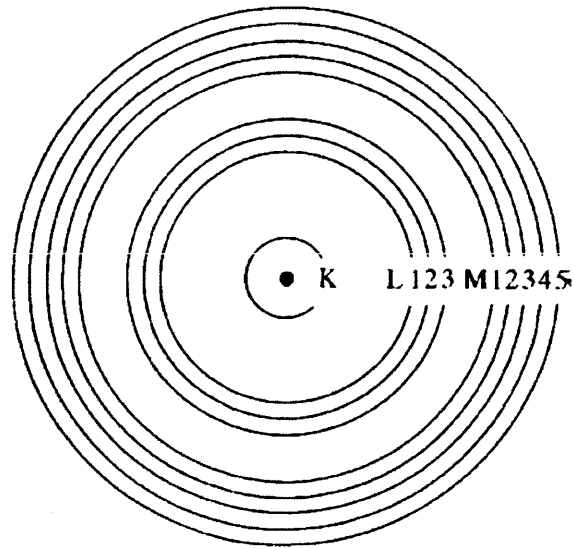
Figure 4-2: Schematics of the inner atomic shells. X-ray is produced by electron transitions between these shells (Reed, 2005).
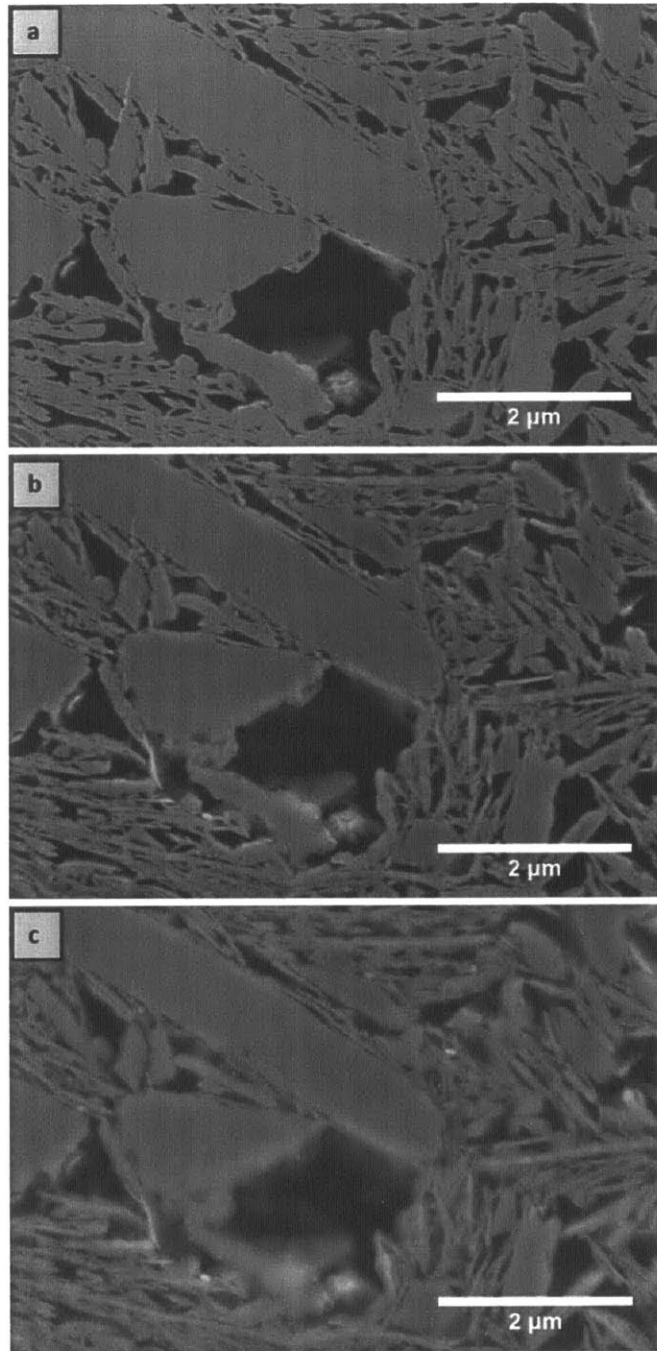
Figure 4-3: Secondary electron images taken at different accelerating voltages: a) 1 kV, b) 3 kV, and c) 5 kV. As accelerating voltage increases the clarity of the surface decreases. Accelerating voltages between 1-2 kV are suitable for the purpose of this study.
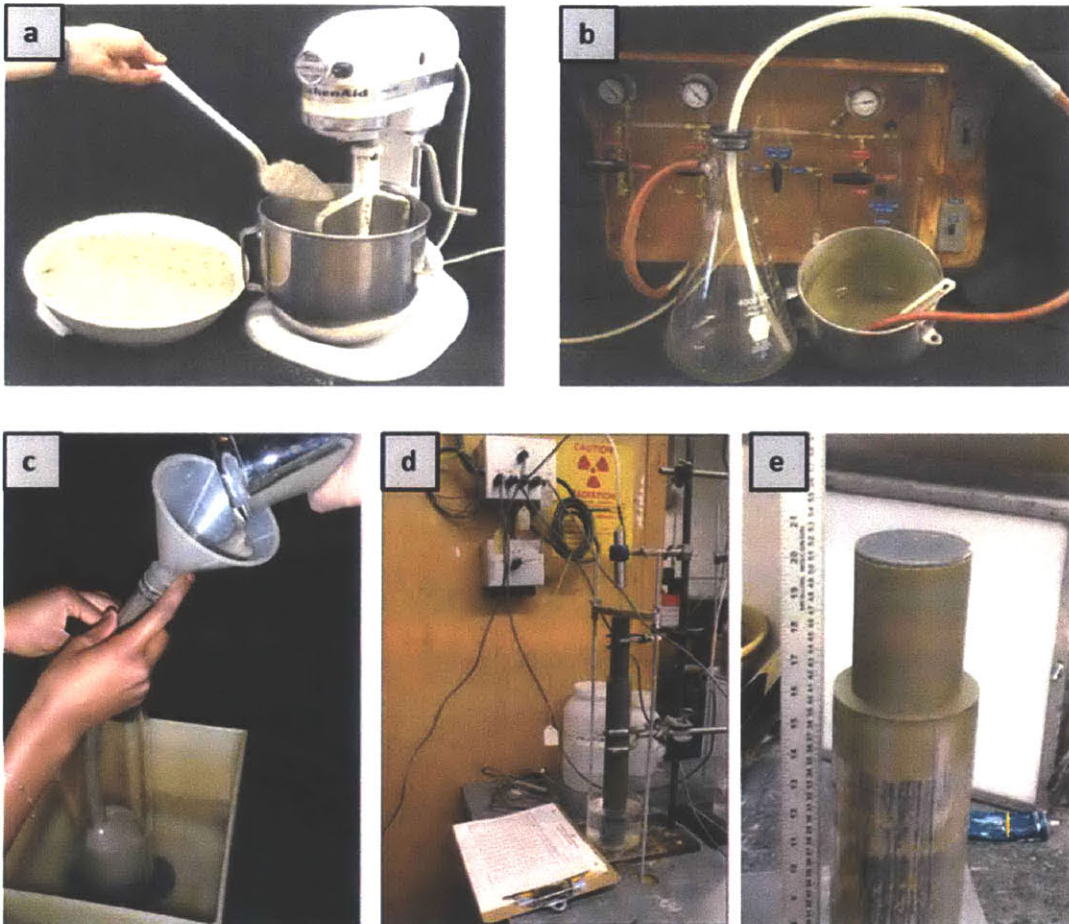
Figure 4-4: This figure summarizes the main stages of the resedimentation technique used to prepare mudrock samples. The main stages consist of a) mixing dry clay powder with water to form homogeneous slurry, b) the slurry is then vacuumed to remove entrapped air, c) and poured in a consolidometer, d) to be subjected to 1-D compression by applying incremental loading until the desired stress is reached, and e) finally the sample is extruded for further testing.
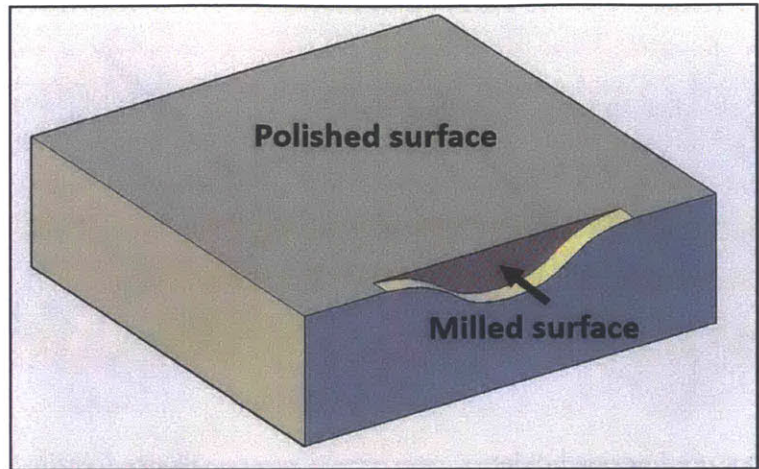
Figure 4-5: A schematic that illustrates the surfaces that should be polished using sand paper to reduce ion milling artifacts that may result from irregular surfaces.
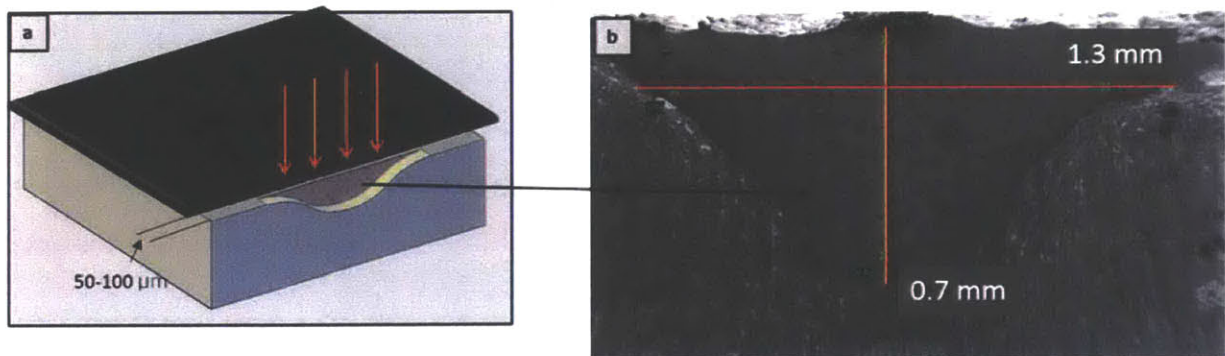
Figure 4-6: a) a schematic that illustrates the position of the mask in cross section polishing, and b) an SEM image of a polished area for RBBC mudrock sample.
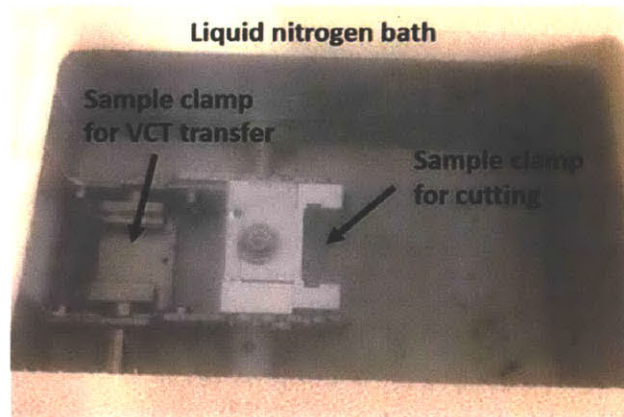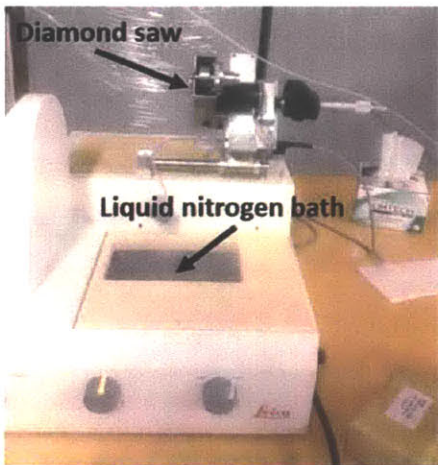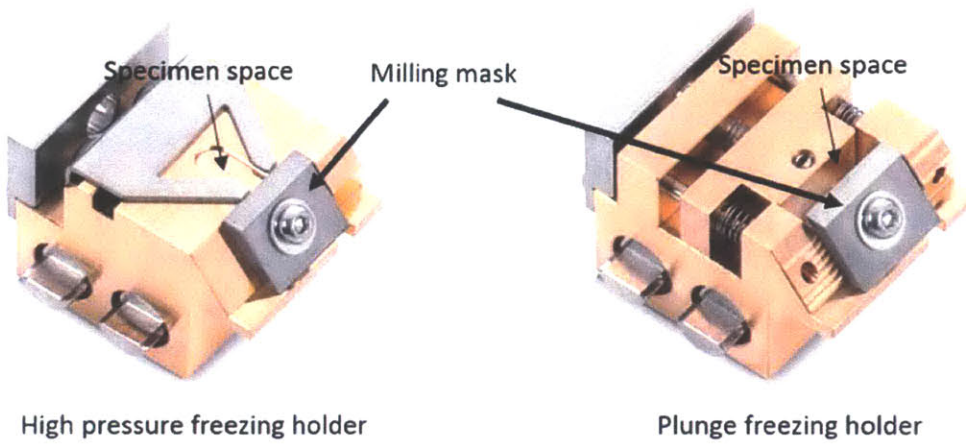
Figure 4-7: Sample holders for high pressure freezing and plunge freezing (top), and Custom-built cryo diamond saw (Leica Microsystems, Vienna) (bottom).
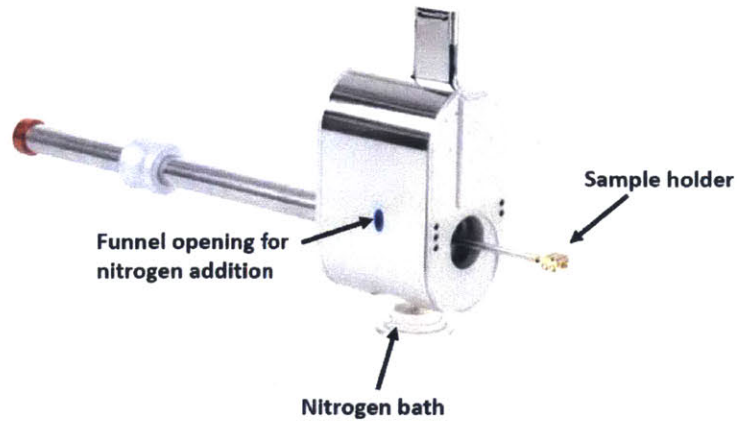
Figure 4-8: Vacuum-cryo-transfer system (VCT, #EM VCT100, Leica Microsystems, Vienna).
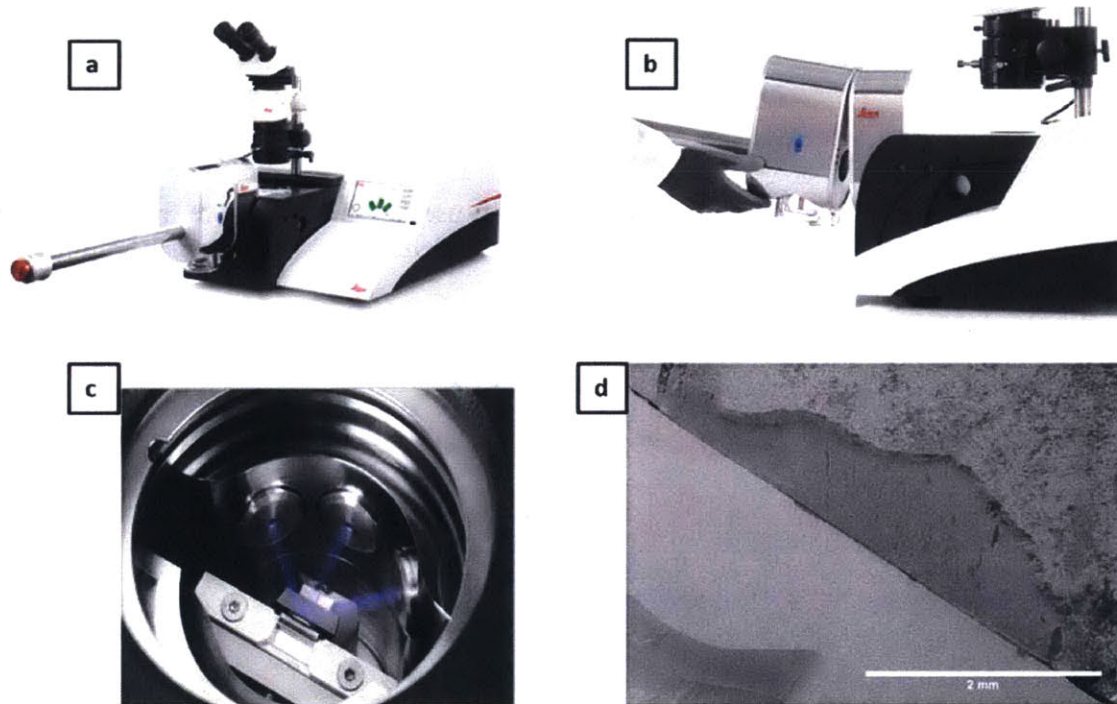
Figure 4-9: a) the Leica TIC3X tool used in this investigation for cryo -ion-milling of mudrocks., b) VCT docking station, c) triple argon ion beam system, and d) a cryo-milled surface of an RGOM mudrock sample.
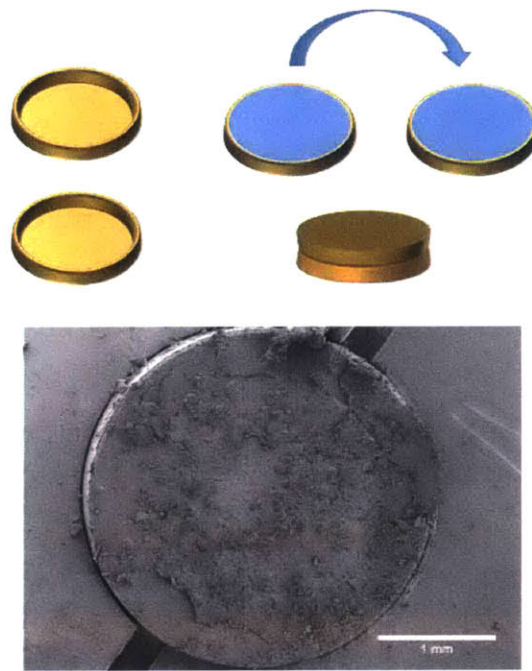
Figure 4-10: A schematic that shows aluminum planchettes used for high pressure freezing (top), and an SEM image of a fractured surface for a high pressure frozen GOM-EI sample (bottom)
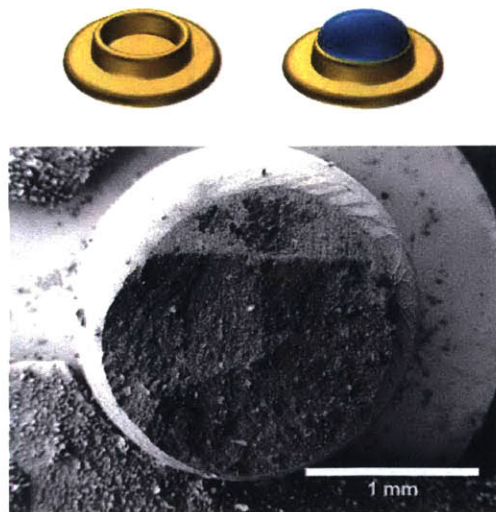
Figure 4-11: A schematic that shows copper planchettes used for plunge freezing (top), and a cryo-SEM image of a fractured surface for a plunge frozen GOM-EI sample (bottom).

5 QUANTIFICATION OF SEM IMAGES OF MUDROCK SAMPLES

5.1 Introduction

This chapter describes the image analysis tools and methods used in this investigation to characterize the pore space of mudrock samples. Section 5.2 discusses the steps used to process and threshold Scanning Electron Microscopy (SEM) images obtained for mudrock samples. These steps include image processing, segmentation, and image analysis. Section 5.3 introduces the Integration of Magnifications (IOM) method we developed to obtain representative information about the pore space of mudrocks. Section 5.4 employs 2D simulations to validate the proposed IOM method, and explore the sensitivity of this method to imaging parameters. Finally, section 5.5 discusses an example application of the IOM method on a mudrock sample to obtain porosity and pore size distribution information.

5.2 Image Analysis

SEM images contain topographical and compositional information about the microstructure of samples. A typical size of an SEM image is 1024 x 768 pixels. Each pixel contains an 8-bit number that represents brightness, and can be displayed in an image as different shades of gray that range from 0 (black) to 255 (white). Therefore, images can be represented as a 2D distribution of gray values, f(x, y), in which x and y are a function of the pixel size of the image. For example, Figure 5-1 shows an SEM image for an RGOM sample resedimented at 0.2 MPa (RGOM-EI-0.2) along with its histogram of gray values. The gray scale histogram shows two peaks at grey values 0 and 75. The peak at the grey value of 0 corresponds to the pore space in the image (black color), whereas the peak around the grey value of 75 corresponds to particles (grey color). The main focus of image analysis is quantifying features of interest in SEM micrographs such as pores and particles. This process consists of three main steps. First, the image is processed to enhance features of interest and to remove noise. Second, the filtered image is segmented to separate features of interest for further analysis. Finally, the separated features are analyzed to obtain information such as size distribution and volume fractions. These steps were performed using ImageJ software.

5.2.1 Image Processing

The quality of image analysis results depends on the quality of the acquired images. As a consequence, special care is given to enhance features of interest in images before segmentation. Image processing in this investigation is limited mainly to noise removal. This is because today's SEMs are capable of producing high quality images, and no further processing was required such as background removal and contrast enhancement. In this investigation, two main filters were used for noise removal: nonlocal means filter and Median filter. Nonlocal means filtering provides the best results in terms of removing noise without changing the fine details of the microstructure. Figure 5-2 shows an example of image filtering for noise removal. While the nonlocal means filter preserved microstructural details, the median filter slightly blurs the image and hence may lead to loss of important microstructural details. When the noise level is low, the nonlocal means filter was sufficient to remove noise and produce high quality image. On the other hand, when the noise level is high, both the nonlocal means filter and the median filter were used for noise removal. These filters were implemented using ImageJ. The median filter is a built-in plugin in ImageJ, while the non-local means filter can be implemented using an ImageJ plugin (https://code.google.com/p/ij-non-local-means). Trial-and-error was used to decide the best input parameter to remove noise without changing the fine details of the image.

5.2.2 Segmentation

Image segmentation is the process of separating segments of interest in an image, such as pores and particles, for further analysis. These segments must have uniform features such as gray level for efficient segmentation. Figure 5-3a shows an SEM image of the RGOM-EI-0.2 sample, in which pores are shown in black and particles in gray. In this image, pores are separated from each other by particles, and they possess a relatively uniform gray level. There are several methods used for image segmentation that range from manual to fully automated methods. In this study, we use thresholding, which involves separating features of interest based on differences in gray level. The process is performed semi-manually using ImageJ by choosing the threshold limit that best represents the pore space. Figure 5-3b shows that the threshold limit between pores and particles is not clearly defined. In ImageJ, the threshold limit can be set by the user to best represent the pore space. This value was chosen to be 73, as shown in Figure 5-3b and Figure 5-3c. This process is repeated for all images acquired in this study to separate the

86

pore space. Manual thresholding is user-dependent and a variability of ± 10 % is expected (Houben, 2013). The results of image thresholding is a binary micrograph with pixel values of 0 that represent the particles and values of 1 that represent the pore space. Each separate pore is represented by a set of pixels that are connected and separated from other pores by white pixels. In the case of particles, it was not possible to separate individual particles using thresholding because most particles are in contact as can be seen in Figure 5-3a. Image analysis software treat all connected areas as one segment.

5.2.3 Magnification and Resolution

Resolution of SEM micrographs is a function of magnification and the imaging parameters. High magnification images provide high resolution and small field of view, while low magnification images provide low resolution and large field of view. Figure 5-4 shows three SEM images of the RGOM-EI-0.2 mudrock sample acquired at three different magnifications of: 111.6 KX, 30 KX, and 6 KX. The widths of the field of view corresponding to these magnifications are 2.74 μm (Figure 5-4a), 10 μm (Figure 5-4b), and 50 μm (Figure 5-4c), respectively. These images show the loss of resolution and details of the microstructure at low magnifications. As a consequence, the choice of magnification depends on the information of interest, as well as the smallest feature that we would like to resolve. For example, Figure 5-5 shows that the smallest pore that we can properly measure in an SEM image with a magnification of 111.6 KX is 10 nm, while the smallest pore that can be measured in an SEM image with a magnification of 30 KX is 30 nm. The next section addresses this issue for mudrocks and proposes a new method to obtain representative information about the pore space.

5.3 Integration of Magnifications (IOM)

5.3.1 Introduction

Mudrocks are highly heterogeneous sedimentary rocks that consist mainly of clay minerals, silt inclusions, and other minerals in trace amounts. The heterogeneous nature of mudrocks has made its microfabric more complex than other sedimentary rocks. In particular, obtaining representative information about the pore space is challenging, given that mudrocks contain pores that range in size from nanometers to microns. As a consequence of this wide-scale and heterogeneous nature, it is not possible to use one image at a specific magnification to obtain

representative porosity information. In this investigation, we develop the integration of magnification (IOM) method, which combines porosity information obtained from images acquired at different magnifications to represent the entire pore space of mudrocks. This method involves dividing the pore space into several length scales, and using the right magnification and number of images to represent each length scale. High magnification images provide high resolution and small field of view, while low magnification images provide low resolution and large field of view. Therefore, high magnification images are used to target the nanometer-sized porosity, while low magnification images are used to target the bigger porosity. As discussed in the next paragraphs, the new methodology will circumvent the need to stitch together hundreds of images to provide representative information about mudrocks.

To further illustrate this methodology, Figure 5-6 shows a schematic that represents SEM images at different magnifications. In this schematic, black circles represent pores, while grey represents particles. Assuming that all the circles (pores) in this schematic range in size from d_{min} to d_{max}, Figure 5-6 shows that what appears as a solid matrix in the low magnification schematic (Figure 5-6b), is in fact a porous matrix in the high magnification schematic (Figure 5-6a). As discussed above, this is to model the fact that the resolution of low magnification images is lower than that of high magnification images (see Figure 5-4). To calculate the porosity from these two schematics, the pores visible at each magnification have to be clearly defined. In this example, assume that the minimum size that can be characterized in the low magnification schematic is d_{min2}. To calculate the total porosity, the high magnification schematic (Figure 5-6a) is used to account for pores with sizes that range from d_{min} to d_{min2}, while the low magnification schematic (Figure 5-6b) is used to account for pores with sizes that range from d_{min2} to d_{max}. The integration of magnifications (IOM) method consists of calculating the porosity in the high magnification schematic (Mag 1), and then using the obtained porosity to calculate final porosity in the low magnification schematic (Mag 2). The high magnification porosity can be calculated using the following formula:

$$n_1 = \frac{A_{p1}}{A_{T1} - A_{Lp1}} - \frac{A_{Lp1}}{A_{Ti} - A_{Lp1}} \tag{5-1}$$

where n_1 is the porosity of Mag 1-pores (d_{min} to d_{min2}), A_{T1} is the total area of pores and particles in the schematic at Mag 1, A_{p1} is the area of target pores at Mag 1 with a size range of

d_{min} to d_{min2}, and A_{Lp1} is the area of the pores larger than d_{min2} at Mag 1. The pores larger than d_{min2} are excluded at high magnification, as shown by the second term of equation (5–1). These pores will be accounted for at the low magnification schematic (Mag 2). Once Mag 1-porosity has been calculated, the following equation can be used to calculate the Mag 2-porosity and the final porosity:

$$n_f = \frac{A_{p2}}{A_{T2}} + \frac{n_1 \times (A_{T2} - A_{p2})}{A_{T2}} \qquad (5\text{--}2)$$

where n_f is the final porosity, A_{T2} is the total area of pores and particles, A_{p2} is the area of target pores at Mag 2 with a size range of d_{min2} to d_{max}. Equation (5–2) can be rewritten in the form:

$$n_f = n_2 + n_1 \times C \qquad (5\text{--}3)$$

where n_2 is the Mag 2-porosity, and C is the ratio of solid area to total area as shown in equation (5–2). The same procedure can be used to calculate the porosity if more magnifications are used to represent the pore space. The number of magnifications that should be used to represent the pore space depends mainly on the size range in question, and the statistical variability of porosity. In the next section, we use 2D simulations of synthetic microstructures to validate the IOM method.

5.4 2-D Simulations

The main purpose of the 2-D simulations is to validate the IOM method used in this thesis to calculate porosity. The 2-D simulations consist of three main steps. First, we construct a synthetic microstructure with specific parameters such as volume fraction and size distribution. Second, we probe the synthetic microstructure with frames of different sizes. This step simulates the process of using different magnifications to represent different pore sizes. Small frames represent high magnification images, and hence target small sizes. Large frames represent low magnification images, and hence target large sizes. Finally, we use statistical analysis to determine the confidence interval of the measured properties using the IOM method.

5.4.1 Synthetic Microstructure

We use a MATLAB code to build a synthetic microstructure with specific parameters such as volume fraction and size distribution. The synthetic microstructure consists of circles randomly distributed in a box of known size. The first step in the MATLAB code is to specify

input parameters, which include volume fraction, maximum circle diameter, and size distribution. We use lognormal size distribution because it represents the microstructure of mudrocks. The user can specify the size distribution parameters such as the mean and standard deviation. In this example, the area fraction was set to 0.1022 and the maximum circle diameter is 506. The mean and standard deviation of the lognormal size distribution were set to 3 and 1, respectively. The box size was chosen to be 400 times the largest circle diameter, which in this example provides a box with a size of 200,000. The big box size was chosen to provide flexibility when changing the parameters of the simulations, such as the size and number of frames used later to probe the synthetic microstructure. To generate the list of circles with these parameters, we use the MATLAB function published by (Tschopp et al., 2008). Our MATLAB code passes the input parameters to this function, which returns a vector of circles that satisfy input parameters. In this example, the number of circles generated with the above parameters is around 1.8 million, with a minimum circle diameter of 6, and a maximum circle diameter of 506. Figure 5-7 shows the size distribution of the circles generated using these parameters. The list of circles are then randomly placed in the box with the size of 200,000. The placement is carried out one circle at a time, and no overlap with other circles is allowed. The MATLAB code picks a circle from the list, generates random coordinates for the center, and performs an overlap check with already placed circles. If there is an overlap with another circle, the coordinates are rejected and the process is repeated until there is no overlap. Figure 5-8 shows sub-windows of the generated synthetic microstructure with the parameters specified in this section.

The next step in the 2-D simulations is to use frames of different sizes to measure properties of interest. In this example, we focus on measuring area fraction and size distribution, but the concept can be applied on any property of interest. The number of frame sizes to be used depends on the size range in question. In the synthetic microstructure described above, circle diameters range from 6 to 506. We use two frame sizes to probe this range: small frames to represent high magnification images, and large frames to represent low magnification images. Equations (5–1) and (5–2) can be used to calculate the area fraction of circles in this synthetic microstructure. The analysis using the IOM method depends on the number of frames at each magnification, the size of frames at each magnification, and the range of sizes targeted by these frames. The range of size targeted by each frame is defined by the size limits d_{min}, d_{min2}, and d_{max}. The next paragraphs address the influence of these factors on the final results.

5.4.2 Number of Frames

The question that we would like to answer regarding the number of frames at each magnification is to what degree does the mean of a sample of n frames represent the population of pores targeted by these frames? As mentioned above, we use two frame sizes to probe the synthetic microstructure in this example. To isolate the influence of the number of frames, the size of frames and the size limits $(d_{min}, d_{min2}, d_{max})$ are fixed, while the number of frames is varied from 10 to 50. The size limit d_{min2} was set to 200, which means that Mag 1 frames target circles with a diameter range of 6 to 200, while Mag 2 frames target circles with a diameter range of 200 to 506. In this synthetic microstructure, the area fraction of circles targeted in Mag 1 (6 to 200) is 0.0736, while the area fraction of circles targeted at Mag 2 (200-506) is 0.0309. Squared frames were used with a side length a. The ratio of the frame side length, a, to the maximum circle diameter at each magnification, D_{max}, was set to 40. The maximum circle diameters at Mag 1 and Mag 2 are d_{min2} and d_{max}, respectively. The case of a sample of 10 frames is used here to illustrate the manner by which the simulations were performed. The simulations start at Mag 1 by setting the size of the frame to 40 x D_{max}, which is 200 in this example. Then, x and y coordinates are randomly generated for 10 frames, imposing a criterion of no overlap to prevent sampling the same area twice. For each frame, a list of circles is collected and stored. Equation (5–1) is then used to calculate the Mag 1-area fraction, which provides a vector of 10 values. The mean of this sample of 10 frames is then calculated and stored for further analysis. This process is repeated 50 times, which results in a vector of 50 values for the Mag 1-area fraction obtained from 50 different samples of 10 frames. Then, we use this vector of 50 values to calculate the mean and the standard deviation. The standard deviation in this case is referred to as the standard error of the mean (Streiner, 1996; Altman and Bland, 2005; Harding, 2014). The standard error of the mean represents the variability of the mean between different samples, provided that a large number of samples could be obtained. It is worth mentioning that the standard error and the standard deviation are two different measures that provide different information. While the standard deviation provides a measure of the dispersion of individual measurements around their mean, the standard error provides a measure of the variability associated with using different samples to estimate the mean of the population (Streiner, 1996; Altman and Bland, 2005; Harding, 2014). The confidence interval, CI, of the mean can then be estimated using:

$$CI = \mu \mp z \times s_e \qquad (5\text{--}4)$$

where μ is the mean area fraction at the magnification of interest, z is a multiplier calculated based on the required confidence interval, and s_e is the standard error of the mean. For example, for the 95% confidence interval z is equal to 1.96. The same procedure is repeated for samples of 20, 30, 40, and 50 frames, for which we obtain the mean and the standard error. Figure 5-9a shows the mean of the Mag 1-area fraction, as a function of the number of frames, along with the 95% confidence interval shown by the error bars. Figure 5-9b shows the coefficient of variation as a function of the number of frames for Mag 1-area fractions. The coefficient of variation is calculated as the standard error divided by the mean. Figure 5-9b shows that the coefficient of variation decreases as the number of frames increases. Also, these results reveal the level of variability as a function of the number of frames used in each sample, which ranges from 1.5% to 0.5%.

The same procedure is repeated at Mag 2, where equation (5–2) is used to calculate the Mag 2-area fraction, n_2, and the final area fraction, n_f. Similar to the Mag 1-area fraction, for each sample of n frames, we obtained a mean and a standard error. Figure 5-9c shows the mean of the Mag 2-area fraction as a function of the number of frames, along with the 95% confidence interval shown by the error bars. Figure 5-9d shows the coefficient of variation as a function of the number of frames for the Mag 2-area fraction. Similar to the Mag 1-area fraction, the coefficient of variation decreases as the number of frames increases. The range of variability is slightly larger than for Mag 1, and ranges from 2.5% to 0.5%. A comparison between Figure 5-9a and Figure 5-9c shows that the standard error in both cases is comparable. Therefore, the higher coefficient of variation at Mag 2 is attributed to the low mean area fraction (0.0309) compared to that at Mag 1 (0.0736). Keeping in mind equation (5–3), the mean and standard deviation of the final area fraction can be calculated using the following equations:

$$\overline{n_f} = \overline{n_2} + \overline{n_1} \times C \qquad (5\text{--}5)$$

$$se_f = \sqrt{se_2^2 + se_1^2 \times C^2} \qquad (5\text{--}6)$$

where, $\overline{n_f}$ is the average final area fraction, se_2 is the standard error of the final area fraction, se_2 is the standard error of the Mag 2-area fraction, and se_1 is the standard error of the Mag 1-area fraction. Figure 5-9e shows the mean of the final area fraction as a function of the number of frames along with the 95% confidence interval shown by the error bars. Figure 5-9f shows the

coefficient of variation as a function of the number of frames for the final area fractions. The coefficient of variation decreases as the number of frames increases, and ranges from 1% to 0.5%. The above results show that the variability decreases as the number of frames increases. Furthermore, the variability in the Mag 1-area fraction and the Mag 2-area fraction is different due to the differences in the mean of the area fraction at each magnification. The final coefficient of variation is low and is governed by the larger area fraction, which is Mag 1 in this case.

5.4.3 Size of Frames

In this section, we would like to investigate the influence of the chosen size of frames on the calculated area fraction. To isolate the influence of the size of frames, the number of frames, n, was set to 30. The size limit, d_{min2} was set to 200, which means that at Mag 1 frames target circles with a diameter range of 6 to 200 and area fraction of 0.0736, and Mag 2 frames target circles with a diameter range of 200 to 506 and area fraction of 0.0309. Squared frames were used with a side length a. The ratio of the frame side length, a, to the maximum circle diameter at each level, D_{max}, was varied from 10 to 50. The maximum circle diameters at Mag 1 and Mag 2 are d_{min2} and d_{max}, respectively. For each a/D_{max} ratio, 50 samples with a size of 30 frames were collected and used to calculate the mean and the standard error. The simulations of the a/D_{max} ratio were performed in a similar manner to the simulations of the number of frames illustrated in the previous section. Figure 5-10 shows the mean area fraction and coefficient of variation as a function of the a/D_{max} ratio for the Mag 1-area fraction (Figure 5-10a, b), Mag 2-area fraction (Figure 5-10c, d), and the final area fraction (Figure 5-10e, f). The mean and standard error of the final area fraction were calculated using equations (5–5) and (5–6). Furthermore, the confidence interval was calculated using equation (5–4). In general, Figure 5-10 shows that the coefficient of variation of the area fraction at each Magnification decreases as the size of the frame increases. The coefficient of variation at Mag 1 ranges from 3% to 0.5% (Figure 5-10b). The coefficient of variation at Mag 2 is higher than that at Mag 1, and ranges from 6% to 0.5% (Figure 5-10d). This difference is due to the lower mean of the area fraction at Mag 2 (0.0309) compared to that at Mag 1 (0.0736).

5.4.4 Size Interval

The above results showed that the area fraction at each level is an important factor in deciding its coefficient of variation. The area fraction at each magnification is a function of the

93

size interval targeted at each level and defined by the size limits: d_{min}, d_{min2}, d_{max} (see Figure 5-11). In this synthetic microstructure, $d_{min} = 6$ and $d_{max} = 506$. The size interval can be varied by changing d_{min2}. In other words, the d_{min2} bar in Figure 5-11 was shifted to the right. This shift widens the diameter range in Mag 1, and narrows the diameter range in Mag 2. For example, if $d_{min2} = 100$, then the size range targeted at Mag 1 is 6 to 100, while the size range targeted at Mag 2 is 100 to 506. To investigate the influence of the size interval at the final results, the following values for d_{min2} were used: 50, 100, 200, and 300. To isolate the influence of the size, the number of frames, n, was set to 30, and the size of frames at Mag 1 was set to 8000, and 25,000 at Mag 2. For each size interval, 50 samples with a size of 30 frames were collected, and used to calculate the mean and the standard error. The simulations of the size interval were performed in a similar manner to the simulations of the number of frames and frame sizes illustrated in the previous two sections. The results of area fractions and coefficients of variation were plotted against the ratio of the maximum circle diameter to the minimum circle diameter at each magnification. In the example above, this ratio would be 100/6, d_{min2}/d_{min}, for Mag 1, and 506/100, d_{max}/d_{min2} for Mag 2. Figure 5-12a shows the coefficient of variation as a function of the ratio of the maximum circle diameter to the minimum circle diameter at Mag 1-, Mag 2-, and the final area fractions. Figure 5-12b shows the mean area fractions for Mag 1 and Mag 2 along with the final area fraction. Figure 5-12a shows that as the range of diameters for Mag 1 increases (shift to the right in Figure 5-11), the coefficient of variation increases. Conversely, as the circle diameter range decreases at Mag 2 (shift to the right in Figure 5-11), the coefficient of variation decreases. This trend is attributed to the fact that as the circle diameter range is increased at Mag 1, the standard deviation increases along with the mean area fraction, which leads to a slight increase in the coefficient of variation. On the other hand, as the circle diameter ranges decrease at Mag 2, the standard deviation slightly decreases along with the mean area fraction. The decrease in the mean area fraction leads to the increase in the coefficient of variation. Furthermore, the final coefficient of variation is biased towards the magnification with the highest mean area fraction (see Figure 5-12a and Figure 5-12b), and the coefficient of variation at the two levels is equal when the mean area fraction at each level is almost the same. Furthermore, Figure 5-12b shows that regardless of the size interval at each magnification, the final area fraction is equal to 0.1022, which is the area fraction we used to generate the synthetic microstructure. These results suggest that if size intervals at each magnification (d_{min2} in Figure

94

5-11) are chosen such that area fractions at each level are almost equal, the variability would be minimized.

5.4.5 Simulations and Imaging in Practice

The above results were obtained using 50 samples of n frames, where n was varied between 10 and 50. In practice, this approach is not possible for several reasons, such as cost, instrument availability, and complications related to the amount of generated data. The alternative approach in practice is to obtain one sample of n frames at each magnification, which can then be used to calculate the final area fraction and the associated confidence interval – which, in turn, can be estimated using the standard error. Luckily, an estimate of the standard error can be calculated based on the standard deviation of one sample of n frames using the following formula (Streiner, 1996; Altman and Bland, 2005; Harding, 2014):

$$s_e = \frac{\sigma_s}{\sqrt{n}} \tag{5-7}$$

where σ_s is the standard deviation of the sample, and n is the number of frames. To compensate for the higher uncertainty associated with using an estimate of the standard error derived from one sample only, a higher multiplier is used to calculate the confidence interval, CI, which is given by:

$$CI = \mu_s \mp t \times s_e \tag{5-8}$$

where μ_s is the mean of the sample, and t is a multiplier obtained from the student's t-distribution based on the required confidence interval, and the size of the sample. For example, the multiplier, t, for a sample of size 20 frames and a confidence interval of 95%, is equal to 2.093. This is a powerful technique because it means that we can use one set of frames at each magnification to calculate the area fraction and the associated confidence interval. Parameters such as the size of frames, number of frames, or size interval can be used to control the confidence interval, as outlined in the previous sections. To illustrate this concept using simulations, the number of frames was set to 20, and the a/D_{max} ratio was set to 40. The size limit d_{min2} was set to 120, which means that at Mag 1 frames target circles with a diameter range of 6 to 120 and area fraction of 0.0511, and Mag 2 frames target circles with a diameter range of 120 to 506 and area fraction of 0.0539. In these simulations, a sample of 20 frames at Mags 1 and 2 were collected and analyzed for 50 iterations. In each iteration, equations (5–1)

and (5–2) are used to calculate the Mag 1- and Mag 2-area fractions, respectively. This provides us with 20 values of mean area fractions at each magnification. These values are used to calculate the mean and the standard deviation. The standard error and the 95% confidence interval are then calculated using equations (5–7) and (5–8), respectively. Figure 5-13 shows the calculated final area fraction along with its 95% confidence interval shown by the error bars for the 50 iterations. The true area fraction of the synthetic microstructure (0.1022) fell out of the 95% confidence interval only three times, which is 6% of the 50 iterations. In other words, the estimated confidence interval included the true mean of the microstructure 94% of the time. These results show that the confidence interval of the true area fraction can be estimated using only one sample of n frames at each magnification. Parameters such as the number of frames, and the size of frames can be varied to obtain a narrow or wide confidence interval. This technique will be applied later to real mudrock samples to obtain representative information about the porosity.

5.4.6 Size Distribution

This section describes the application of the IOM method to obtain the size distribution of circles. Size distributions are of great interest and provide important information about the microstructure of materials. The main objective here is to use one sample of frames of size n at Mags 1 and 2 to calculate the size distribution of circles, and compare it with the true size distribution of the synthetic microstructure shown in Figure 5-7. The simulations start at Mag 1 by generating x and y coordinates for n frames, imposing a criterion of no overlap to prevent sampling the same area twice. For each frame, a list of circles is collected and stored, which results in a vector of diameters within the specified range of Mag 1 (6 – 120), d_1. This procedure is repeated for Mag 2, which results in another vector of diameters within the specified range of Mag 2 (120 -506), d_2. The area of circles for Mag 1, a_1, and Mag 2, a_2, are calculated using the obtained vectors d_1 and d_2, respectively.

The next step in the simulations is to adjust the calculated areas a_1 and a_2 based on their relative proportions to obtain a representative total area, a_T, that can be used in the calculations of the size distribution. If we consider a_1 as the reference, then the adjusted area at Mag 2, a'_2, is given by the following formula:

$$a'_2 = a_1 \times \frac{n_2}{n_1} \qquad (5\text{--}9)$$

where, n_2 is the Mag 2-area fraction calculated using equation (5–2), and n_1 is the Mag 1-area fraction calculated using equation (5–1). Both n_2 and n_1 are calculated based on the same sample of n frames, used to obtain the diameter vectors d_2 and d_1, respectively. The total area, a_T, that can be used in the size distribution calculations is given by:

$$a_T = a'_2 + a_1 \qquad (5\text{--}10)$$

The size distribution calculations start with the Mag 2 vector of diameters, d_2, which includes circles with a diameter range of 120 to 506. Bins of width 1 are generated in the range of 120 to 506, and the frequency of each diameter in these bins is calculated. The percent passing corresponding to each bin is then calculated using the following formula:

$$p_{2,m} = \frac{a_T - \left(\frac{a'_2}{a_2}\right)\left(\sum_{i=1}^{m} a_{b2,i}\right)}{a_T} \qquad (5\text{--}11)$$

where, $p_{2,m}$ is the percent finer of the diameter grouping in each bin at Mag 2, m is a bin number with the largest diameter corresponding to number 1, and $a_{b2,i}$ is the area of circles in the ith bin at Mag 2. The scaling factor a'_2/a_2 is important because the area of Mag 2 diameters was adjusted to obtain a representative total area, a_T. The calculations then proceed to the Mag 1 vector of diameters, d_1, where the percent finer is calculated using the following formula:

$$p_{1,m} = \frac{a_T - a'_2 - \left(\frac{a_1}{a_1}\right)\left(\sum_{i=1}^{m} a_{b1,i}\right)}{a_T} \qquad (5\text{--}12)$$

where, $p_{1,m}$ is the percent finer of the diameter grouping in each bin at Mag 1, m is a bin number with the largest diameter corresponding to number 1, and $a_{b1,i}$ is the area of circles in the ith bin at Mag 1. The scaling factor a_1/a_1 is equal to 1 because the adjustment was performed based on a_1. This factor would be important in the case where three magnifications were used to obtain the size distribution. Finally, the results of Mags 1 and 2 are combined to obtain the final size distribution. To illustrate the method through an example, the number of frames was set to 20, and the a/D_{max} ratio was set to 40. The size limit, d_{min2} was set to 120, which means that at Mag 1 frames target circles with a diameter range of 6 to 120 and area fraction of 0.0511, and Mag 2 frames target circles with a diameter range of 120 to 506 and area fraction of 0.0539. The simulations were repeated 10 times using these parameters, which resulted in 10 different size

distribution curves. Figure 5-14 shows the obtained size distribution curves along with the true size distribution shown in Figure 5-7. Figure 5-14 shows that the method accurately calculates the size distribution of the synthetic microstructure using a sample of 20 frames at Mags 1 and 2. Furthermore, Figure 5-14 shows that the 10 curves produced by the 10 trials matched the true size distribution of the synthetic microstructure. This result shows that the method is repeatable. In the next section, this method will be applied to calculate the pore size distribution of mudrock samples.

5.5 Application of Integration of Magnifications Method to Mudrocks

The application of the IOM method to mudrocks is illustrated in detail in this section using as a reference the images obtained for a Gulf of Mexico sample resedimented at 0.2 MPa (RGOM-EI-0.2). The first step in the IOM method is the determination of the number of magnifications needed to represent the microstructure, followed by the determination of the size interval targeted at each magnification. These points will be addressed based on knowledge of the microstructure of mudrocks, and the insights gathered from the simulations in the previous section. This section starts with a qualitative description of the microstructure of RGOM-EI-0.2, which applies to most mudrock samples studied in this investigation. The details of the IOM method are then discussed to obtain the porosity and the pore size distribution of the RGOM-EI-0.2 sample.

5.5.1 Description of the Microstructure

Figure 5-15 presents images of the RGOM-EI-0.2 sample acquired at different magnifications as shown by the scale bar in each image. As described in section 5.2.3, high magnification images provide a small field of view and high resolution, while low magnification images provide a large field of view and low resolution. Therefore, these images reveal different aspects of the microstructure of the RGOM-EI-0.2 sample due to the wide range of pore sizes and particles in mudrocks. In these images, black represents pore space while grey represents clay particles and silt inclusions. High magnification images show the existence of clay stacks, which consist of clay particles forming face-face contacts (Figure 5-15a, b). Furthermore, these stacks form face-edge and face-face contacts with other clay stacks and particles. Low magnification images show that silt inclusions are randomly distributed in a matrix of clay

particles (Figure 5-15c, d). These inclusions range in size from a few microns to approximately 10 microns (Figure 5-15e, f). Furthermore, Figure 5-15 shows that mudrock porosity can be divided into two main categories: clay porosity and interparticle porosity. Clay porosity consists of elliptical pores with high aspect ratio (Figure 5-15a, b). These pores exist mainly between clay particles in clay stacks, and range in size from nanometers to a hundred nanometers, approximately. Interparticle porosity, on the other hand, exists between clay stacks forming face-edge contacts, between clay stacks and silt inclusions, and at the boundaries of silt inclusions (Figure 5-15c, d). The majority of these pores range in size from a hundred nanometers to a few microns. Furthermore, their shapes range from elliptical with low aspect ratio to angular. Interparticle pores as large as 2 μm can be found in mudrock SEM images, but these pores are rare (Figure 5-15e).

5.5.2 Magnifications and Size intervals

The previous section showed that the majority of pores in mudrocks range in size from nanometers to hundreds of nanometers, with the existence of a few large pores on the order of 2 μm. Furthermore, simulations in section 5.4 showed that the coefficient of variation decreases as the a/D_{max} ratio increases. Given the size range of pores in mudrocks, we decided that three magnifications would be sufficient to represent the microstructure. Based on the largest pore size of 2-3 μm, the lowest magnification was chosen to be 6 KX, which provides a field of view of 50 μm, and an a/D_{max} ratio of 17-25. The highest magnification was chosen such that it provides a balance between resolution and the field of view. Figure 5-4 shows the relationship between resolution and magnification. A magnification of 111.6 KX provides a field of view of 2.74 μm, and a minimum detectable pore of approximately 10 nm (Figure 5-4a). A magnification of 11.43 KX provides a field of view of 10 μm, and a minimum detectable pore size of approximately 30 nm (Figure 5-4b). While the 30 KX provides high resolution, the small field of view makes the use of this magnification impractical for the purpose of obtaining representative porosity information about mudrocks. Therefore, we chose the highest magnification to be 30 KX as it provides a good balance between resolution and field of view. Finally, the intermediate magnification was chosen to be 12 KX, which provides a field of view of 25 μm.

The minimum pore size is governed by the resolution of the SEM, as well as the minimum number of pixels required to properly quantify the pore. As a rule of thumb, the

minimum number of pixels required to quantify a pore using image analysis tools is 10 pixels. At a magnification of 11.4 KX, the pixel size is 9.76 nm, and hence the minimum quantifiable pore area is 953 nm^2. The equivalent circular diameter based on this area is 35 nm. It is worth mentioning that there is no contradiction between the numbers quoted in Figure 5-4b (30 nm), and the number calculated based on the 10-pixels criterion. The 30 nm in Figure 5-4b were obtained for the short axis of the elliptical pore, while the 35 nm were obtained by assuming that the pore can be represented by a circle. We chose the 35 nm as the minimum detectable pore size in mudrocks at a magnification of 30 KX for the purpose of consistency, because pore size distributions will be presented in terms of equivalent circular diameter.

Figure 5-12 shows that the specified size interval at each magnification influences the variability of the area fraction, and the final calculated area fraction is independent of the chosen size interval at each magnification. In other words, the specified size interval at each magnification will always yield the right area fraction, but with different variability. The following size intervals were found to provide a reasonable standard deviations: 10 nm to 151 nm, 151 nm to 675 nm, and 675 nm to 2 μm, for magnifications 1, 2, and 3, respectively. Figure 5-16 provides a summary of the three magnifications used in this investigation to represent the pore space of mudrocks along with the corresponding field of view and size interval.

Finally, the imaging of the microstructure of mudrocks is performed randomly, and covers the entire milled area (Figure 5-17). Twenty images are acquired at each magnification, which provides a total of 60 images to characterize the pore space of mudrocks. As described above, the high magnification images (11.43 KX) target small clay porosity (35-151 nm), and hence the clay matrix is imaged and the big particles are avoided. The low and intermediate magnifications are used to probe the pore space randomly. The next section illustrates the use of the IOM method to calculate the porosity and pore size distribution of the RGOM-EI-0.2 mudrock sample.

5.5.3 Porosity and Pore Size Distribution

The porosity calculations using the IOM method follow the equations outlined in section 5.3.1. The porosity corresponding to each magnification can be calculated using the following formula:

$$n_i = \frac{A_{pi}}{A_{Ti} - A_{Lpi}} - \frac{A_{Lpi}}{A_{Ti} - A_{Lpi}} \qquad (5\text{--}13)$$

where, n_i is the porosity corresponding to Mag i, A_{Ti} is the total area of pores and particles at Mag i, A_{pi} is the area of target pores at Mag i, and A_{Lpi} is the area of big pores at Mag i. This formula is a generalization of equation (5–1), which was written for Mag 1 only. The final porosity is then calculated using the following formula:

$$n_f = n_l + n_{l-1}C_l + n_{l-2}C_lC_{l-1} + \cdots \qquad (5\text{--}14)$$

where n_f is the final porosity and l is the number of magnifications, which is three in our case. C_l is the ratio of solid area to total area at Mag l, and is given by

$$C_l = \frac{(A_{Tl} - A_{pl\_}A_{Lpl})}{A_{Tl} - A_{Lpl}} \qquad (5\text{--}15)$$

where, A_{Tl} is the total area of pores and particles at the Mag l, A_{pl} is the area of target pores at Mag l, and A_{Lpl} is the area of big pores at Mag l. The above formulas represent a generalization of equation (5–3), which was written for the case of two magnifications only. The standard error and the confidence interval can be calculated using equations (5–7) and (5–8), respectively. Similarly, the generalization of equation (5–6), used to calculate the final standard error, takes the form:

$$se_f = \sqrt{se_l^2 + B \times \sum_{i=1}^{l-1} se_i^2} \qquad (5\text{--}16)$$

where se_f is the standard error of the final porosity, se_l is the standard error of the porosity associated with the lowest magnification (Mag l), and se_i is the standard error of the porosity associated with Mag i. B represents the constant associated with each magnification. In equation (5–17), B would be C_l for Mag l, and $C_l C_{l-1}$ for Mag l-l. Figure 5-18 shows the porosity of the RGOM-EI-0.2 mudrock sample obtained using the IOM method. The results show the porosity corresponding to each magnification, as well as the final porosity obtained by combining the three magnifications using equation (5–14). The scale bars represents the 95% confidence interval of the mean obtained using the standard error. The final porosity of the RGOM-EI-0.2 mudrock sample is 0.16. The porosity at Mags 1, 2, and 3 was found to be 0.0458 $\mp$ 0.0024, 0.0755 $\mp$ 0.0020, and 0.0447 $\mp$ 0.0043, respectively. Furthermore, the calculated

101

standard error based on 20 images at each magnification is relatively low. These results suggest that 20 images at each magnification is sufficient to represent the pore space of the RGOM-EI-0.2 mudrock sample.

The pore size distribution analysis follows the discussion outlined in section 5.4.6. Similarly, equations (5–9) through (5–12) were written for the case of two magnifications. To generalize these equations for the case of several magnifications, the total area used in the size distribution calculations is given by:

$$a_T = \sum_{i=1}^{l} a_i'$$ (5–18)

where a_i', is the adjusted area of pores at Mag i, and can be calculated using the following formula:

$$a_i' = a_c \times \frac{n_i}{n_c}$$ (5–19)

where c can be any of the magnifications used in the IOM method, a_c and n_c represent the area of pores and porosity associated with that magnification, and n_i represents the porosity associated with Mag i. The size distribution then starts with the lowest magnification, and the percent finer is given by:

$$p_{l,m} = \frac{a_T - \left(\frac{a_l'}{a_l}\right)\left(\sum_{i=1}^{m} a_{bl,i}\right)}{a_T}$$ (5–20)

Where $p_{l,m}$ is the percent finer of diameter grouping in each bin at the lowest magnification (Mag l), m is a bin number with the largest diameter corresponding to number 1, and $a_{bl,i}$ is the area of circles in the ith bin at Mag l. The size distribution calculations then proceed to the next magnifications, and the percent passing can be calculated using:

$$p_{k,m} = \frac{a_T - \sum_{j=k+1}^{l} a_j' - \left(\frac{a_k'}{a_k}\right)\left(\sum_{i=1}^{m} a_{bk,i}\right)}{a_T}$$ (5–21)

where $p_{k,m}$ is the percent finer of the diameter grouping in each bin at Mag k, m is a bin number, with the largest diameter corresponding to number 1, and $a_{bk,i}$ is the area of circles in the ith bin at Mag k. The size distribution calculations for mudrocks were performed on equivalent circular diameters of pores. Figure 5-19 shows the pore size distribution of the RGOM-EI-0.2 mudrock

sample obtained using the IOM method. The equivalent diameter of RGOM-0.2 pores ranges from 35 nm to 3800 nm. As discussed in section 5.5.2, the minimum size is governed by the resolution of images at a magnification of 11.43 KX.
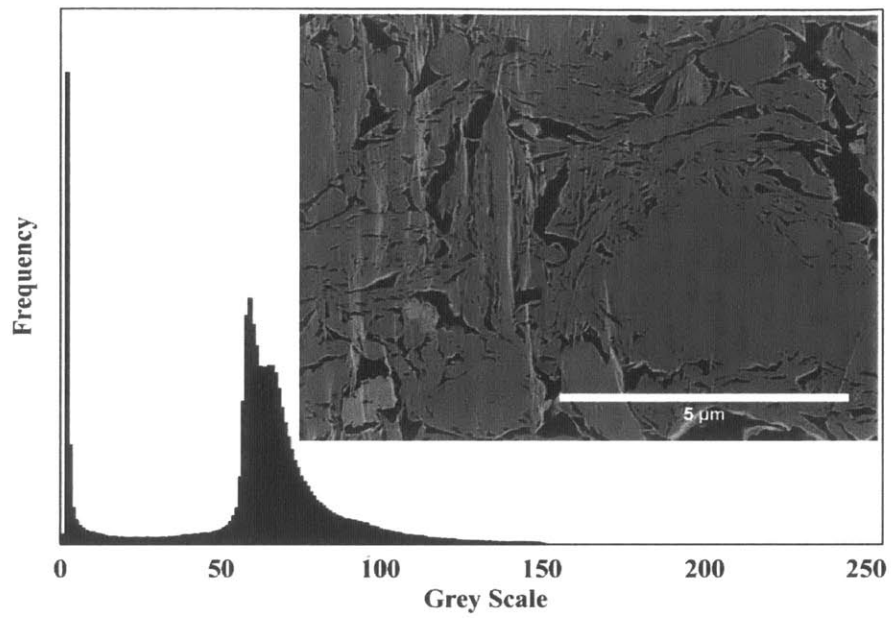
Figure 5-1: An SEM image for an RGOM sample resedimented at 0.2 MPa (RGOM-EI-0.2) along with its grey scale histogram. The histogram was obtained using ImageJ software.
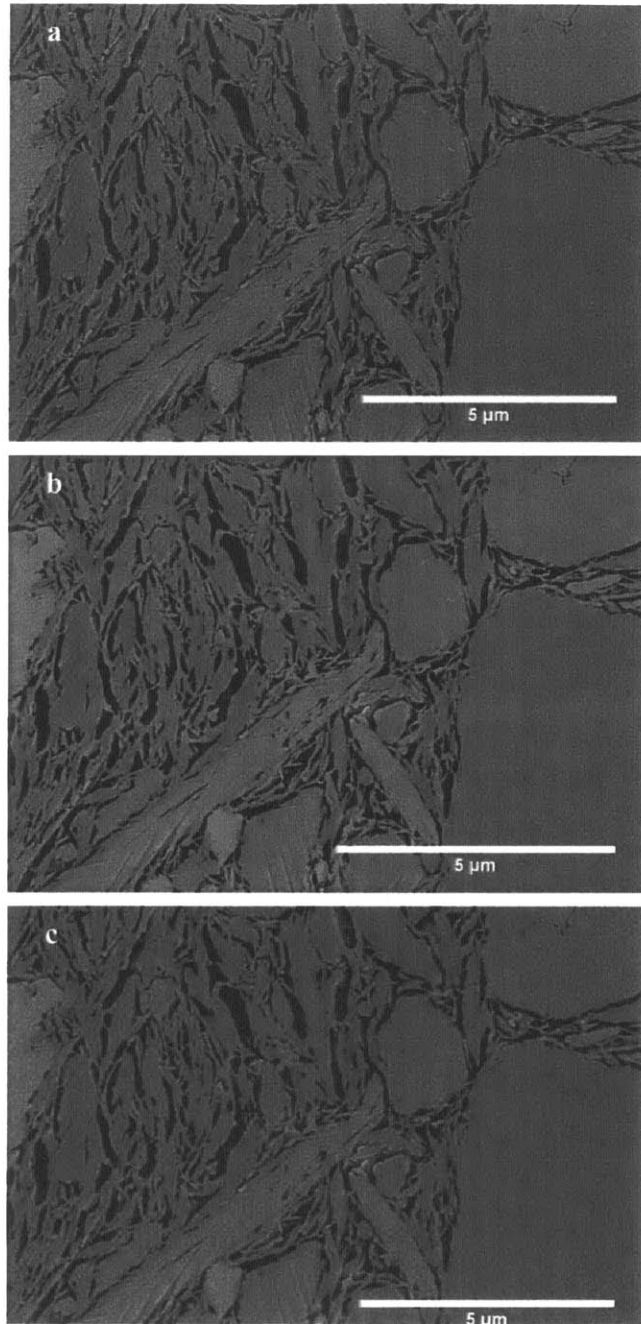
Figure 5-2: An example of image filtering for noise removal: a) unfiltered image, b) filtered image using the nonlocal means filter, and c) filtered image using the median filter.
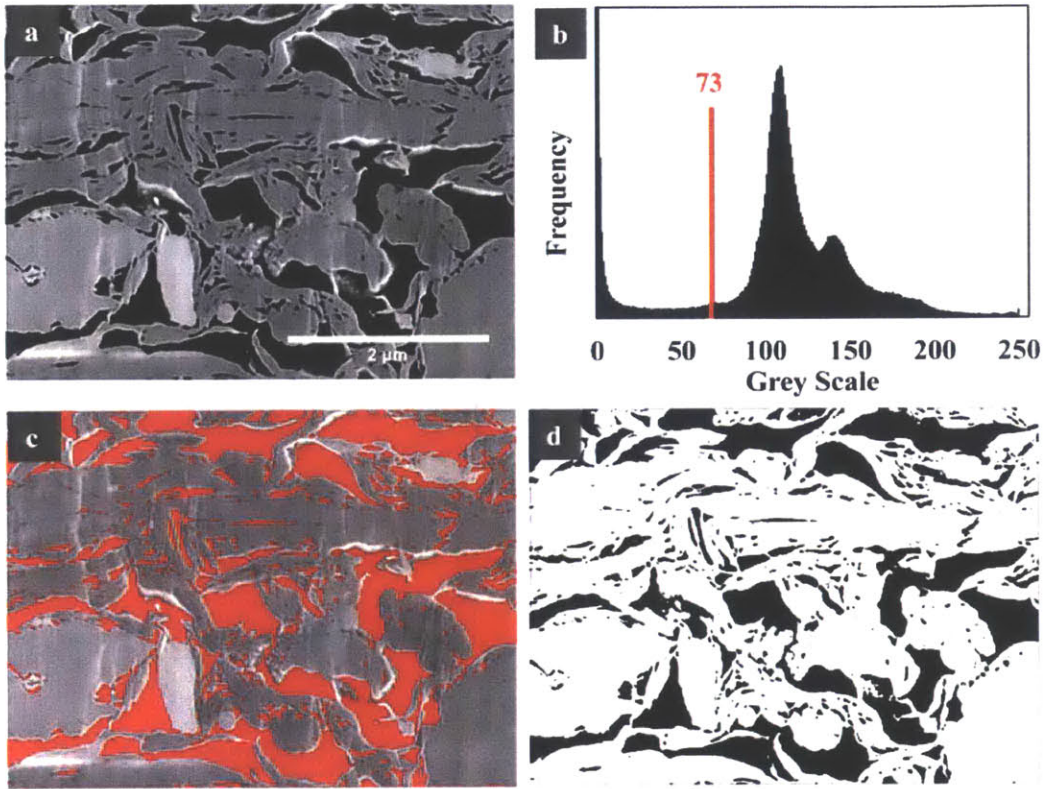
Figure 5-3: a) An SEM image of the RGOM-EI-0.2 sample, b) the histogram of grey values corresponding to the SEM image, c) thresholding of the pore space, and d) binary image of the thresholded pore space.
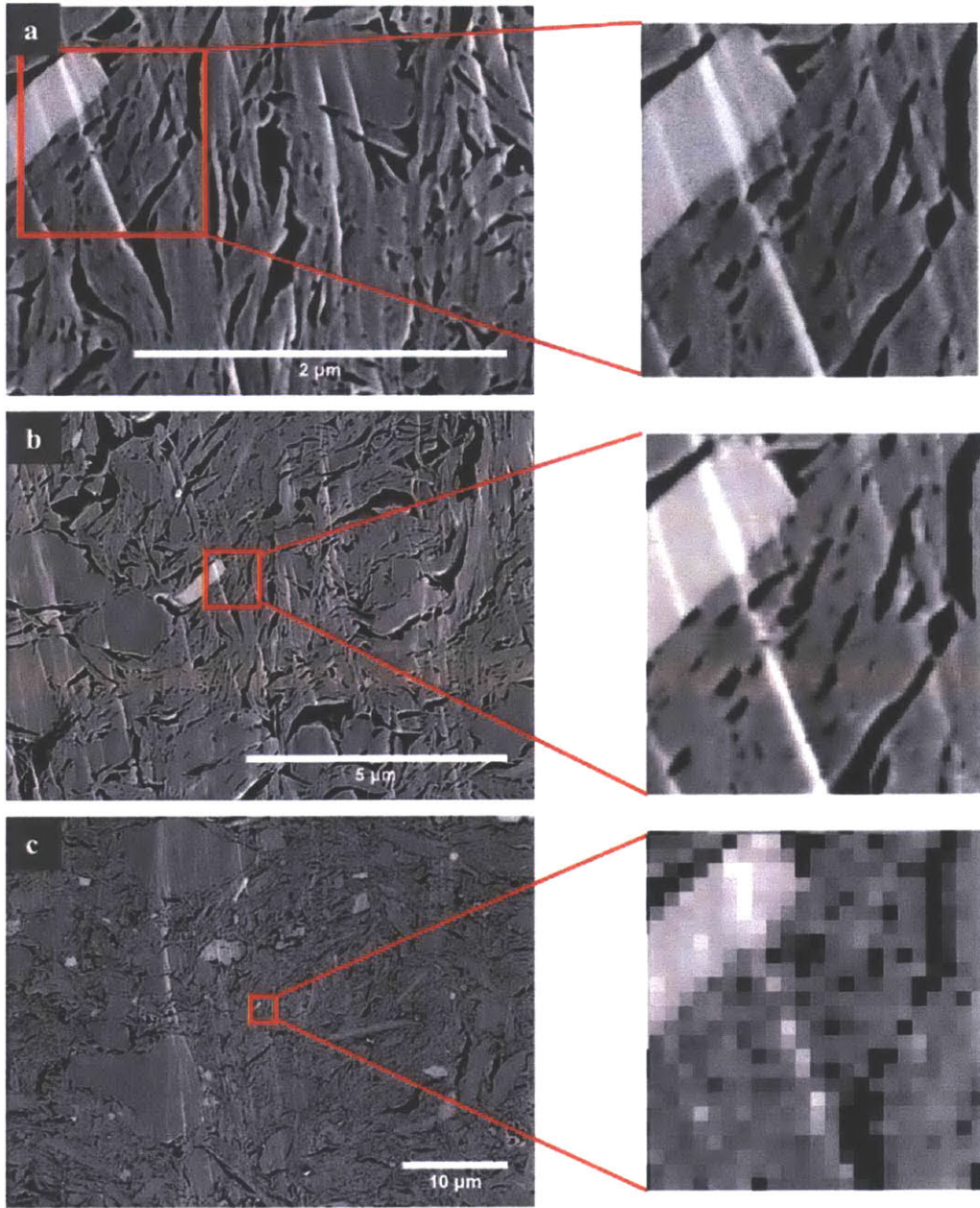
Figure 5-4: SEM images of the RGOM-EI-0.2 sample acquired at different magnifications: a) 111.6 KX, b) 30 KX, and c) 6 KX. These images show the relationship between magnification and resolution.
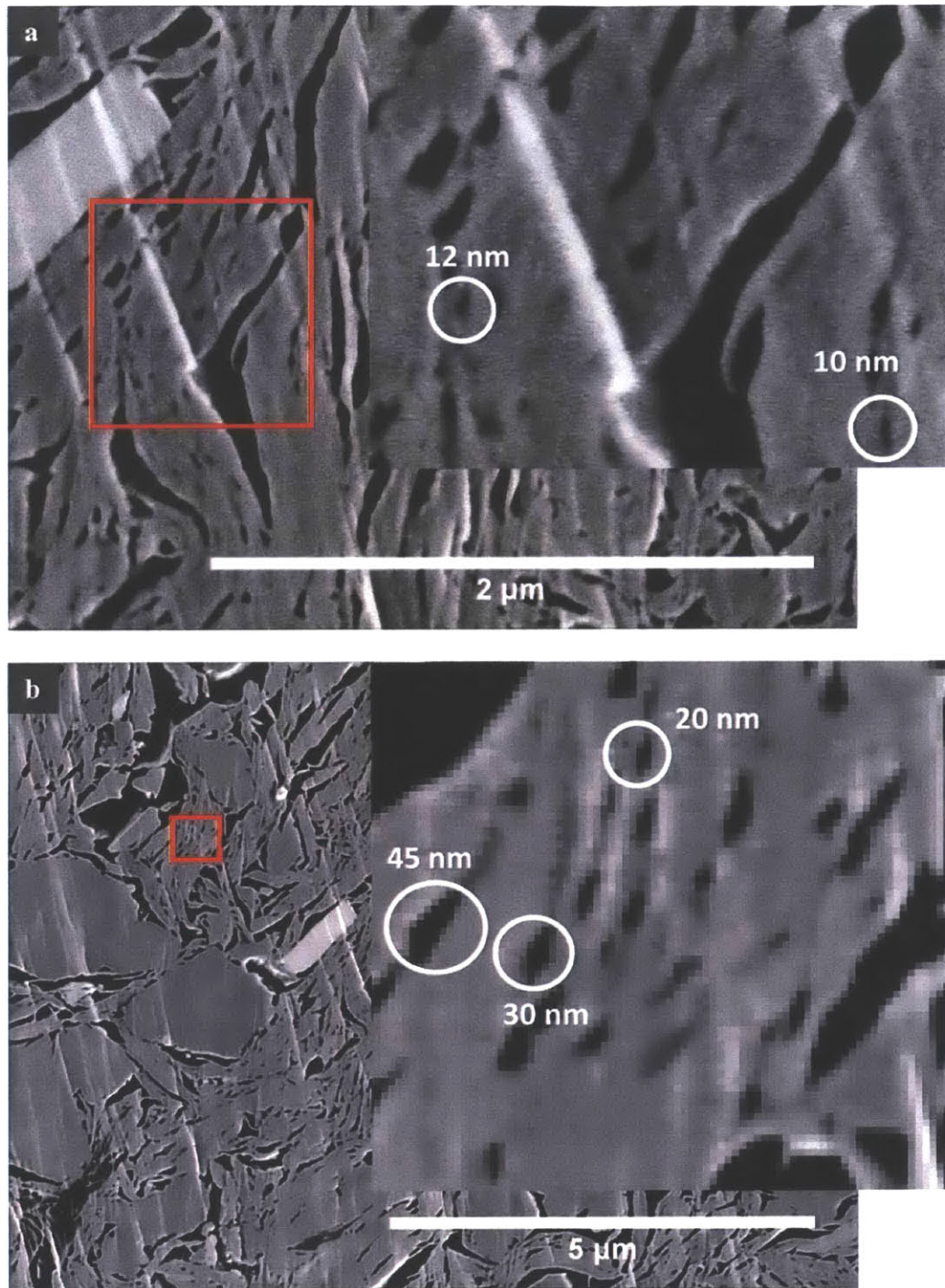
Figure 5-5: SEM images of the RGOM-EI-0.2 sample at magnifications of: a) 111.6 KX and b) 30 KX. The smallest pore that can be measured in these images is a function of magnification.

108

High Magnification
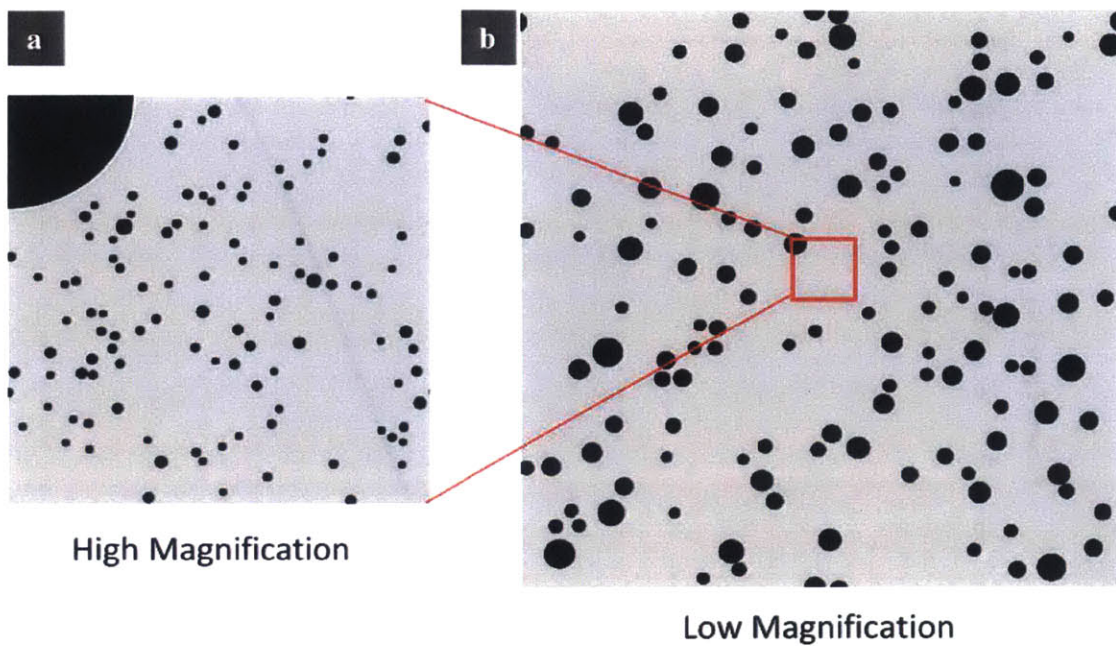
Low Magnification

Figure 5-6: A schematic that represents SEM images of mudrock samples at different magnifications: a) high magnification, and b) low magnification. Black circles represent pores while grey represents particles. These schematics show that what appears as a solid matrix at low magnification is in fact a porous matrix at high magnification. This schematic will be used to illustrate the IOM method we developed to obtain representative information about the pore space of mudrocks.
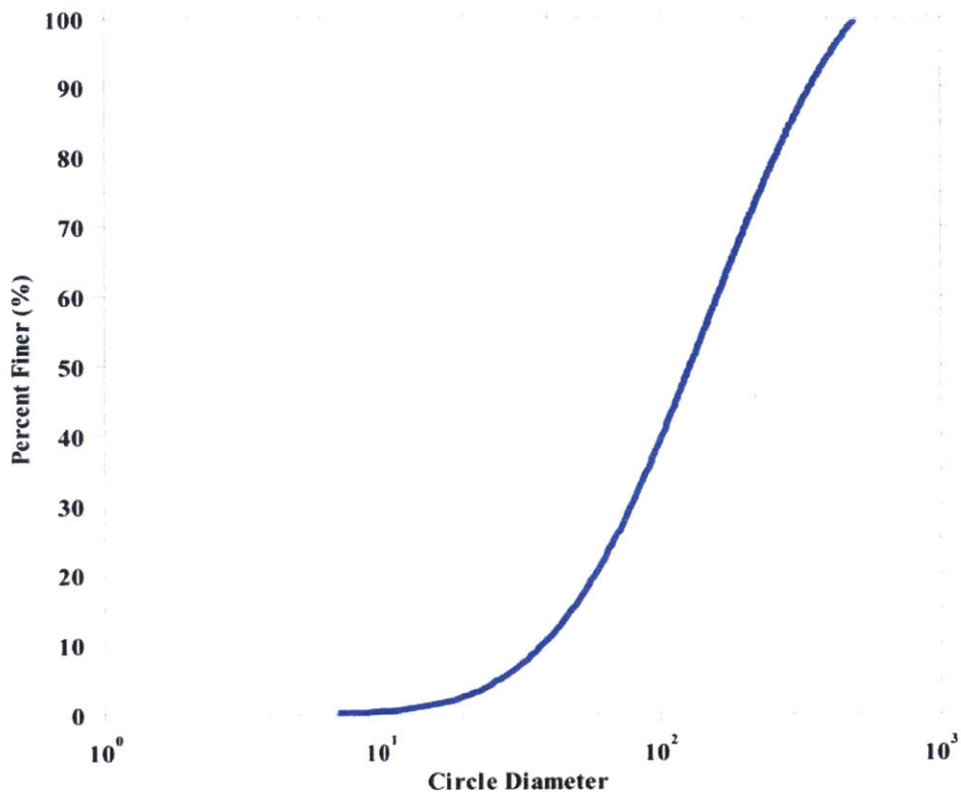
Figure 5-7: Size distribution of circles generated for the synthetic microstructure used in this section to validate the IOM method. We used a lognormal size distribution with a volume fraction of 0.1022, a mean of 3, and a standard deviation of 1. Approximately 1.8 million circles were generated with these parameters with a size range of 6 to 506.
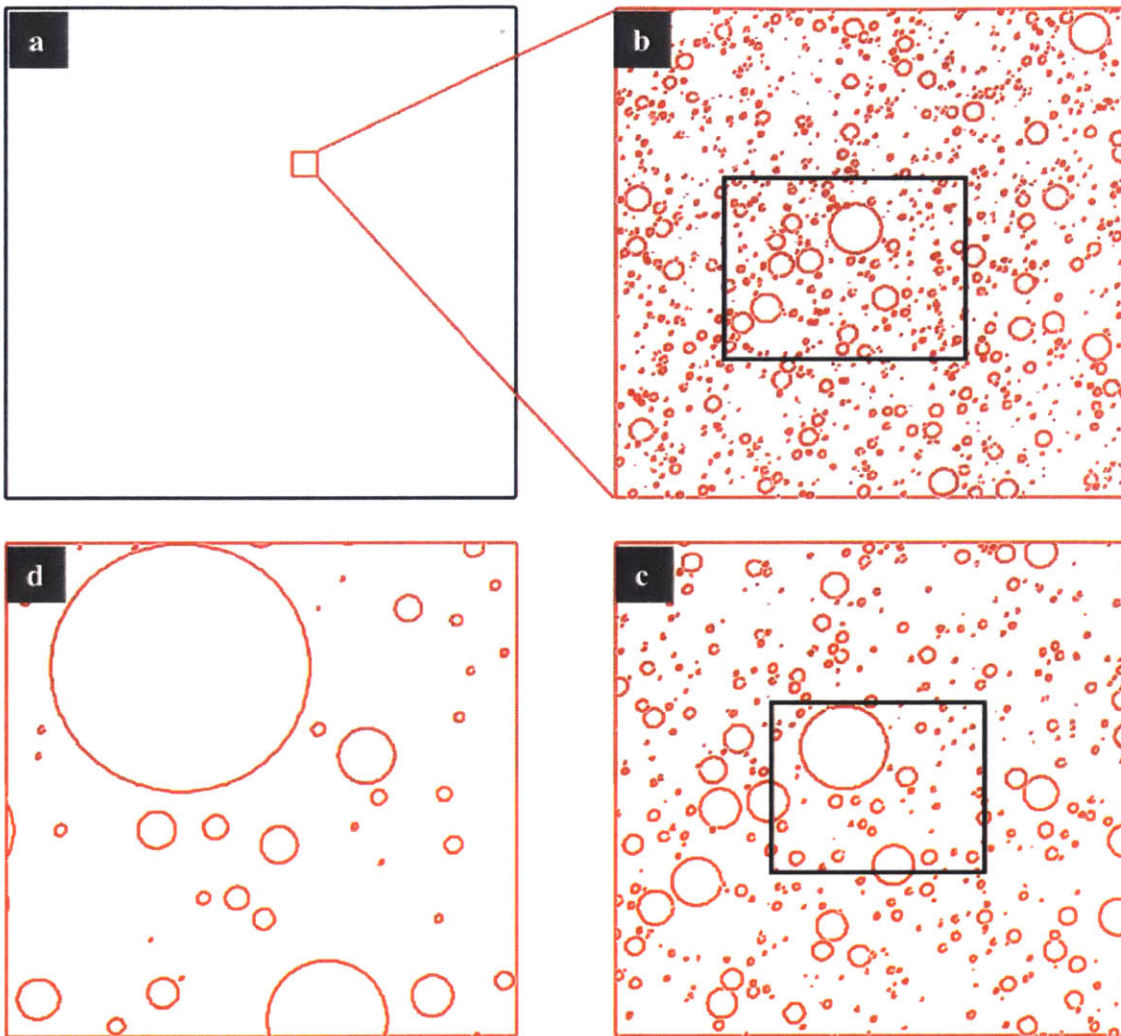
Figure 5-8: An example synthetic microstructure with a volume fraction of 0.1022 and the lognormal distribution shown in Figure 5-7. The circles were placed randomly, provided that there was no overlap with other circles. The boxes in this figure have different sizes of a) 200,000, which is the entire synthetic microstructure; b) 5000; c) 3000; and d) 1000.
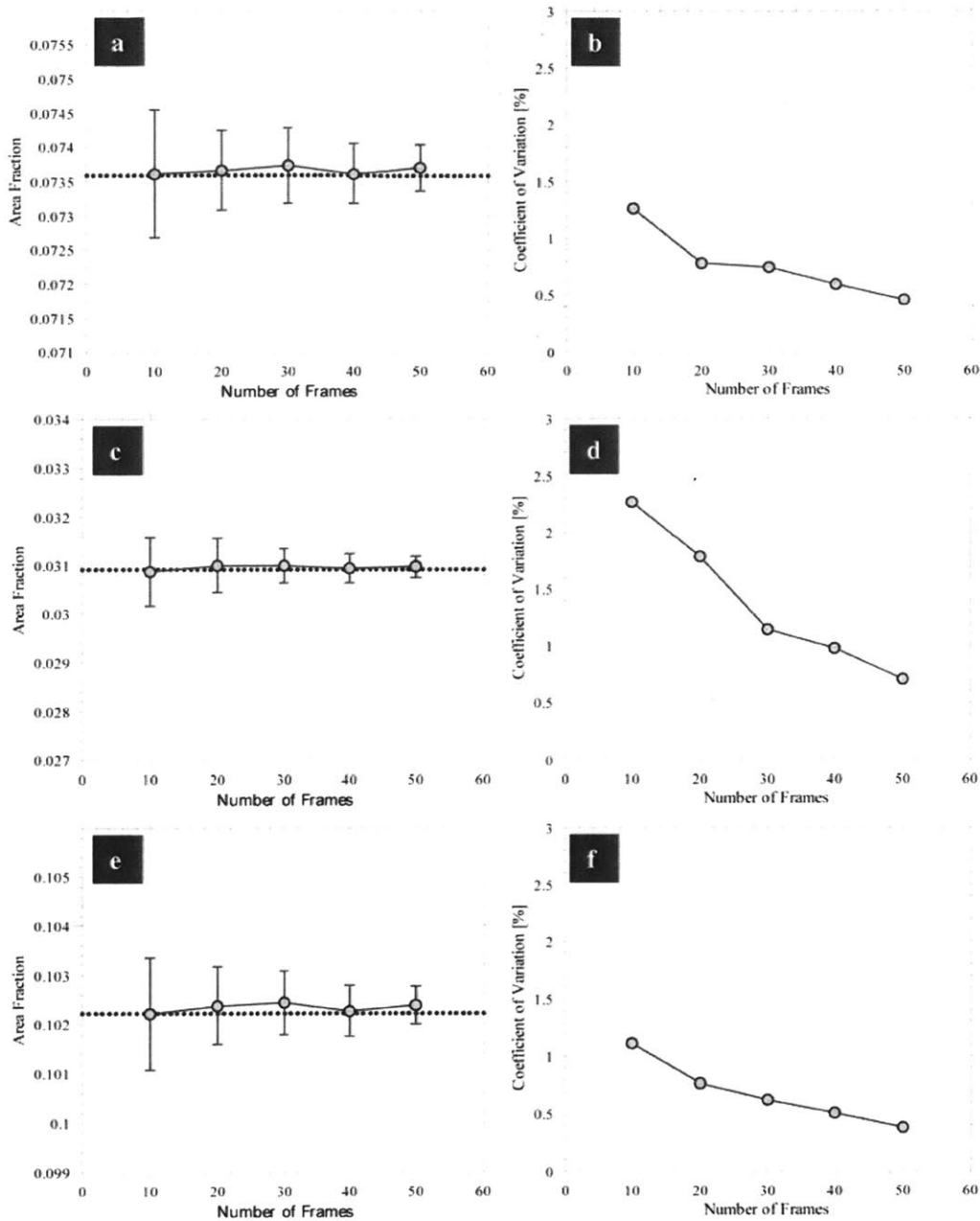
Figure 5-9: Mean and coefficient of variation of area fraction as a function of the number of frames for a, b) Mag 1-area fraction; c, d) Mag 2-area fraction; and e, f) final area fraction. These results were obtained by varying the number of frames while keeping the frame size and the size interval fixed. The ratio of the frame side, a, to the maximum circle diameter at each level, D_{max}, was set to 40. The size interval at level 1 ranged from 6, d_{min}, to 200, d_{min2}. The size interval at level 2 ranged from 200, d_{min2}, to 506, d_{max}.
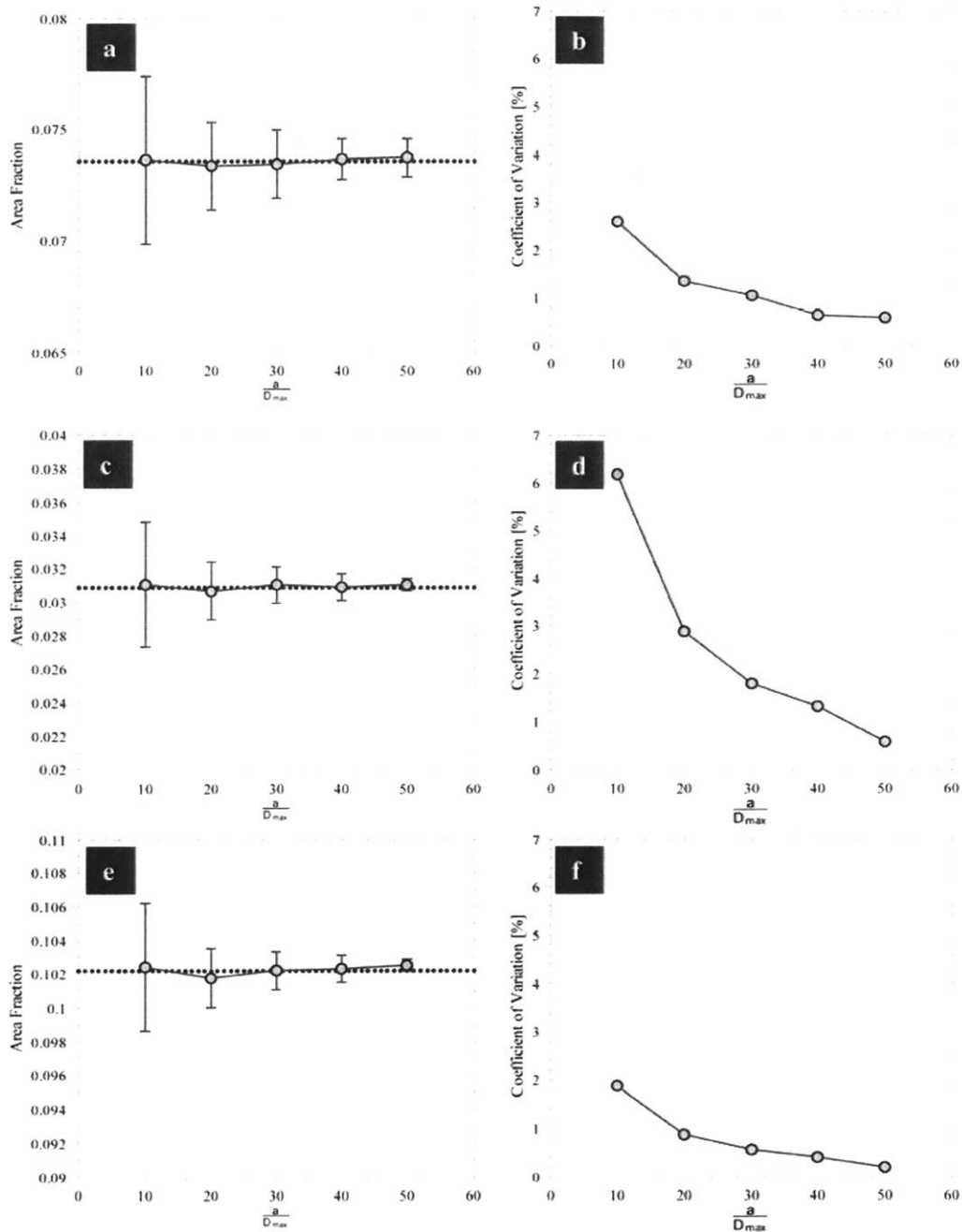
Figure 5-10: Mean and coefficient of variation of area fraction as a function of the ratio of the frame side, a, to the maximum circle diameter, D_{max}, for a, b) Mag 1-area fraction; c, d) Mag 2-area fraction; and e, f) final area fraction. These results were obtained by varying the a/D_{max} ratio from 10 to 50, while keeping the number of frames and the size interval fixed. The number of frames was set to 30. The size interval at Mag 1 ranged from 6, d_{min}, to 200, d_{min2}. The size interval at Mag 2 ranged from 200, d_{min2}, to 506, d_{max}.
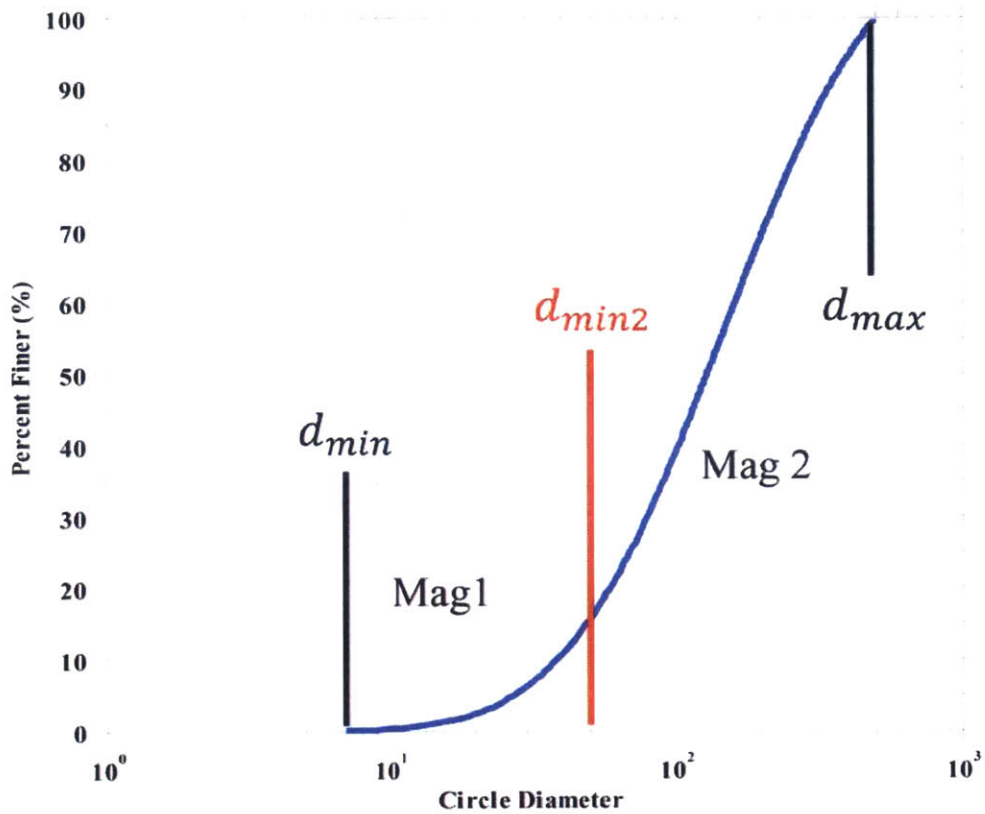
Figure 5-11: The size distribution of the synthetic microstructure used to run the simulations in this section. This figure illustrates how the size interval at each magnification is set. While d_{min} and d_{max} are constant, d_{min2} can be varied to control the size interval included in each magnification.
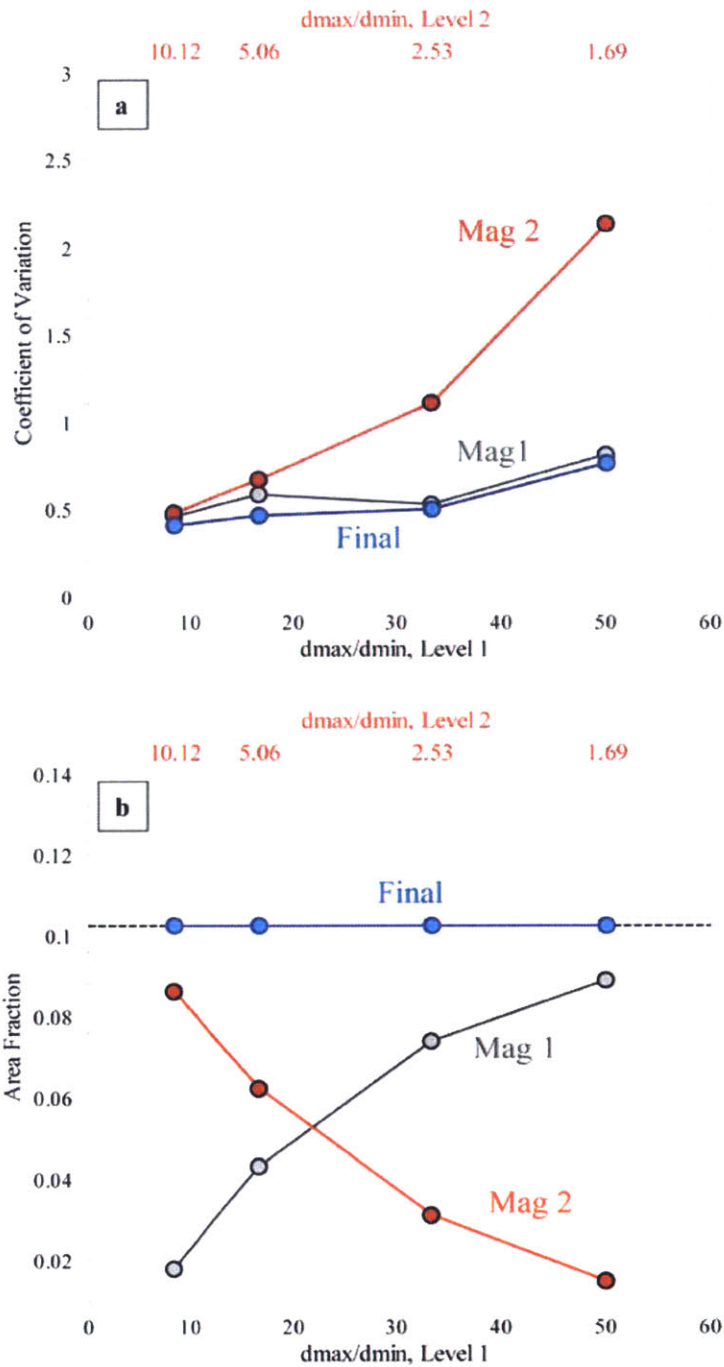
Figure 5-12: a) Coefficient of variation as a function of the ratio of the maximum circle diameter to the minimum circle diameter at Mag 1-, Mag 2-, and the final area fractions. b) Mean area fraction as a function of the ratio of the maximum circle diameter to the minimum circle diameter at Mag 1-, Mag 2-, and the final area fractions. These results were obtained by varying the size interval by setting the d_{min2} bar to 50, 100, 200, and 300 (Figure 5-11). The a/D_{max} ratio was set to 40, and the number of frames to 20.

115
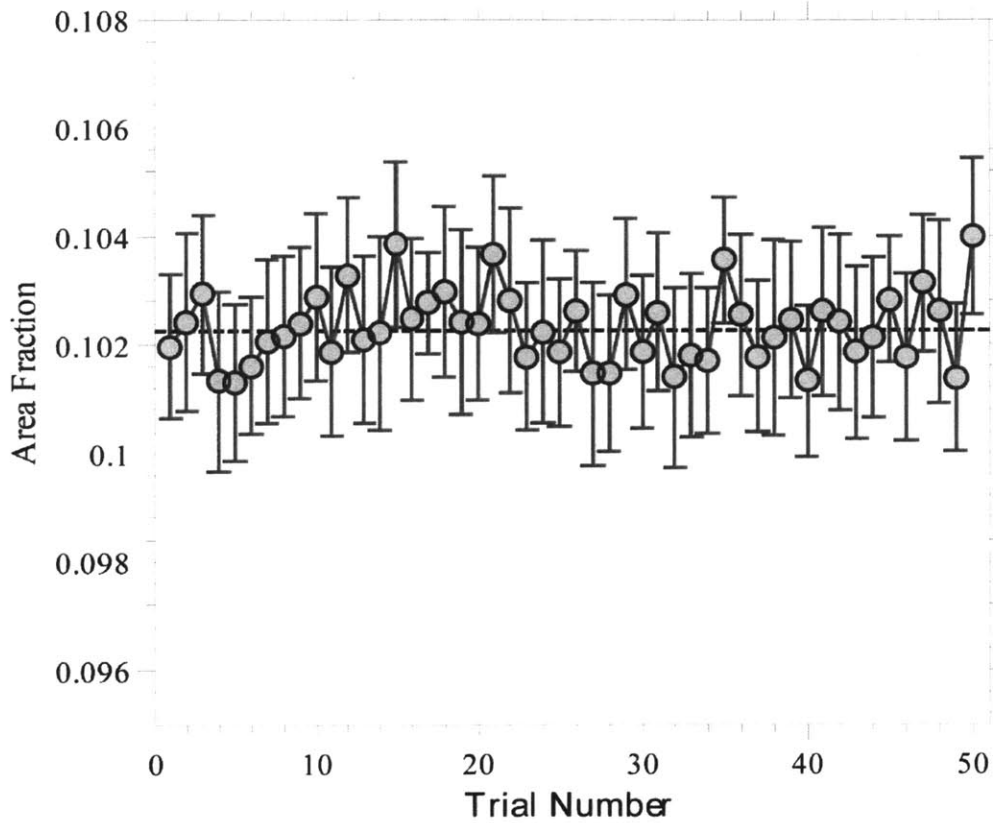
Figure 5-13: Mean final area fraction as a function of trial number. For each trial, the a/D_{max} ratio was set to 40, and the number of frames to 20. The size interval at level 1 ranged from 6, d_{min}, to 120, d_{min2}. The size interval at level 2 ranged from 120, d_{min2}, to 506, d_{max}. Each trial consisted of combining 20 frames at levels 1 and 2 to obtain the final area fraction using the method outlined above.
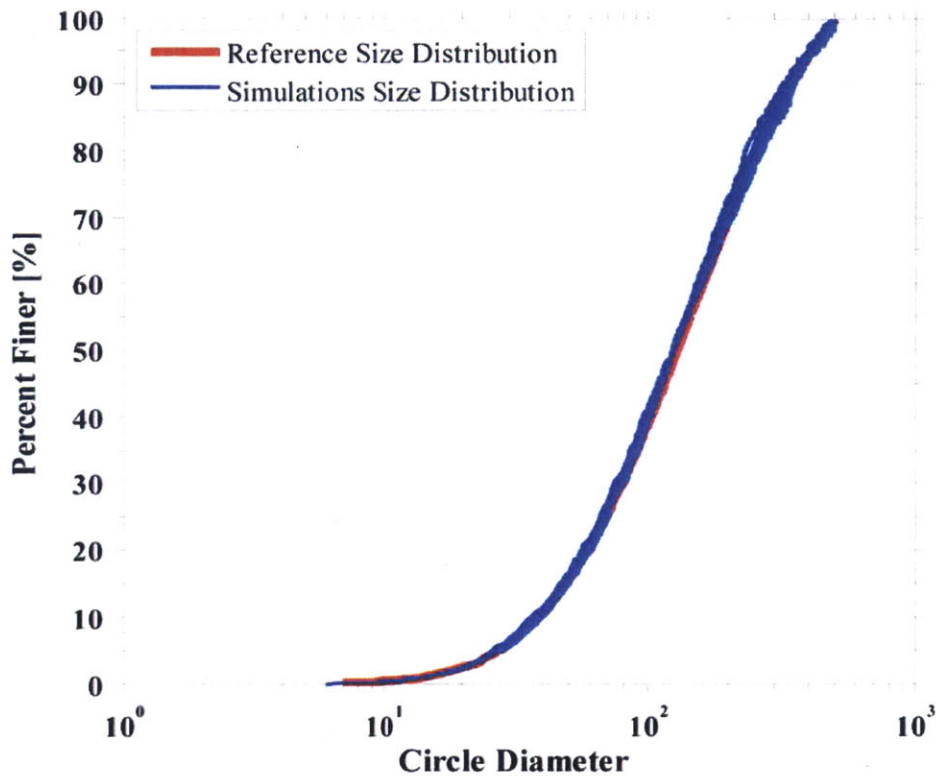
Figure 5-14: Size distribution curves obtained using simulations (blue curves) along with the reference size distribution curve used to build the synthetic microstructure in this example (red curve). For the simulations, the a/D_{max} ratio was set to 40, and the number of frames to 20. The size interval at Mag 1 ranged from 6, d_{min} , to 120, d_{min2} . The size interval at Mag 2 ranged from 120, d_{min2}, to 506, d_{max}. The simulations were repeated for 10 trials to obtain 10 different size distribution curves. Each trial consisted of combining diameters obtained from 20 frames at levels 1 and 2 to obtain the final size distribution curve using the IOM method.
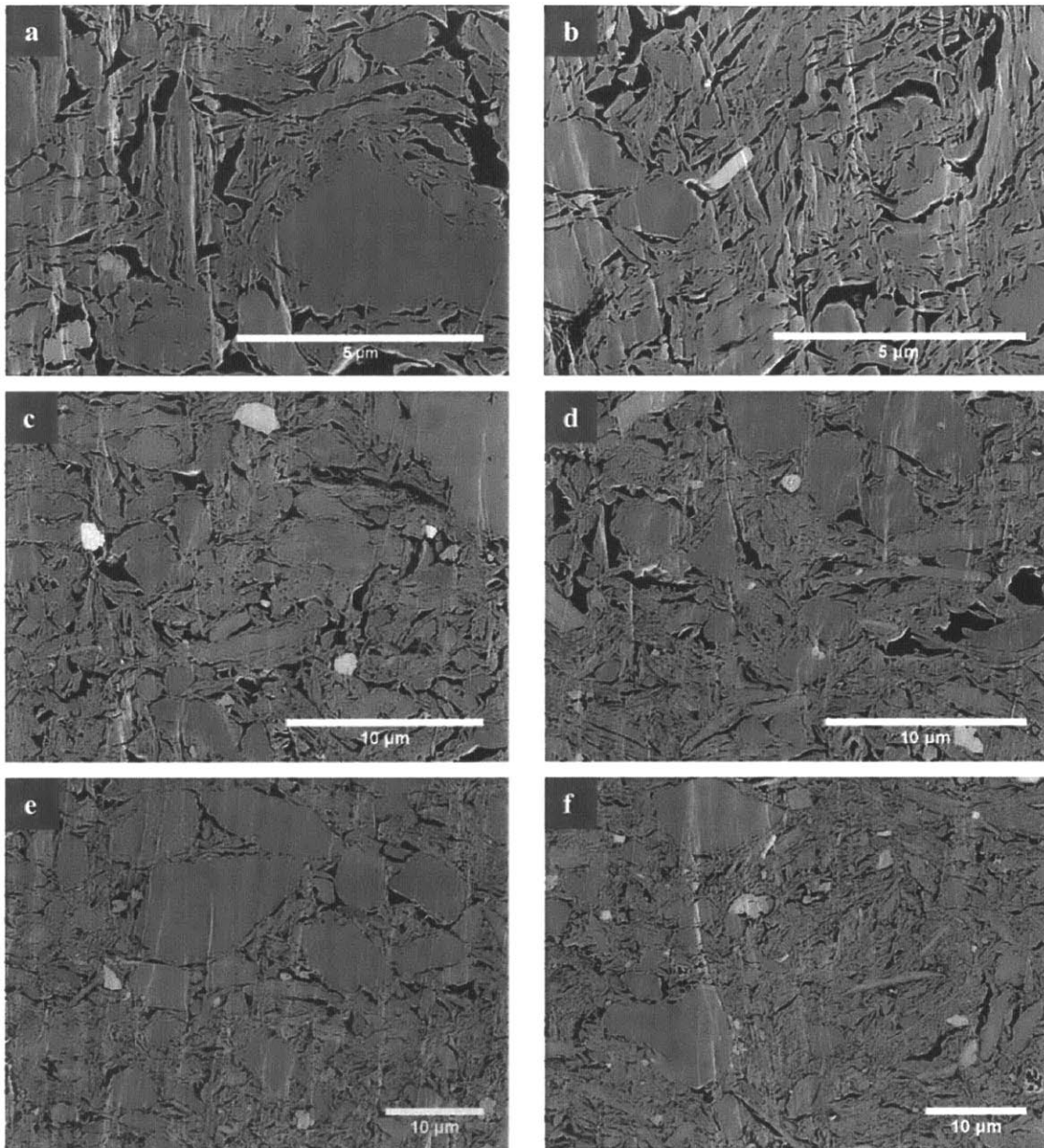
Figure 5-15: Images of a Gulf of Mexico sample resedimented at 0.2 MPa. The images were acquired at different magnifications, as shown by the scale bars.

Mag 1: 30 KX	Mag 2: 12 KX	Mag 3: 6 KX
Field of view: 10 μm	Field of view: 25 μm	Field of view: 50 μm
Interval [nm]: 35–151	Interval [nm]: 151–675	Interval [nm]: > 675
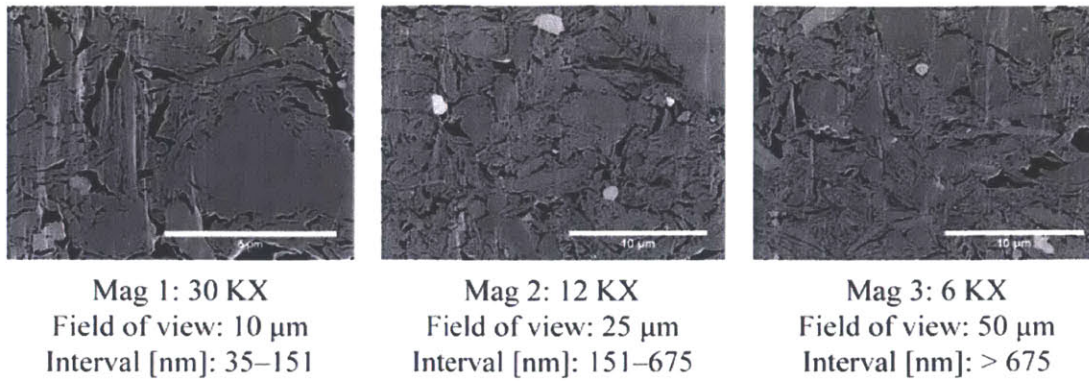
Figure 5-16: A summary of the three magnifications used in this investigation to represent the pore space of mudrocks, along with the corresponding field of view and size interval.
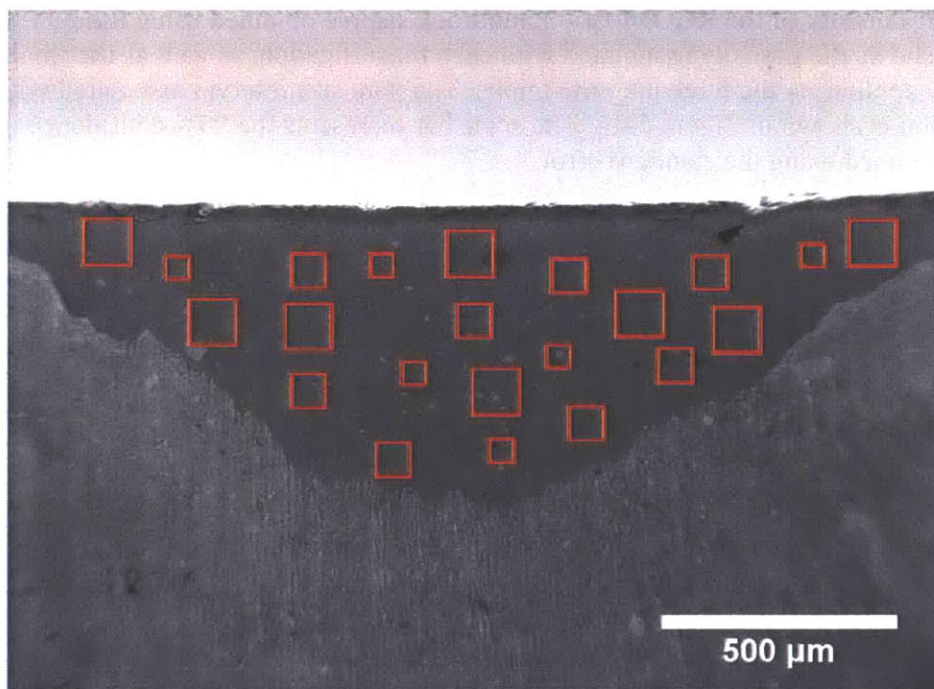
Figure 5-17: An SEM image of an ion-milled surface of the RGOM-EI-0.2 mudrock sample. This image illustrates the process of imaging the microstructure of mudrocks in the IOM method. The imaging is performed randomly and covers the entire milled area. Red squares with different sizes represent images acquired at different magnifications (not to scale).

119
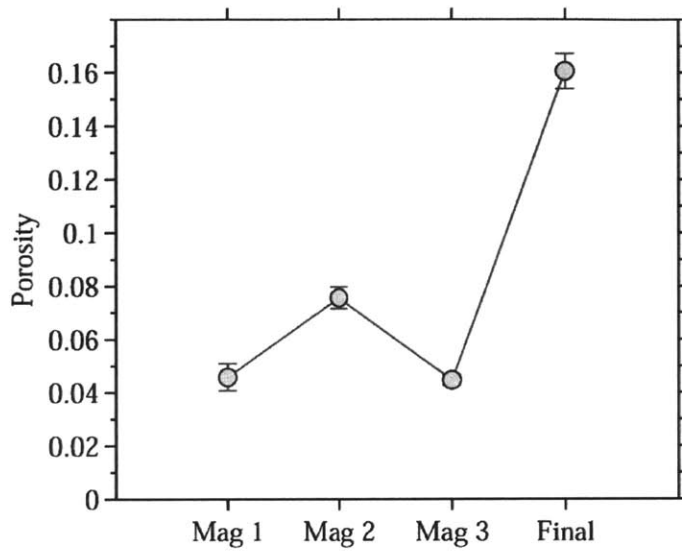
Figure 5-18: Porosity of the RGOM-EI-0.2 mudrock sample obtained using the IOM method. The figure shows the porosity associated with each magnification, as well as the final porosity obtained by combining the three magnifications. The pore size interval associated with each magnification is shown in Figure 5-16. The scale bar represents the 95% confidence interval of the mean obtained using the standard error.
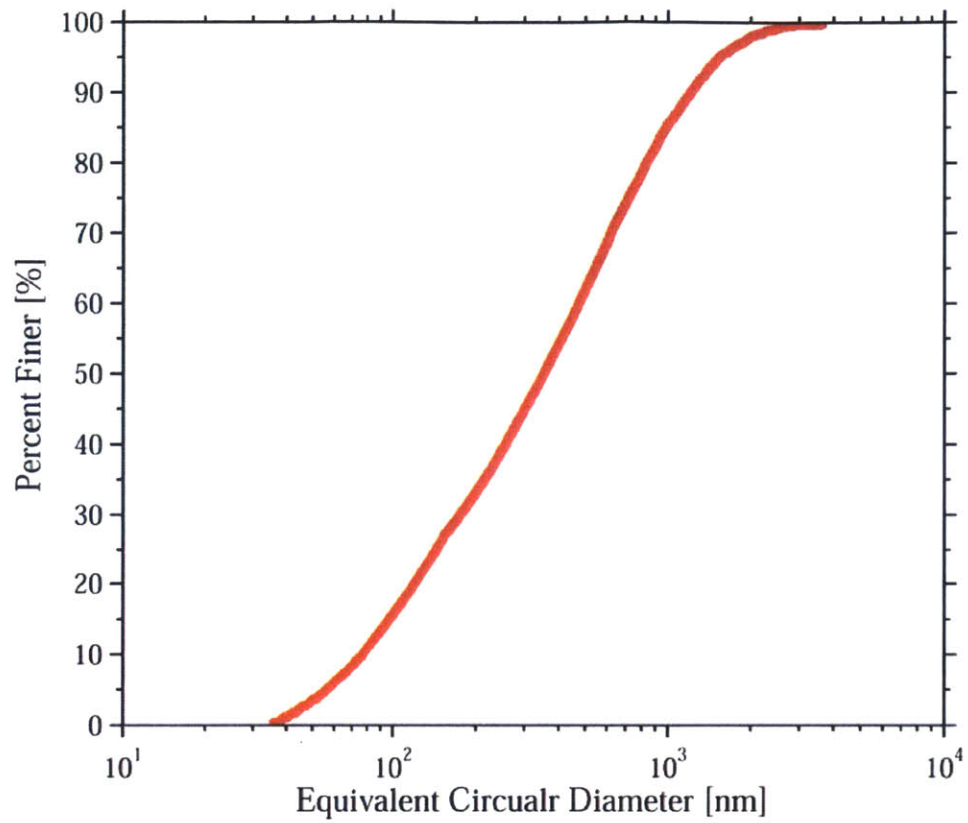
Figure 5-19: The pore size distribution of the RGOM-EI-0.2 mudrock sample obtained using the IOM method. This curve is obtained by combining the pores from the three different magnifications.

6 MICROSTRUCTURE OF CLAY SLURRIES

6.1 Introduction

This chapter presents the results of plunge freezing and high pressure freezing experiments of GOM-EI and BBC clay slurry samples. Section 6.2 summarizes the experimental program performed to investigate the microstructure of clay slurries, as well as the influence of plunge freezing on the microstructure of clay slurries (Table 6-1). Section 6.3.1 presents the results of plunge freezing experiments performed in this investigation on GOM-EI and BBC clay slurries. On the other hand, Section 6.3.2 presents the results of high pressure freezing of GOM-EI and BBC slurries. Section 6.4 discusses the results obtained using plunge freezing and high pressure freezing, and provides interpretation for the observed trends.

6.2 Experimental Program

The experimental program in this chapter was conducted on Gulf of Mexico–Eugene Island (GOM-EI) and Boston Blue Clay (BBC) soils. GOM-EI is predominantly a smectitic soil whereas BBC is predominantly an illitic soil. The properties of the two soils were discussed in detail in Chapter 3. The two soils were leached to remove the natural salt from the soil, and mixed at three NaCl salt concentrations: 1 g/l, 16 g/l, and 64 g/l. Slurry samples were prepared by mixing a small amount of soil (50% by weight) with NaCl saltwater. The porosity of these samples, calculated using phase relations, is around 0.75. The slurry was then shaken using a mechanical agitator for 10 minutes, and left overnight to fully hydrate. Plunge freezing and high-pressure freezing experiments were conducted following the protocols described in Chapter 4.

The experiments in this chapter were designed to investigate the microstructure of GOM-EI and BBC clay slurries, as well as the effect of the plunge freezing method on their microstructure. Our experimental program consisted of the following experiments (Table 6-1):

1. Plunge freezing experiments of GOM-EI and BBC soils at three different pore salinities: 1 g/l, 16 g/l, and 64 g/l. The microstructure of these samples was investigated using a cryo-SEM as described in Chapter 4.

2. High-pressure freezing experiments of GOM-EI and BBC soils at three different pore salinities: 1 g/l, 16 g/l, and 64 g/l. The microstructure of these samples was then investigated using a cryo-SEM as described in Chapter 4.

3. Three GOM-EI slurry samples were plunge-frozen in three different cryogens with different cooling efficiencies: ethane (90 K), nitrogen slush (63 K), and liquid nitrogen (77 K).

4. Plunge freezing experiment of a saltwater sample at a salt concentration of 64 g/l. The frozen sample was imaged using a cryo-SEM, and investigated using Energy Dispersive Spectroscopy (EDS) to reveal the distribution of salt in the sample.

5. A controlled sublimation experiment was performed on a plunge-frozen 16 g/l saltwater sample. The sample was sublimated and imaged at three different stages. In the first stage the temperature was raised to -90°C, which is the temperature used to sublimate plunge-frozen GOM-EI and BBC clay slurries in this investigation. In the second stage, the temperature was raised to -50 °C, and in the final stage the sample was left at -50 °C for 30 minutes.

6.3 Results

6.3.1 The Microstructure of Plunge-Frozen Samples

The microstructure of plunge-frozen GOM-EI clay slurries reveals a striking honeycomb structure (Figure 6-1). In these images, black represents the pore space from where the ice was sublimated, whereas grey represents clay particles. The sublimation of surface ice left behind a honeycomb structure that does not collapse after the removal of water (Figure 6-1a1, b1, c1). This structure consists of clay aggregates joined with face-edge and edge-edge contacts (Figure 6-1a3, a5, b3, c3). The term aggregates refer to the stacking of clay minerals with face-face contacts (see Chapter 2). At a pore salinity of 1 g/l, the honeycomb structure is characterized by less-defined circular cells, in which clay particles are connected with face-edge contacts, and to a less extent face-face contacts (Figure 6-1a2). At high pore salinities, on the other hand, the honeycomb structure transforms into a well-defined structure with rectangular cells in which clay aggregates are connected with face-face contacts and face-edge contacts (Figure 6-1b2, c2). Furthermore, the thickness of the clay aggregates is a strong function of pore salinity. At a pore salinity of 1 g/l (Figure 6-1a3), the aggregates are composed of a few particles. The number of

particles in an aggregate increases noticeably at high pore salinities (Figure 6-1b5, c4). A few micrographs at a magnification of 2.35 KX (e.g., Figure 6-1a1) were analyzed to measure the average cell size of the honeycomb structure, as well as the porosity of the samples (Table 6-2). The calculated average cell size ranged from 1.87 μm to 1.94 μm with no apparent trend with pore salinity. The porosity of these samples ranged from 0.49 to 0.53. The calculated porosity is significantly less than the porosity of the GOM-EI samples calculated using phase relations (~0.75).

The microstructure of plunge-frozen BBC clay slurries also reveals a honeycomb structure similar to that observed in GOM-EI slurries (Figure 6-2). The sublimation of surface ice left behind a honeycomb structure that does not collapse after the removal of water (Figure 6-2f). This structure consists of clay aggregates joined with face-edge and edge-edge contacts (Figure 6-2). Similar to GOM-EI, the honeycomb structure becomes more ordered as salinity increase. At a pore salinity of 1 g/l, the microstructure of BBC clay slurries is characterized by a less-defined honeycomb structure, in which clay aggregates form face-edge contacts (Figure 6-2b). At high salinities, on the other hand, the honeycomb structure transforms into a well-defined structure with circular cells, in which clay aggregates are connected with face-face contacts and face-edge contacts (Figure 6-2c, f). Unlike GOM-EI samples, no apparent increase in the thickness of clay aggregates can be observed as salinity increases. The number of particles in an aggregate does not change as pore salinity increases (Figure 6-2b, d, f). A few micrographs at a magnification of 2.35 KX (e.g., Figure 6-2a) were analyzed to measure the average cell size of the honeycomb structure, as well as the porosity the samples (Table 6-3). The calculated average cell size was found to be 1.2 μm at pore salinities of 1 g/l and 16 g/l, and 1.4 μm at a pore salinity of 64 g/l. The porosity of these samples ranged from 0.39 to 0.44. The calculated porosity is significantly less than the porosity of the BBC samples calculated using phase relations (~0.75).

Several authors used plunge freezing to investigate the structure of clay slurries and showed the formation of a honeycomb structure at various conditions (see Chapter 2). Plunge freezing was followed by either freeze drying to remove water for conventional SEM imaging (O'Brien, 1971; Osipov and Sokolov, 1978; Stawinsk et al., 1990), or directly imaged using the cryo-SEM technique (Zbik et al., 2008, 2010; Du et al., 2009, 2010; Morris and Żbik, 2009). In

the following discussion, we show that the honeycomb structure is an artifact of plunge freezing, and does not represent the microstructure of clay slurries.

To better understand the honeycomb structure we observe in the plunge-freezing experiments of GOM-EI and BBC slurries (Figure 6-1 and Figure 6-2), we plunge-froze a NaCl-saltwater sample (64 g/l). Once again, a honeycomb structure developed. However, it is more ordered and has sharper boundaries (Figure 6-3a) than that of GOM-EI and BBC slurries. We interpret that ice crystallization leads to the formation of a segregated structure in which salt ions are excluded from the crystal lattice and trapped between the growing ice crystals. Thus, in Figure 6-3a, the black areas represent areas of pure ice, whereas the walls of the honeycomb represent a mixture of ice and salt ions. Energy Dispersive Spectroscopy (EDS) shows that the walls of the honeycomb cells contain NaCl as seen by the presence of Na and Cl peaks, while the center of these cells contains only pure ice as seen by the absence of Na and Cl peaks (Figure 6-3b).

The effect of the cooling rate on the microstructure is further examined by comparing the results of plunge-frozen GOM-EI slurries (64 g/l) in three different cryogens: ethane, nitrogen slush, and liquid nitrogen (Figure 6-4). Ethane is the most efficient cryogen with average cooling rates reported in the literature of approximately 10-13 10^3Ks^{-1}. The average cooling rate for nitrogen slush and liquid nitrogen is 1-2 10^3Ks^{-1} and 0.5 10^3Ks^{-1}, respectively (Echlin, 1992, p. 71).The three experiments produce a similar honeycomb structure, but with a significant difference in cell size. The sample frozen in ethane (90 K) shows the smallest cell size (Figure 6-4a), whereas the sample frozen in liquid nitrogen (77 K) shows the largest cell size (Figure 6-4c). The average calculated cell diameter is 0.7 μm, 2.2 μm, and 4.6 μm for the samples frozen in ethane, nitrogen slush, and liquid nitrogen, respectively (Table 6-2). The honeycomb cell size is thus a strong function of the cooling rate generated in plunge freezing. The ice crystals produced in ethane plunge-freezing are the smallest followed by nitrogen slush and liquid nitrogen.

The influence of sublimation on the microstructure was investigated on a plunge-frozen NaCl saltwater sample (Figure 6-5). The saltwater sample (16 g/l) was plunge-frozen in nitrogen slush. The sample was then imaged at three different temperatures: -90 °C, -50 °C, and -50 °C after 30 minutes. At -90 °C, a honeycomb structure forms that consists of pure ice in the middle

of the cells and a mixture of ice and salt ions at the boundaries (Figure 6-5a). At -50 °C, the mixture of ice and salt ions (cell boundaries) start to sublimate as shown by the appearance of holes, and the formation of perforated walls (Figure 6-5b). These walls completely collapse after holding the temperature for 30 minutes at -50 °C (Figure 6-5c). These results show that the segregated crystalline structure, formed in plunge freezing experiments, sublimates at different rates. Pure ice sublimates at a faster rate than the mixture of ice and salt ions, a process that gives the apparent honeycomb structure when frozen samples are sublimated for a short time.

6.3.2 High Pressure Freezing Results

Figure 6-6 shows the microstructure of high-pressure frozen GOM-EI samples at different pore salinities. In these images dark grey represents the matrix of frozen ice, and light grey represents clay particles. The microstructure of high-pressure frozen GOM-EI slurries consists of individual clay particles (Figure 6-6a4, b4, c4) and aggregates of clay particles (Figure 6-6a3, b5, c3) that are randomly distributed in a matrix of frozen ice. The clay aggregates consist of clay platelets joined together with face-face contacts (e.g., Figure 6-6c3). The orientation of platelets within an aggregate ranges from parallel to form face-face contacts only (Figure 6-6a2, c3), to slightly inclined to form a combination of face-edge and face-face contacts (Figure 6-6c2, c5). The thickness of individual clay particles and aggregates was manually measured in five high magnification images at each pore salinity. The thickness of clay aggregates increases as pore salinity increases. At 1 g/l, the thickness of clay aggregates ranges from 20 to 100 nm. At 16 g/l, the thickness of clay aggregates ranges from 50 nm to 250 nm. At 64 g/l, the aggregates range in size from 30 nm to 400 nm. The aggregates and individual particle orientations appear to be random (Figure 6-6a1, b1, and c1). However, neighboring aggregates and particles tend to orient themselves parallel to each other (Figure 6-6a5, b5, c2). Furthermore, there is a decrease in individual particle density, and the increase in aggregate density as pore salinity increases (Figure 6-6a2, b2, and c2). Particles and aggregates are distributed in a matrix of frozen water (dark grey), with significant pore space. To calculate the porosity of the samples, 18 images at a magnification of 10 KX (e.g., Figure 6-6a1) were thresholded using ImageJ (Table 6-2). The average calculated porosity at the three pore salinities is 0.81. This value is in general agreement with the porosity of the slurry samples calculated using phase relations (~0.75). It is worth mentioning that these numbers represent qualitative estimates of the slurry

samples' porosity, because broken surfaces are hard to quantify and threshold due to the irregular surfaces. Quantitative assessment of the porosity and surface details requires the use of flat ion milled surfaces.

Figure 6-7 shows the microstructure of high-pressure frozen BBC slurry samples at different pore salinities. Similar to GOM-EI samples, the microstructure of high-pressure frozen BBC slurries consists of individual clay particles (Figure 6-7a2, b2) and clay aggregates (Figure 6-7a3, b3) that are randomly distributed in a matrix of frozen ice. The clay aggregates consist of clay platelets joined together with face-face contacts (e.g., Figure 6-7b3). The thickness of individual clay particles and aggregates was manually measured in a few high magnification images at each pore salinity. The thickness of clay aggregates in BBC slurries showed less sensitivity to pore salinity compared to that of GOM-EI slurries. At pore salinities of 16 g/l and 64 g/l, the thickness of clay aggregates ranges from 100 nm to 300 nm. Similar to GOM-EI slurries, the aggregates and individual particle orientations appear to be random (Figure 6-7a1, b1). However, neighboring aggregates and particles tend to orient themselves parallel to each other (Figure 6-7a3, b3). The density of clay aggregates increases as pore salinity increases (Figure 6-7a1, b1). Particles and aggregates are distributed in a matrix of frozen water (dark grey), with significant pore space. To calculate the porosity of the samples, a few images at a magnification of 10 KX (e.g., Figure 6-7a1) were thresholded using ImageJ (Table 6-3). The average calculated porosity at the two pore salinities is 0.83. This value is in general agreement with the porosity of the slurry samples calculated using phase relations (~0.75). It is worth mentioning that these numbers represent qualitative estimates of the slurry samples' porosity, because broken surfaces are hard to quantify and threshold due to the irregular surfaces. Quantitative assessment of the porosity and surface details requires the use of flat ion milled surfaces.

6.4 DISCUSSION

6.4.1 Honeycomb structure

Plunge freezing experiments of clay slurries in the literature are performed based on the assumption that the cooling rate is high enough to prevent ice crystallization, and hence, preserves the clay microstructure (see Chapter 2). The honeycomb structure observed in plunge

freezing experiments of clay slurries is commonly quoted in the literature and used as the foundation for the understanding of the origin of sedimentary deposits, clay suspensions behavior, and the development of computational models. The presence of hexagonal ice crystals in plunge-frozen GOM-EI samples was demonstrated thorough cryogenic wide angle X-ray scattering (cryo-WAXS) experiments performed by Michael Whittaker for Northwestern University (Deirieh et al., 2015). In these experiments, cryo-WAXS spectra of plunge-frozen GOM-EI slurry samples showed the presence of hexagonal ice peaks, while the spectra of reference dry GOM-EI soil did not record the peaks associated with hexagonal ice peaks. These results prove that the cooling rate generated in a plunge freezing experiment is not high enough to prevent crystallization. The formation of ice crystals alone is not an indicator that plunge freezing destroys the microstructure, because it does not take into account the size of the ice crystals (Moor, 1987). For example, frozen biological samples with microcrystalline ice (~20 nm) were considered preserved in some cases (Moor, 1987). This criterion implies that if ice crystals are smaller than important surface details, freezing will be considered satisfactory. In the case of clay slurries, these surface details include the size of pores, as well as the spatial distribution of particles. The determination of ice crystals size from the cryo-WAXS results was not possible due to the complexity of the cryo-WAXS spectra generated from GOM-EI samples. Instead, the size of the honeycomb cells that form during plunge freezing can be used as an indicator of the size of ice crystals. The size of these cells (also called segregation compartment) provides a good measure of freezing quality in most cases (Sitte et al., 1987).

The results of plunge freezing in different cryogens provide a rough estimate of the size of ice crystals in GOM-EI slurries. Ethane is the most efficient cryogen with average cooling rates reported in the literature of approximately 10-13 $10^3 Ks^{-1}$. The average cooling rate for nitrogen slush and liquid nitrogen is 1-2 $10^3 Ks^{-1}$ and 0.5 $10^3 Ks^{-1}$, respectively (Echlin, 1992, p. 71). The cell size of the sample frozen in ethane is 0.7 µm, and 2.2 µm in nitrogen slush, and 4.7 µm in liquid nitrogen (Figure 6-4). The ice crystals produced in ethane plunge-freezing are the smallest followed by nitrogen slush and liquid nitrogen. This trend is in agreement with the fact that the size of ice crystals is inversely proportional to the cooling rate (Moor, 1987). Ice crystals with a size range of 0.7 to 4.7 µm, cause dramatic changes in the microstructure of clay slurries.

The plunge-frozen NaCl saltwater sample illustrates the influence of ice crystals on the microstructure (Figure 6-3). Ice crystallization leads to the formation of a segregated

microstructure, in which salt ions are trapped between the growing ice crystals. The segregated microstructure consists of pure ice crystals surrounded by a mixture of ice and salt ions (Figure 6-3). The sublimation rate for the mixture of salt and ice is slower than that of pure (Figure 6-5). Therefore, when the plunge-frozen sample is sublimated to reveal fresh surface details for imaging, the surface of ice recedes faster than the boundaries, a process that reveals a honeycomb structure when the sample is imaged.

6.4.2 Microstructure of clay slurries

The main advantage of high pressure freezing is its ability to vitrify water in aqueous samples preventing ice crystals from damaging the microstructure. The water content of samples is an important factor in achieving full vitrification. Using electron diffraction technique, Studer et al. (1995) showed that high-pressure frozen cartilage samples with a water content of 65 % and a solute concentration of 4-8 % were fully vitrified. They also concluded that the water content is more important than the solute concentration for achieving full vitrification. Erk et al. (1996) used X-ray cryo diffraction technique and showed that high pressure frozen lipid samples with a water content of 10-30 % were fully vitrified. Furthermore, Cryo-WAXS spectra showed that hexagonal ice does not form in high-pressure frozen GOM-EI samples (Deirieh et al., 2015). These results provided a proof that high pressure freezing vitrifies clay slurry samples and preserves the microstructure.

High-pressure freezing results showed that the microstructure of clay slurries consists of clay particles and clay aggregates randomly distributed in pore fluid. GOM-EI is predominantly composed of illite-smectite (I/S) mixed layer clay minerals with 70-80 % expandability whereas BBC is predominantly an illitic soil (see Chapter 3). The thickness of fundamental particles of I/S clay is a function of expandability. Average fundamental particle thickness was found to be 2 nm for expandability values above 50 %. The thickness of illite and kaolinite particles varies depending on the origin and mode of occurrence. Reported thickness of illite particles ranged from 4 nm to 9 nm, and from 16.7 nm to 150 nm for kaolinite. See Wilson (2013, p. 497) for a detailed discussion. A quantitative estimation of individual clay particles thickness from cryo-SEM images is not possible because this kind of analysis requires ion-milled surfaces. Nonetheless, we are able to differentiate between individual clay particles and clay aggregates using high magnification images (e.g., Figure 6-6a3). If the separation between clay platelets is

less than the resolution of SEM, the differentiation between clay aggregates and individual clay particles becomes impossible. In this investigation, we use the term aggregate to refer to a group of clay particles making face-face contacts that are visible in SEM images. The term clay particle on the other hand, refers to individual particles where it is not possible to observe the stacking from SEM images. No attempt was made in this investigation to further identify the stacking of clay aggregates.

The size of clay aggregates of GOM-EI slurries is a strong function of pore salinity. At 1 g/l and 16 g/l, clay aggregates consist of a few particles with a size that ranges from 20 nm to 250 nm. At small particle separation, aggregates and particles orient parallel to each other. This suggests that the double layer repulsion rotates particles and aggregates to adopt a parallel orientation. At 64 g/l, two types of particle associations can be observed. In the first type, clay particles are joined with face-face contacts to form aggregates with a size range from 250-400 nm (Figure 6-6c3). These aggregates are similar to the aggregates that formed at low pore salinities, but with a larger thickness. In the second type, aggregates and particles are joined together with face-edge contacts to form a floc ((Figure 6-6c2, c5). The term floc is used in the literature to describe the formation of face-edge and edge-edge contacts (Van Olphen, 1977, p. 96). In these flocs, clay particles are slightly bent at both edges to form face-edge contacts with the clay aggregates.

The increase in aggregate size with pore salinity can be explained in terms of the forces that govern clay particles interactions. Two types of forces are involved in these interactions: the double layer repulsive forces and van der Waals attractive forces. The summation of these forces results in the net interaction curve that govern particles interactions (Figure 6-8). This curve consists of a minimum peak at small separation that represents attraction, and a maximum peak at larger separation that represents double layer repulsion. The double layer repulsion serves as a barrier that prevents particles from agglomeration when they reach a position at which the attraction minimum occurs. As salt concentration increases, the energy barrier decreases until it completely disappears at high salt concentrations, at which point the rate of agglomeration is the highest (Van Olphen, 1977). The increase in the thickness of clay aggregates in GOM-EI slurries is thus caused by the decrease in the double layer repulsion barrier as salt concentration increases. This decrease in the energy barrier increases the rate of aggregation, as well as the number of particles that possess enough energy to pass the energy barrier to reach the minimum

attraction peak. Furthermore, the high solid content, which puts particles at close separation, contributes to the aggregation. The increase in aggregate size with pore salinity for GOM-EI slurries leads to the reduction in particle density as pore salinity increases. As a consequence, particle separation increases with pore salinity. At 1 g/l and 16 g/l, particle separation ranges from 100 nm to a few hundreds of nanometers. At 64 g/l, this number ranges from hundreds of nanometers to microns. A quantitative estimation of the average particle separation requires flat ion milled surfaces. On the other hand, the size independence of BBC clay aggregates suggests that the changes in the double layer repulsion peak are minimal at salt concentrations above 16 g/L.

6.4.3 Gel Structure

Our plunge-freezing analysis demonstrates that the honeycomb structure observed in clay slurries at different pore salinities is an artifact of plunge-freezing. The cells are generated by the formation of ice crystals and the exclusion of saline rich and clay particles (Figure 6-9). The cell size of the honeycomb structure is controlled by cooling rate and pore salinity. The size of these cells is much larger than microstructural features such as particle size and average particle separation, which leads to dramatic changes in the microstructure. In contrast, in high pressure frozen samples, we did not observe a honeycomb structure, and only the size of clay aggregates is a function of pore salinity. High pressure freezing preserves the clay slurries and prevents ice crystallization that may destroy the microstructure. Clay slurries have a microstructure characterized by a cardhouse structure dominated by face-edge contacts between building blocks of individual clay particles and clay aggregates. The building block of the cardhouse structure transforms from individual clay particles to thick clay aggregates as pore salinity increases. The absence of face-edge contacts is attributed to the randomness of the microstructure and the high porosity of the samples. Furthermore, the contacts between the building blocks are localized point contacts that would occur very infrequently in a given 2-D section. Nonetheless, a few face-edge contacts can be found in images of clay slurries at different pore salinities. Even though we do not yet have proof that there are no ice crystals in the high pressure frozen samples, these experiments are compelling evidence for ice segregation in the plunge-frozen samples.

Our results demonstrate that one of the widely accepted models for clay suspensions, the honeycomb structure, is fundamentally an artifact of plunge freezing and does not reflect the in-situ behavior. In the field of geological sciences, this contrasts a fundamental view of fabric evolution that has inferred the presence of honeycomb structures that gradually evolve to an oriented fabric (Bennett et al., 1991; O'Brien and Pietraszek-Mattner, 1998; Slatt and O'Brien, 2011). These results greatly contribute to the understanding of the mechanisms that dominates the development sedimentary rocks at early stages of deposition (Bennett et al., 1991). Furthermore, in the field of colloid science of commercial clay suspensions, our results support the model of a cardhouse structure (van Olphen, 1964; Khandal and Tadros, 1988) over the honeycomb model (Terzaghi, 1925; Casagrande, 1932; Weiss and Frank, 1961) and the electrostatic repulsion stabilization model (Norrish, 1954; Callaghan and Ottewill, 1974).

Table 6-1: Summary of the experimental program performed to investigate the microstructure of clay slurries

	Purpose of the Experiment	Sample	Freezing Method*	Cryogen**	Salinity [g/l]
1	Microstructure of plunge-frozen clay slurries	GOM-EI	PF	SN2	1, 16, 64
		BBC	PF	SN2	1, 16, 64
2	Microstructure of high-pressure frozen clay slurries	GOM-EI	HPF	-	1, 16, 64
		BBC	HPF	-	16, 64
3	Influence of Ice Segregation	Saltwater	PF	LN2	64
4	Influence of cooling rate	GOM-EI	PF	LN2	64
			PF	SN2	64
			PF	Ethane	64
5	Influence of sublimation	GOM-EI	PF	SN2	64

*PF refers to plunge freezing, while HPF refers to high pressure freezing

133

Table 6-2: Summary of the results of the GOM-EI clay slurries

Purpose of the Experiment	Cryogen	Salinity [g/l]	Porosity	Cell Size [μm]	Aggregate Size Range [nm]
Microstructure of plunge-frozen samples	Nitrogen slush	1	0.53	1.94 ± 0.65	20-100
	Nitrogen slush	16	0.49	1.86 ± 0.59	30-220
	Nitrogen slush	64	0.49	1.87 ± 0.48	100-460
Influence of the cooling rate	Liquid nitrogen	64		4.62 ± 0.66	-
	Nitrogen slush	64		1.78 ± 0.41	-
	Ethane	64		0.78 ± 0.18	-
Microstructure of high-pressure frozen samples	Nitrogen	1	0.83	-	30-130
	Nitrogen	16	0.8	-	50-250
	Nitrogen	64	0.81	-	30-450

Table 6-3: Summary of the results of the BBC clay slurries

Purpose of the Experiment	Cryogen	Salinity [g/l]	Porosity	Cell Size [μm]	Aggregate Size Range [nm]
Microstructure of plunge-frozen samples	Nitrogen slush	1	0.39	1.14 ± 0.33	
	Nitrogen slush	16	0.44	1.18 ± 0.42	100-400
	Nitrogen slush	64	0.41	1.42 ± 0.55	
Microstructure of high-pressure frozen samples	Nitrogen	16	0.82	-	100-200
	Nitrogen	64	0.85	-	
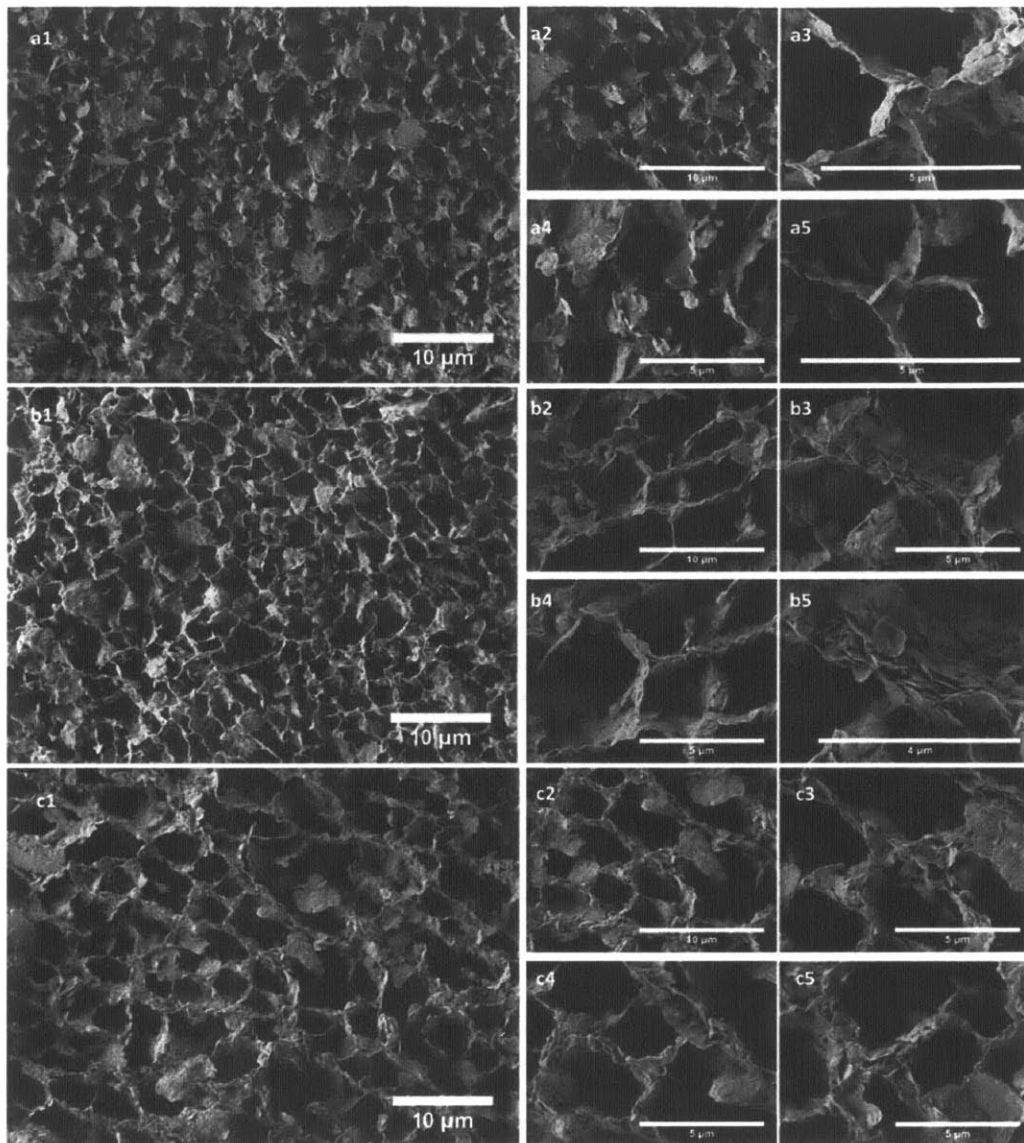
Figure 6-1: Cryo-SEM images of plunge-frozen GOM-EI slurry samples at different NaCl pore salinities: a1-a5) 1 g/l; b1-b5) 16 g/L; c1-c5) 64 g/L.
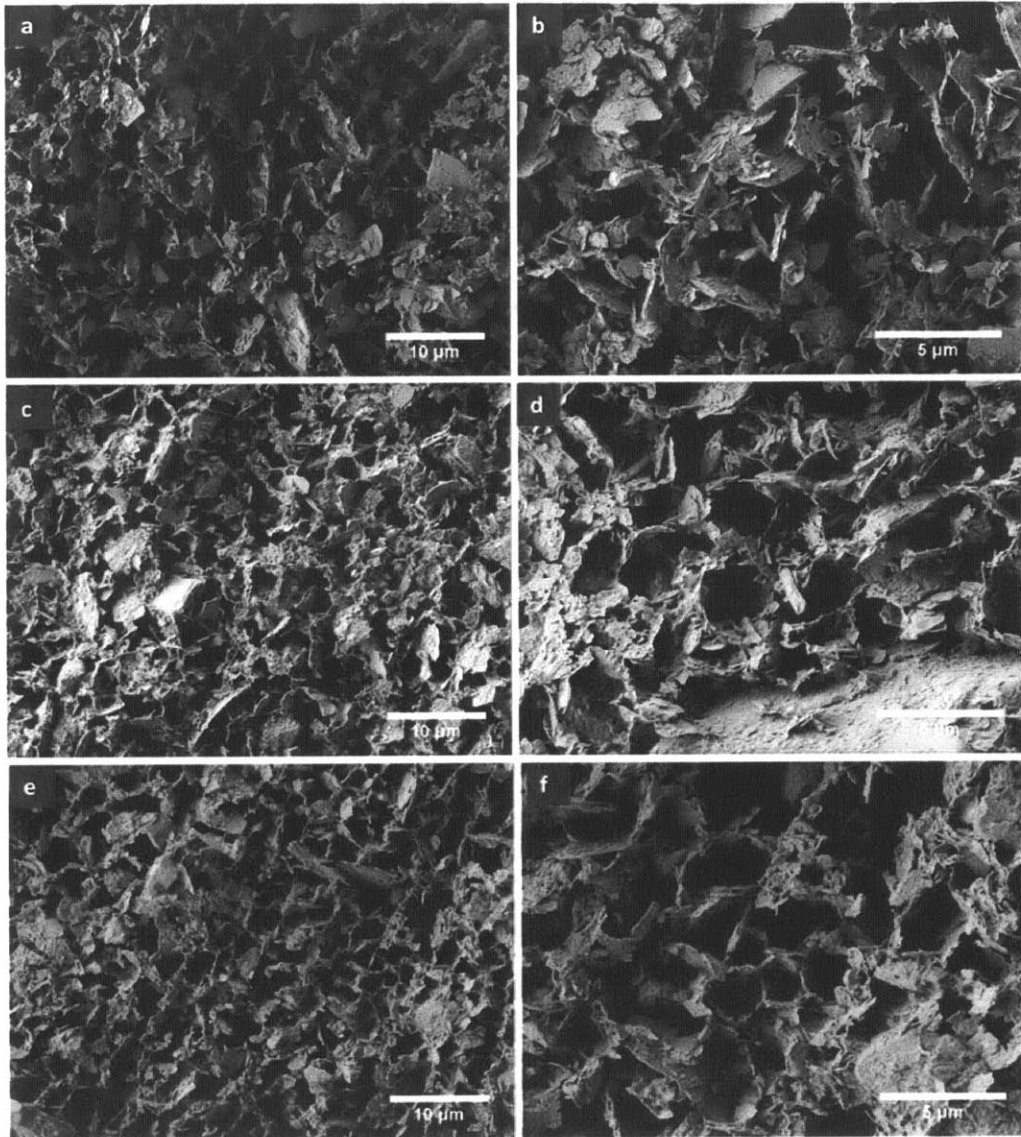
Figure 6-2: Cryo-SEM images of plunge-frozen BBC slurry samples at different NaCl pore salinities: a, b) 1 g/l; c, d) 16 g/L; e, f) 64 g/L.
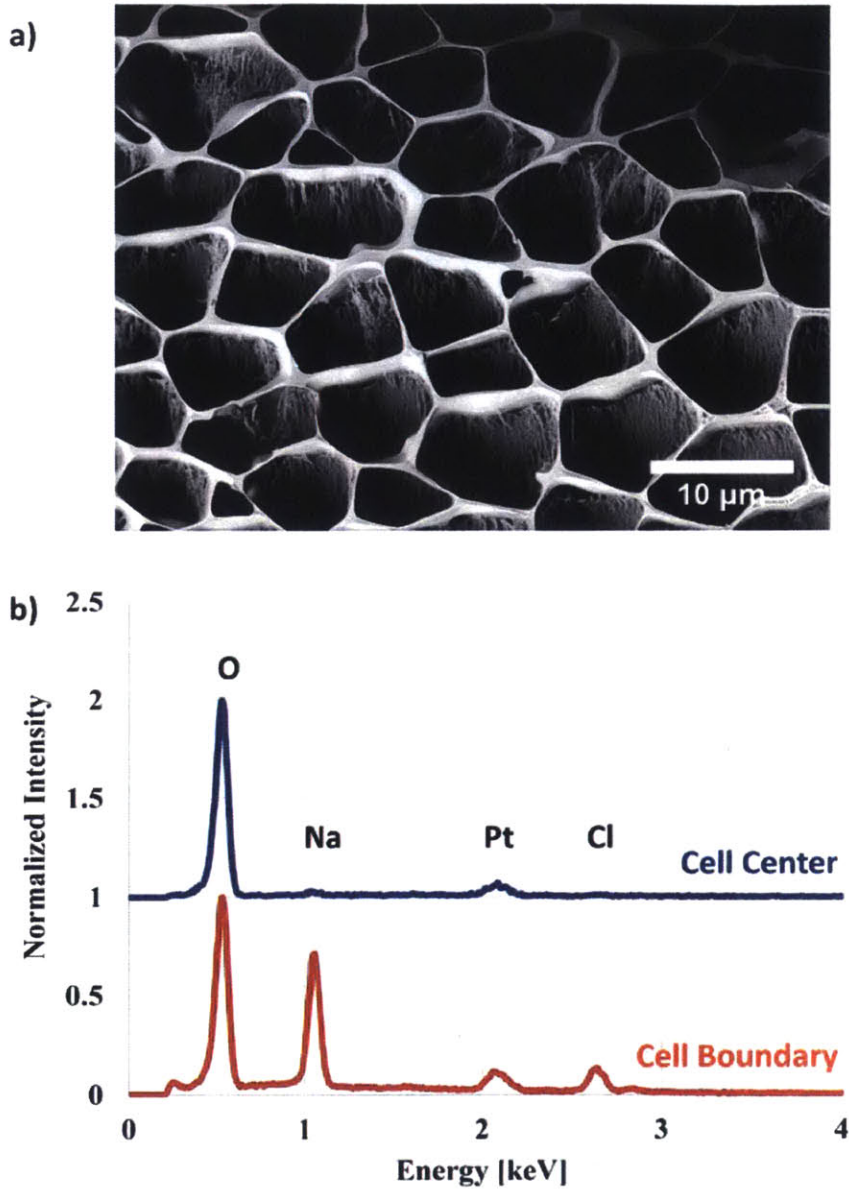
Figure 6-3: a) A cryo-SEM image of a plunge frozen salt-water sample at 64 g/l, and b) EDS spectra obtained for two spots: at the boundaries of the honeycomb cells, and at the center of the honeycomb cells.
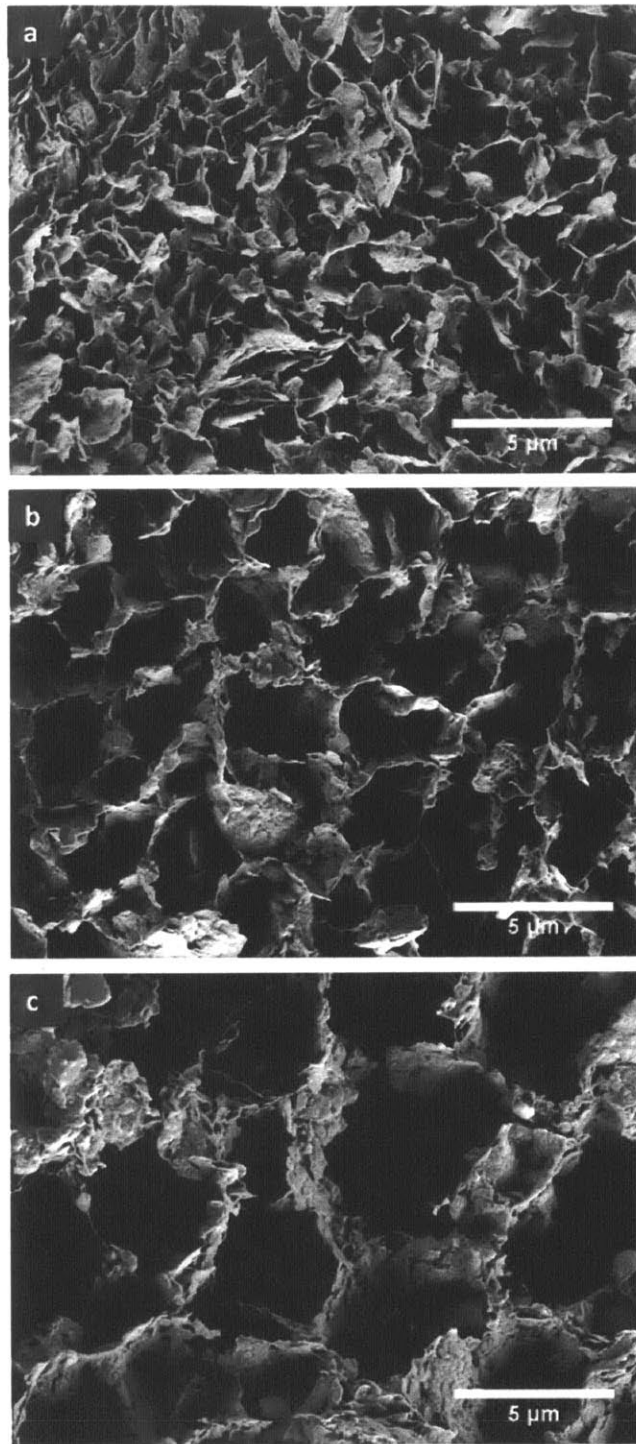
Figure 6-4: Cryo-SEM images of plunge freezing experiments of GOM-EI slurries in three different cryogens: a) ethane, b) nitrogen slush, and c) liquid nitrogen.
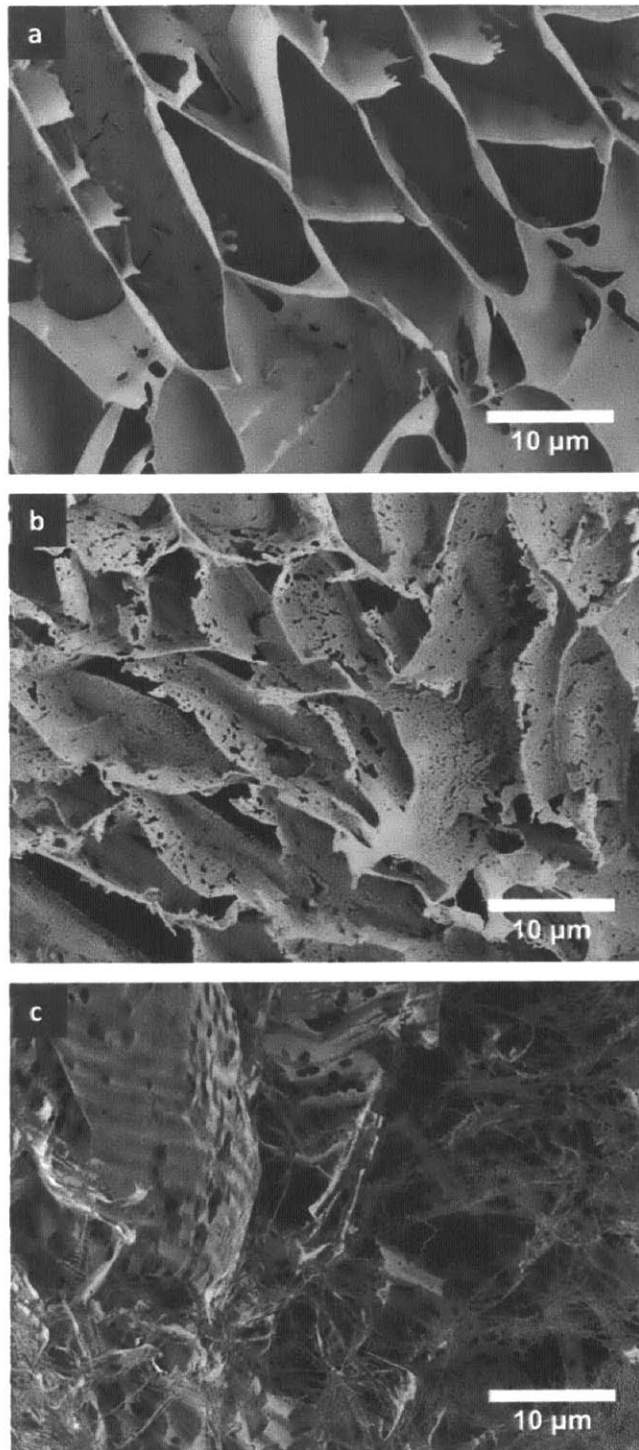
Figure 6-5: Cryo-SEM images of plunge freezing experiments in three different cryogens: a) ethane, b) nitrogen slush, and c) liquid nitrogen.
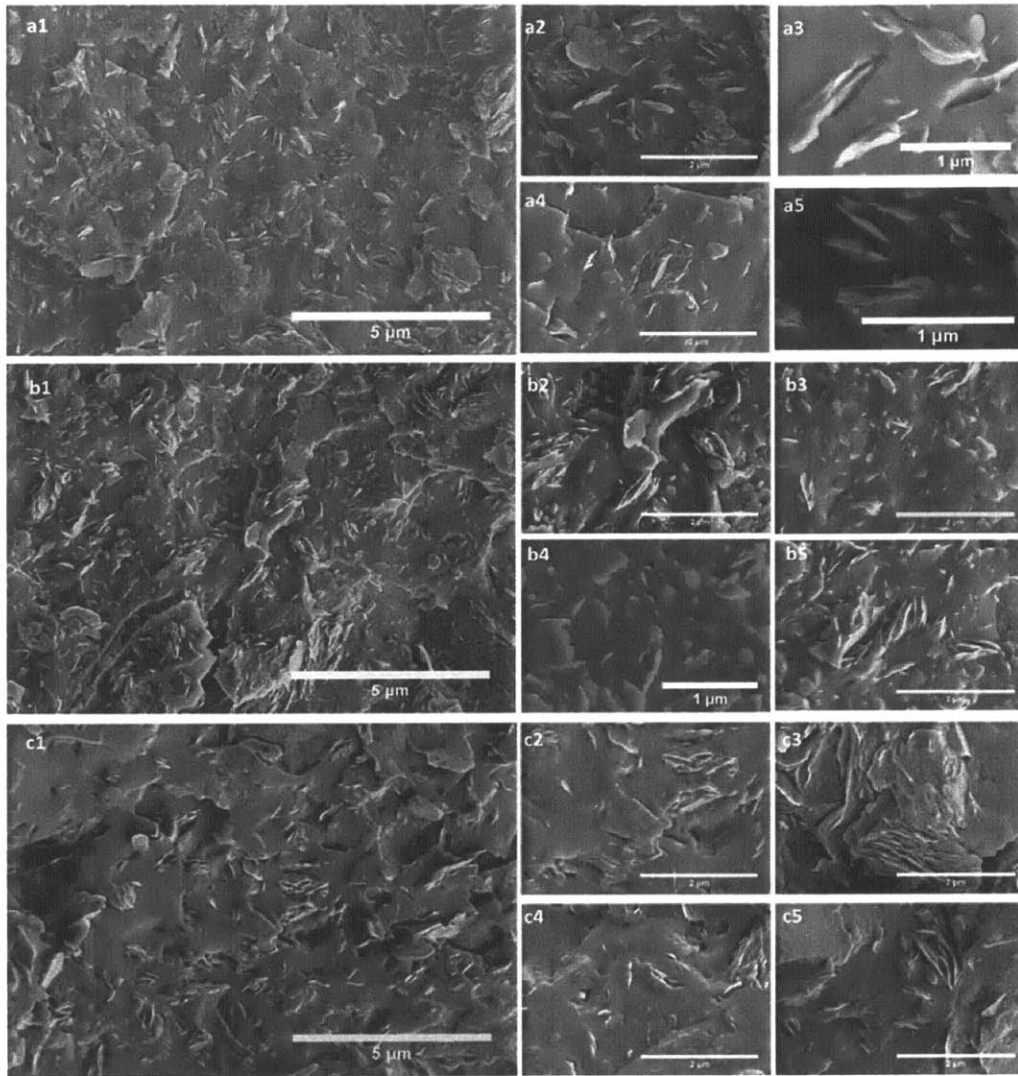
Figure 6-6: Cryo-SEM images of high-pressure frozen GOM-EI samples at different NaCl pore salinities: a1-a5) 1 g/L, b1-b5) 16 g/L, and c1-c5) 64 g/L
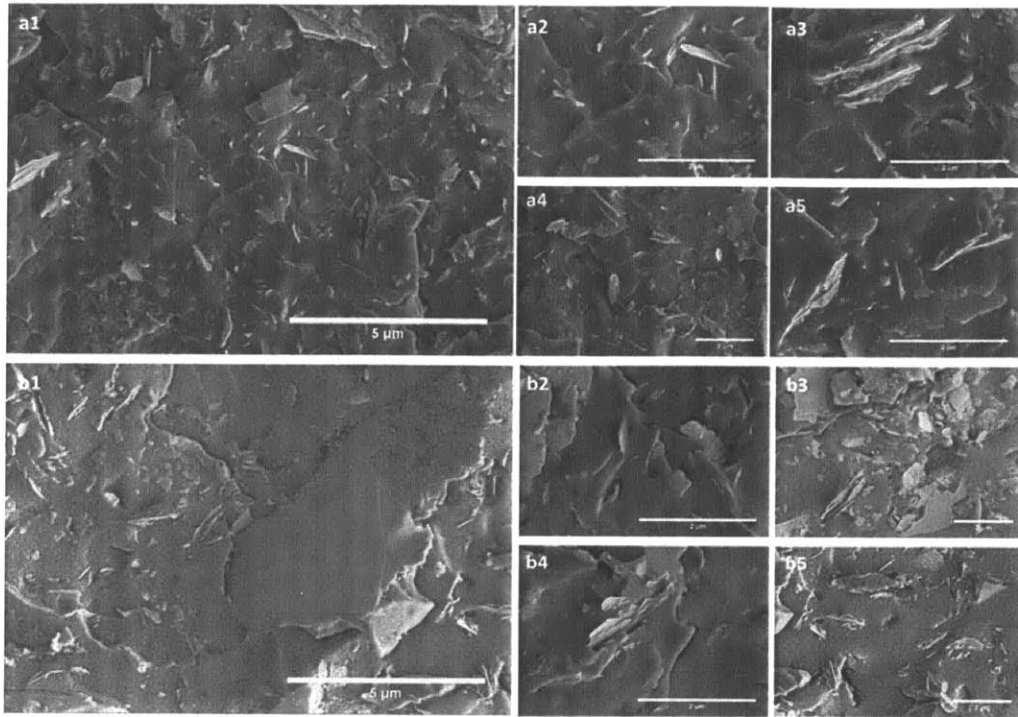
Figure 6-7: Cryo-SEM images of high-pressure frozen BBC samples at different NaCl pore salinities: a1-a5) 16 g/L, b1-b5) 64 g/L.
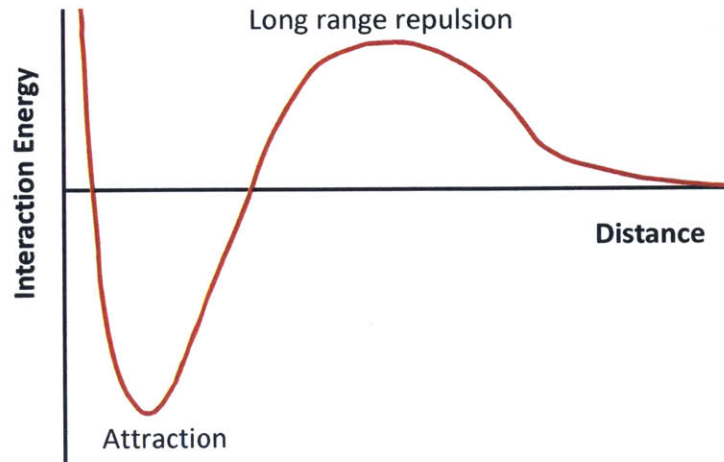
Figure 6-8: Illustrative net interaction curve for clay minerals, which presents the interaction energy as a function of the separation distance. The total interaction energy results from the summation of double layer repulsive energy and van der Waals attraction energy. This curve consists of a minimum peak at small separation that represents attraction and a maximum peak at larger separation that represents double layer repulsion.
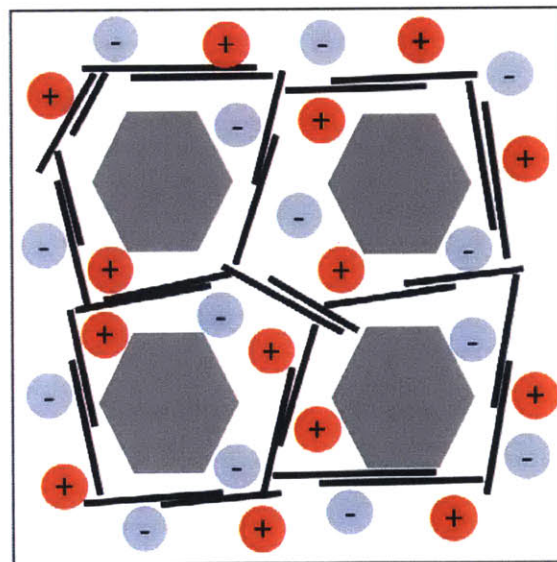
Figure 6-9: A schematic illustration that shows the process by which the honeycomb structure in clay slurries forms in plunge freezing experiments. This structure forms as ice crystals push salt and clay minerals to the boundaries of the growing ice front. Ice segregation process leads to drastic changes in the solutions properties that form the apparent clay particles associations. Black lines represent clay particles, whereas blue and red circles represent salt ions.

7 THE MICROSTRUCTURE OF RESEDIMENTED MUDROCK SAMPLES

7.1 Introduction

This chapter presents the porosity results performed on RGOM-EI and RBBC mudrocks. Table 7-1 summarizes the experimental program performed in this investigation to measure the porosity of the studied mudrock samples. Section 7.2 provides a qualitative description of the microstructure of the imaged RGOM-EI and RBBC mudrocks. This description includes the microstructure of oven-dried and wet mudrock samples. Section 7.3 presents the porosity results obtained using different techniques including wet lab porosity, oven-dried lab porosity, MIP porosity, oven-dried imaging porosity, and cryo-imaging porosity. The various porosity results are summarized in Figure 7-7 and Figure 7-8 for RGOM-EI and RBBC mudrocks, respectively. Section 7.4 discusses the influence of the resolution of SEM on the measured imaging porosity. The pore space of mudrocks was divided into two categories: visible SEM porosity (>35 nm) and sub-35nm porosity (<35 nm). The limit of 35 nm represents the resolution of SEM in this investigation. Section 7.5 addresses the influence of oven drying on the microstructure of RGOM-EI and RBBC mudrocks. This section discusses in detail the influence of drying on the visible SEM porosity and on the sub-35nm porosity. Finally, Section 7.6 addresses the influence of the consolidation stress on the microstructure of RGOM-EI and RBBC mudrocks. Similar to the influence of drying, the influence of the consolidation stress on the microstructure of mudrocks was described in terms of the visible SEM porosity and the sub-35nm porosity.

7.2 Qualitative Description of the Microstructure

This section presents a qualitative description of the microstructure of the investigated mudrock samples (see Table 7-1). Two types of imaging techniques were used: conventional SEM and cryo-SEM. Conventional SEM was used to image oven-dried mudrock samples, while cryo-SEM was used to imaged wet mudrock samples. The main features of the microstructure of these samples are described in this section. The pore classification scheme propose by Loucks et al., (2012) is used to describe the pore space of the imaged samples. Furthermore, the clay terminology used to describe the microstructure of clay slurries is used for the resedimented

143

samples. In particular, the terms flocculation and aggregation as defined in Chapter 2. Low magnification and high magnification images are used to describe the microstructure. High magnification images provide a small field of view and high resolution, while low magnification images provide a large field of view and low resolution.

7.2.1 Oven-Dried RGOM-EI Samples

The microstructure of oven-dried RGOM-EI samples is shown in Figure 7-1and Figure 7-2. The SEM images in Figure 7-1 were acquired at a magnification of 6 KX, which provides a relatively large field of view (50 μm), while the SEM images in Figure 7-2 were acquired at a magnification of 30 KX, which provides a relatively small field of view (10 μm). In these images the pore space is shown in black whereas the particles are shown in gray. These images show that the inclusions of mainly quartz and feldspar are randomly distributed in a matrix of clay particles (Figure 7-1). The shape of these inclusions range from circular (e.g., Figure 7-1d) to rectangular (e.g., Figure 7-1b) with no preferred orientation. The size of silt inclusions ranges from a few microns to 20 microns, but these inclusions are rare. The clay matrix is composed mainly of clay aggregates forming face-edge and face-face contacts with other aggregates (Figure 7-2). When clay aggregates make face-face contacts, it becomes difficult to separate the boundaries of each aggregate (e.g., Figure 7-2b, c). Therefore, it is not possible to obtain a representative value for the size of these aggregates. However, aggregates with a size range of 200 nm to 400 nm approximately can be observed. The clay aggregates also form either face-edge or face-face contacts with silt inclusions. The face-edge contacts lead to the formation of large pores at the boundary of silt inclusions. The clay aggregates tend to align horizontally, which is the direction perpendicular to the applied stress. Furthermore, bending of clay aggregates is observed in a few locations (e.g., Figure 7-2b).

Two types of pores can be identified in RGOM-EI samples: inter-particle pores (interP), and intra-particle pores (intraP). InterP pores include pores between clay aggregates, between silt inclusions, and at the boundary of silt inclusions. These pores develop when clay aggregates form face-edge contacts with aggregates or with silt inclusions. The majority of these pores range in size from a hundred nanometers to hundreds of nanometers. Furthermore, their shape range from elliptical with high aspect ratio to angular with low aspect ratio. InterP pores as large as a few microns can be found in SEM images of RGOM-EI samples, but these pores are not

144

abundant. On the other hand, IntraP pores include pores within clay aggregates. This types of porosity develops between stacks of clay particles in an aggregate. The shape of these pores is mainly elliptical with high aspect ratio. The size of intraP pores range from a few nanometers to less than a hundred nanometers.

7.2.2 Oven-Dried RBBC Samples

The description of the microstructure of oven-dried RBBC mudrocks is similar to that of RGOM-EI mudrocks discussed above (Figure 7-3 and Figure 7-4). Two magnifications were used to image the microstructure of oven-dried RBBC samples: 6 KX (Figure 7-3) and 30 KX (Figure 7-4). Similar to RGOM-EI samples, the microstructure of RBBC samples consists of quartz and feldspar inclusions that are randomly distributed in a matrix of clay particles (Figure 7-3). The shape and size of these aggregates is similar to that of RGOM-EI samples. The clay matrix is composed mainly of clay aggregates forming face-edge and face-face contacts with other aggregates (Figure 7-4). The clay aggregates in RBBC samples are more porous and contain bigger pores than the aggregates in the RGOM-EI samples. The shape and size of clay particles in the RBBC samples is larger than the RGOM-EI samples. This difference is attributed to the differences in clay mineralogy between the two samples. Other features of the microstructure such as the size of aggregates and orientation are similar to those of RGOM-EI samples. The types of pores identified in oven-dried RBBC samples is similar to those of RGOM-EI samples; interP pores and intraP pores. The size of interP and intraP pores in RBBC mudrocks is larger than those in RGOM-EI mudrocks.

7.2.3 Wet RGOM-EI and RBBC Samples

The microstructure of wet RGOM-EI and RBBC samples is presented in Figure 7-5 and Figure 7-6, respectively. Similar to oven-dried samples, the cryo-SEM images were acquired at two different magnifications of 6 KX and 30 KX. The purpose of this section is only to describe the microstructure of wet samples. A comparison of the wet and oven-dried samples is discussed later in this chapter.

In the cryo-SEM images the pore space is shown in black whereas the particles are shown in gray. These images show that quartz and feldspar silt inclusions are randomly distributed in a matrix of clay matrix for both RGOM-EI and RBBC samples (Figure 7-5a, c and Figure 7-6a,c). The shape of these inclusions range from circular to rectangular with no preferred orientation.

145

The size of silt inclusions ranges from a few microns to 20 microns, but these inclusions are rare. The features of the microstructure observed in the wet samples is similar to those of the oven-dried samples. The clay matrix is composed mainly of clay aggregates forming face-edge and face-face contacts with other aggregates (Figure 7-5b, d and Figure 7-6b, d). The size of these aggregates is approximately 200 nm to 400 nm. The clay aggregates also form either face-edge or face-face contacts with silt inclusions. The face-edge contacts lead to the formation of large pores at the boundary of silt inclusions. The clay aggregates tend to align along the bedding plane, which is the direction perpendicular to the applied stress. Furthermore, the description of the pore space of the wet samples is similar to that of the oven-dried samples. Two types of pores can be identified in wet RGOM-EI and wet RBBC samples: InterP and intraP pores. The shape and the size of these pores matches that of the oven-dried samples.

7.3 Porosity Measurements

This section presents the porosity values obtained in this investigation for RGOM-EI and RBBC mudrock samples. The porosity was measured using different methods including wet and oven-dried macroscopic lab porosity, Mercury Porosimetry Intrusion (MIP), oven-dried imaging porosity, and cryo-imaging porosity of wet samples (see Chapter 4). These measurements were performed on samples resedimented at a wide range of stress values. Table 7-1 summarizes the experimental program performed in this thesis to measure the porosity of the mudrock samples. The various porosity results are summarized in Figure 7-7 and Figure 7-8 for RGOM-EI and RBBC mudrocks, respectively. The next sections discuss these porosity measurements in detail.

7.3.1 Oven-Dried and Wet Macroscopic Porosity

This section presents the results of the macroscopic porosity measurements. These measurements were performed on both wet and oven-dried samples of RGOM-EI and RBBC mudrocks (see Table 7-1). The difference between the wet and oven-dried lab porosity provides a measure of shrinkage that mudrock samples undergo upon drying.

Table 7-2 presents a summary of the wet and oven-dried lab porosity values performed in this investigation on RGOM-EI and RBBC mudrock samples. The porosity of RGOM-EI mudrocks was measured for samples with a resedimentation stress range of 0.2 to 65 MPa. The Porosity of RBBC mudrocks was measured for samples with a resedimentation stress range of

0.2 to 100 MPa. The wet and oven-dried lab porosity results presented in Table 7-2 are also summarized in Figure 7-7 and Figure 7-8 for RGOM-EI and RBBC mudrocks, respectively. Wet lab porosity of RGOM-EI mudrock samples ranges from 0.576 at 0.2 MPa to 0.265 at 65 MPa (blue points, Figure 7-7), while oven-dried lab porosity range from 0.297 at 0.2 MPa to 0.212 at 65 MPa (purple points, Figure 7-7). These results show that RGOM-EI mudrock samples undergo a dramatic drying shrinkage that ranges from 50% at 0.2 MPa to 20% at 65 MPa. On the other hand, wet lab porosity of RBBC mudrock samples ranges from 0.507 at 0.2 MPa to 0.2 at 100 MPa (blue points, Figure 7-8), while the oven-dried lab porosity ranges from 0.4 at 0.2 MPa to 0.2 at 100 MPa (purple points, Figure 7-8). These results show that RBBC mudrocks undergo a drying shrinkage that ranges from 20% at 0.2 MPa to 0% at 10 MPa and higher stresses.

The above results show that the drying shrinkage is significantly higher for RGOM-EI mudrocks compared to that of RBBC mudrocks. Furthermore, there is no drying shrinkage in RBBC mudrocks at stresses higher than 10 MPa. On the other hand, the drying shrinkage in RGOM-EI mudrocks is significant at stresses as high as 65 MPa. Figure 7-7 shows that the extension of the wet lab porosity line and the oven-dried lab porosity line will meet at a stress of approximately 105 MPa. This value represents the stress after which no drying shrinkage occurs in RGOM-EI mudrocks. The difference in drying shrinkage between RGOM-EI and RBBC mudrocks is attributed to the differences in their mineralogy. While RGOM-EI mudrocks are predominantly smecitic, RBBC mudrocks are predominantly illitic. The sensitivity of smectite clay minerals to water and shrinkage is well documented in the literature, and it is much higher than illite clay minerals. This explains the high drying shrinkage in RGOM-EI mudrocks compared to that of RBBC illite.

7.3.2 Mercury Porosimetry Intrusion (MIP) Porosity

In this study, the MIP porosity measurements were performed on oven-dried samples. The MIP porosity results are presented in Table 7-2, and also summarized in Figure 7-7 and Figure 7-8 for RGOM-EI and RBBC mudrocks, respectively. The MIP porosity was measured for three RGOM-EI samples resedimented at three different stresses of 0.1 MPa, 8 MPa, and 21 MPa. The porosity of the RGOM-EI samples ranges from 0.255 at 0.1 MPa to 0.203 at 21 MPa (Figure 7-7). These porosity values are slightly less than the oven-dried lab porosity, and the difference decreases as the resedimentation stress increases. The difference between the two

porosity values can be attributed to the differences in the resolution of the two techniques. MIP experiments intrude pore throats down to 3 nm, while the oven-dried lab porosity measures smaller pores caused by the loss of water after drying at 110°C. Furthermore, the difference between the two porosity values may be attributed to the unconnected part of the pore space. These results show that RGOM-EI mudrocks contain a significant amount of pores smaller than 3 nm and unconnected pores. On the other hand, the MIP porosity measurements were performed on three RBBC samples resedimented at three different stresses of 0.1 MPa, 1 MPa, and 10 MPa (Figure 7-8). The MIP porosity of the RBBC samples ranges from 0.41 at 0.1 MPa to 0.37 at 10 MPa. The MIP porosity matches the oven-dried lab porosity. Unlike RGOM-EI samples, these results show that the pore space of RBBC mudrock samples does not contain pores smaller than 3 nm or unconnected pores.

7.3.3 Oven-Dried Imaging Porosity

This section presents the oven-dried imaging porosity results for RGOM-EI and RBBC mudrock samples. These porosity results were calculated from the SEM images of oven-dried samples using the IOM method (see chapter 5). Table 7-1 summarizes the mudrock samples that were used to obtain the oven-dried imaging porosity. These samples were chosen to represent a wide range of stresses. Three magnifications were used to represent the pore space of mudrock samples. Table 7-3 summarizes the number of images at each magnification of the samples tested in this investigation. The range of pore sizes targeted at each magnification were: 35 nm to 151 nm, 151 nm to 675 nm, and >675 nm for magnifications of 30 KX, 12 KX, and 6 KX, respectively. These magnifications are called Mag 1, Mag2, and Mag 3, respectively (see Chapter 5).

Table 7-4 summarizes the porosity results of RGOM-EI samples obtained at each magnification, as well as the final porosity obtained using the IOM method. Furthermore, Table 7-4 presents the standard error of the mean porosity at each magnification obtained using the procedure outlined in Chapter 5. Figure 7-9 shows a graphical presentation of these results. The oven-dried imaging porosity of RGOM-EI ranges from 0.161 at 0.2 MPa to 0.094 at 10 MPa (Figure 7-9a). The standard error values at each magnification range from 2% to 9%. The coefficient of variation is calculated by dividing the standard error by the porosity corresponding to each magnification (Figure 7-9b). Despite the relatively high variability of the standard error

at each magnification, the final coefficient of variation is less than 5% (see Chapter 5). These results show that the number of images used at each magnification is sufficient to represent the pore space of the investigated mudrock samples.

Table 7-5 summarizes the porosity results of RBBC samples obtained at each magnification, as well as the final porosity obtained using the IOM method. Furthermore, Table 7-5 presents the standard error of the mean porosity at each magnification obtained using the procedure outlined in Chapter 5. Figure 7-10 shows a graphical presentation of these results. The oven-dried imaging porosity of RBBC mudrocks ranges from 0.24 at 0.2 MPa to 0.105 at 20 MPa (Figure 7-10a). The coefficient of variation at the three magnifications used in the IOM method ranges from 2% to 13% (Figure 7-10b). The coefficient of variation value of 13% corresponds to Mag 3 of RBBC-20 mudrock sample. As can be seen in Table 7-5, the porosity at this magnification is 0.005, and the coefficient of variation is very sensitive when the mean approaches a value of zero. Therefore, the high coefficient of variation at this magnification is attributed to the very low porosity at this magnification. Despite the high fluctuations of the coefficient of variation at each magnification, the final coefficient of variation is less than 5% for all samples (see Chapter 5). These results show that the number of images used at each magnification is sufficient to represent the pore space of the investigated mudrock samples.

7.3.4 Cryo-Imaging Porosity

This section presents the cryo-imaging porosity results for RGOM-EI and RBBC mudrock samples. These porosity results were calculated from the SEM images of wet samples using the IOM method (see chapter 5). Table 7-1 summarizes the mudrock samples that were imaged to obtain the cryo imaging porosity. Two wet RGOM-EI mudrock samples at stresses of 0.2 MPa and 6 MPa were imaged. On the other hand, two wet RBBC mudrock samples at stresses of 1 MPa and 10 MPa were imaged. The RBBC samples were prepared using plunge freezing, followed by cryo ion milling and cryo-imaging (see Chapter 4). We showed in this investigation that plunge freezing produces ice crystals that destroy the fabric of clay slurry samples. The validity of these conclusions on resedimented mudrock samples with significantly less water content is still under investigation. Plunge freezing of samples of low water content may lead to the formation of small Ice crystals that may not disturb the microstructure. Similar to oven-dried samples, three magnifications were used to represent the pore space of wet mudrock

149

samples. Table 7-6 summarizes the number of cryo-SEM images used at each magnification to represent the pore space of the wet samples tested in this investigation. The range of pore sizes targeted at each magnification were: 10 nm to 151 nm, 151 nm to 675 nm, and > 675 nm for magnifications 1, 2, and 3, respectively.

Table 7-7 summarizes the cryo-imaging porosity results of the wet RGOM-EI samples obtained at each magnification, as well as the final porosity obtained using the IOM method. Furthermore, Table 7-7 presents the standard error of the mean porosity at each magnification obtained using the procedure outlined in Chapter 5. Figure 7-11 shows a graphical presentation of these results. The porosity of RGOM-EI ranges from 0.108 at 1 MPa to 0.119 at 6 MPa (Figure 7-11a). The porosity values show little sensitivity to stress level. The coefficient of variation at each magnification ranges from 4% to 18% (Figure 7-11b). The high coefficient of variation of 18% is attributed to the very low porosity at that magnification. Despite the high variability of the coefficient of variation at each magnification, the final coefficient of variation is less than 6% (see Chapter 5). These results show that the number of images used at each magnification is sufficient to represent the pore space of the investigated mudrock samples.

Table 7-8 summarizes the cryo-imaging porosity results of the wet RBBC samples obtained at each magnification, as well as the final porosity obtained using the IOM method. Furthermore, Table 7-8 presents the standard error of the mean porosity at each magnification obtained using the procedure outlined in Chapter 5. Figure 7-12 shows a graphical presentation of these results. The porosity of wet RBBC ranges from 0.133 at 1 MPa to 0.088 at 10 MPa (Figure 7-12a). These samples were prepared using plunge freezing, and more results are required to confirm that plunge freezing preserves the microstructure of resedimented mudrock samples. The coefficient of variation at each magnification ranges from 2% to 9% (Figure 7-12b). Despite the high variability of the coefficient of variation at each magnification, the final coefficient of variation is less than 3% (see Chapter 5). These results show that the number of images used at each magnification is sufficient to represent the pore space of the investigated mudrock samples.

7.3.5 Discussion of Porosity Measurements

The wet lab porosity measurements provide an accurate measure of the porosity of the resedimented mudrock samples for two reasons. First, the resedimented samples are fully

saturated, and the measured water content accurately represent the pore space. Second, the drying was performed immediately after the samples had been extruded, and hence there was no water loss due to air drying that may result from long-term storage or transportation of samples. The measured wet lab porosity is a function of the amount of water that is evaporated at 110°C for 24 hours (see Chapter 4). To better understand the measured porosity, one needs to determine the water removed by this temperature. The water in the pore space of mudrocks can be divided into three different categories: bound water, capillary water, and free water. Mitchell et al., (2005) stated that the bound water is removed when the sample is heated at 100°C to 300°C. Wang et al., (2011) utilized Thermogravimetery (TG) and differential scanning calorimetry (DSC) techniques to determine the temperature required to remove all of the bound water for 9 soil samples with different clay contents and particle size distributions. They showed that a temperature of 200°C was required to remove all of the bound water in the samples. Furthermore, they showed that around 80% of the water in the pore space is removed by heating the sample at 110°C for 24 hours, and the remaining water represents tightly bound water and requires temperatures up to 200°C. Therefore, the porosity calculated using the conventional drying methods does not include the water layers that are tightly bound to the surface of clay minerals. The choice of whether or not to include the tightly bound water in the porosity calculations depends on the purpose of the study. For example, if the researcher is interested in permeability, the tightly bound water does not contribute to permeability and can be ignored. On the other hand, if the researcher is interested in acoustic measurements, the tightly bound water may influence the results and should be considered. The purpose of this investigation is to assess the influence of shrinkage that occurs as a result of the conventional drying methods on the microstructure of mudrocks. Therefore, the exclusion of the tightly bound water does not influence the conclusions of this study.

The porosity trends obtained in Figure 7-7 and Figure 7-8 match the trends obtained in the literature as outlined in Chapter 2. In particular, the SEM imaging porosity of oven-dried samples is significantly less than the MIP porosity and the oven-dried lab porosity. This discrepancy is due to the differences of the resolution of the used methods. The minimum pore diameter measured using the IOM method is 35 nm, while the resolution of MIP is 3 nm. These results show that a significant amount of mudrocks porosity is smaller than 35 nm. This topic is

discussed in detail in the next section. Furthermore, the MIP porosity, which was performed on oven-dried samples, is significantly less that the wet lab porosity. These results show that the use of such methods on oven-dried samples provide porosity values that does not represent the in-situ state of the samples. Rather, these methods represent the dry state of the material, which is quite different than the in-situ state of the material as shown in Figure 7-7 and Figure 7-8. The MIP porosity can be compared with the oven-dried lab porosity because both methods involve the use of the same drying procedures. The MIP porosity of RGOM-EI mudrocks is less than the oven-dried lab porosity. On the other hand, the MIP porosity of RBBC mudrocks matches the oven-dried lab porosity. The discrepancy between the MIP and oven-dried lab porosity can be used to infer information about the microstructure of mudrocks. For example, the differences between the MIP porosity and oven-dried porosity of RGOM-EI samples suggest that the pore space of these samples either contain pores smaller than 3 nm or unconnected pores. On the other hand, the studied RBBC mudrocks do not contain pores smaller than 3 nm or unconnected pores.

7.4 Influence of SEM Resolution on Imaging Porosity

Two types of imaging porosity measurements were obtained in this investigation: cryo-imaging porosity, and oven-dried imaging porosity. The quantification of the influence of the resolution of SEM on the imaging porosity of mudrock samples can be achieved by comparing the imaging porosity and the reference lab porosity. In this investigation, the wet and oven-dried lab porosity are considered the reference porosity values. Wet lab porosity serves as the reference porosity for cryo-imaging porosity, whereas oven-dried lab porosity serves as the reference porosity for oven-dried imaging porosity. As discussed above, wet and oven-dried lab porosities provide precise porosity measures of RGOM-EI and RBBC samples. Therefore, the difference between SEM imaging porosity and the reference lab porosity is due to the resolution of SEM. In other words, the difference between the two measurements is a consequence of the pores that are smaller than the resolution of SEM. In this investigation, the smallest pore that can be quantified in SEM images is 35 nm. This number is a function of the highest magnification used (30 KX) to image mudrock samples, as well as the minimum of 10 pixels required to properly quantify pores (see chapter 5). The magnification of 30 KX was chosen based on practical considerations because it provides a good balance between the obtained resolution and the size of the field of view.

Figure 7-7 and Figure 7-8 show that the SEM imaging porosity is significantly less than the reference lab porosity for RGOM-EI and RBBC mudrocks, respectively. In both cases, cryo-imaging porosity (light blue points) is compared with the wet lab porosity (dark blue points), whereas oven-dried imaging porosity (red points) is compared with the oven-dried lab porosity (purple points). These results show that the SEM porosity of RGOM-EI mudrocks reveals only 22-33% of the wet lab porosity and 39-54% of the oven-dried lab porosity. On the other hand, SEM imaging porosity of RBBC mudrocks reveals only 26-30% of the wet lab porosity and 33-60% of the oven-dried lab porosity. Therefore, SEM imaging porosity reveals only a fraction of the porosity of mudrock samples, and the remaining porosity is smaller than 35 nm. To investigate the pore space smaller than 35nm, we used Transmission Electron Microscopy (TEM) as discussed in the next section.

7.4.1 TEM Imaging of RGOM-EI samples

TEM imaging was used to investigate the pore space of two oven-dried RGOM-EI mudrock samples: RGOM-EI-1 MPa and RGOM-EI-10 MPa (Figure 7-13 and Figure 7-14, respectively). These images reveal the pore space at sub-nm resolution. Two types of TEM images were acquired: bright field and dark field images. In bright field images, the pore space appears bright, whereas the particles appear darker. In dark field imaging, the pore space appears black whereas particles appear brighter. The dark field TEM images of RGOM-EI-1 MPa show that the clay aggregates, described in Section 7.2, are highly porous, and contain pores with a wide range of sizes. In particular, pores that are smaller than 10 nm are abundant (Figure 7-14). These pores represent the spacing between individual clay particles in an aggregate. TEM images of RGOM-EI-10 MPa sample reveal a similar microstructure. Pores smaller than 10 nm are abundant in clay aggregates as shown in the bright field TEM images (bright color, Figure 7-14b, d). A comparison between the TEM images of the two samples shows that the amount of pores smaller than 10 nm is similar (e.g., Figure 7-13b vs. Figure 7-14e). These images are taken for a very small field of view and provide qualitative information about the pore space below the resolution of SEM. Therefore, no attempt was made to calculate the porosity of these images.

The TEM images further support the conclusion that the discrepancy between SEM imaging porosity and the reference lab porosity is due to the missing pores smaller than the resolution of SEM, which is 35 nm in this investigation. In the previous section we showed that

SEM imaging porosity reveals only a fraction of the reference lab porosity (~30%). These results suggest that around 70% of the pore space in mudrocks is smaller than 35 nm. To further illustrate the influence of SEM resolution on the imaging porosity, we added another high magnification in IOM method to increase the resolution limit of SEM as discussed in the next section.

7.4.2 Extension of the IOM Method

As discussed above, the resolution of SEM is mainly a function of the highest magnification used to image the microstructure. In this investigation, the highest magnification used in the IOM method is 30 KX, which provides a resolution of 35 nm. To improve this resolution limit, we added another high magnification to the analysis performed using the IOM method (see Chapter 5). The added magnification is 100 KX, which provides a resolution of approximately 11 nm. Two samples were imaged at this magnification: RGOM-EI-0.2 MPa and RGOM-EI-1 MPa. Twenty five images were acquired for each sample at this magnification (e.g., see Figure 7-15). These images show the porous clay aggregates described in Section 7.2. When adding the forth magnification to the IOM method analysis, the SEM imaging porosity increases from 0.160 to 0.208 for the RGOM-EI-0.2 MPa sample, and from 0.136 to 0.187 for the RGOM-EI-1 MPa sample (see Figure 7-16). These results show that the amount of porosity below 11 nm is significant. Figure 7-17 shows that the amount of pores smaller than 11 nm not detected in thresholding is significant. It was not possible to threshold these pores because there is not enough gray color contrast at high magnification imaging, and manual thresholding would be required to detect these pores. The above results further support the conclusion that the porosity smaller than the resolution of SEM is significant, and only a small fraction (~30%) is visible in SEM images. In the next section, we use the IOM method to back-calculate the porosity smaller than the SEM resolution.

7.4.3 Sub-35nm Porosity

The above discussion showed that the pores smaller than 35 nm are mainly associated with the clay matrix. Therefore, the sub-35nm porosity is defined as the volume of pores smaller than 35 nm divided by the total volume of the clay matrix (see Figure 7-18). The 35 nm limit was chosen in this investigation because all of the samples were imaged at this resolution, and the 11 nm limit was obtained for two samples only. The sub-35nm porosity can be evaluated in our

samples by comparing the reference lab porosity with the imaging porosity. This section describes the method we used to back-calculate the sub-35nm porosity using the IOM method. Recall from Chapter 5 that the final porosity can be calculated using the following equation:

$$n_f = n_l + n_{l-1}C_l + n_{l-2}C_lC_{l-1} + \cdots \qquad (7\text{--}1)$$

where n_f is the final porosity and l is the number of magnifications, which is three in our case. C_l is the ratio of solid area to total area at Mag l, and is given by

$$C_l = \frac{(A_{Tl} - A_{pl\_}A_{Lpl})}{A_{Tl} - A_{Lpl}} \qquad (7\text{--}2)$$

where, A_{Tl} is the total area of pores and particles at the Mag l, A_{pl} is the area of target pores at Mag l, and A_{Lpl} is the area of big pores at Mag l. To estimate the missing clay porosity, assume that l is equal to 4 instead of 3. The added magnification is assumed to target pores smaller than 35 nm and is designated Mag 0. With these information at hand, equation (1-4) can be written as follows:

$$n_f = n_3 + C_3 \times n_2 + C_2C_3 \times n_1 + C_1C_2C_3 \times V_c \times n_0 \qquad (7\text{--}3)$$

where n_0 is the sub-35nm porosity. n_f in this case becomes the known reference porosity, and V_c is the volume fraction of clay minerals in mudrock samples. The use of the clay fraction in this equation is because the sub-35nm porosity is mainly in the clay aggregates. The volume fraction of clay minerals in RBBC and RGOM-EI mudrocks is 0.56 and 0.65, respectively (see chapter 3). In other words, the use of the clay volume fraction in equation (1-5), V_c, ensures that the missing clay porosity is only assigned to the clay minerals of the sample. The next paragraph further illustrates this method through an example application on the RGOM-EI-1 MPa mudrock sample.

The sub-35nm porosity can be calculated by comparing the SEM imaging porosity and the reference lab porosity. As discussed above, there are two types of porosity measurements in this investigation: wet and oven-dried porosity. As a consequence, we have enough information to calculate wet and oven-dried sub-35nm porosity values. The wet sub-35nm porosity can be calculated by comparing cryo-imaging porosity (Table 7-7) with the reference wet lab porosity (Table 7-2). Using the information for the wet RGOM-EI-1 MPa sample, equation (1-6) becomes:

$$0.482 = 0.016 + C_3 \times 0.062 + C_2 C_3 \times 0.032$$
$$+ C_1 C_2 C_3 \times 0.65 \times n_0 \tag{7-4}$$

where C_i is given by equation (1-2). The wet sub-35nm porosity, n_0, can be calculated from equation (1-4), and is equal to 0.585. The same procedure can be applied to calculate the dry sub-35 nm porosity by comparing the oven-dried imaging porosity (Table 7-4) with the reference oven-dried lab porosity (Table 7-2). Using the information for the dry RGOM-EI-1 MPa sample, equation (1-6) becomes:

$$0.276 = 0.028 + C_3 \times 0.07 + C_2 C_3 \times 0.041$$
$$+ C_1 C_2 C_3 \times 0.65 \times n_0 \tag{7-5}$$

The dry sub-35nm porosity, n_0, can be calculated from equation (1-5), and is equal to 0.221. The same procedure is used to calculate the wet and dry sub-35nm porosity for all imaged samples in this investigation.

Table 7-9 presents the wet and the oven-dried sub-35nm porosity values for the tested samples in this investigation, and Figure 7-19 shows a graphical presentation of these results. The oven-dried sub-35nm porosity of RGOM-EI mudrock samples is almost constant and ranges from 0.222 to 0.249 (red points, Figure 7-19a). The wet sub-35nm porosity for RGOM-EI samples ranges from 0.585 at 1 MPa to 0.378 at 6 MPa (light blue, Figure 7-19a). On the other hand, the oven-dried sub-35nm porosity of RBBC mudrock samples ranges from 0.316 to 0.38 (red points, Figure 7-19b). The oven-dried sub-35nm value at 10 MPa requires further consideration as discussed later, and therefore ignored here. The wet sub-35nm porosity of RBBC samples ranges from 0.577 at 1 MPa to 0.425 at 10 MPa (light blue, Figure 7-19b).

7.4.4 Discussion of the Influence of Resolution

In this section we showed that the SEM imaging porosity reveals only a fraction of the total porosity of mudrocks. These conclusions match those in the literature obtained by comparing the SEM porosity of large mosaics with MIP porosity (see Chapter 2). In this investigation we showed that the MIP porosity represents the dry state of materials, and it may underestimate the porosity of mudrocks depending on the mineralogy. Furthermore, we used the wet and oven-dried lab porosity as the reference porosity, which provides more accurate porosity values than MIP. We also showed that the IOM method, developed in this investigation, is a powerful tool that provides representative information about the microstructure of mudrocks. This method can be used as an alternative to the time-consuming and expensive method of large

156

BIB mosaics of SEM images. We also showed that the IOM method can be used to utilize the full resolution of SEM by imaging samples at a magnification of 100 KX, which provides a resolution of 11 nm. Obtaining this resolution using the large SEM mosaics requires stitching together thousands of images, which may take many days to acquire. Finally, the use of the wet and oven-dried lab porosity values enabled us to back-calculate the sub-35nm porosity for wet and oven-dried samples. We showed that the wet sub-35nm porosity is significantly higher than the oven-dried sub-35nm porosity.

7.5 Influence of Drying Shrinkage on the Microstructure of Mudrocks

The above results showed that RGOM-EI and RBBC mudrocks undergo dramatic drying shrinkage when oven-dried at 110°C for 24 hours (see Figure 7-7 and Figure 7-8). Furthermore, SEM imaging porosity reveals only a fraction of the reference lab porosity (~30%), and approximately 70% of the pore space in mudrocks is smaller than 35 nm. The next sections address the influence of drying shrinkage on both the visible SEM porosity (>35nm) and the sub-35nm porosity, which is mainly associated with clay minerals as shown above.

7.5.1 Visible SEM porosity

This section discusses the influence of drying shrinkage on the visible SEM porosity (>35nm) for both RGOM-EI and RBBC mudrocks. A comparison of SEM images of oven-dried samples and cryo-SEM images of wet samples provides a qualitative understanding of the influence of drying. On the other hand, a comparison of the porosity values and pore size distributions obtained using the IOM method of oven-dried and wet samples provides a quantitative assessment of the influence of drying on the microstructure of mudrocks.

RGOM-EI Mudrock Samples

The influence of drying shrinkage on RGOM-EI mudrocks is investigated on two samples: RGOM-EI-1 MPa, and RGOM-EI-6 MPa. Figure 7-20 through Figure 7-23 show cryo- and oven-dried SEM images of the two RGOM-EI mudrock samples. These figures include two different magnifications of 12 KX (Figure 7-20 and Figure 7-22) and 30 KX (Figure 7-21 and Figure 7-23). The use of low magnification and high magnification images enables the assessment of the influence of drying shrinkage on large pores and small pores. A comparison of oven-dried and cryo-SEM images of sister samples show that the microstructure of oven-dried

157

and wet mudrock samples is quite similar. The microstructure of wet and oven-dried samples is composed of silt inclusions randomly distributed in a matrix of clay minerals for both samples. Furthermore, two types of porosity can be observed in the wet and oven-dried samples: interP and intraP as discussed in Section 7.2 (Figure 7-21 and Figure 7-23). The shape, size, and orientation of these pores is similar in both samples and no differences can be readily identified. A clear difference between the wet and oven-dried samples is the formation of cracks in the clay matrix in the dried samples (Figure 7-20 and Figure 7-22). This kind of cracks is largely absent in the wet mudrock samples. The size of these cracks is approximately a few microns. It is worth mentioning that these cracks are different than the pores that form at the boundary of silt inclusions, which are present in both wet and oven-dried samples. The shape and location of these cracks suggest that they may have formed as a result of tension forces in the clay matrix.

The measured SEM imaging porosity of wet and oven-dried samples is similar (Figure 7-7). The slight differences in the imaging porosity values between the wet and oven-dried samples can be attributed to the loss of resolution that may occur during cryo-imaging of samples. Imaging under cryogenic conditions is very challenging, and it is usually hard to obtain consistent conditions for all samples. Nonetheless, these differences are very small and can be considered negligible. In addition to the imaging porosity, we calculated the pore size distributions (PSD) of the samples using the IOM method (see Chapter 5). These PSDs were calculated for the visible SEM porosity, which represents approximately 30% of the reference lab porosity as discussed in the previous section. The PSDs of the RGOM-EI-1 MPa sample show that for pores larger than 170 nm the oven-dried sample contain slightly larger pores than the wet sample, and for pores smaller than 170 nm, the oven-dried sample contain pores slightly smaller than the wet sample (Figure 7-24a). The difference between the two curves was calculated by subtracting the oven-dried percent-finer from the wet percent-finer at each pore diameter (Figure 7-24b). The difference curve shows two peaks at pore diameters of 605 nm and 100 nm. At 605 nm the oven-dried sample PSD is coarser by 6%, whereas at 100 nm the oven-dried PSD is finer by 2%. The PSDs of the RGOM-EI-6 MPa sample show that for pores larger than 160 nm the oven-dried sample contain slightly larger pores than the wet sample, and for pores smaller than 160 nm the oven-dried sample contain pores slightly smaller than the wet sample (Figure 7-25a). The difference curve shows two peaks at pore diameters of 450 nm and

95 nm (Figure 7-25b). At 450 nm the oven-dried sample PSD is coarser by 10%, whereas at 94 nm the oven-dried PSD is finer by 4%.

RBBC Mudrock Samples

The influence of drying shrinkage on the microstructure of RBBC mudrocks is investigated on two samples: RBBC-1 MPa, and RBBC-10 MPa. Figure 7-26 through Figure 7-29 show cryo- and oven dried SEM images of the two RBBC mudrock samples. These figures include two different magnifications of 12 KX (Figure 7-26 and Figure 7-28) and 30 KX (Figure 7-27 and Figure 7-29). A comparison of the oven-dried and cryo-SEM images of sister samples show that the microstructure of oven-dried and wet mudrock samples is similar. In general, the microstructures of the wet and oven-dried RBBC samples is similar for the RBBC-1 MPa sample, and slightly different for the RBBC-10 MPa sample. The microstructure of the wet and oven-dried samples is composed of silt inclusions randomly distributed in a matrix of clay minerals for both samples. Similar to RGOM-EI samples, interP and intraP pores were identified in the wet and oven-dried samples. The shape, size, and orientation of these pores is similar in both samples and no differences can be readily identified. Unlike the RGOM-EI samples, no cracks in the clay matrix could be identified in the oven-dried RBBC samples. In the case of the RBBC-10 MPa sample, the high magnification images reveal some differences between the oven-dried and the wet samples (Figure 7-29). The microstructure of the oven-dried sample is highly porous compared to that of the wet sample. The increase in porosity appears as an increase in the size of the interP pores and intraP pores. The clay aggregates in the oven-dried sample are more porous than those in the wet sample. This trend was confirmed by imaging another oven-dried RBBC-10 sample (not reported). This trend is not clear and requires further investigation keeping in mind that the drying shrinkage of RBBC samples at 10 MPa is zero, which means that these sample underwent zero volume changes (Figure 7-8).

The measured SEM imaging porosity of the wet and oven-dried samples is similar for the RBBC-1 MPa sample and very different for the RBBC-10 MPa sample (Figure 7-7). The behavior of the RBBC-10 MPa sample requires further investigation and is ignored in the following discussion. On the other hand, the slight differences in the imaging porosity between the wet and oven-dried RBBC-1 MPa sample can be attributed to the loss of resolution that may occur during cryo-imaging of samples. Imaging under cryogenic conditions is very challenging and it is usually hard to obtain consistent conditions for all samples. Nonetheless, these

159

differences are very small and can be considered negligible. The PSDs of the RBBC-1 MPa sample were calculated for the visible SEM porosity, which represents approximately 30% of the reference lab porosity as discussed in the previous section. The PSDs of the wet and oven-dried RBBC-1 MPa sample are almost identical (Figure 7-30a). The difference between the two curves was calculated by subtracting the oven-dried percent-finer from the wet percent-finer at each pore diameter (Figure 7-30b). The difference curve shows tow peaks at pore diameters of 700 nm and 90 nm. At 700 nm the oven-dried sample PSD is coarser by 3%, whereas at 90 nm the PSD of the oven-dried sample is finer by 2%.

7.5.2 Sub-35nm Porosity

This section addresses the influence of drying shrinkage on the sub-35nm porosity, which constitutes approximately 70% of the reference lab porosity of mudrocks. Section 7.4.3 described the method we used in this investigation to back-calculate the sub-35nm porosity using a combination of SEM imaging porosity and reference lab porosity (Figure 7-19). Two types of sub-35nm porosity were calculated: wet sub-35nm porosity and oven-dried sub-35nm porosity. In the next paragraphs, we compare the wet and oven-dried sub-35nm porosity to assess the influence of drying shrinkage on the pores smaller than 35 nm.

The oven-dried sub-35nm porosity of the oven-dried RGOM-EI samples is almost constant and ranges from 0.22 to 0.25 (Figure 7-19a). The wet sub-35nm porosity ranges from 0.59 at 1 MPa to 0.38 at 6 MPa. These results show that as RGOM-EI samples are oven-dried, the porosity smaller than 35 nm shrinks from 0.59 to 0.22 at 1 MPa and from 0.38 to 0.24 at 6 MPa. On the other hand, the oven-dried sub-35nm porosity of the oven-dried RBBC samples ranges from 0.32 to 0.40 (Figure 7-19b). The results of the RBBC-10 MPa sample are excluded from this discussion as more results are need to understand the behavior of this sample. The wet sub-35nm porosity of the RBBC-1 MPa sample is 0.58. Similar to the RGOM-EI samples, these results show that as RBBC samples are oven-dried, the porosity smaller than 35 nm shrinks from 0.58 to 0.40 at 1 MPa.

7.5.3 Evolution of the Pore Space during Shrinkage

The above sections descried the influence of shrinkage in terms of the measured porosity values. To understand the influence of drying shrinkage on the evolution of the different pore sizes, the above results are presented in terms of the void ratio. The void ratio normalizes the

160

volume of pores relative to the volume of solids, which does not change as samples undergo drying shrinkage. It is worth mentioning that the porosity is calculated relative to the total volume of the sample, which changes as the sample undergo drying shrinkage. Therefore, void ratio values emphasize the changes in different pore sizes as the sample volume changes. The evolution of the pore space is discussed in terms of the two pore families identified in this investigation: SEM pores (>35 nm) and the sub-35nm pores (<35 nm).

The evolution of the pore space for the RGOM-EI samples and the RBBC sample is presented in Figure 7-31 and Figure 7-32, respectively. The SEM pores (>35 nm) of the RGOM-EI 1 MPa sample shrink by 28%, while the syb-35nm pores (<35 nm) shrink by 71% (Figure 7-31a). The SEM pores of the RGOM-EI 6 MPa sample shrink by 14%, while the sub-35nm pores shrink by 48% (Figure 7-31b). On the other hand, the SEM pores of the RBBC 1 MPa sample shrink by 11%, while the sub-35nm pores shrink by 33%. These results show that the volume of SEM pores, as well as the volume of sub-35nm pores shrink as mudrocks undergo drying shrinkage. The shrinkage is more significant in the sub-35nm pores in both samples. This trend can be explained by the high surface tension forces that develop in these pores due to drying.

7.5.4 Discussion of the Influence of Drying on the Microstructure of Mudrocks

As discussed in Chapter 2, two techniques were utilized in the literature to address the influence of drying shrinkage on the microstructure of soils and mudrocks: SEM and MIP. These techniques provided contradictory conclusions about the influence of shrinkage on the microstructure of mudrocks. While the SEM studies showed that there is no difference in the visible SEM porosity, MIP studies reported that large pores in the range of visible SEM porosity collapse upon drying.

The SEM studies used mainly plunge freezing and freeze drying to preserve the microstructure of samples. These studies provided a qualitative comparison between dried samples and freeze-dried samples and concluded that drying does not change the microstructure of mudrocks. These studies discussed only the influence of drying on the visible SEM pores, and ignored the pore space below the resolution of SEM. Furthermore, these studies failed to explain the source of volume changes due to drying shrinkage. In this investigation, we provided both a qualitative and a quantitative assessment of the influence of drying shrinkage on the

161

microstructure of mudrocks. The pore space of mudrocks was divided into two categories: visible SEM porosity (>35 nm) and sub-35nm porosity (<35nm). The influence of drying shrinkage on the visible SEM porosity was found to be minimal. The calculated wet and oven-dried SEM porosity values were very similar. One the other hand, the sub-35nm porosity collapses to a constant value upon drying. The porosity values do not reveal pore evolution trends. Instead, the void ratio is used as the volume of pores is normalized relative to the solid phase, which does not change upon drying. The SEM pores and the sub-35nm pores undergo shrinkage as mudrocks are oven-dried. The shrinkage in the sub-35nm pores is more significant than that in the SEM pores. Contrary to the current understanding in the literature, these results show that the observed macroscopic shrinkage has two components: shrinkage in the sub-35nm pores, as well as shrinkage in the visible SEM pores.

On the other hand, MIP studies assumed that plunge freezing and freeze drying preserves the microstructure of mudrocks. These methods were used as a reference against which oven-dried samples were compared. All of the MIP studies concluded that oven drying and air drying cause a dramatic reduction in pore volume, and that the reduction in pore volume results from the collapse of large pores, with small pores remain unchanged (see Chapter 2). The definition of large pores and small pores differed from one study to another. In general, large pores usually refer to interP pores while small pores refer to intraP pores or pores between clay particles. These conclusions contradict our results, which showed that both the SEM pores and sub-35nm pores shrink. Furthermore, the majority of shrinkage occurs in the sub-35nm pores. The use of cryo and conventional SEM in this investigation provided a visual evidence of the influence of drying on the microstructure of mudrocks. Furthermore, the qualitative comparison of the cryo and oven-dried SEM images matched the quantitative analysis performed on approximately 60 images. In addition, MIP does not provide accurate pore size distribution information about materials due to the lack of pore accessibility to mercury (Diamond, 2000). Diamond (2000) stated that the MIP method does not provide accurate pore size distribution information about cement pastes due to the lack of accessibility of most of the pore space to mercury. Therefore, we conclude that the previous understanding of the influence of drying shrinkage on the microstructure of soils and mudrocks is an artifact of the MIP method. Instead, the results of this investigation, which provided visual and quantitative assessment of the influence of drying should be adopted.

7.6 Influence of the Consolidation Stress on the Microstructure

This section addresses the influence of the consolidation stress on both the visible SEM porosity (>35nm) and the sub-35nm porosity, which is mainly associated with clay minerals as shown above. The consolidation stress is the maximum effective stress that the mudrock samples have been subjected to during the resedimentation technique (see Chapter 4).

7.6.1 Visible SEM Porosity

Section 7.5.1 showed that the wet and oven-dried imaging porosity values are almost the same. Therefore, we use the oven-dried samples to investigate the influence of the applied consolidation stress on the visible SEM porosity of mudrocks. A comparison of the SEM images acquired for samples consolidated at different stresses provide a qualitative understanding of the influence of consolidation stress on the visible SEM porosity. On the other hand, a comparison of the porosity values and pore size distributions, obtained using the IOM method of mudrock samples subjected to different consolidation stresses provides a quantitative understanding of the influence of the consolidation stress on the visible SEM porosity.

RGOM-EI Mudrock Samples

The microstructure of oven-dried RGOM-EI samples was described in Section 7.2.1, and is presented in Figure 7-1and Figure 7-2. The development of visible SEM porosity as a function of consolidation stress will be described in terms of the two types of pores described in Section 7.2.1: inter-particle pores (interP), and intra-particle pores (intraP). The low magnification SEM images shown in Figure 7-1 does not reveal striking differences in the microstructure of RGOM-EI mudrocks as the consolidation stress increases. The microstructure of RGOM-EI mudrocks at high consolidation stresses appears slightly less porous than that of samples at low consolidation stresses. In particular, fewer large interP pores can be observed in samples at 6 MPa and 10 MPa than samples at 0.2 MPa and 1 MPa (Figure 7-1). The high magnification images shown in Figure 7-2 clearly show the difference as a function of the consolidation stress. The samples consolidated at stresses of 6 MPa and 10 MPa contain fewer and smaller interP pores than the samples consolidated at 0.2 MPa and 1 MPa. Furthermore, the clay aggregates appear to be less porous at high stresses. This trend is very obvious in the high magnification images presented in Figure 7-33. These images show that as stress increases from 0.2 MPa to 1 MPa the loss in the

intraP pores is negligible (Figure 7-33a, b). As stress increases to 6 MPa and 10 MPa, the loss in the intraP pores becomes clear as shown by the less-porous clay aggregates (Figure 7-33c, d).

The measured SEM imaging porosity of the oven-dried RGOM-EI samples ranges from 0.16 to 0.10 (Figure 7-7). These results are consistent with the observed trend in the SEM images, which shows that the increase in consolidation stress leads to the compression of the interP and intraP pores. In addition to the imaging porosity, we calculated the pore size distributions (PSD) of the oven-dried RGOM-EI samples using the IOM method (see Chapter 5). These PSDs were calculated for the visible SEM porosity, which represents approximately 30% of the reference lab porosity as discussed above (Figure 7-34). As the consolidation stress increases to 6 MPa, the PSDs of the oven-dried RGOM-EI samples become finer. This trend does not hold at 10 MPa, and the pore size distribution becomes coarser. This behavior contradicts the observations from SEM images which showed the loss of intraP and interP pores as stress increases. Keeping in mind the high magnification images in Figure 7-33, which showed the significant loss in the intraP pores, the PSD trend at 10 MPa could be explained by the fact that as the stress increases to 10 MPa most intraP pores are compressed below the resolution of SEM, and the rate of compression of the intraP pores is higher than the rate of compression of the interP pores. In other words, at high stresses the friction resistance between particles increases, which leads to the reduction in the collapse of interP pores. At the same time, the collapse of intraP pores is independent of friction resistance and is a function of the electrostatic double layer forces. Despite the PSD curve at 10 MPa, the SEM images and the PSD calculations show that as stress increases both interP and intraP pores are compressed. Furthermore, the difference between the PSDs is relatively small. For example, the pore diameter corresponding to a percent finer than 50%, D_{50}, is approximately 350 nm at 0.2 MPa and 280 nm at 6 MPa

RBBC Mudrock Samples

The microstructure of oven-dried RBBC samples was described in Section 7.2.2, and is presented in Figure 7-3 and Figure 7-4. The development of the visible SEM porosity as a function of the consolidation stress will be described in terms of the interP and the intraP pores. The low magnification SEM images presented in Figure 7-3 show a clear loss in porosity as stress increases. In particular, the size and amount of interP pores decrease with stress. This trend is also obvious in the high magnification images presented in Figure 7-4. In addition, the intraP

pores decrease slightly as stress increases. The decreases in the intraP pores in RBBC mudrocks is less significant than that of RGOM-EI samples.

The measured SEM imaging porosity of the oven-dried RGOM-EI samples ranges from 0.24 to 0.11 (Figure 7-8). These results are consistent with the observed trend in the SEM images, which shows that the increase in consolidation stress leads to a significant reduction in the porosity as shown by the loss in the interP pores and to a less extent the intraP pores. In addition to the imaging porosity, we calculated the PSD of the oven-dried RBBC samples using the IOM method (see Chapter 5). These PSDs were calculated for the visible SEM porosity, which represents approximately 30% of the reference lab porosity as discussed above (Figure 7-35). As the consolidation stress increases to 20 MPa, the PSDs of oven-dried RBBC samples become finer. As discussed above, the behavior of the RBBC-10 MPa sample requires more tests and therefore will not be discussed here. The difference between the PSD curves is significant. For example, the pore diameter corresponding to a percent finer than 50%, D_{50}, is approximately 500 nm at 0.2 MPa and 180 nm at 20 MPa.

7.6.2 Sub-35nm Porosity

The calculations of the sub-35nm porosity was explained in detail in Section 77.4.3. Two types of sub-35nm porosity values were calculated: oven-dried and wet sub-35nm porosity. Our results showed that the drying shrinkage collapses the sub-35nm porosity to approximately a constant value. Therefore, the wet sub-35nm porosity will be used to evaluate the influence of the consolidation stress because it represents the in-situ state of the mudrock samples. Figure 7-19 shows that two wet sub-35nm porosity values were calculated for both RGOM-EI and RBBC samples. This is because we were only able to cryo-image two RGOM-EI and RBBC samples. Furthermore, Section 7.5.1 showed that the wet SEM imaging porosity is equal to the oven-dried SEM imaging porosity. These results mean that we can use the oven-dried SEM porosity to obtain the wet sub-35nm porosity. This task can be achieved by comparing the oven-dried imaging porosity to the wet lab porosity to calculate the wet sub-35nm porosity (see Section 7.4.3). This approach was used to calculate the wet-sub35nm porosity of the RGOM-EI samples and the RBBC samples. Figure 7-36 presents the wet sub-35nm porosity as a function of the consolidation stress. In this figure, the red points represent the wet sub-35nm porosity values that were calculated using the oven-dried SEM porosity, while the light-blue points represent the

sub-35nm porosity values that were calculated using the wet SEM imaging porosity. The wet sub-35nm porosity of RGOM-EI samples decreases from approximately 0.67 at 0.2 MPa to 0.4 at 10 MPa (Figure 7-36). On the other hand, the wet sub35nm of RBBC samples decreases from approximately 0.67 at 0.2 MPa to 0.38 at 20 MPa. These results show that the influence of the consolidation stress on the sub-35nm porosity is significant.

7.6.3 Evolution of the Pore Space as a Function of the Consolidation Stress

Similar to the drying shrinkage, the void ratio of the different pore sizes is used to investigate the evolution of the pore space as a function of the consolidation stress. Unlike the porosity, the void ratio normalizes the volume of pores relative to the volume of solids, which does not change during compression. The evolution of the pore space is discussed in terms of the two pore families identified in this investigation: SEM pores (>35 nm) and the sub-35nm pores (<35 nm).

The evolution of the pore space as a function of the consolidation stress is presented in Figure 7-37. The void ratio of the two pore sizes of the RGOM-EI mudrocks decreases as the consolidation stress increases (Figure 7-37a). The void ratio of the SEM pores decreases from 0.4 at 0.2 MPa to 0.15 at 10 MPa, while the void ratio of the sub-35nm pores decreases from 1 at 0.2 MPa to 0.4 at 10 MPa. Similarly, the void ratio of the two pore sizes of the RBBC mudrock samples decreases as the consolidation stress increases (Figure 7-37b). The void ratio of the SEM pores decreases from 0.50 at 0.2 MPa to 0.15 at 20 MPa, while the void ratio of the sub-35nm pores decreases from 0.55 at 0.2 MPa to 0.25 at 20 MPa. Contrary to the current understanding in the literature, these results show that the compression of the pore space has two components: the SEM pores (>35 nm) and the sub-35nm pores (<35 nm). Furthermore, while the void ratio of the SEM pores is comparable for RGOM-EI and RBBC mudrocks, the void ratio of the sub-35nm pores of the RGOM-EI mudrocks is significantly higher than that of the RBBC mudrocks. This trend is attributed to the difference in the mineralogy of the two mudrocks.

7.6.4 Discussion of the Influence of the Consolidation Stress

As discussed in Chapter 2, the studies that addressed the influence of the consolidation stress on the microstructure of mudrocks utilized MIP as the main technique to describe the evolution of the pore space. The MIP measurements were performed on freeze-dried samples, and the authors assumed that freeze drying preserves the microstructure of mudrock samples. Furthermore, all of

these studies showed that an increase in the applied stress leads to the collapse of large macro pores, with very little to no effect on the small micro pores. The separation between macro and micro pores differed from one study to another. In general, macro pores refer to interP pores while micro pores refer to intraP pores. The conclusions in this investigation differed significantly from those in the literature.

The influence of the consolidation stress was discussed in terms of visible SEM pores and the sub-35nm pores. The wet sub-35nm pores was used because it represents the in-situ state of the material. Our results showed that as the consolidation stress increases, both the interP and intraP pores are compressed for both RGOM-EI and RBBC mudrocks. The compression of the intraP pores in the RGOM-EI samples is more significant than that of the RRBC samples at high stresses. The compression of the visible SEM pores and the sub-35nm pores is simultaneous. In the other words, the decrease of the void ratio at each stress increment consists of two components: a decrease in the void ratio of the visible SEM pores and a decrease in the void ratio of the sub-35nm pores. These conclusions are significantly different than those published in the literature (see Chapter 2). Similar to the studies that addressed the influence of drying shrinkage on the microstructure, the studies that addressed that influence of the consolidation stress utilized MIP. As discussed in Section 7.5.4, MIP does not provide accurate pore size information about materials. Therefore, we conclude that the conclusions about the influence of the consolidation stress in the literature are an artifact of MIP. Instead, the results of this study should be adopted as they provide both visual and quantitative evidence about the influence of the consolidation stress on the microstructure.

Table 7-1: Summary of the testing program performed in this thesis to characterize the pore space of resedimented mudrock samples.

Sample Name	Maximum Resedimentation Stress [MPa]	Macroscopic Porosity	MIP	Oven-Dried SEM Imaging	Cryo-SEM Imaging
RGOM-EI Samples					
RGOM-EI-0.1	0.1		✓		
RGOM-EI-0.2	0.2	✓		✓	✓
RGOM-EI-1	1	✓		✓	✓
RGOM-EI-6	6	✓		✓	
RGOM-EI-8			✓		
RGOM-EI-10	10	✓		✓	
RGOM-EI-21			✓		
RGOM-EI-33	30	✓			
RGOM-EI-40	40	✓			
RGOM-EI-65	65	✓			
RBBC Samples					
RBBC-0.1	0.1		✓		
RBBC-0.2	0.2	✓		✓	✓
RBBC-1	1	✓	✓	✓	✓
RBBC-10	10	✓	✓	✓	
RBBC-20	20	✓		✓	
RBBC-30	30	✓			
RBBC-40	40	✓			
RBBC-100	100	✓			

Table 7-2: Summary of the wet and oven-dried macroscopic lab porosity results.

Sample	Maximum Resedimentation Stress [MPa]	Wet Lab Porosity	Oven-dried Lab Porosity	MIP · Porosity
RGOM-EI				
RGOM-EI-0.1	0.1			0.255
RGOM-EI-0.2	0.2	0.576	0.297	
RGOM-EI-1	1	0.482	0.276	
RGOM-EI-6	6	0.363	0.260	
RGOM-EI-8	8			0.255
RGOM-EI-10	10	0.351	0.257	
RGOM-EI-21	21			0.203
RGOM-EI-33	30	0.306	0.220	
RGOM-EI-40	40	0.296	0.218	
RGOM-EI-65	65	0.275	0.212	
RBBC				
RBBC-0.1	0.1			0.414
RBBC-0.2	0.2	0.510	0.400	
RBBC-1	1	0.448	0.376	0.385
RBBC-10	10	0.340	0.326	0.373
RBBC-20	20	0.286	0.317	
RBBC-30	30	0.265	0.294	
RBBC-40	40	0.254	0.261	
RBBC-100	100	0.213	0.229	

Table 7-3: Number of SEM images at each magnification used to represent the pore space of oven-dried mudrock samples. These images were used to calculate the final porosity using the IOM method

Sample	Mag 1	Mag 2	Mag 3
RGOM-EI-0.2	20	22	20
RGOM-EI-1	24	22	23
RGOM-EI-6	35	22	24
RGOM-EI-10	21	19	20
RBBC-0.2	27	22	18
RBBC-1	22	24	22
RBBC-10	23	21	22
RBBC-20	23	23	23

Table 7-4: Summary of oven-dried imaging porosity values for RGOM-EI mudrock samples obtained using the Integration of Magnifications (IOM) method.

Sample	Mag 1		Mag 2		Mag 3		Final	
	μ	se	μ	se	μ	se	μ	se
RGOM-EI-0.2	0.046	0.002	0.075	0.002	0.045	0.001	0.160	0.003
RGOM-EI-1	0.041	0.002	0.070	0.002	0.028	0.002	0.136	0.003
RGOM-EI-6	0.037	0.001	0.051	0.003	0.018	0.002	0.104	0.004
RGOM-EI-10	0.026	0.001	0.053	0.003	0.022	0.002	0.099	0.004

Table 7-5: Summary of oven-dried imaging porosity values for RBBC mudrock samples obtained using the Integration of Magnifications (IOM) method.

Sample	Mag 1		Mag 2		Mag 3		Final	
	μ	se	μ	se	μ	se	μ	se
RBBC-0.2	0.043	0.002	0.117	0.002	0.097	0.003	0.241	0.004
RBBC-1	0.042	0.001	0.086	0.002	0.038	0.002	0.162	0.003
RBBC-10	0.061	0.003	0.104	0.003	0.043	0.002	0.201	0.005
RBBC-20	0.046	0.003	0.055	0.005	0.005	0.001	0.105	0.005

Table 7-6: Number of cryo-SEM images at each magnification used to represent the pore space of wet mudrock samples. These imaging were used to calculate the final cryo-imaging porosity using the IOM method

Sample	Mag 1	Mag 2	Mag 3
RGOM-EI-0.2 Cryo	12	8	2
RGOM-EI-1 Cryo	15	15	14
RGOM-EI-6 Cryo	17	17	16
RBBC-1 Cryo	27	27	24
RBBC-10 Cryo	32	26	26

Table 7-7: Summary of cryo-imaging porosity results of wet RGOM-EI mudrock samples obtained using the IOM method.

Sample	Mag 1		Mag 2		Mag 3		Final	
	μ	se	μ	se	μ	se	μ	se
RGOM-EI-1 Cryo	0.032	0.002	0.062	0.003	0.016	0.002	0.108	0.004
RGOM-EI-6 Cryo	0.041	0.004	0.070	0.002	0.010	0.002	0.119	0.005

Table 7-8: Summary of cryo-imaging porosity results of wet RBBC mudrock samples obtained using IOM method.

Sample	Mag 1		Mag 2		Mag 3		Final	
	μ	se	μ	se	μ	se	μ	se
RBBC-1 Cryo	0.035	0.002	0.073	0.001	0.028	0.002	0.133	0.003
RBBC-10 Cryo	0.023	0.001	0.057	0.002	0.009	0.001	0.088	0.002

Table 7-9: Oven-dried and wet sub-35nm porosity results for RGOM-EI and RBBC mudrock samples. These results were calculated using the IOM method

Sample	Maximum Effective Stress [MPa]	Oven-dried Sub-35nm Porosity	Wet Sub-35nm Porosity
RGOM-EI-0.2	0.2	0.222	
RGOM-EI-1	1	0.221	0.585
RGOM-EI-6	6	0.245	0.378
RGOM-EI-10	10	0.249	
RBBC-0.2	0.2	0.316	
RBBC-1	1	0.399	0.577
RBBC-10	10	0.233	0.425
RBBC-20	20	0.381	

Figure 7-1: SEM images of oven-dried RGOM-EI samples at different resedimentation stresses: a) 0.2 MPa, b) 1 MPa, c) 6 MPa, and d) 10 MPa. The images were acquired at a magnification 6 KX.
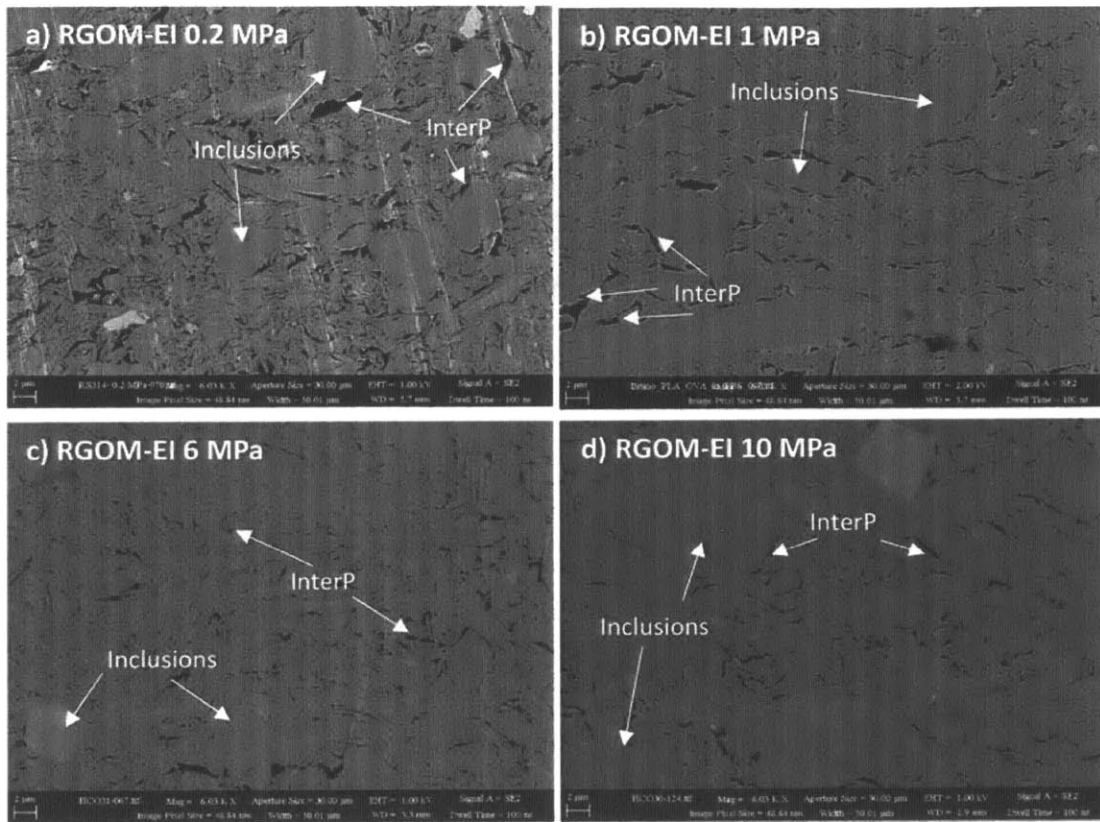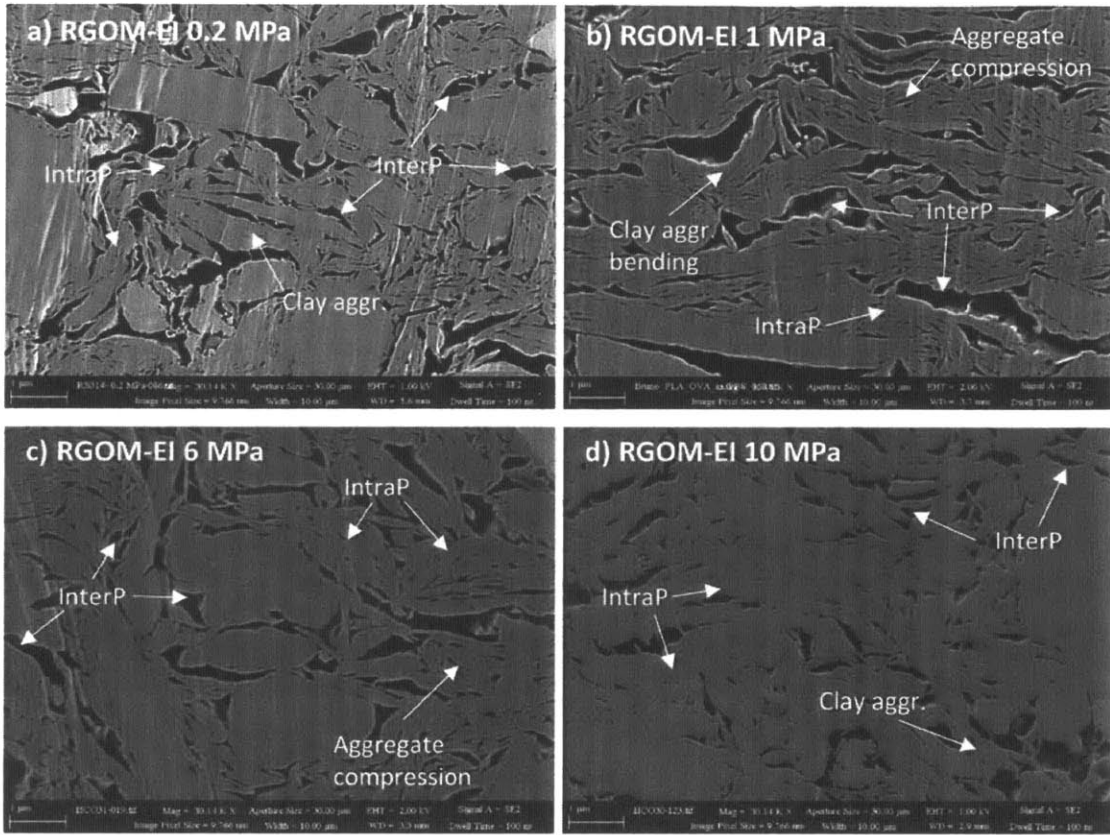
Figure 7-2: SEM images of oven-dried RGOM-EI samples at different resedimentation stresses: a) 0.2 MPa, b) 1 MPa, c) 6 MPa, and d) 10 MPa. The images were acquired at a magnification 30 KX.

Figure 7-3: SEM images of oven-dried RBBC samples at different resedimentation stresses: a) 0.2 MPa, b) 1 MPa, c) 10 MPa, and d) 20 MPa. The images were acquired at a magnification 6 KX.

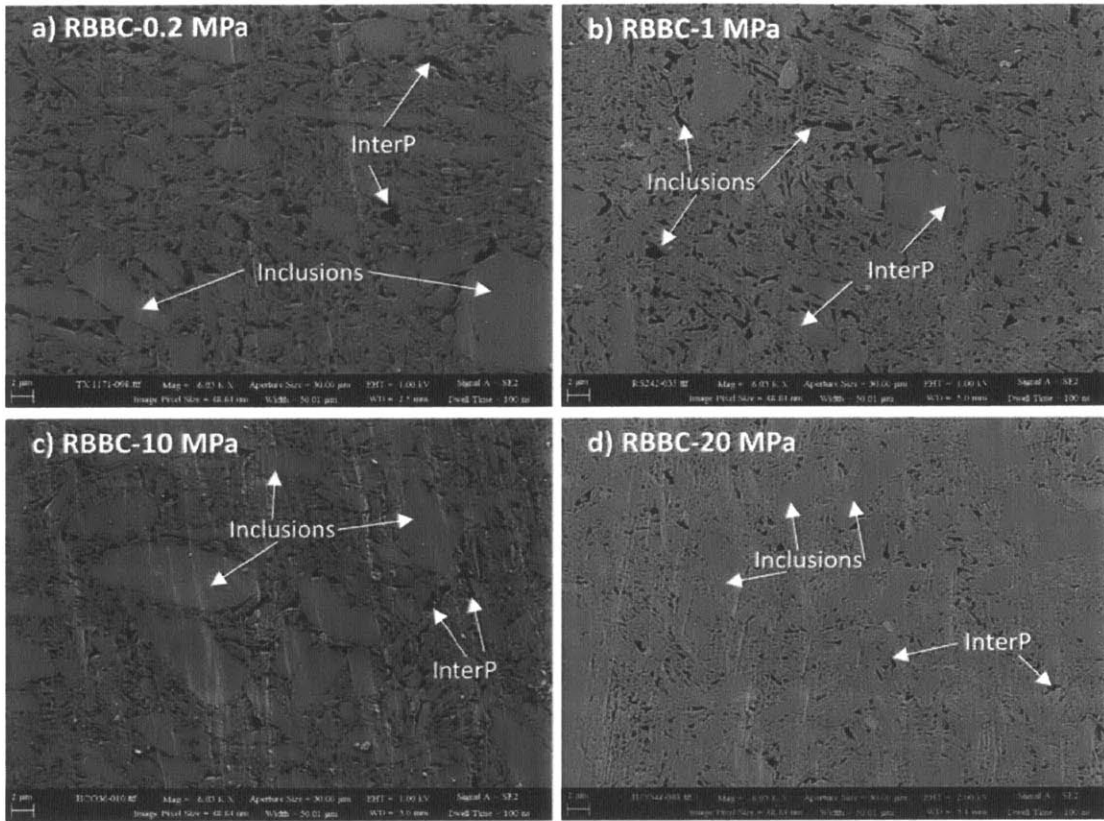Figure 7-4: SEM images of oven-dried RBBC samples at different resedimentation stresses: a) 0.2 MPa, b) 1 MPa, c) 10 MPa, and d) 20 MPa. The images were acquired at a magnification 30 KX.
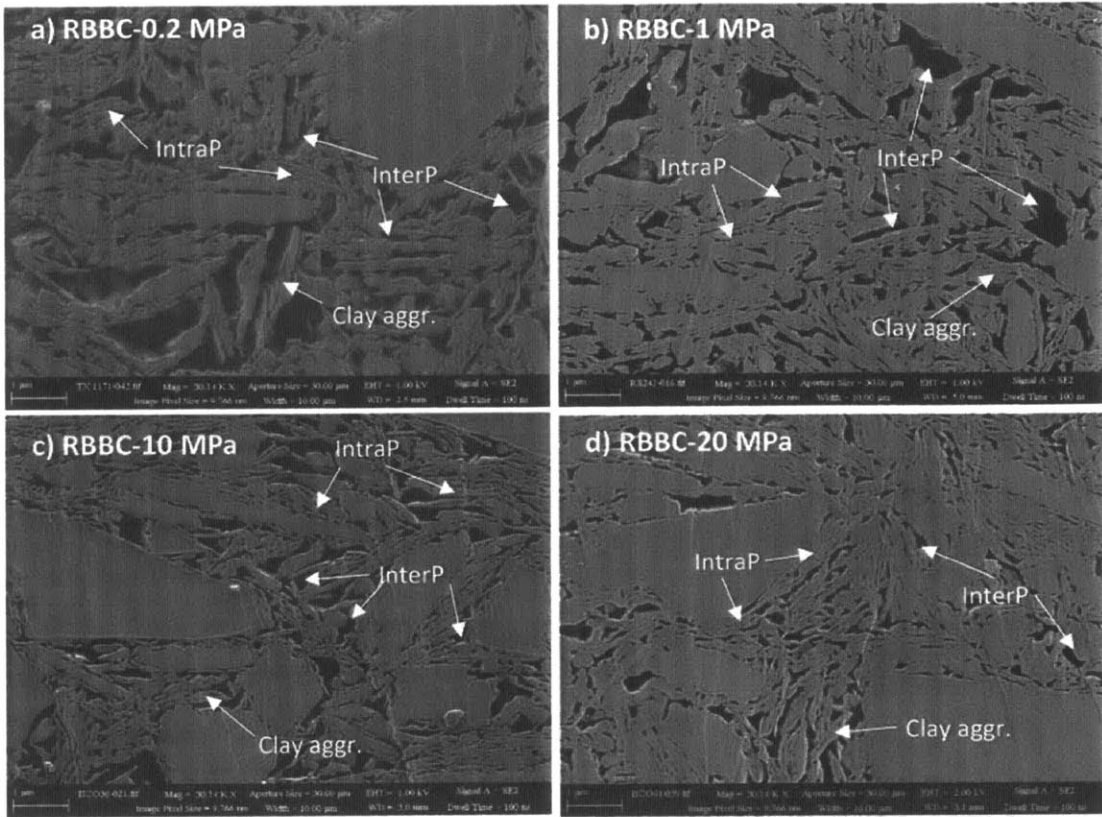
Figure 7-5: Cryo-SEM images of wet RGOM-EI samples at different resedimentation stresses: a, b) 1 MPa, b) and c, d) 6 MPa.

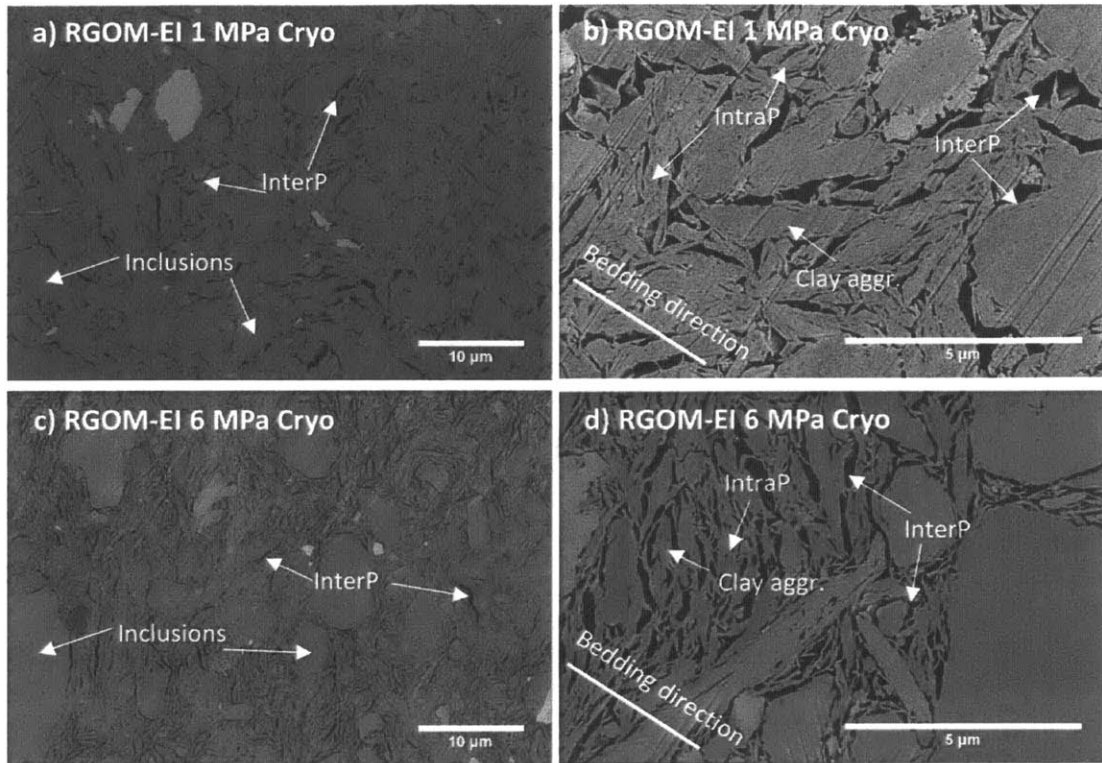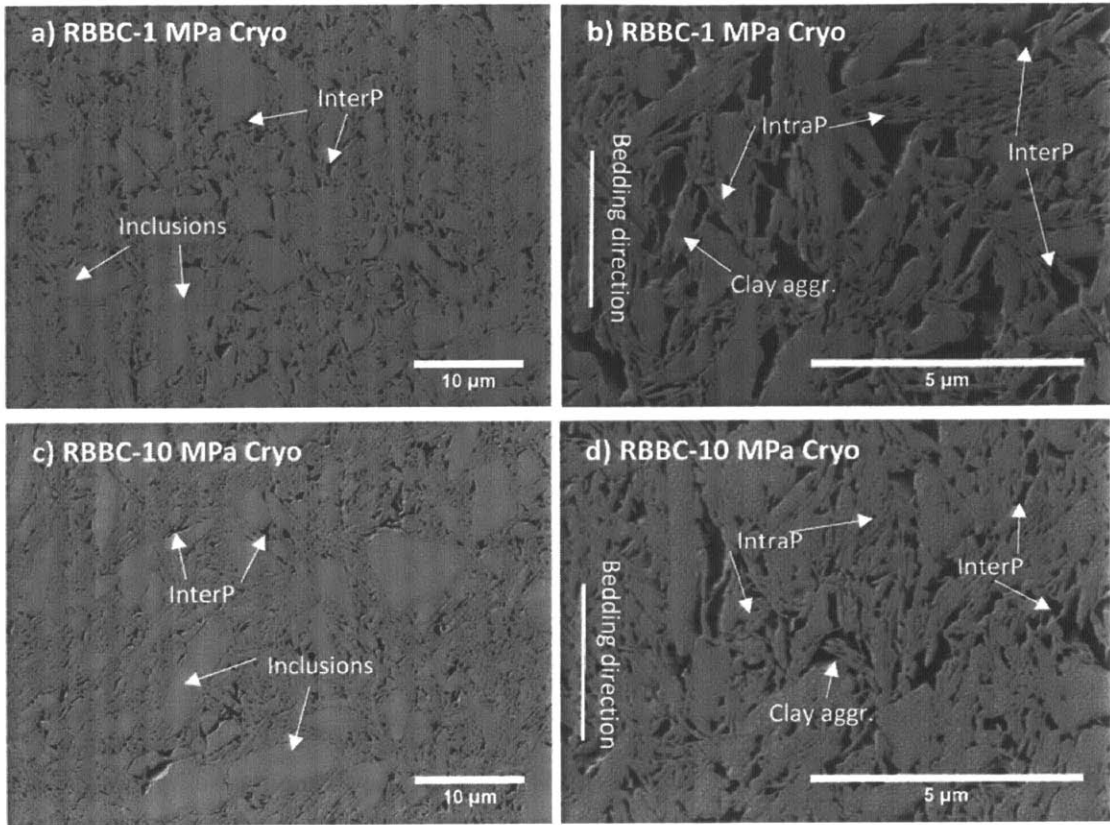Figure 7-6: Cryo-SEM images of wet RBBC samples at different resedimentation stresses: a, b) 1 MPa, b) and c, d) 10 MPa.
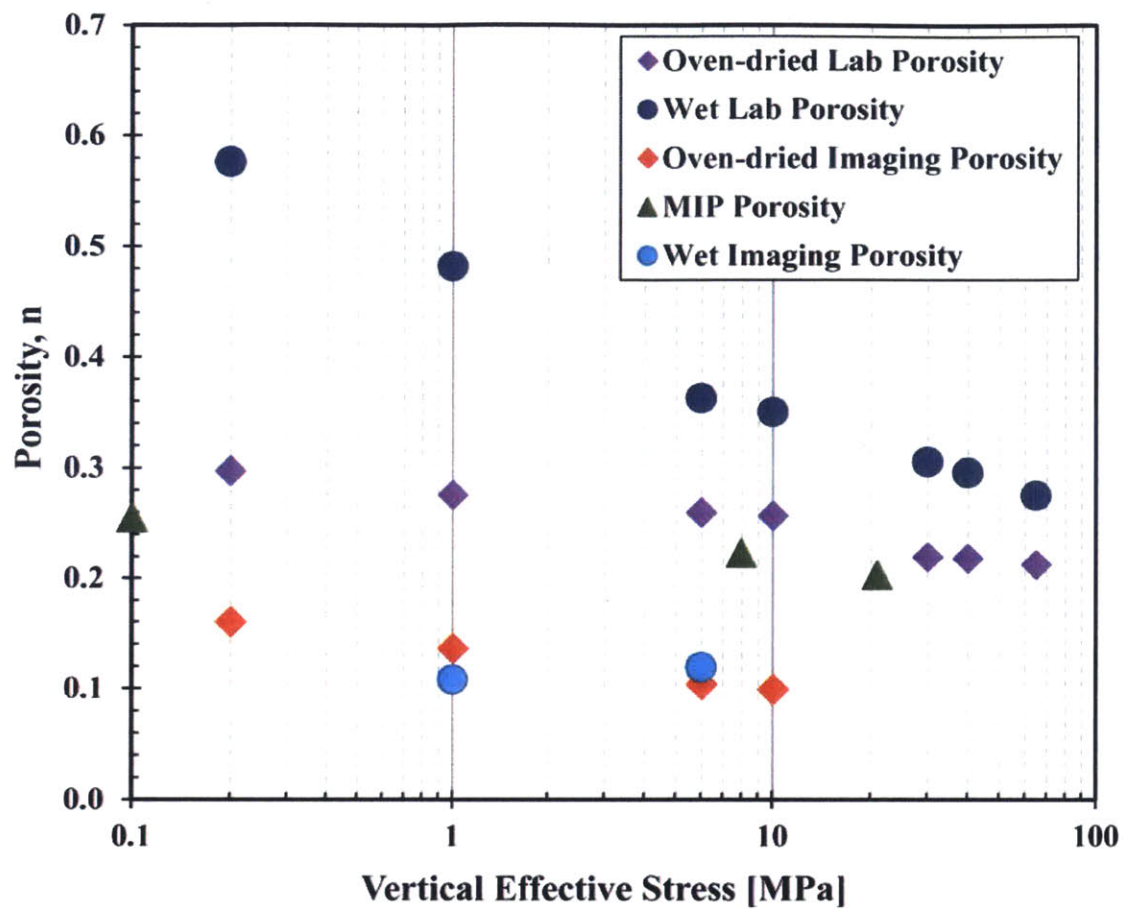
Figure 7-7: Summary of Porosity measurements performed in this study of RGOM-EI mudrock samples as a function of vertical effective stress. The porosity measurements include wet and oven-dried lab porosity, and wet and oven-dried imaging porosity
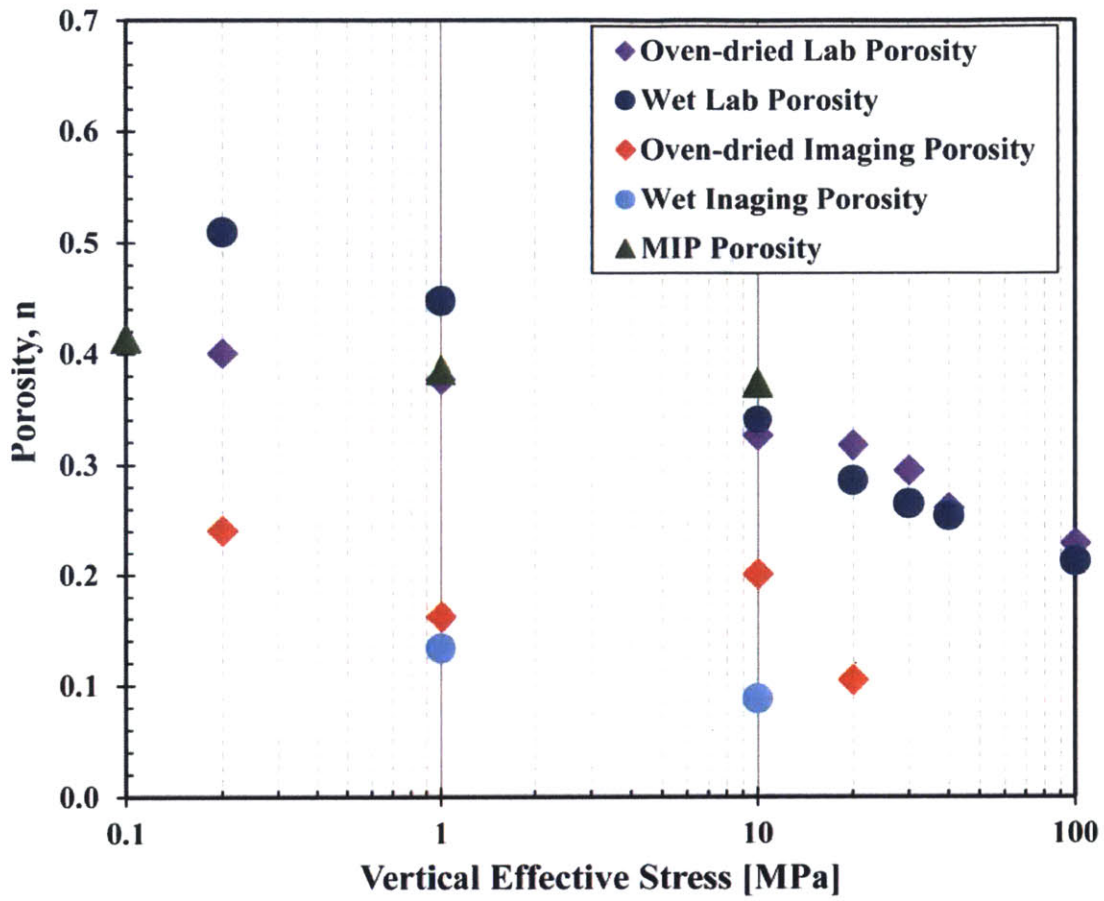
Figure 7-8: Summary of Porosity measurements performed in this study of RBBC mudrock samples as a function of vertical effective stress. The porosity measurements include wet and oven-dried lab porosity, and wet and oven-dried imaging porosity

Figure 7-9: a) Oven-dried porosity values for RGOM-EI mudrock samples obtained using the IOM method. The error bars represent the 95% confidence interval obtained using the standard error of the mean. b) The coefficient of variation of the porosity values at different magnifications used in the IOM method (bottom). The coefficient of variation was calculated as the standard error divided by the porosity at each magnification. The porosity and the standard error values for different magnifications are summarized in Table 7-5 Table 7-4
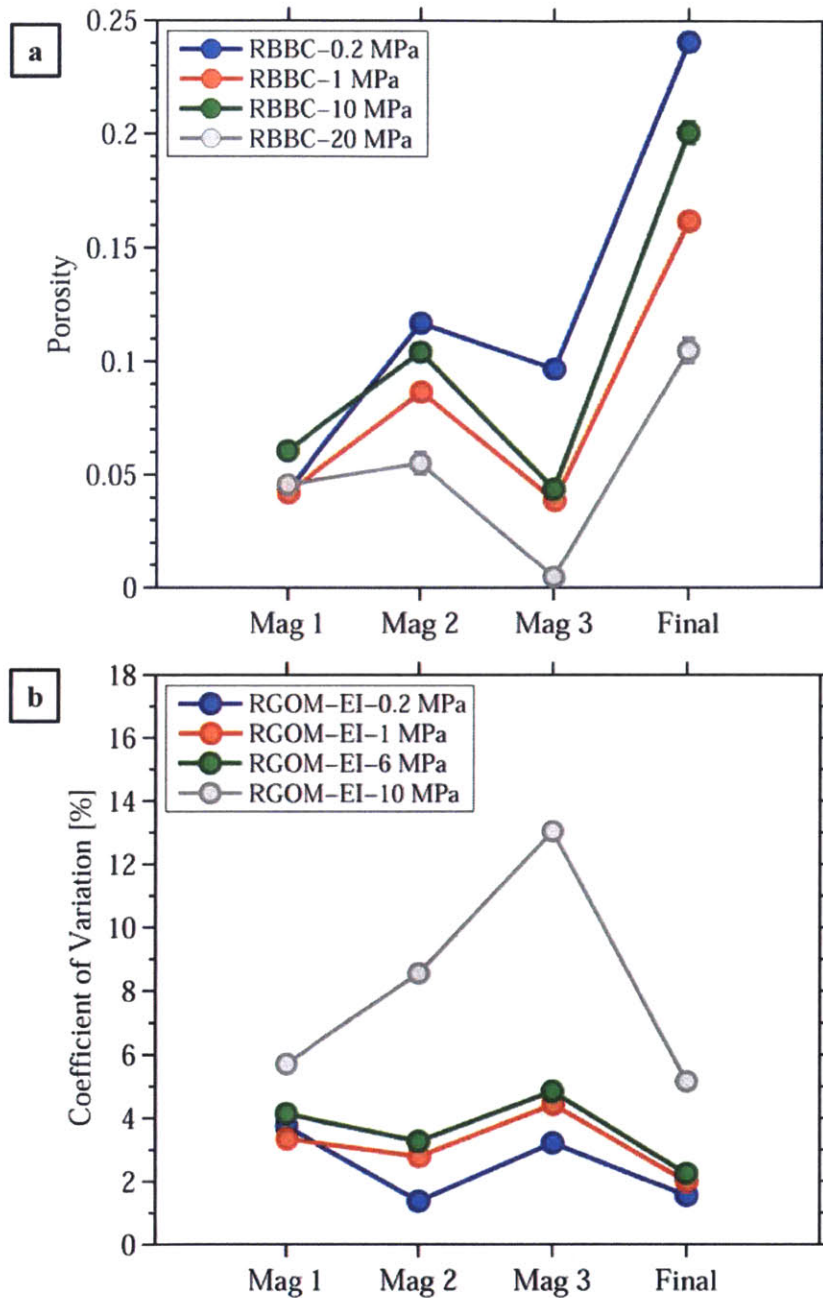
Figure 7-10: a) Oven-dried porosity values for RBBC mudrock samples obtained using the IOM method. The error bars represent the 95% confidence interval obtained using the standard error of the mean. b) The coefficient of variation of the porosity values at different magnifications used in the IOM method (bottom). The coefficient of variation was calculated as the standard error divided by the porosity at each magnification. The porosity and the standard error values for different magnifications are summarized in Table 7-4
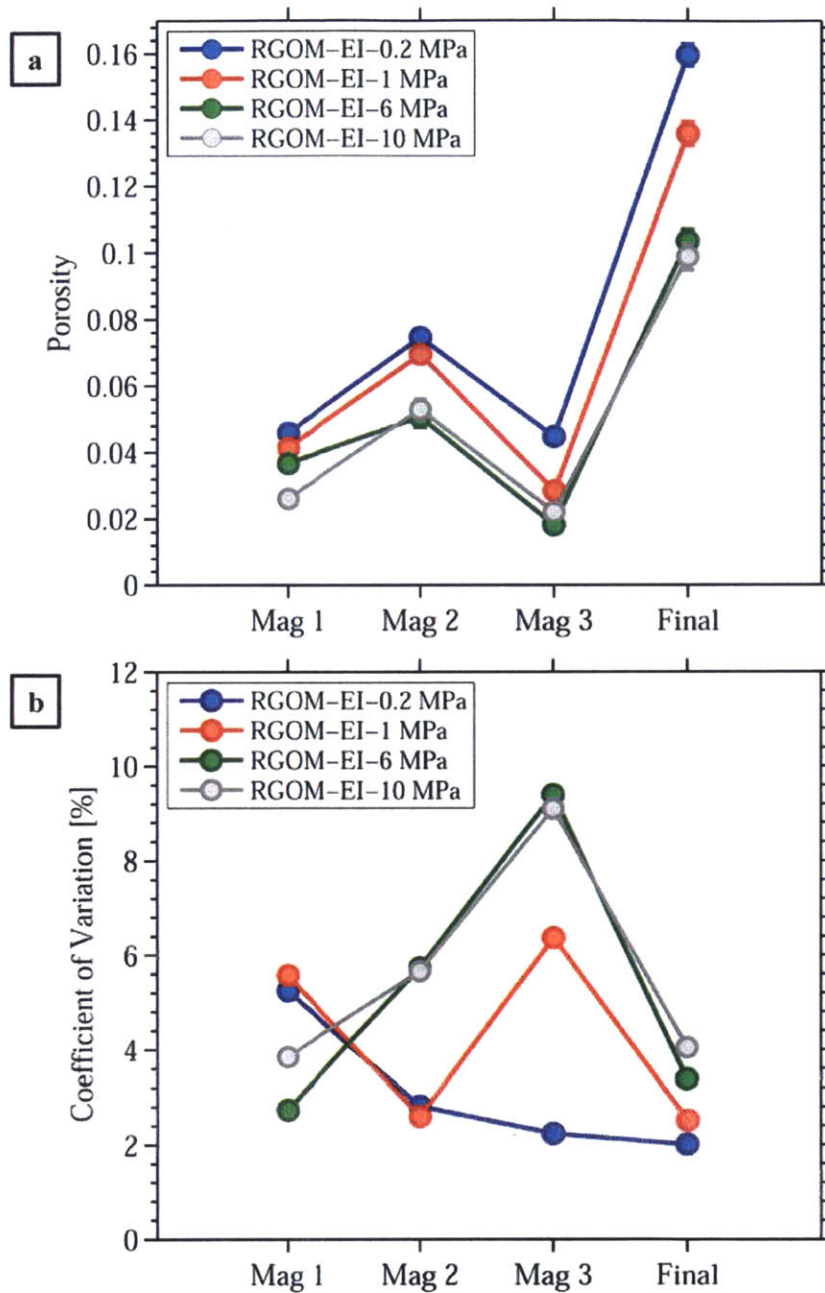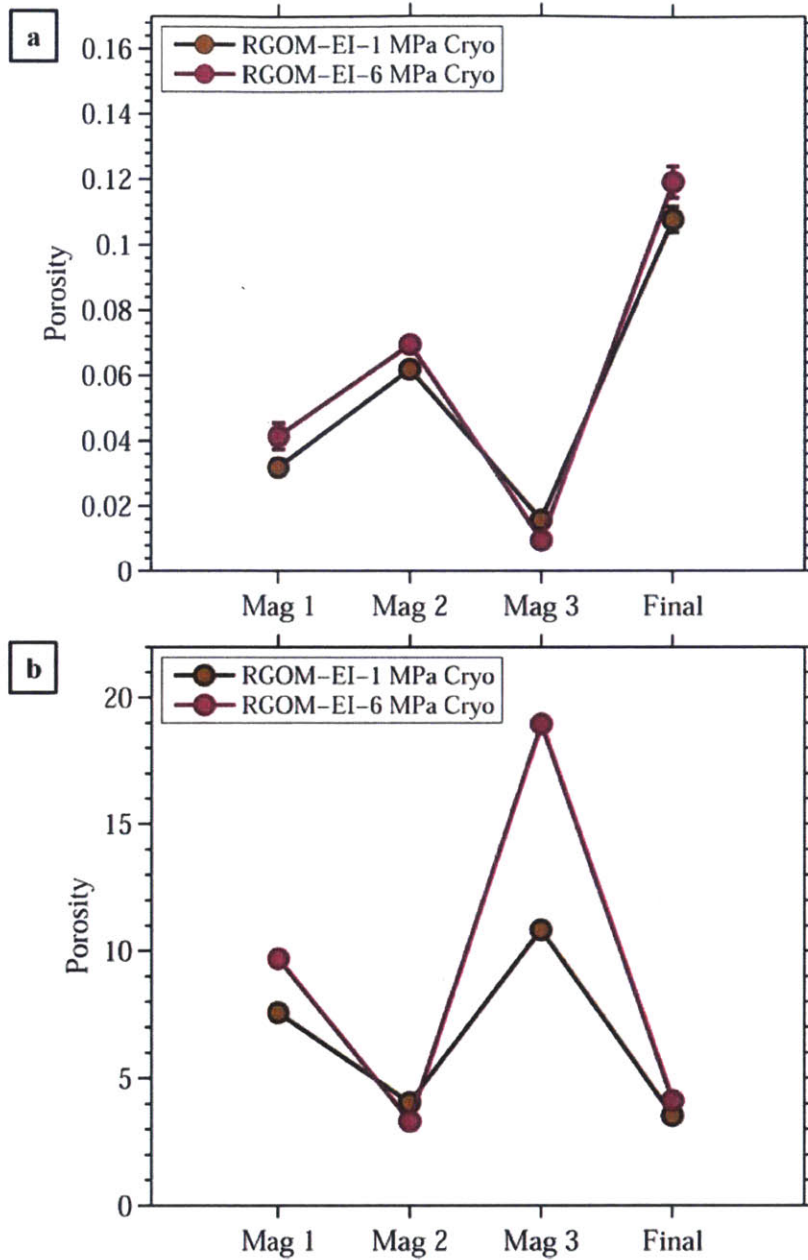
Figure 7-11: a) Cryo imaging porosity values for RGOM mudrock samples obtained using the IOM method. The error bars represent the 95% confidence interval obtained using the standard error of the mean. b) The coefficient of variation of the porosity values at different magnifications used in the IOM method (bottom). The coefficient of variation was calculated as the standard error divided by the porosity at each magnification. The porosity and the standard error values for different magnifications are summarized in Table 7-7

183
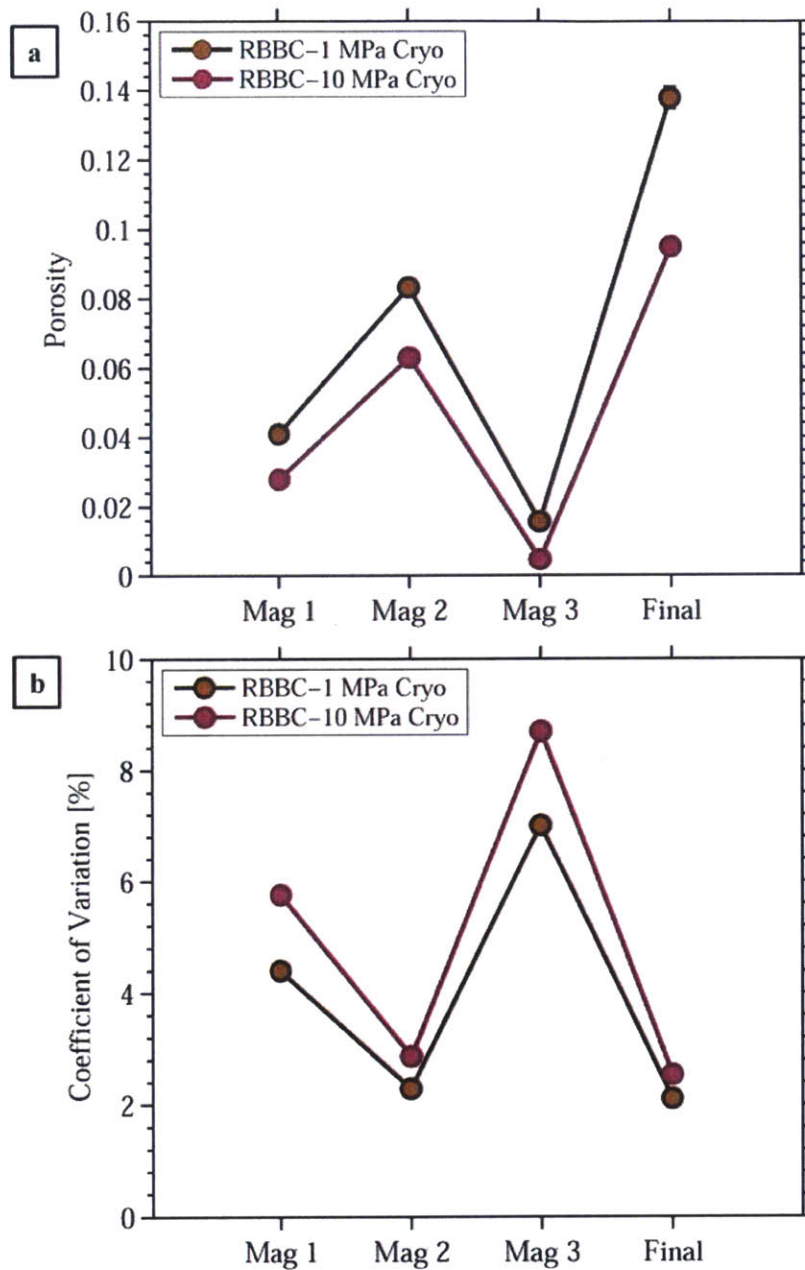
Figure 7-12: a) Cryo imaging porosity values for RBBC mudrock samples obtained using the IOM method. The error bars represent the 95% confidence interval obtained using the standard error of the mean. b) The coefficient of variation of the porosity values at different magnifications used in the IOM method (bottom). The coefficient of variation was calculated as the standard error divided by the porosity at each magnification. The porosity and the standard error values for different magnifications are summarized in Table 7-8
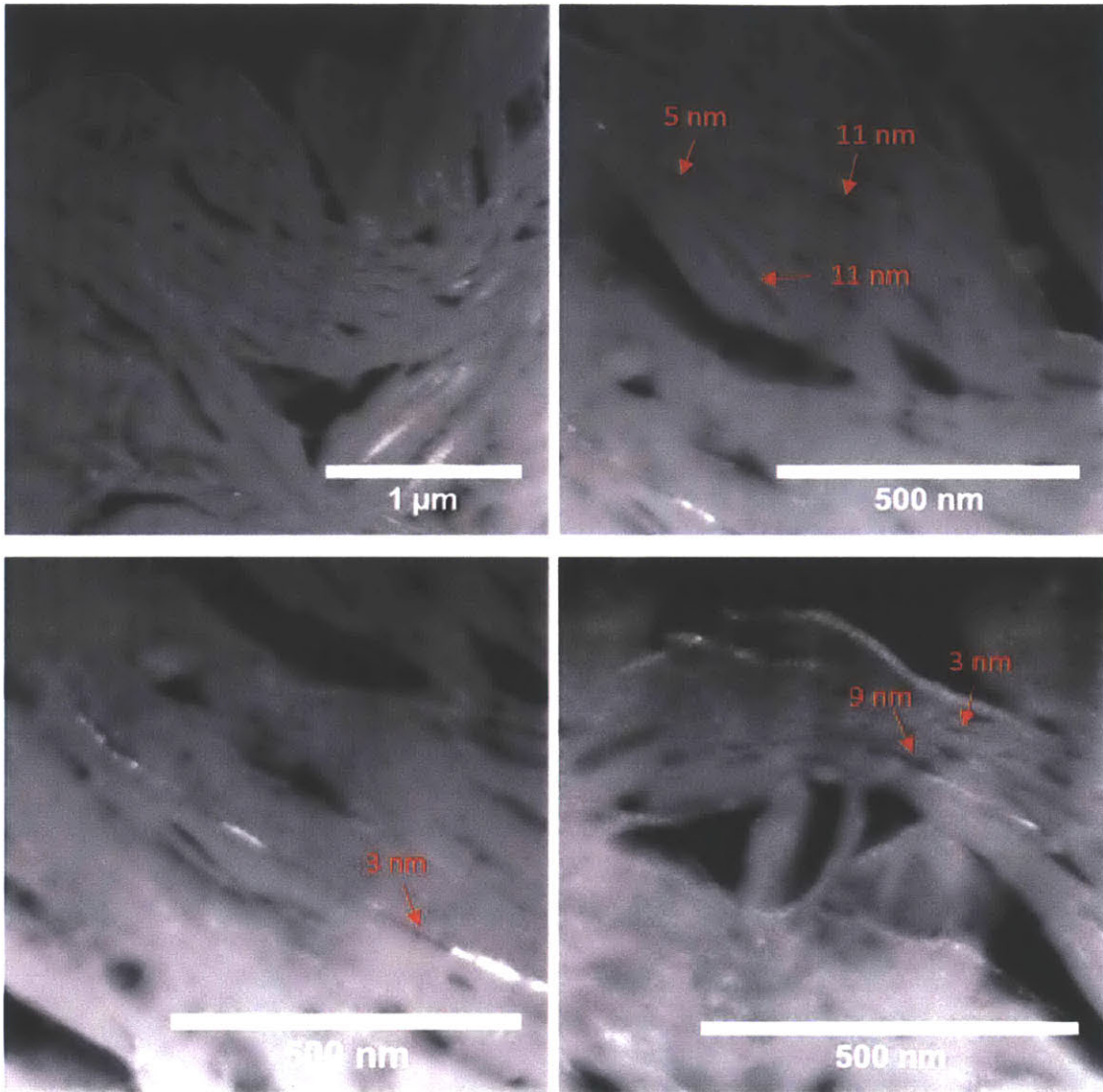
Figure 7-13: TEM images of oven-dried RGOM-EI-1 MPa mudrock sample. The images reveal the porous clay matrix, which contains pores as small as 3 nm
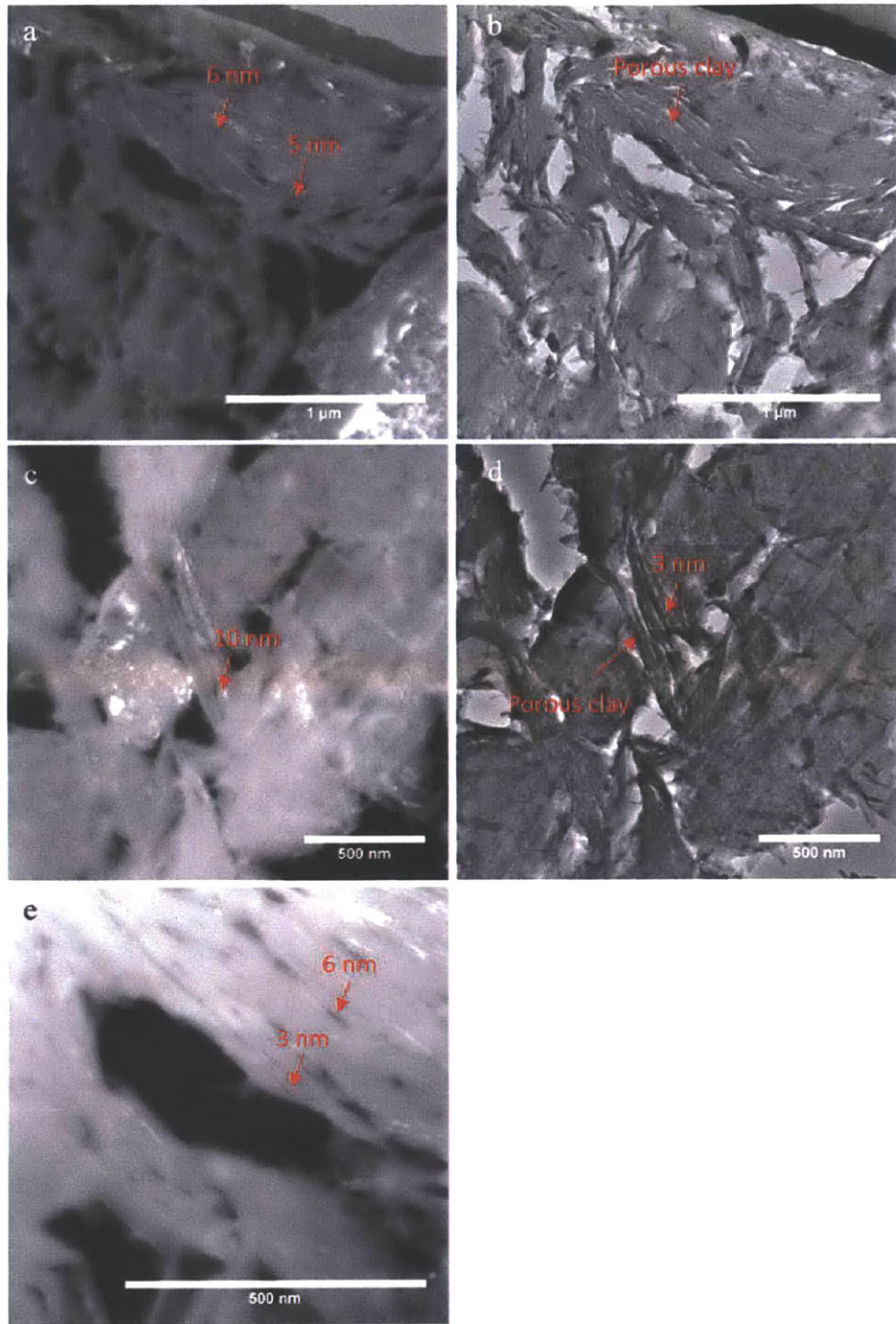
Figure 7-14: TEM images of oven-dried RGOM-EI-10 MPa mudrock sample. a, c, e) dark field TEM images, and b, d) bright field TEM images. The images reveal the porous clay matrix, which contains pores as small as 3 nm
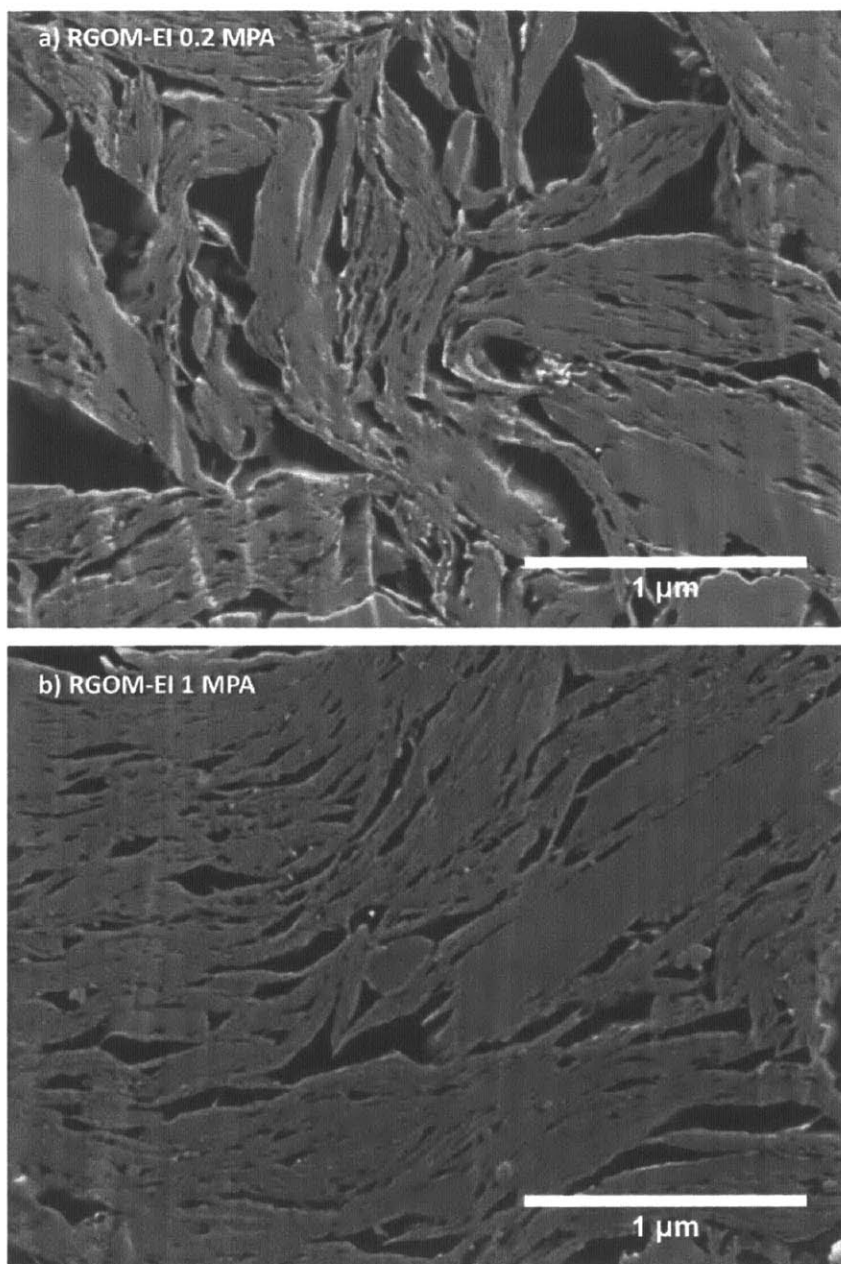
Figure 7-15: SEM images of oven-dried RGOM-EI samples acquired at a magnification of 100 KX.
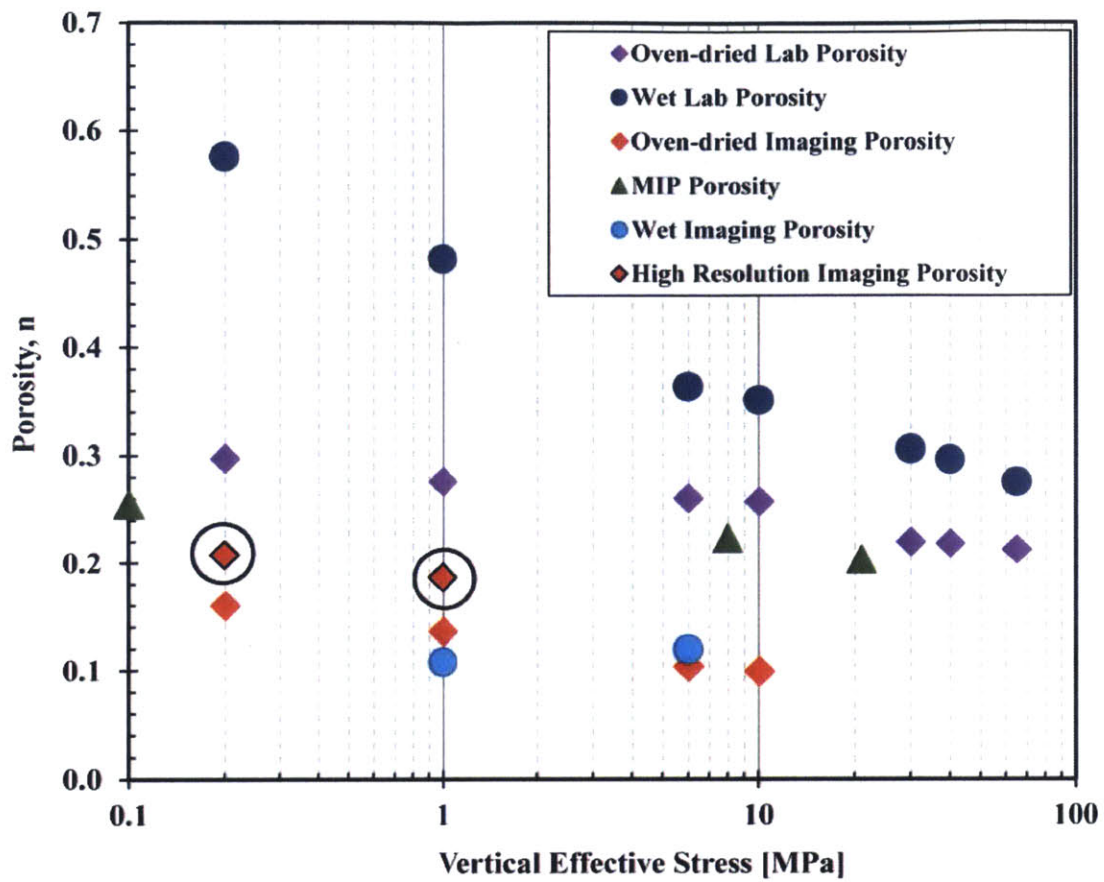
Figure 7-16: This figure shows the increase in SEM imaging porosity when high magnification images of 100 KX are used in the IOM method.
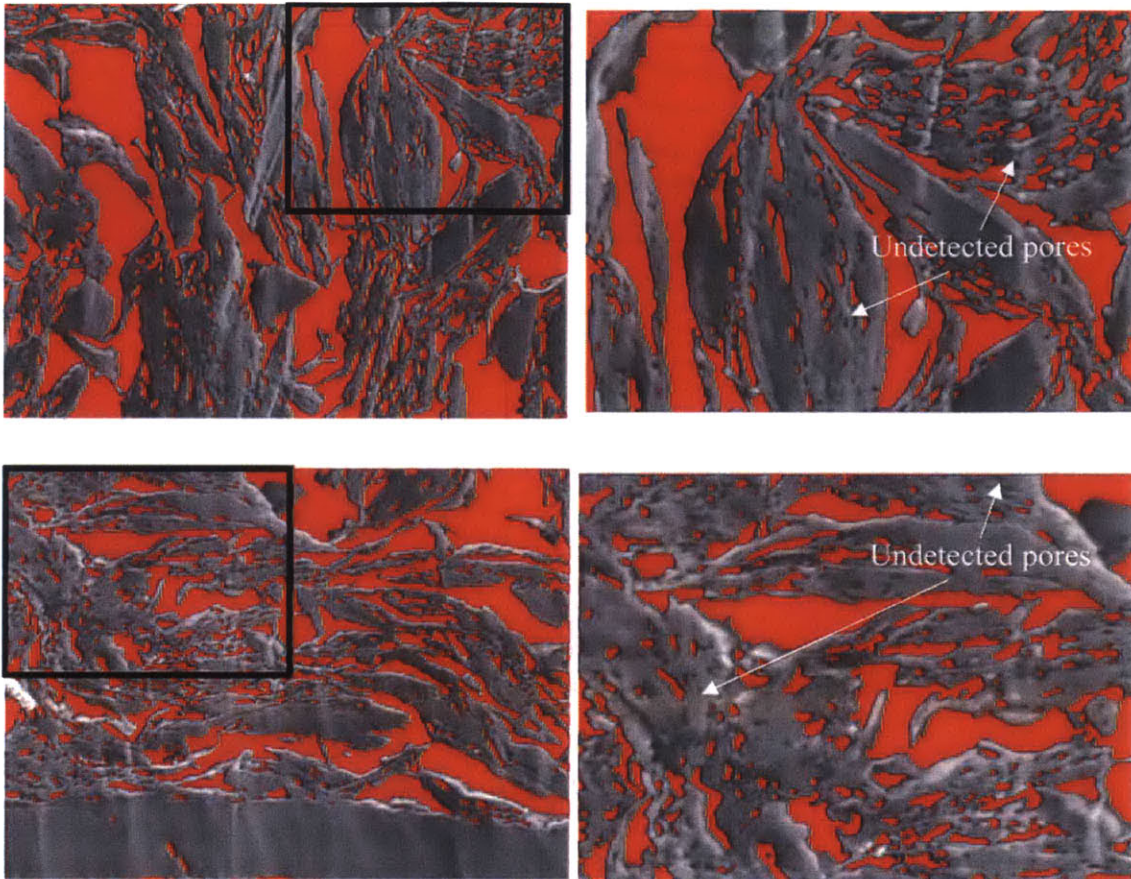
Figure 7-17: An example of image-thresholding of high magnification images of RGOM-EI-0.2 MPa sample. The red color represents the detected pore space. This image show that there are pores that were not detected using thresholding.
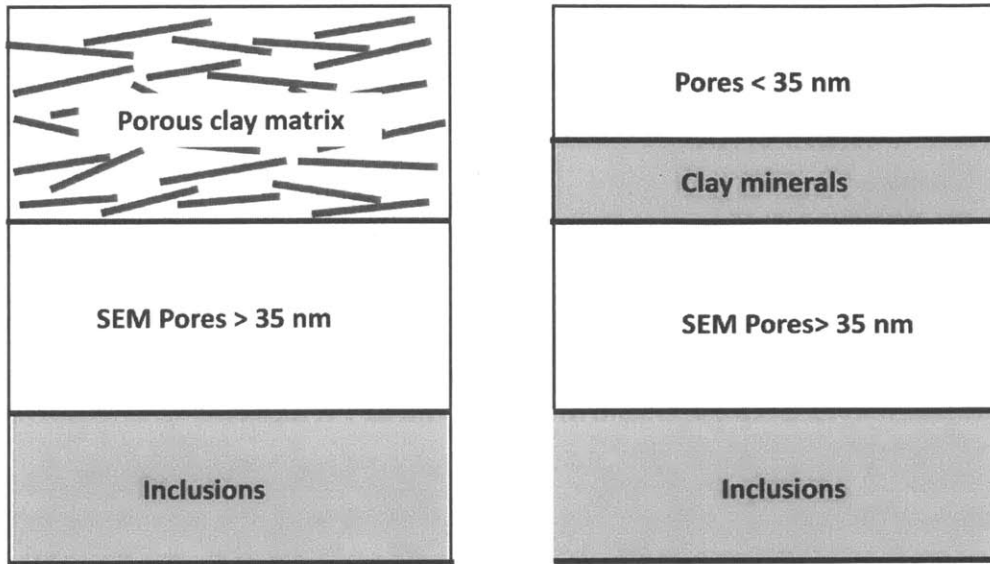
$$sub\_35nm\ porosity = \frac{[Vpores < 35nm]}{[Vpores < 35] + [Vclay]}$$

Figure 7-18: These diagrams illustrate the main phases of mudrock samples observed in SEM images. These phases include inclusions, pores larger than 35nm, and the porous clay matrix. The porous clay matrix can further be divided into a solid phase of clay minerals and pores smaller than 35 nm, and not resolvable in SEM images. The sub_35nm Porosity corresponds to the clay matrix only.
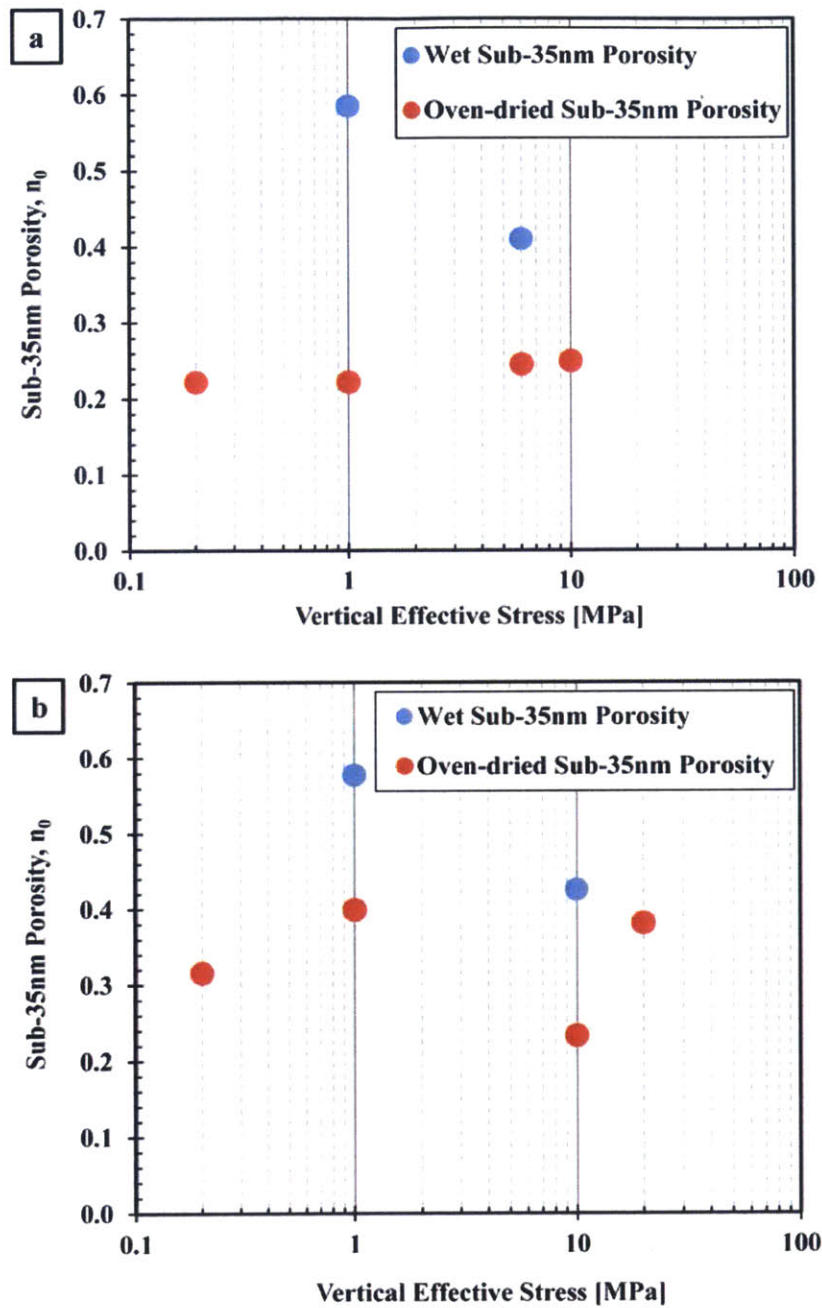
Figure 7-19: Wet and oven-dried sub-35nm porosity calculated using the IOM method for a) RGOM-EI and b) RBBC mudrock samples. These results are also summarized in Table 7-9

Figure 7-20: Cryo-SEM images and oven-dried SEM images of RGOM-EI-1 MPa mudrock sample. These images were acquired at a magnification of 12 KX, and provide a good understanding of the changes that occur in large pores due to drying shrinkage.
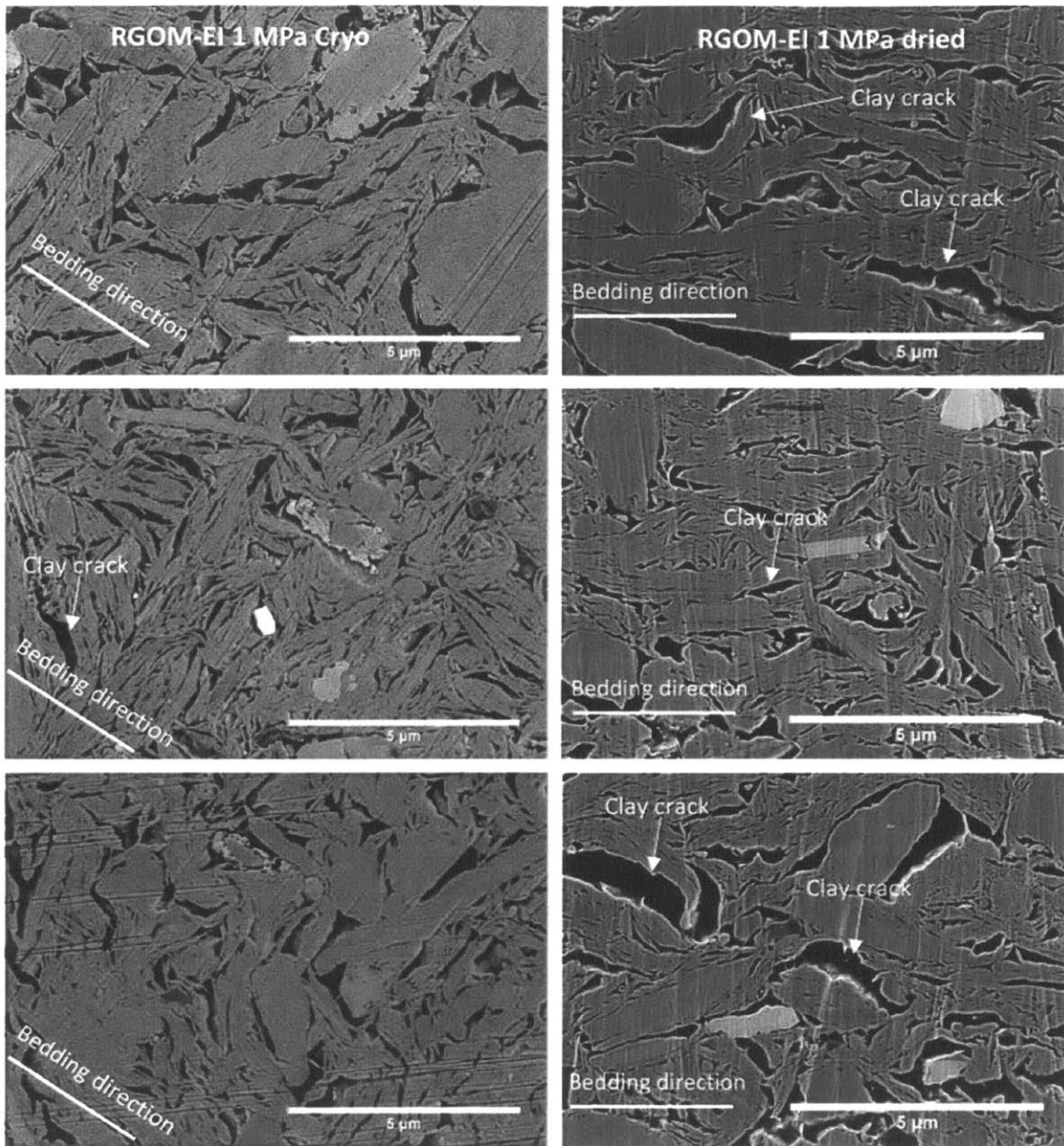
Figure 7-21: Cryo-SEM images and oven-dried SEM images of RGOM-EI-1 MPa mudrock sample. These images were acquired at a magnification of 30 KX, and provide a good understanding of the changes that occur in small pores due to drying shrinkage.
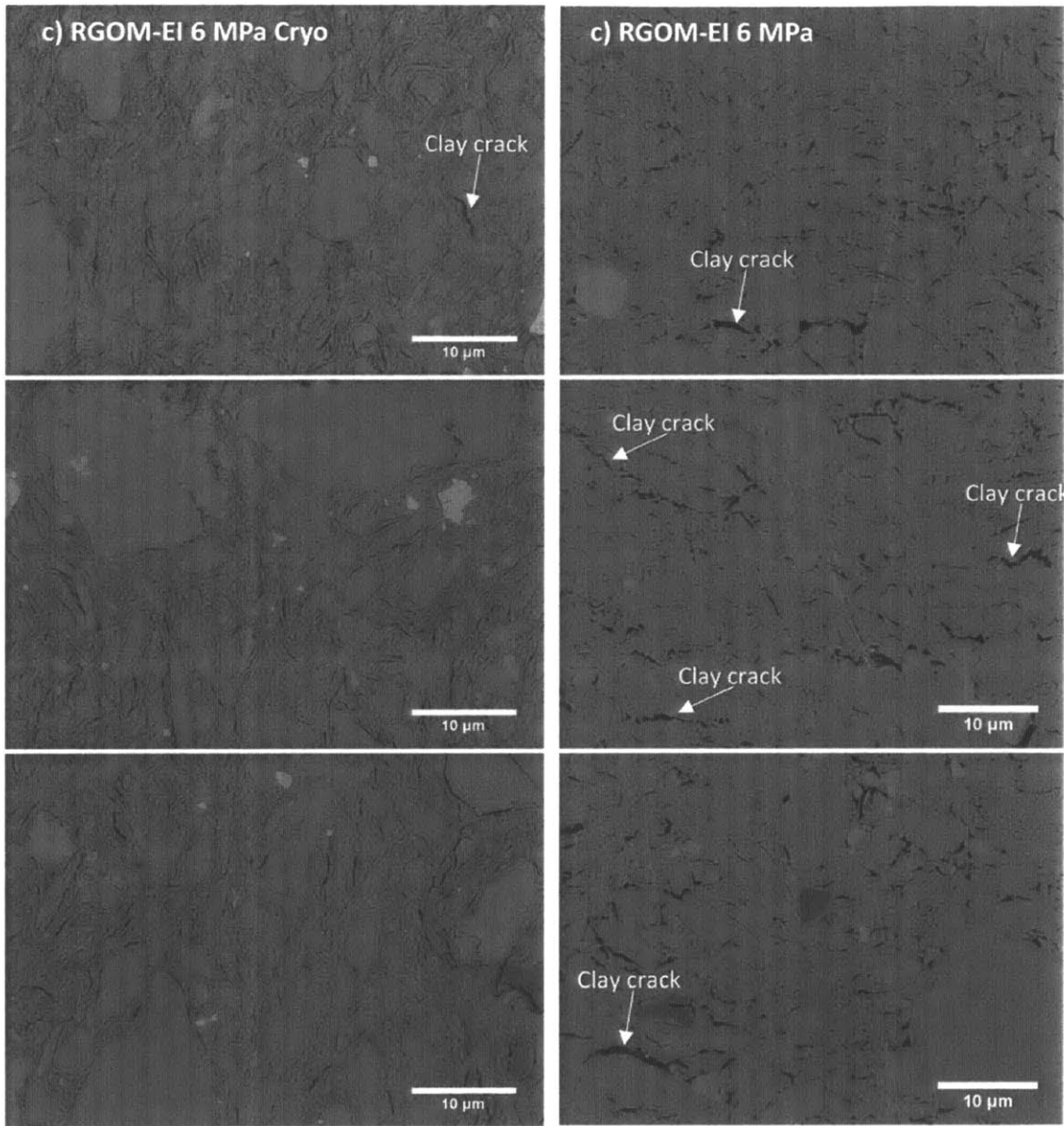
Figure 7-22: Cryo-SEM images and oven-dried SEM images of RGOM-EI-6 MPa mudrock sample. These images were acquired at a magnification of 12 KX, and provide a good understanding of the changes that occur in large pores due to drying shrinkage.
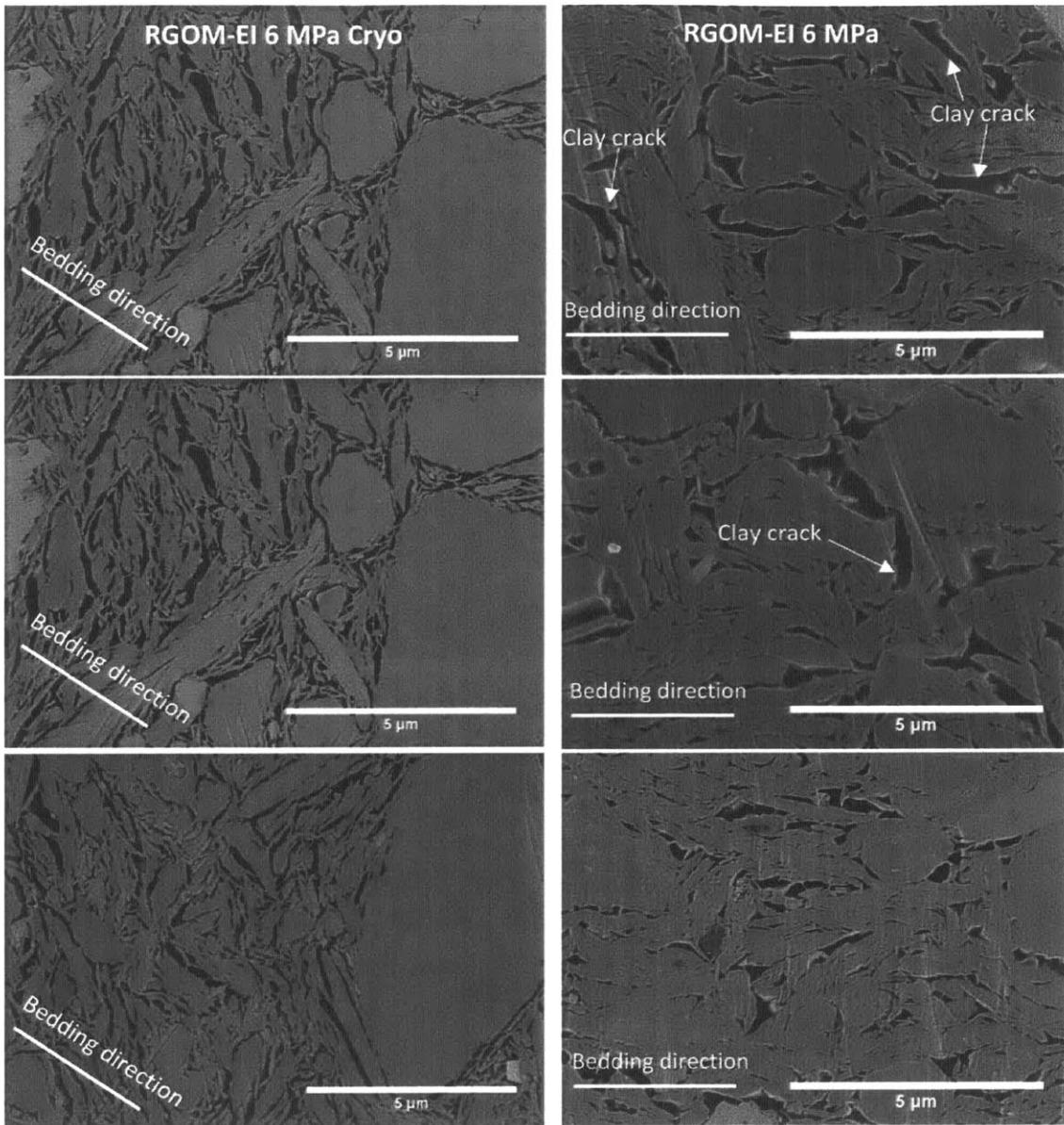
Figure 7-23: Cryo-SEM images and oven-dried SEM images of RGOM-EI-6 MPa mudrock sample. These images were acquired at a magnification of 30 KX, and provide a good understanding of the changes that occur in small pores due to drying shrinkage
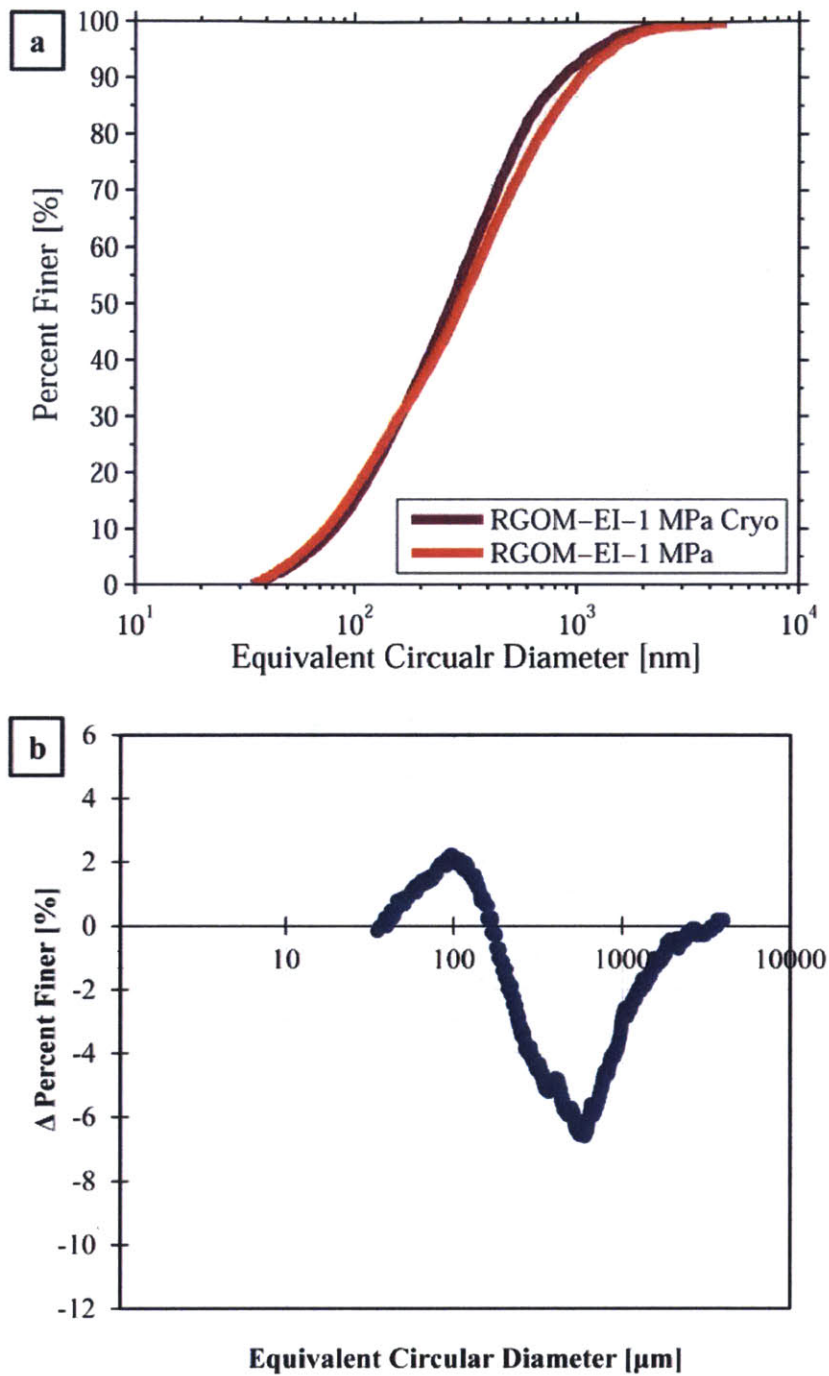
Figure 7-24: a) PSDs of wet and oven-dried RGOM-EI-1 MPa mudrock samples, and b) difference between the two curves. The difference data was calculated by subtracting the oven-dried percent finer from the wet percent finer at each pore diameter.
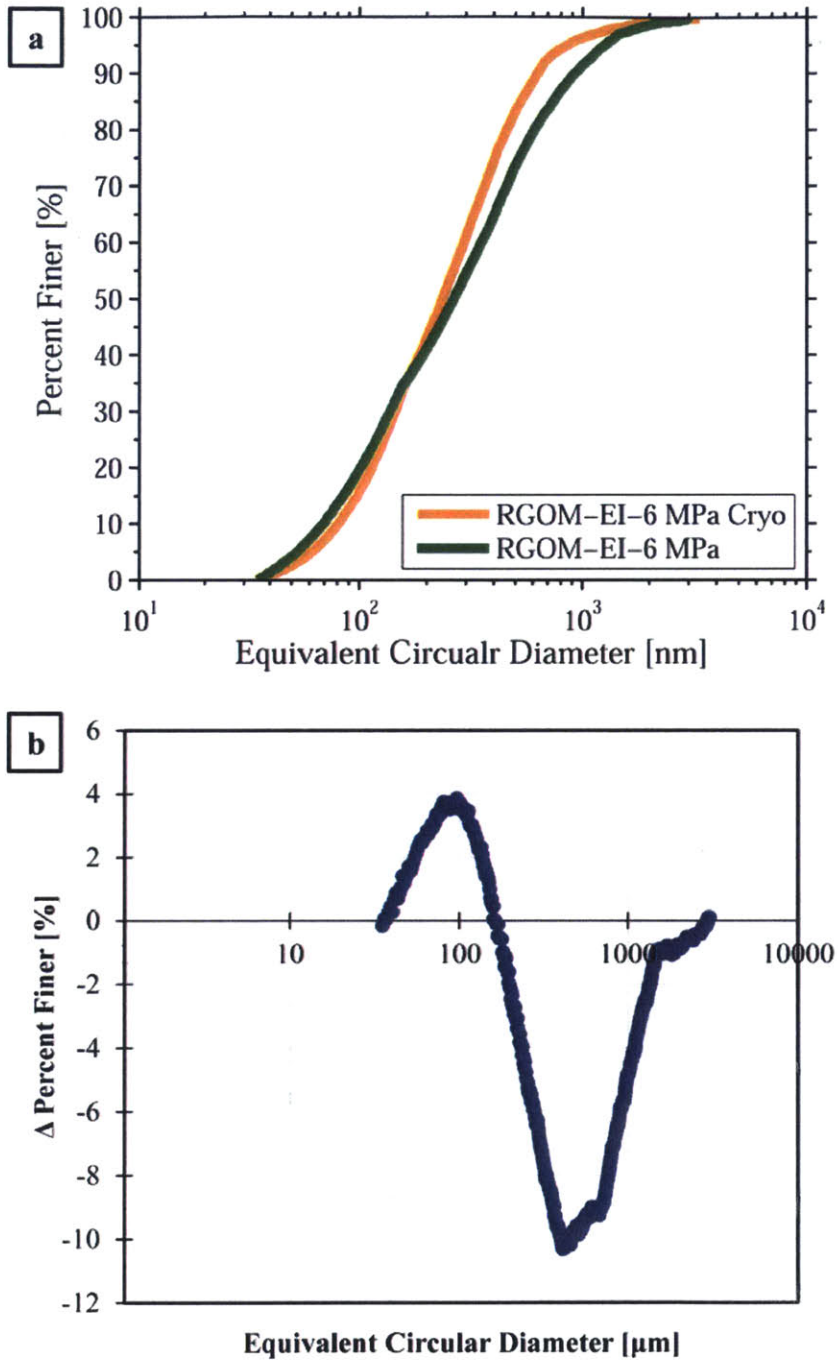
Figure 7-25: a) PSDs of wet and oven-dried RGOM-EI-1 MPa mudrock samples, and b) difference between the two curves. The difference data was calculated by subtracting the oven-dried percent finer from the wet percent finer at each pore diameter.
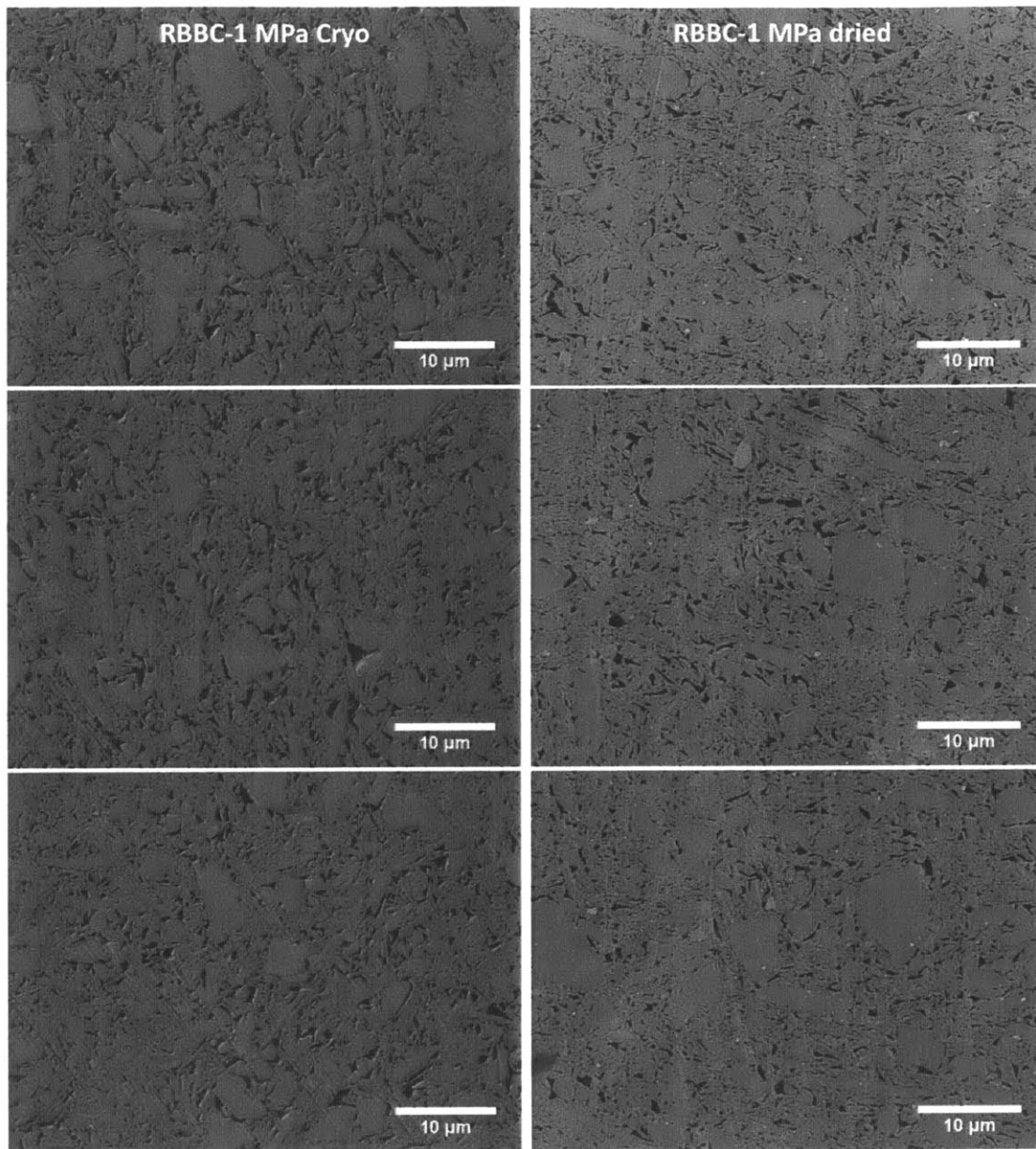
Figure 7-26: Cryo-SEM images and oven-dried SEM images of RBBC-1 MPa mudrock sample. These images were acquired at a magnification of 12 KX, and provide a good understanding of the changes that occur in large pores due to drying shrinkage
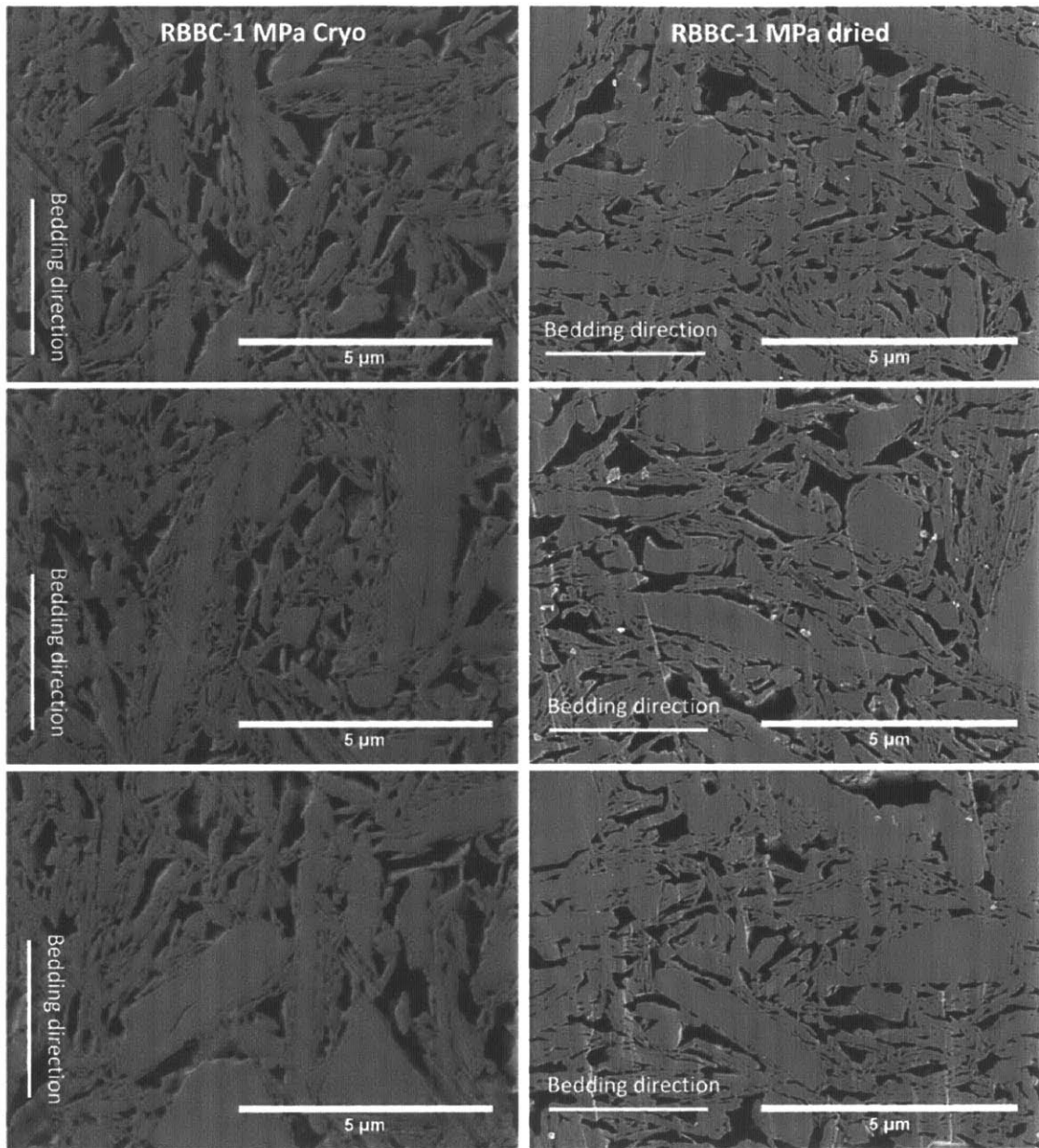
Figure 7-27: Cryo-SEM images and oven-dried SEM images of RBBC-1 MPa mudrock sample. These images were acquired at a magnification of 30 KX, and provide a good understanding of the changes that occur in small pores due to drying shrinkage.
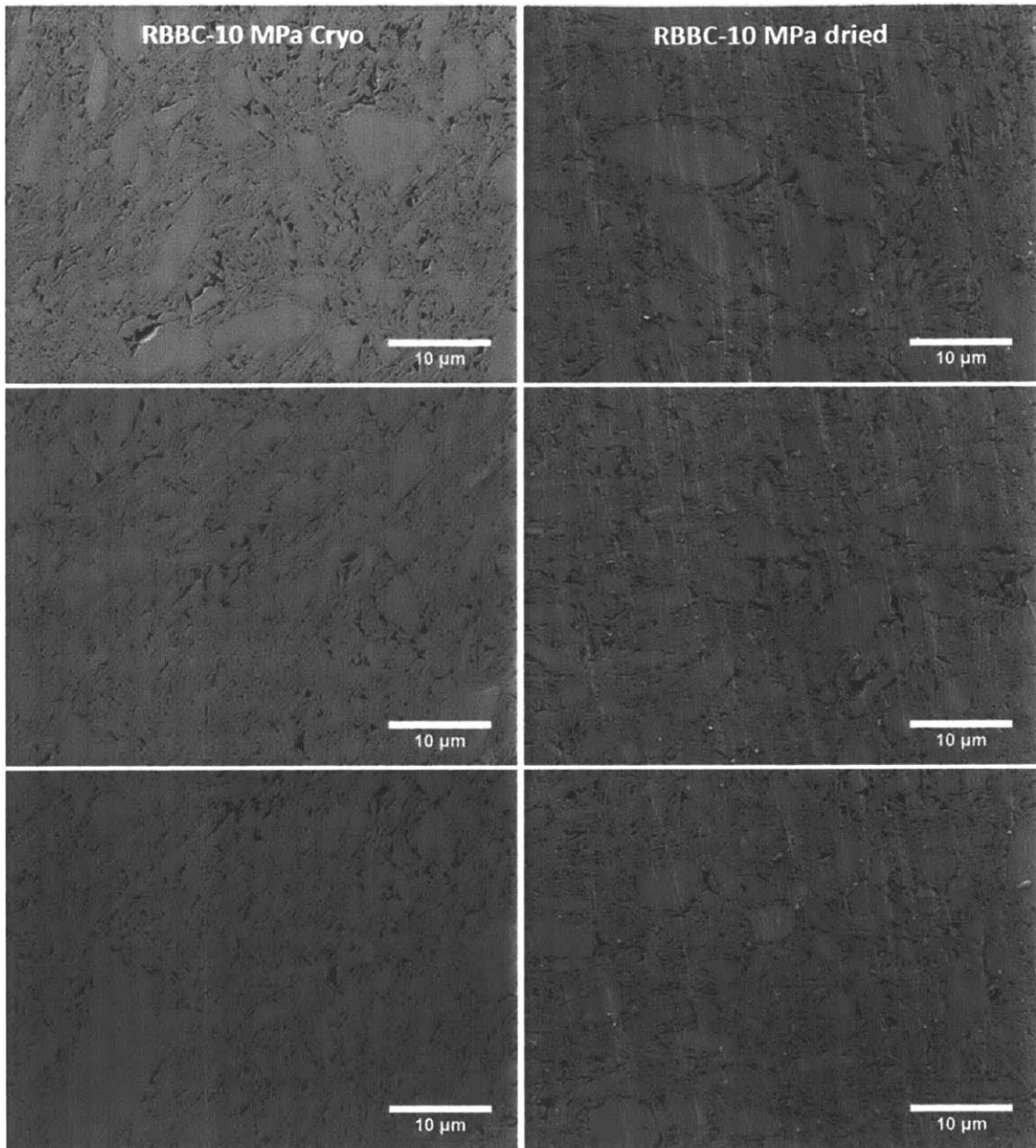
Figure 7-28: Cryo-SEM images and oven-dried SEM images of RBBC-10 MPa mudrock sample. These images were acquired at a magnification of 12 KX, and provide a good understanding of the changes that occur in large pores due to drying shrinkage.
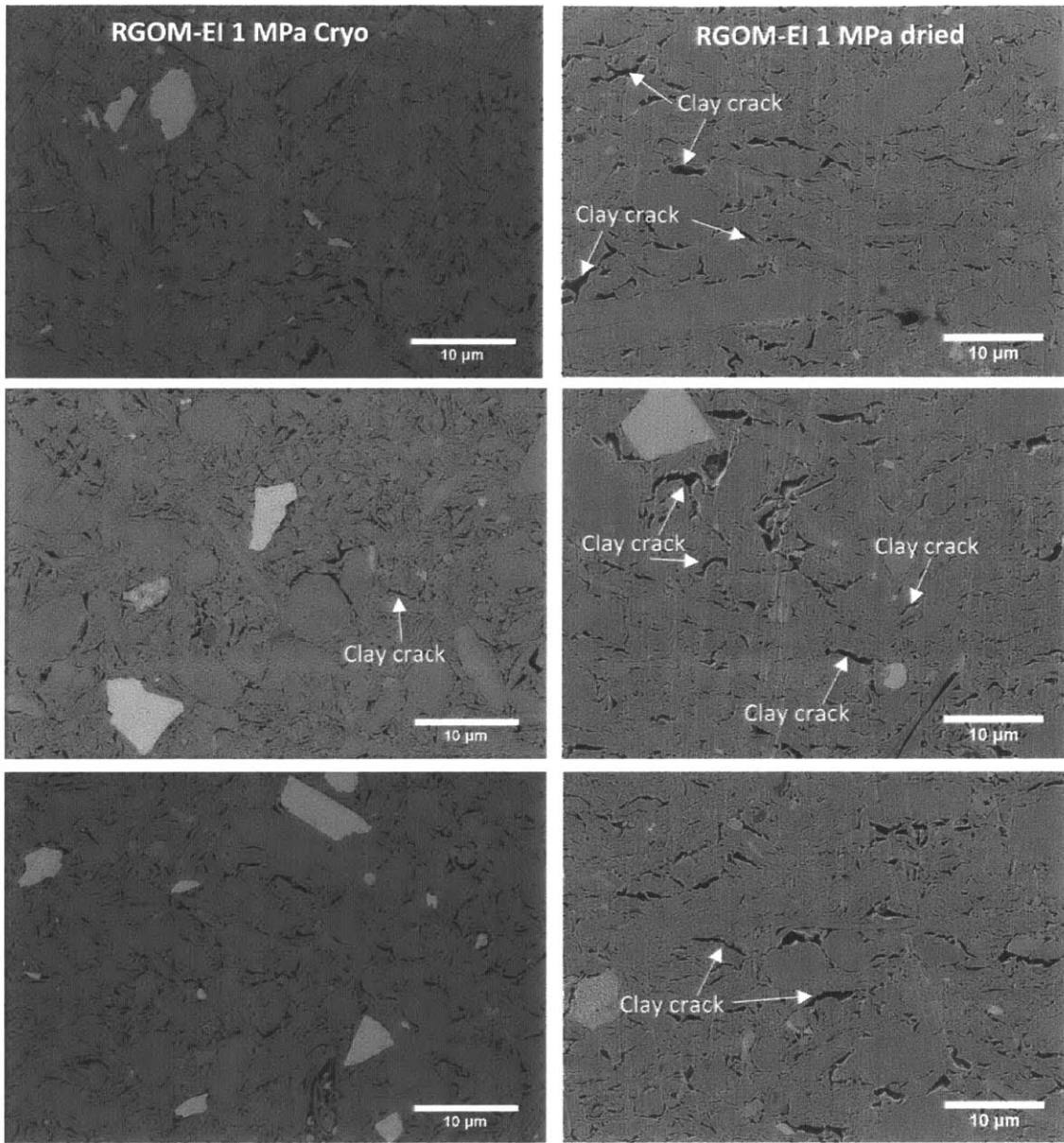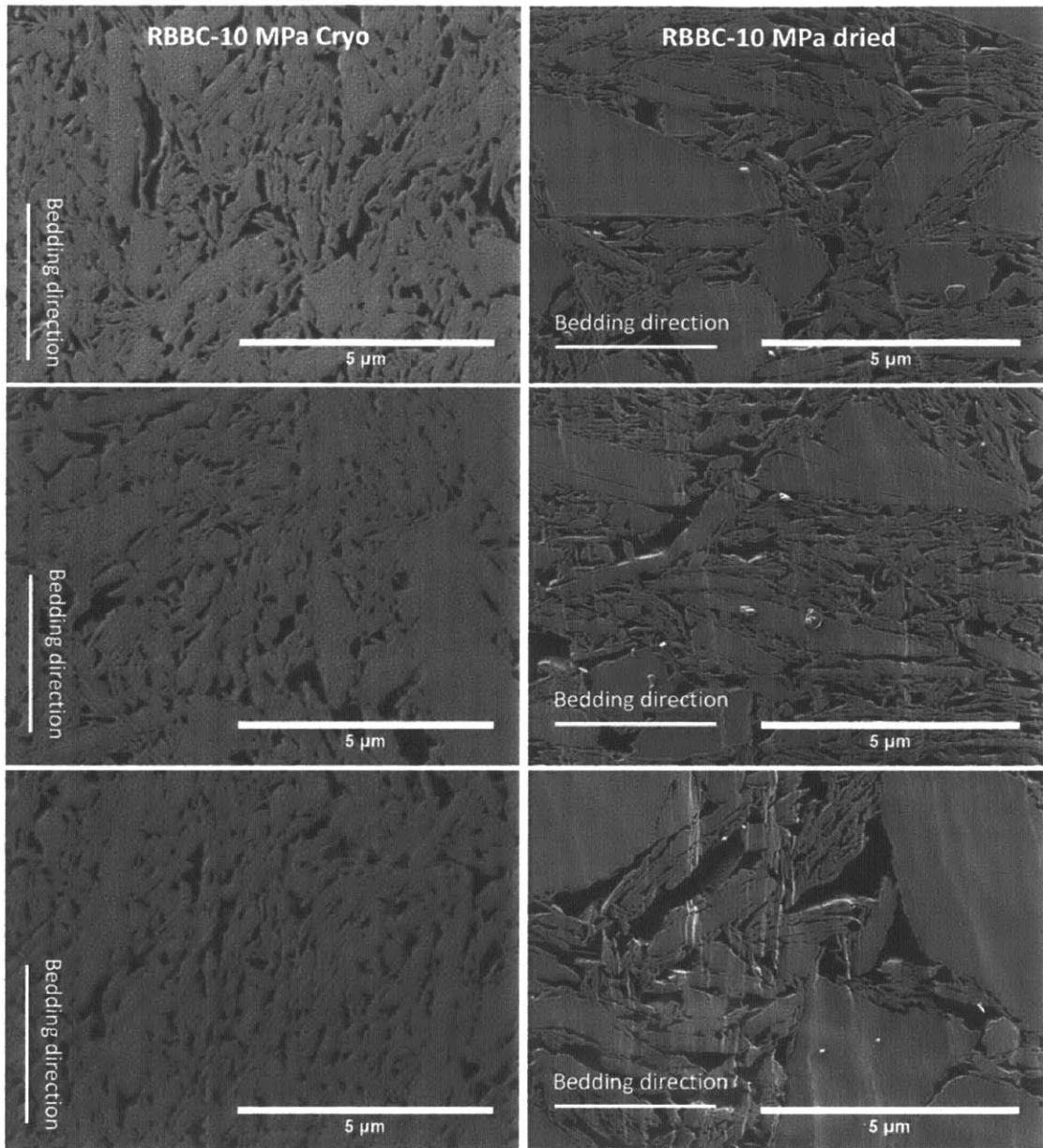
Figure 7-29: Cryo-SEM images and oven-dried SEM images of RBBC-10 MPa mudrock sample. These images were acquired at a magnification of 30 KX, and provide a good understanding of the changes that occur in small pores due to drying shrinkage.
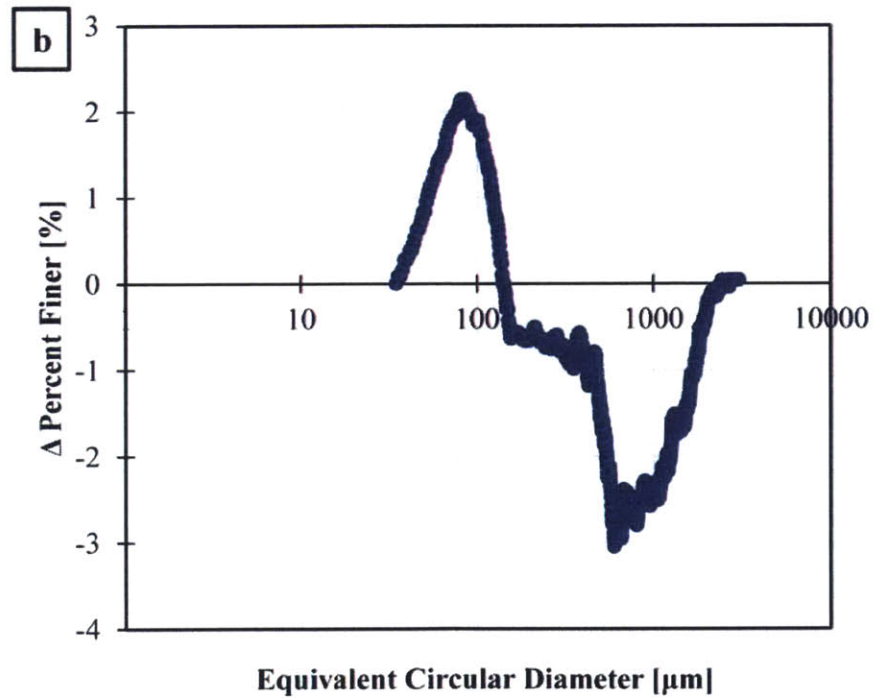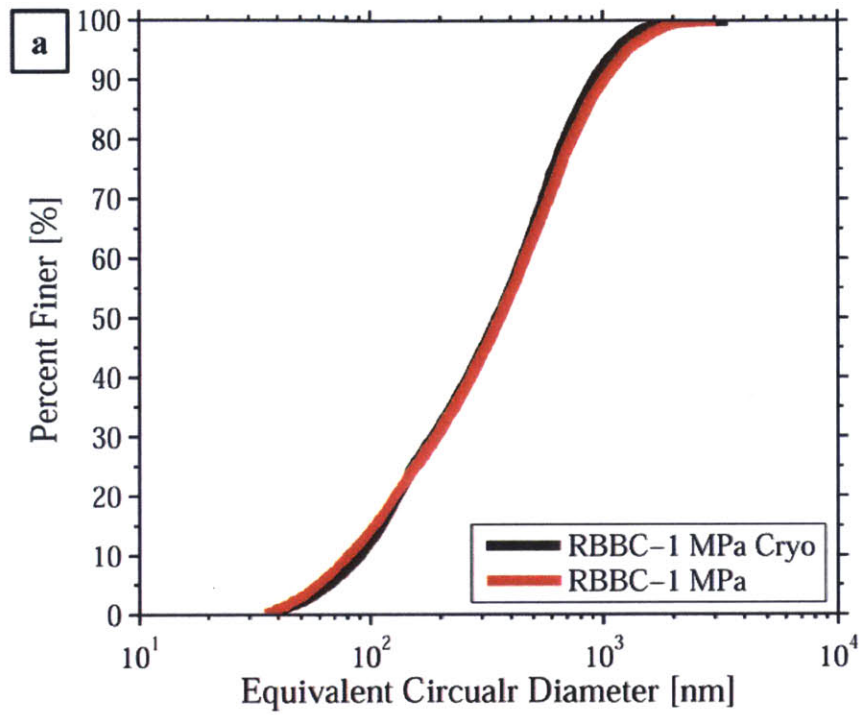
Figure 7-30: a) PSDs of wet and oven-dried RBBC-1 MPa mudrock samples, and b) difference between the two curves. The difference data was calculated by subtracting the oven-dried percent finer from the wet percent finer at each pore diameter.
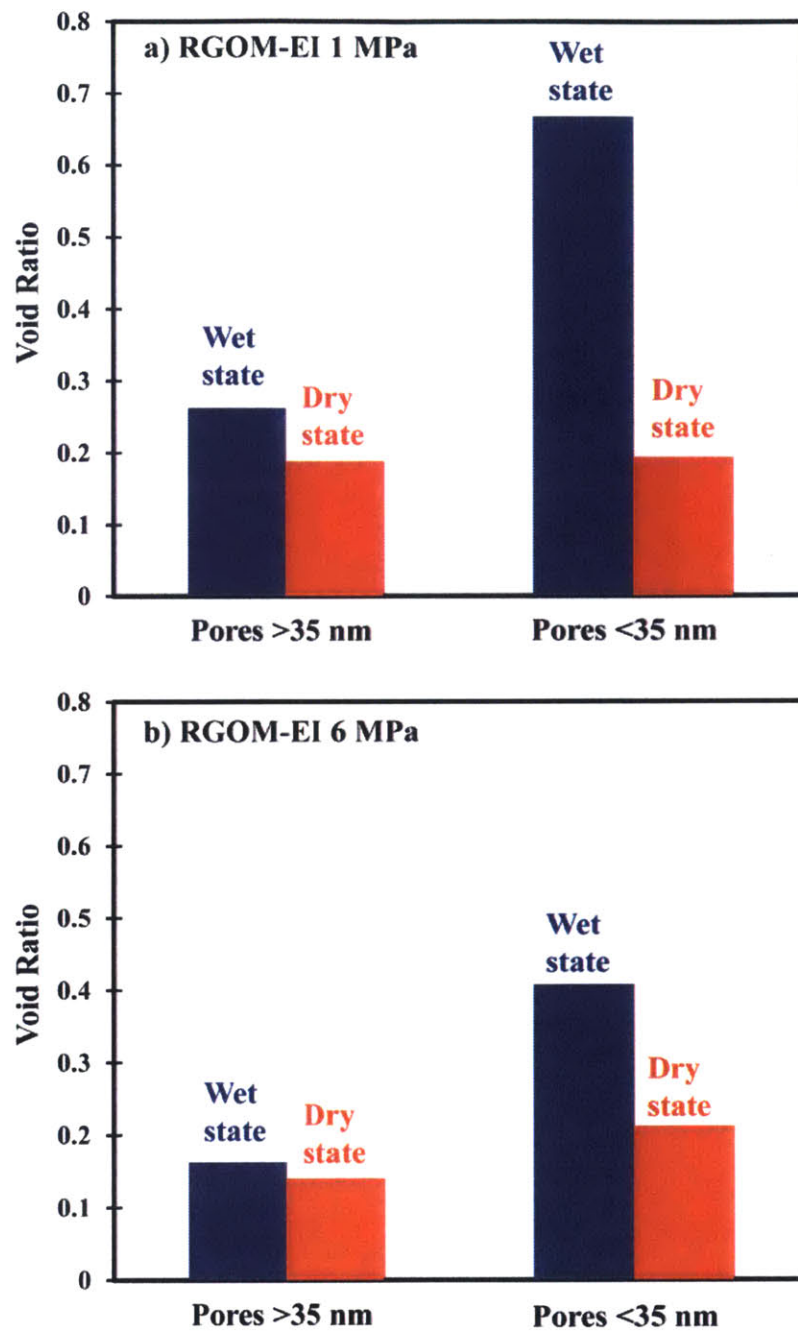
Figure 7-31: The evolution of the SEM pores (>35 nm) and the sub-35nm (<35 nm) as a function of drying shrinkage for two RGOM-EI samples: a) RGOM-EI 1MPa and b) RGOM-EI 6 MPa. The wet state represents the information obtained from cryo-SEM images, while the dry state represents the information obtained using the oven-dried SEM images.
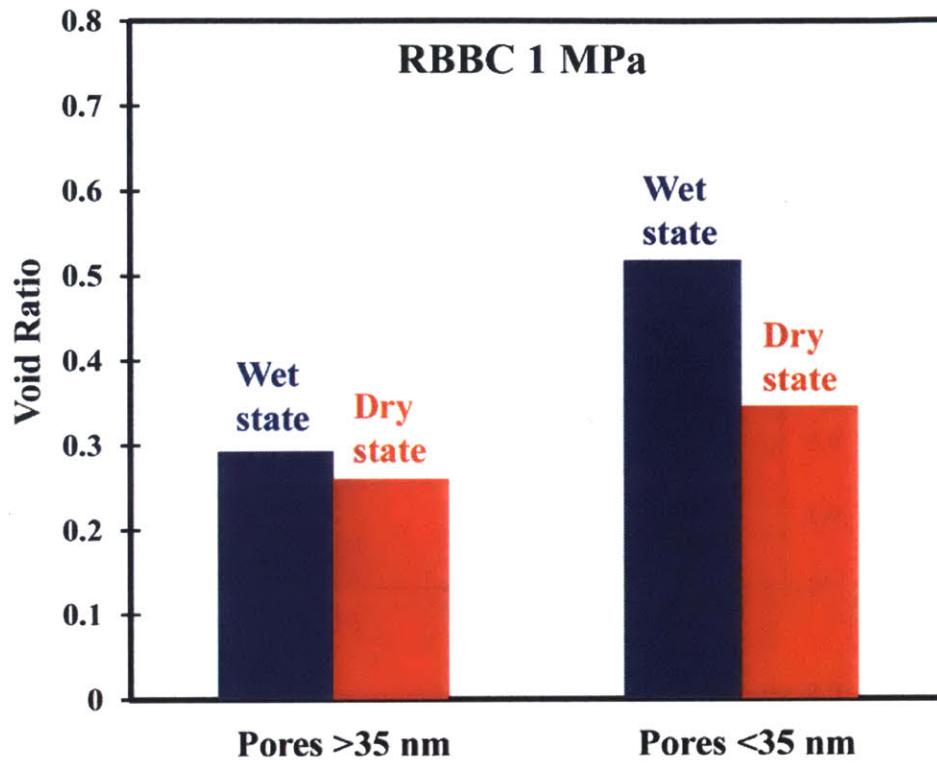
Figure 7-32: The evolution of the SEM pores (>35 nm) and the sub-35nm (<35 nm) as a function of drying shrinkage for the RBBC 1MPa sample. The wet state represents the information obtained from cryo-SEM images, while the dry state represents the information obtained using the oven-dried SEM images.
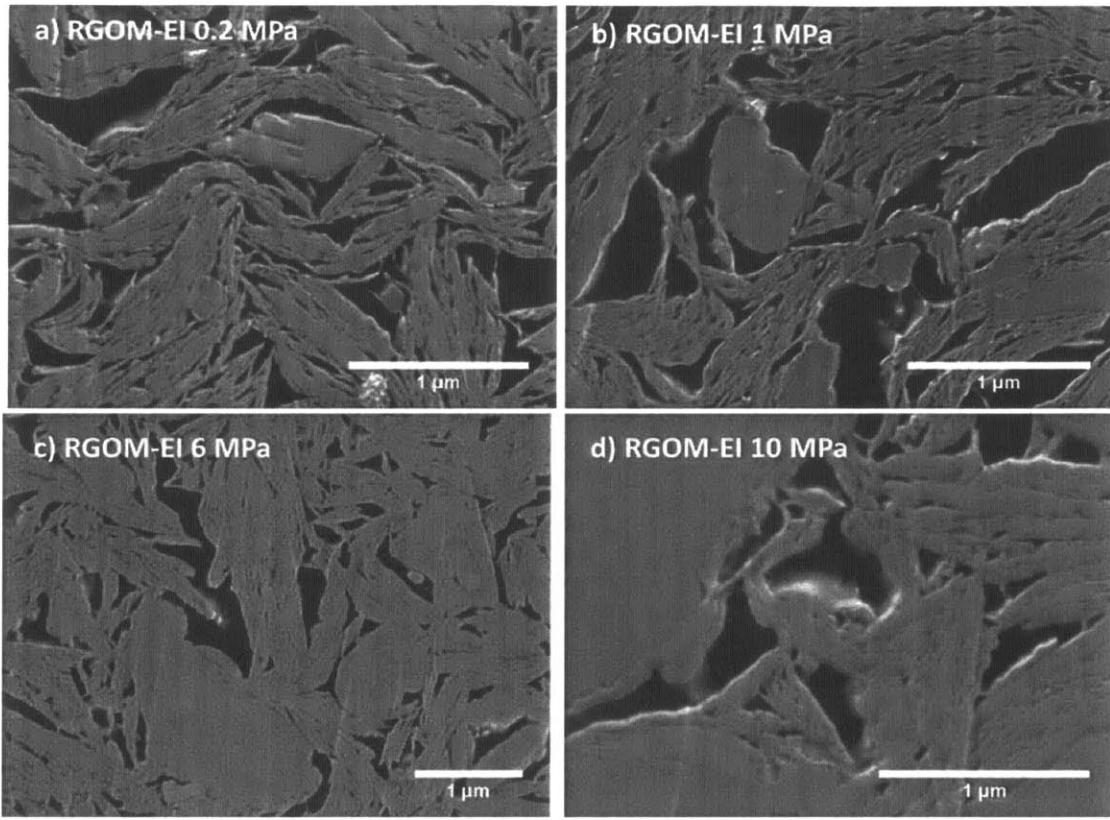
Figure 7-33: SEM images of oven-dried RGOM-EI samples at different resedimentation stresses: a) 0.2 MPa, b) 1 MPa, c) 6 MPa, and d) 10 MPa. The images were acquired at different magnifications.
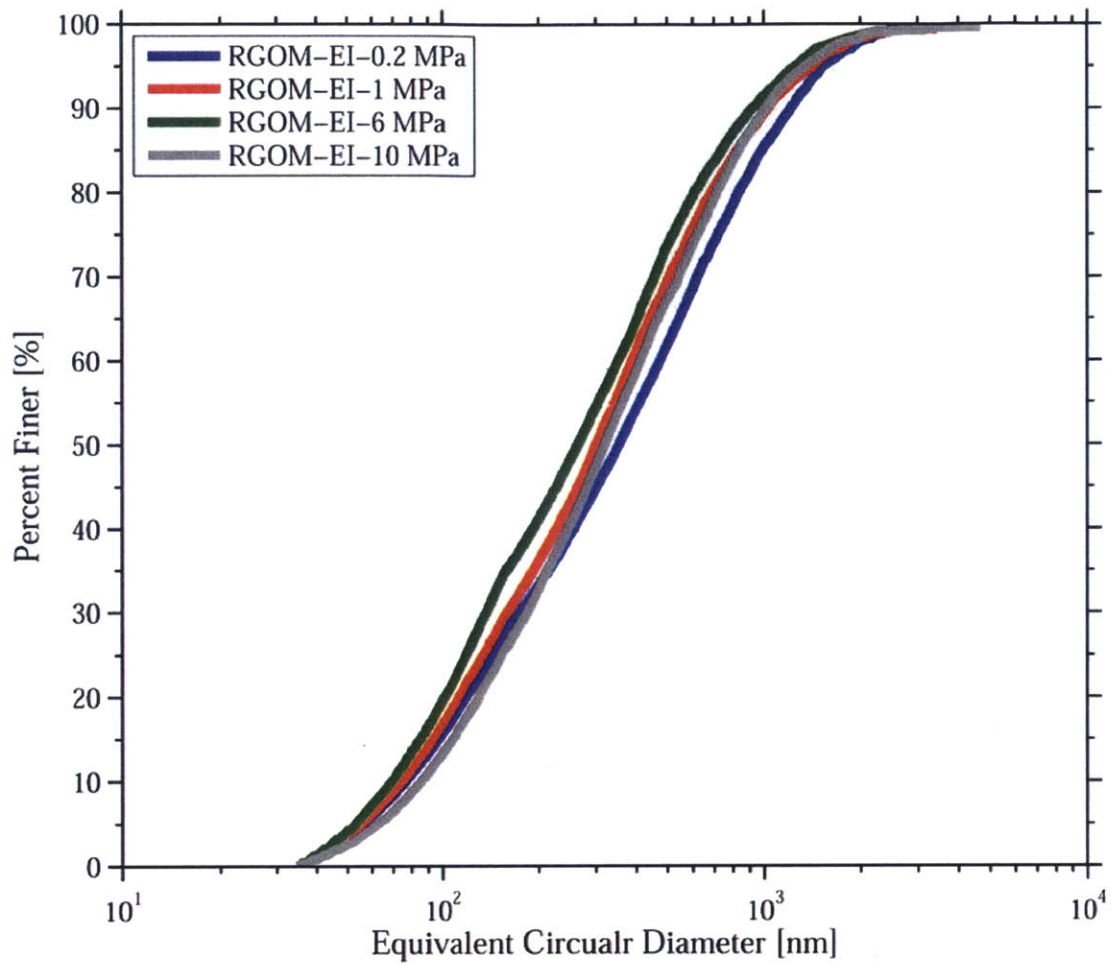
Figure 7-34: Pore size distribution of oven-dried RGOM-EI mudrock samples obtained using the IOM method
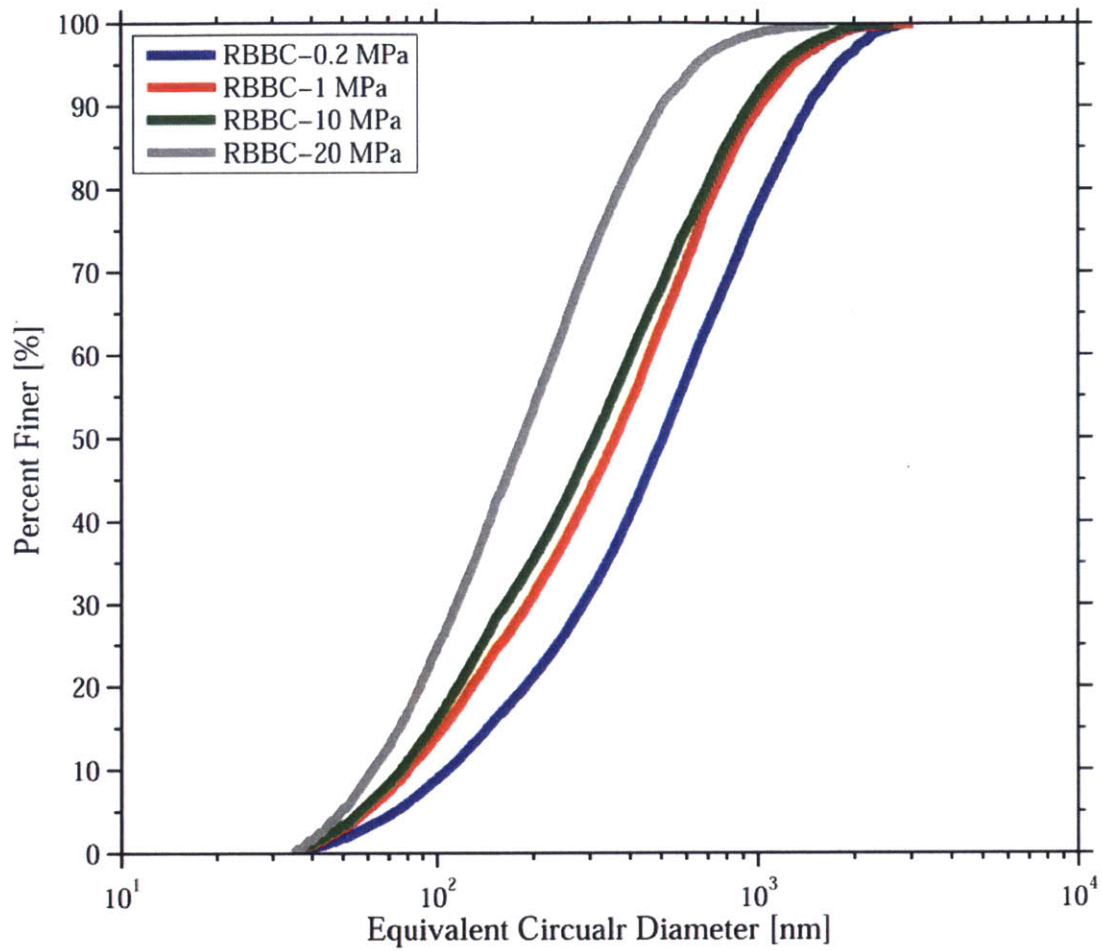
Figure 7-35: Pore size distribution of oven-dried RBBC mudrock samples obtained using the IOM method
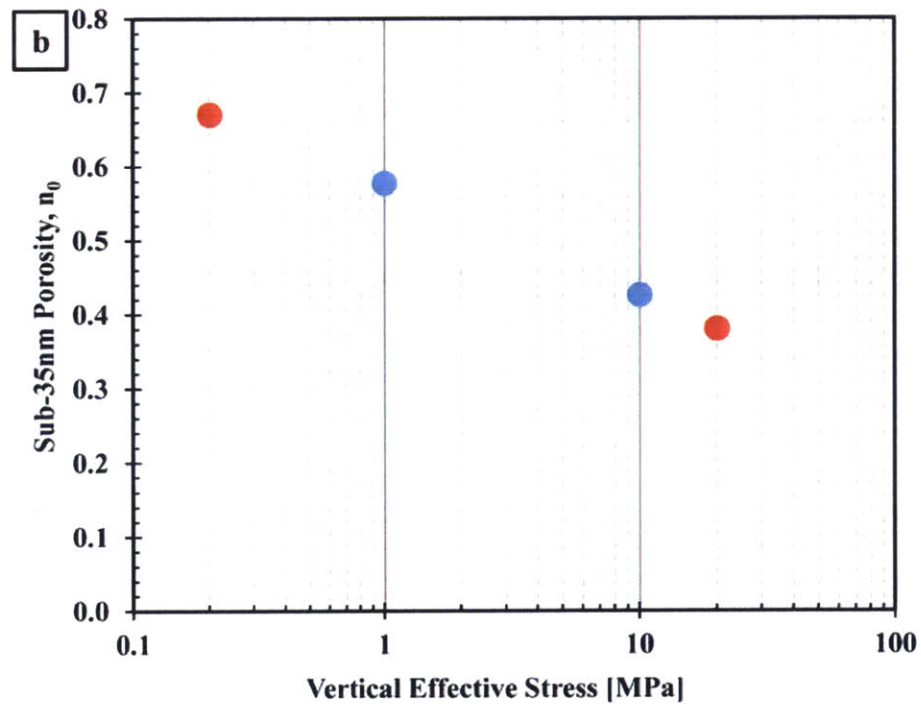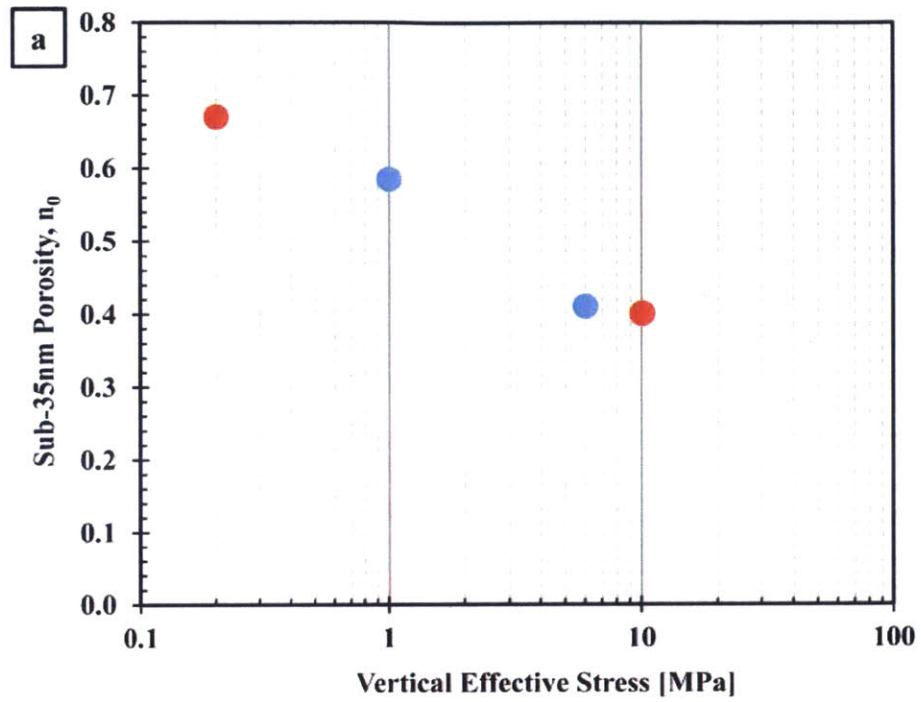
Figure 7-36: Wet sub-35nm porosity for a) RGOM-EI samples and b) RBBC samples. Red points represent the samples for which we did have wet imaging porosity, and the wet sub-35nm porosity was calculated using the oven-dried imaging porosity.
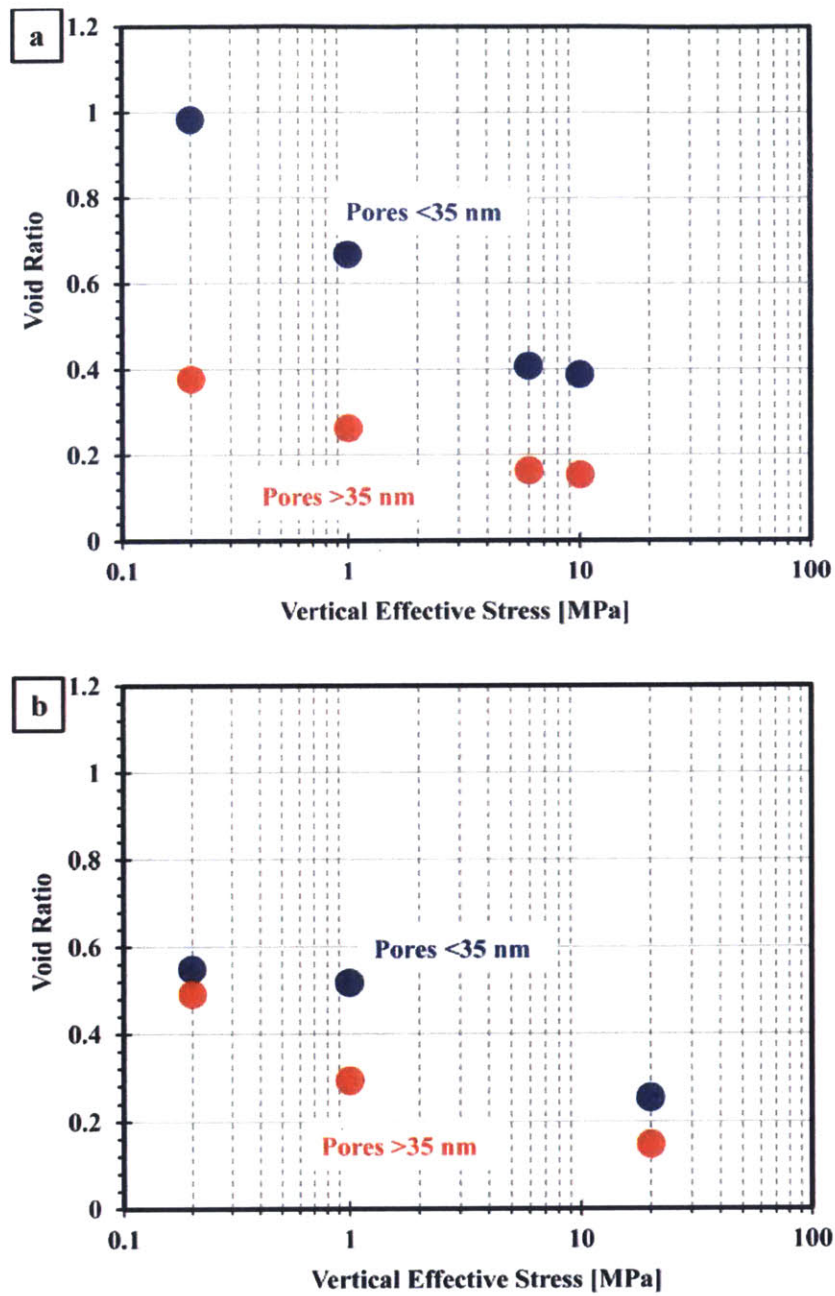
Figure 7-37: The evolution of the SEM pores (>35 nm) and the sub-35nm (<35 nm) as a function of the consolidation stress for a) the RGOM-EI mudrock samples and b) the RBBC mudrock samples.

8 CONCLUSIONS AND FUTURE WORK

8.1 The Microstructure of Clay Slurries

The Microstructure of clay slurries was investigated using cryo-SEM, which enables the imaging of materials in their in-situ state. We used two techniques to prepare the slurry samples for imaging: high-pressure freezing and plunge freezing. The microstructure of plunge-frozen GOM-EI and BBC clay slurries revealed a striking honeycomb structure. This structure consists of clay aggregates joined with face-edge and edge-edge contacts. Furthermore, as pore salinity increases the honeycomb structure transforms into a well-defined structure. On the other hand, the microstructure of high-pressure frozen clay slurries consists of individual clay particles and aggregates of clay particles randomly distributed in a matrix of frozen ice. The thickness of clay aggregates in GOM-EI slurries increases with pore salinity. In contrast, the thickness of BBC clay aggregates is independent of pore salinity. While the orientation of clay aggregates and clay particles appear to be random, neighboring aggregates and particles tend to orient themselves parallel to each other.

Our plunge-freezing analysis demonstrates that the honeycomb structure observed in clay slurries at different pore salinities is an artifact of plunge-freezing. The cells are generated by the formation of ice crystals and the exclusion of salt ions and clay particles. The cell size of the honeycomb structure is controlled by the cooling rate. The size of these cells is much larger than microstructural features such as particle size and average particle separation, which leads to dramatic changes in the microstructure. In contrast, we did not observe a honeycomb structure in high pressure frozen samples, and only the size of clay aggregates is a function of pore salinity. High pressure freezing preserves the clay slurries and prevents ice crystallization that may destroy the microstructure. Clay slurries have a microstructure characterized by a cardhouse structure dominated by face-edge contacts between the building blocks of individual clay particles and clay aggregates. The building block of the cardhouse structure transforms from individual clay particles to thick clay aggregates as pore salinity increases. The absence of face-edge contacts is attributed to the randomness of the microstructure and the high porosity of the samples. Furthermore, the contacts between the building blocks are localized point contacts that would occur very infrequently in a given 2-D section. Nonetheless, a few face-edge contacts can

be found in images of clay slurries at different pore salinities. Our results demonstrate that one of the widely accepted models for clay suspensions, the honeycomb structure, is fundamentally an artifact of plunge freezing and does not reflect the in-situ behavior. In the field of geological sciences, this contrasts a fundamental view of fabric evolution that has inferred the presence of honeycomb structures that gradually evolve to an oriented fabric.

8.2 The Integration of Magnifications Method

Mudrocks are highly heterogeneous sedimentary rocks that contain pores and particles that range in size from nanometers to microns. As a consequence of this wide-scale and heterogeneous nature, it is not possible to use one SEM image at a specific magnification to obtain representative porosity information. In this investigation, we developed the Integration of Magnifications (IOM) method, which combines porosity information obtained from images acquired at different magnifications to represent the entire pore space of mudrocks. This method involves dividing the pore space into several length scales, and using a specific magnification and number of images to represent each length scale. High magnification images provide high resolution and small field of view, while low magnification images provide low resolution and large field of view. Therefore, high magnification images are used to sample the nanometer-sized porosity, while low magnification images are used to sample the bigger porosity. The new methodology will circumvent the need to stitch together hundreds of images to provide representative information about mudrocks. The porosity calculations using the IOM method can be calculated using the following formula:

$$n_i = \frac{A_{pi}}{A_{Ti} - A_{Lpi}} - \frac{A_{Lpi}}{A_{Ti} - A_{Lpi}} \qquad (8\text{--}1)$$

where, n_i is the porosity corresponding to Mag i, A_{Ti} is the total area of pores and particles at Mag i, A_{pi} is the area of target pores at Mag i, and A_{Lpi} is the area of big pores at Mag i. The final porosity is then calculated using the following formula:

$$n_f = n_l + n_{l-1}C_l + n_{l-2}C_lC_{l-1} + \cdots \qquad (8\text{--}2)$$

where n_f is the final porosity and l is the number of magnifications. C_l is the ratio of solid area to total area at Mag l, and is given by

$$C_l = \frac{(A_{Tl} - A_{pl} - A_{Lpl})}{A_{Tl} - A_{Lpl}} \tag{8–3}$$

where, A_{Tl} is the total area of pores and particles at the Mag l, A_{pl} is the area of target pores at Mag l, and A_{Lpl} is the area of big pores at Mag l.

The IOM method was first validated using 2-D simulations. The 2-D simulations consist of three main steps. First, we construct a synthetic microstructure of circles with specific parameters such as volume fraction and size distribution. Second, we probe the synthetic microstructure with frames of different sizes. This step simulates the process of using different magnifications to represent different pore sizes. Small frames represent high magnification images, and hence target small sizes. Large frames represent low magnification images, and hence target large sizes. Finally, we use statistical analysis to determine the confidence interval of the measured properties using the IOM method. The 2-D simulations were used to investigate the influence of critical parameters on the final results. These parameters include the number of images at each magnification, the choice of the size of images, and the pore size range targeted at each magnification. Finally, the IOM method was applied on mudrock samples to obtain porosity and pore size distribution information.

8.3 The Microstructure of Resedimented Mudrock Samples

8.3.1 Porosity Measurements

The microstructure of resedimented mudrock samples was investigated using cryo-SEM and conventional SEM techniques. The cryo-SEM technique was used to image the microstructure of wet mudrock samples in their in-situ state. On the other hand, the conventional SEM technique was used to image the microstructure of oven-dried mudrock samples. The IOM method was then used to calculate the wet imaging porosity and the oven-dried imaging porosity of mudrock samples resedimented over a wide range of stresses. The imaging porosity values were compared with reference bulk porosity values including wet lab porosity, oven-dried lab porosity, and MIP porosity. The wet lab porosity measurements provide an accurate measure of the porosity of the resedimented mudrock samples for two reasons. First, the resedimented samples are fully saturated, and the measured water content accurately represent the pore space. Second, the drying was performed immediately after the samples had been extruded, and hence

there was no water loss due to air drying that may result from long-term storage or transportation of samples. The measured lab porosity using conventional drying methods (110°C) removes all of the water in the pore space except the tightly bound layers of water. The removal of tightly bound water requires heating the samples at a temperature of 200°C.

The SEM imaging porosity of wet and oven-dried samples are significantly less than the MIP porosity, oven-dried lab porosity, and wet lab porosity. This discrepancy is due to the differences in the resolution of the used methods. SEM imaging porosity includes pores larger than 35 nm, while the resolution of MIP is 3 nm. These results show that a significant amount of mudrocks porosity is smaller than 35 nm. Furthermore, the MIP porosity, which was performed on oven-dried samples, is significantly less that the wet lab porosity. These results show that the use of these methods on oven-dried samples provide porosity values that do not represent the in-situ state of the samples. Rather, this method represents the dry state of the material. The MIP porosity can be compared with the oven-dried lab porosity because both methods involve the use of the same drying procedures. The MIP porosity of RGOM-EI mudrocks is less than the oven-dried lab porosity. On the other hand, the MIP porosity of RBBC mudrocks matches the oven-dried lab porosity. The discrepancy between the MIP and oven-dried lab porosity can be used to infer information about the microstructure of mudrocks. For example, the differences between the MIP porosity and oven-dried porosity of RGOM-EI samples suggest that the pore space of these samples either contain pores smaller than 3 nm or unconnected pores. On the other hand, the studied RBBC mudrocks do not contain pores smaller than 3 nm or unconnected pores.

8.3.2 SEM Resolution

Two types of imaging porosity measurements were obtained in this investigation: cryo-imaging porosity, and oven-dried imaging porosity. The quantification of the influence of the resolution of SEM on the imaging porosity of mudrock samples can be achieved by comparing the imaging porosity and the reference lab porosity. In this investigation, the wet and oven-dried lab porosity values are considered the reference porosity values. Wet lab porosity serves as the reference porosity for cryo-imaging porosity, whereas the oven-dried lab porosity serves as the reference porosity for oven-dried imaging porosity. The difference between the SEM imaging porosity and the reference lab porosity is due to the pores that are smaller than the resolution of SEM. In this investigation, the smallest pore that can be quantified in SEM images is 35 nm.

213

This number is a function of the highest magnification used (30 KX) to image mudrock samples, as well as the minimum of 10 pixels required to properly quantify pores. The porosity measurements show that the SEM imaging porosity reveals only a fraction of the porosity of mudrock samples, and the remaining porosity is smaller than 35 nm. The SEM porosity of RGOM-EI mudrocks reveals only 22-33% of the wet lab porosity and 39-54% of the oven-dried lab porosity. On the other hand, the SEM imaging porosity of RBBC mudrocks reveals only 26-30% of the wet lab porosity and 33-60% of the oven-dried lab porosity. To improve the resolution limit of 35 nm, we added another high magnification to the analysis performed using the IOM method. The added magnification is 100 KX, which provides a resolution of approximately 11 nm. Two samples were imaged at this magnification: RGOM-EI-0.2 MPa and RGOM-EI-1 MPa. When adding the forth magnification to the IOM method analysis, the SEM imaging porosity increased from 0.160 to 0.208 for RGOM-EI-0.2 MPa sample, and from 0.136 to 0.187 for RGOM-EI-1 MPa sample. Although the imaging porosity increased with the added magnification, the amount of pores smaller than 11 nm is still significant. For further analysis of the pore space, we only considered the 35 nm resolution limit because most samples were imaged with this resolution.

The sub-35nm porosity is defined as the porosity of the clay matrix, which contain pores smaller than 35 nm. This porosity can be estimated in the mudrock samples by comparing the reference lab porosity with the imaging porosity. As discussed above, there are two types of porosity measurements in this investigation: wet and oven-dried porosity. Wet sub-35nm porosity can be calculated by comparing cryo-imaging porosity with the reference wet lab porosity. On the other hand, oven-dried sub-35nm porosity can be calculated by comparing the oven-dried imaging porosity and the reference oven-dried lab porosity. The oven-dried sub-35nm porosity of RGOM-EI mudrock samples is almost constant and ranges from 0.222 to 0.249. The wet sub-35nm porosity for RGOM-EI samples ranges from 0.585 at 1 MPa to 0.378 at 6 MPa. On the other hand, the oven-dried sub-35nm porosity of RBBC mudrock samples ranges from 0.316 to 0.38. The wet sub-35nm porosity of RBBC samples ranges from 0.577 at 1 MPa to 0.425 at 10 MPa.

8.3.3 The influence of Drying Shrinkage on the Microstructure of Mudrocks

We provided both qualitative and quantitative assessment of the influence of drying shrinkage on the microstructure of mudrocks. The pore space of mudrocks was divided into two main categories: visible SEM porosity (>35 nm) and sub-35nm porosity (35nm). The influence of drying shrinkage on the visible SEM porosity was found to be minimal. The calculated wet and oven-dried SEM porosity values were very similar. The influence of drying shrinkage on the sub-35nm porosity is significant. Our results suggest that the sub-35nm porosity collapses to a constant value upon drying. The porosity values do not reveal pore evolution trends. Instead, the void ratio is used as the volume of pores is normalized relative to the solid phase, which does not change upon drying. The SEM pores and the sub-35nm pores undergo shrinkage as mudrocks are oven-dried. The shrinkage in the sub-35nm pores is more significant than that in the SEM pores. These results show that the observed macroscopic shrinkage has two components: shrinkage in the sub-35nm pores, as well as shrinkage in the visible SEM pores.

Our conclusions about the influence of drying shrinkage on the microstructure of mudrocks contradict those obtained using the MIP technique in the literature. All of the MIP studies concluded that oven drying and air drying cause a dramatic reduction in pore volume, and that the reduction in pore volume results from the collapse of large pores, and small pores remain unchanged. The definition of large pores and small pores differed from one study to another. In general, large pores usually refer to interP pores while small pores refer to intraP pores or pores between clay particles. These conclusions contradict our results, which showed that both the SEM pores and sub-35nm pores shrink. Furthermore, the majority of shrinkage occurs in the sub-35nm pores. The use of cryo and conventional SEM in this investigation provided a visual evidence of the influence of drying on the microstructure of mudrocks. These differences may well be because MIP does not provide accurate pore size distribution information about materials due to the lack of pore accessibility to mercury (Diamond, 2000).

8.3.4 Influence of the Consolidation Stress on the Microstructure of Mudrocks

The influence of the consolidation stress was addressed on the visible SEM porosity and the sub-35nm porosity. Our results showed that as the consolidation stress increases, both the interP and intraP pores are compressed for both RGOM-EI and RBBC mudrocks. The compression of the intraP pores in the RGOM-EI samples is more significant that the RRBC

215

samples at high stresses. Furthermore, we showed that the wet sub-35nm decreases as the consolidation stress increases. The decrease in the visible SEM porosity and the sub-35nm porosity is simultaneous. In the other words, the decrease of porosity at each stress increment consists of two components: a decrease in the visible SEM pores and a decrease in the sub-35nm pores. These conclusions are different than those obtained using the MIP technique. These studies showed that an increase in the applied stress leads to the collapse of large macro pores, with very little to no effect on the small micro pores. The separation between macro and micro pores differed from one study to another. In general, macro pores usually refer to inter-aggregate pores while micro pores refer to intra-aggregates pores or pores between clay particles. Similar to the influence of drying shrinkage, this difference may well be because MIP does not provide accurate pore size information about materials (Diamond, 2000).

8.3.5 Recommendations for Future Work

The following topics require further research:

- In this investigation we presented a qualitative description of the microstructure of clay slurries. Obtaining quantitative information, such as orientation and size histograms of clay aggregates requires the use of ion-milled surfaces. This could be achieved by using the Leica TIC3X cross section polisher. This technique was successfully used to prepare flat surface of wet mudrock samples. In addition to the 2D information, 3D volumes provide useful information about the modes of contact between particles and the 3D structure of clay slurries. 3D volumes of clay slurries could be obtained using a combination of the Leica TIC3X cross section polisher and cryo-FIB sequential milling technique. The cross section polisher produces flat surfaces, a necessary requirement when using the cryo-FIB milling technique to reduce milling artifacts.

- In this investigation we showed that the nanometer-sized pores collapse to a constant value upon drying. This conclusion was inferred by comparing SEM and lab measurements. This conclusion could be further investigated using techniques that access the nanometer-sized clay pores. For example, adsorption experiments using different gases could be used to test samples resedimented over a wide range of stresses. In the adsorption experiments, different gases access different pore sizes and thus provide information about different pore types identified in SEM imaging.

216

- The influence of the used conventional drying methods on the measured porosity requires further investigation. This task can be accomplished using Thermal Gravimetric Analysis (TGA) in combination with conventional methods used to measure porosity such as MIP, the immersion method, and the water-loss method. TGA provides information about the temperature required to remove water from the pore space including the tightly bound water.

- We showed that the plunge freezing method destroys the microstructure of clay slurries due to ice crystallization. This method is used extensively in the preparation of mudrock samples as an alternative to oven drying with the assumption that it preserves the microstructure. However, there is no conclusive evidence in the literature that plunge freezing is a suitable method for the characterization of mudrock samples. An answer to this question requires comparing the microstructure of plunge-frozen and high-pressure frozen samples with a wide range of water contents. Furthermore, the amount of water removed during sublimation is still unknown. This question can be answered by comparing the porosity of plunge-frozen samples and the reference wet lab porosity calculated using conventional drying methods.

References

Abdulhadi, N. O., 2009, An Experimental Investigation into the Stress-Dependent Mechanical Behavior of Cohesive Soil with Application to Wellbore Instability by, Ph.D. Thesis: Massachusetts Institute of Technology, Cambridge, Ma, p. 1–459.

Abend, S., and G. Lagaly, 2000, Sol–gel transitions of sodium montmorillonite dispersions: Applied Clay Science, v. 16, no. 3-4, p. 201–227.

Adams, A., 2014, Permeability Anisotropy and Resistivity Anisotropy of Mudrocks, Ph.D Thesis: Massachusetts Institute of Technology, Cambridge, MA, p. 1–561.

Al-Mukhtar, M., N. Belanteur, D. Tessier, and S. K. Vanapalli, 1996, The fabric of a clay soil under controlled mechanical and hydraulic stress states: Applied Clay Science, v. 11, p. 99–115.

Altman, D. G., and J. M. Bland, 2005, Standard deviations and standard errors: BMJ (Clinical research ed.), v. 331, p. 903.

Bachmann, L., and E. Mayer, 1987, Physics of Water and Ice: Implications for Cryofixation, *in* R. A. Steinbrecht, and K. Zierold, eds., Cryotechniques in Biological Electron Microscopy: Springer Berlin Heidelberg, p. 3–34.

Bald, W. B., 1986, On crystal size and cooling rate.: Journal of microscopy, v. 143, no. August 1985, p. 89–102.

Bennett, R. ., N. . O'Brien, and M. . Hulbert, 1991, Determinants of clay and shale microfabric signatures: processes and mechanisms, *in* R. . Bennett, W. . Bryant, and M. . Hulbert, eds., Microstructure of Fine-Grained Sediments: From Mud to Shale: p. 5–32.

Berman, D. R., 1993, Characterization of the Engineering Properties of Boston Blue Clay at the MIT Campus, S.M. Thesis: Massachusetts Institute of Technology.

Betts, W. S., 2014, Compressibility and permeability of Gulf of Mexico mudrocks, resedimented and in-situ, S.M. Thesis: University of Texas at Austin.

Burton, G. J., J. A. Pineda, D. Sheng, and D. Airey, 2015, Microstructural changes of an undisturbed, reconstituted and compacted high plasticity clay subjected to wetting and drying: Engineering Geology, v. 193, p. 363–373.

Callaghan, I. C., and R. H. Ottewill, 1974, Interparticle forces in montmorillonite gels: Faraday Discussions of the Chemical Society, v. 57, p. 110.

Casagrande, A., 1932, The structure of clay and its importance in foundation engineering: Boston Society Civil Engineers Journal, v. 19, no. 4, p. 168–209.

Casey, B., 2014, The Consolidation and Strength Behavior of Mechanically Compressed Fine-Grained Sediments, Ph.D Thesis: Massachusetts Institute of Technology, Cambridge, MA, p. 1–259.

Cauble, D. F., 1996, An Experimental Investigation of the Behavior of a Model Suction Caisson in a Cohesive Soil, Ph.D. Thesis: Massachusetts Institute of Technology.

Chalmers, G. R., R. M. Bustin, and I. M. Power, 2012, Characterization of gas shale pore systems by porosimetry, pycnometry, surface area, and field emission scanning electron microscopy/transmission electron microscopy image analyses: Examples from the Barnett, Woodford, Haynesville, Marcellus, and Doig uni: AAPG Bulletin, v. 96, no. 6, p. 1099–1119.

Cuisinier, O., and L. Laloui, 2004, Fabric evolution during hydromechanical loading of a compacted silt: International Journal for Numerical and Analytical Methods in Geomechanics, v. 28, no. December 2003, p. 483–499.

Curtis, M., R. Ambrose, C. Sondergeld, and C. Sondergeld, 2010, Structural Characterization of Gas Shales on the Micro-and Nano-Scales, in Canadian Unconventional Resources and International Petroleum Conference.

Curtis, M. E., C. H. Sondergeld, R. J. Ambrose, and C. S. Rai, 2012, Microstructural investigation of gas shales in two and three dimensions using nanometer-scale resolution imaging: AAPG Bulletin, v. 96, no. 4, p. 665–677.

Dahl, R., and L. A. Staehelin, 1989, High-pressure freezing for the preservation of biological structure: theory and practice.: Journal of electron microscopy technique, v. 13, no. 3, p. 165–74.

Deirieh, A., C. I. Y., M. L. Whittaker, J. T. Germaine, D. Joester, and P. B. Flemings, 2015, High Pressure Freezing Reveals that the Honeycomb Structure Observed in Clay Gels is an Artifact of Sample Preparation: In preparation.

Delage, P., and G. Lefebvre, 1984, Study of the structure of a sensitive Champlain clay and of its evolution during consolidation: Canadian Geotechnical Journal, v. 21, no. 1, p. 21–35.

Desbois, G., J. L. Urai, S. Hemes, S. Brassinnes, M. De Craen, and X. Sillen, 2014, Nanometer-scale pore fluid distribution and drying damage in preserved clay cores from Belgian clay formations inferred by BIB-cryo-SEM: Engineering Geology, v. 179, p. 117–131.

Desbois, G., J. L. Urai, and P. a. Kukla, 2009, Morphology of the pore space in claystones – evidence from BIB/FIB ion beam sectioning and cryo-SEM observations: eEarth Discussions, v. 4, p. 15–22.

Dewhurst, D. N., A. C. Aplin, J.-P. Sarda, and Y. Yang, 1998, Compaction-driven evolution of porosity and permeability in natural mudstones: An experimental study: Journal of Geophysical Research, v. 103, no. 97, p. 651–661.

Diamond, S., 2000, Mercury porosimetry. An inappropriate method for the measurement of pore size distributions in cement-based materials: Cement and Concrete Research, v. 30, p. 1517–1525.

Du, J., G. Morris, R. A. Pushkarova, and R. S. C. Smart, 2010, Effect of surface structure of kaolinite on aggregation, settling rate, and bed density.: Langmuir : the ACS journal of surfaces and colloids, v. 26, no. 16, p. 13227–35.

Du, J., R. A. Pushkarova, and R. S. C. Smart, 2009, A cryo-SEM study of aggregate and floc structure changes during clay settling and raking processes: International Journal of Mineral Processing, v. 93, no. 1, p. 66–72.

Dubochet, J., M. Adrian, J. J. Chang, J. C. Homo, J. Lepault, a W. McDowall, and P. Schultz, 1987, Cryoelectron microscopy of vitrified specimens, in R. A. Steinbrecht, and K. Zierold, eds., Cryotechniques in Biological Electron Microscopy: Springer Berlin Heidelberg, p. 114–131.

Dubochet, J., M. Adrian, J. J. Chang, J. C. Homo, J. Lepault, a W. McDowall, and P. Schultz, 1988, Cryo-electron microscopy of vitrified specimens., in Quarterly reviews of biophysics: p. 129–228.

Echlin, P., 1992, Low-Temperature Microscopy and Analysis: Springer Science & Business Media, p. 539.

Erdman, N., R. Campbell, and S. Asahina, 2006, Argon beam cross sectioning: Advanced Materials and Processes, v. 164, no. June, p. 33–35.

Erk, I., M. Michel, and J. Lepault, 1996, Electron cryo-microscopy of vitrified bulk biological specimens: ideal and real structures of water-lipid phases: Journal of microscopy, v. 182, no. November 1995, p. 15–23.

Fahy, B. P., 2014, The Influence of Salinity on the Mechanical Behavior of High Plasticity Soils, S.M. Thesis: Massachusetts Institute of Technology, Cambridge, MA, p. 1–249.

Germaine, J. T., 1982, Development of the Directional Shear Cell for Measuring Cross-Anisotropic Clay Properties, ScD Thesis: Massachusetts Institute of Technology, Camridge, MA.

Giffin, S., R. Littke, J. Klaver, and J. L. Urai, 2013, Application of BIB-SEM technology to characterize macropore morphology in coal: International Journal of Coal Geology, v. 114, p. 85–95.

Goldschmidt, V. M., 1926, Undersokelser over lersedimenter: Nordisk Jordbrugs forskuing, v. 4-7, p. 435 – 445.

Griffiths, F. J., and R. C. Joshi, 1989, Change in pore size distribution due to consolidation of clays: Géotechnique, v. 39, no. 1, p. 159–167.

Harding, B., 2014, Standard errors : A review and evaluation of standard error estimators using Monte Carlo simulations: The Quantitative Methods for Psychology, v. 10, p. 107–123.

Heath, J. E., T. A. Dewers, B. J. McPherson, R. Petrusak, T. C. Chidsey, A. J. Rinehart, and P. S. Mozley, 2011, Pore networks in continental and marine mudstones: Characteristics and controls on sealing behavior: Geosphere, v. 7, no. 2, p. 429–454.

Hemes, S., G. Desbois, J. L. Urai, M. De Craen, and M. Honty, 2013, Variations in the morphology of porosity in the Boom Clay Formation: Insights from 2D high resolution BIB-SEM imaging and Mercury injection Porosimetry: Geologie en Mijnbouw/Netherlands Journal of Geosciences, v. 92, no. 2013, p. 275–300.

Hemes, S., G. Desbois, J. L. Urai, B. Schröppel, and J. O. Schwarz, 2015, Multi-scale characterization of pore microstructures in Boom Clay (HADES, Mol, Belgium) using a combination of μ-CT, BIB-SEM and serial FIB-SEM techniques: Microporous and Mesoporous Materials, v. 208, p. 1–20.

Holzer, L., B. Münch, M. Rizzi, R. Wepf, P. Marschall, and T. Graule, 2010, 3D-microstructure analysis of hydrated bentonite with cryo-stabilized pore water: Applied Clay Science, v. 47, no. 3-4, p. 330–342.

Horan, A. J., 2012, The mechanical behavior of normally consolidated soils as a function of pore fluid salinity: Cambridge, Massachusetts Institute of Technology.

Houben, M. E., 2013, In situ characterization of the microstructure and porosity of Opalinus Clay (Mont Terri Rock Laboratory, Switzerland), Ph.D Thesis: RWTH-Aachen University, p. 169.

Houben, M. E., G. Desbois, and J. L. Urai, 2014, A comparative study of representative 2D microstructures in Shaly and Sandy facies of Opalinus Clay (Mont Terri, Switzerland) inferred form BIB-SEM and MIP methods: Marine and Petroleum Geology, v. 49, p. 143–161.

Houben, M. E., G. Desbois, and J. L. Urai, 2013, Pore morphology and distribution in the Shaly facies of Opalinus Clay (Mont Terri, Switzerland): Insights from representative 2D BIB–SEM investigations on mm to nm scale: Applied Clay Science, v. 71, p. 82–97.

Hu, L. B., H. Péron, T. Hueckel, and L. Laloui, 2013a, Desiccation shrinkage of non-clayey soils: multiphysics mechanisms and a microstructural model: International Journal for Numerical and Analytical Methods in Geomechanics, v. 37, no. 12, p. 1761–1781.

Hu, L. B., H. Péron, T. Hueckel, and L. Laloui, 2013b, Mechanisms and critical properties in drying shrinkage of soils : experimental and numerical parametric studies: Canadian Geotechnical Journal, v. 50, no. 2012, p. 536–549.

Kameda, A., J. Dvorkin, Y. Keehm, A. Nur, and W. Bosl, 2006, Permeability-porosity transforms from small sandstone fragments: Geophysics, v. 71, no. 1, p. N11.

Keller, L. M., L. Holzer, R. Wepf, and P. Gasser, 2011, 3D geometry and topology of pore pathways in Opalinus clay: Implications for mass transport: Applied Clay Science, v. 52, no. 1-2, p. 85–95.

Khandal, R. ., and T. . Tadros, 1988, Application of viscoelastic measurements to the investigation of the swelling of sodium montmorillonite suspensions: Journal of Colloid and Interface Science, v. 125, no. l, p. 122–128.

Klaver, J., G. Desbois, R. Littke, and J. L. Urai, 2015, BIB-SEM characterization of pore space morphology and distribution in postmature to overmature samples from the Haynesville and Bossier Shales: Marine and Petroleum Geology, v. 59, p. 451–466.

Klaver, J., G. Desbois, J. L. Urai, and R. Littke, 2012, BIB-SEM study of the pore space morphology in early mature Posidonia Shale from the Hils area, Germany: International Journal of Coal Geology, v. 103, p. 12–25.

Koliji, A., L. Laloui, O. Cusinier, and L. Vulliet, 2006, Suction induced effects on the fabric of a structured soil: Transport in Porous Media, v. 64, p. 261–278.

Lambe, T. W., 1953, The structure of inorganic soil: Proceedings of the American Society of Civil Engineers, v. 79, p. 1–49.

Loucks, R. G., R. M. Reed, S. C. Ruppel, and U. Hammes, 2012, Spectrum of pore types and networks in mudrocks and a descriptive classification for matrix-related mudrock pores: AAPG bulletin, v. 96, no. 6, p. 1071–1098.

Loucks, R. G., R. M. Reed, S. C. Ruppel, and D. M. Jarvie, 2009, Morphology, genesis, and distribution of nanometer-scale pores in siliceous mudstones of the Mississippian Barnett Shale: Journal of Sedimentary Research, v. 79, no. 12, p. 848 – 861.

Milner, M., R. McLin, and J. Petriello, 2010, Imaging texture and porosity in mudstones and shales: comparison of secondary and ion-milled backscatter SEM methods, in Canadian Unconventional Resources and International Petroleum Conference.

Mitchell, J. K., and K. Soga, 2005, Fundamentals of Soil Behavior: Hoboken, NJ, John Wiley & Sons.

Moor, H., 1987, Theory and Practice of High Pressure Freezing, in R. A. Steinbrecht, and K. Zierold, eds., Cryotechniques in Biological Electron Microscopy: p. 175–191.

Morris, G. E., and M. S. Żbik, 2009, Smectite suspension structural behaviour: International Journal of Mineral Processing, v. 93, no. 1, p. 20–25.

Norrish, K., 1954, The swelling of montmorillonite: Discussions of the Faraday Society, v. 18, p. 120.

O'Brien, N. R., 1971, Fabric of Kaolinite and Illite floccules: Ckay and Clay Minerals, v. 19, no. December 1970, p. 353–359.

O'Brien, N. R., 1995, Origin of Shale Fabric-Clues From Framboids: Northeastern Geology & Environmental Sciences, v. 17, no. 2, p. 146–150.

O'Brien, N. R., and S. Pietraszek-Mattner, 1998, Origin of the fabric of laminated fine-grained glaciolacustrine deposits: Journal of Sedimentary Research, v. 68, p. 832–840.

O'Brien, N. R., and R. M. Slatt, 1990, Argillaceous Rock Atlas: New York, NY, Springer New York.

Van Olphen, H., 1977, An introduction to clay colloid chemistry, for clay technologists, geologists, and soil scientists.: New York, John Wiley & Sons.

Van Olphen, H., 1964, Internal mutual flocculation in clay suspensions: Journal of Colloid Science, v. 19, no. 360, p. 313–322.

Osipov, V. I., and V. N. Sokolov, 1978, Structure formation in clay sediments: Bulletin of the International Association of Engineering Geology, v. 18, no. 1, p. 83–90.

Peron, H., T. Hueckel, L. Laloui, and L. B. Hu, 2009, Fundamentals of desiccation cracking of fine-grained soils: experimental characterisation and mechanisms identification: Canadian Geotechnical Journal, v. 46, p. 1177–1201.

Qi, Y., M. Al-Mukhtar, J.-F. Alcover, and F. Bergaya, 1996, Coupling analysis of macroscopic and microscopic behaviour in highly consolidated Na-laponite clays: Applied Clay Science, v. 11, p. 185–197.

Reed, S. J. B., 2005, Electron Microprobe Analysis and Scanning Electron Microscopy in Geology: Cambridge, Cambridge University Press, doi:10.1017/CBO9780511610561.

Romero, E., 2013, A microstructural insight into compacted clayey soils and their hydraulic properties: Engineering Geology, v. 165, p. 3–19.

Sasanian, S., and T. a. Newson, 2013, Use of mercury intrusion porosimetry for microstructural investigation of reconstituted clays at high water contents: Engineering Geology, v. 158, p. 15–22.

Scherer, G. W., 1990, Theory of Drying: Journal of the American Ceramic Society, v. 73, p. 3–14.

Schieber, J., 2010, Common Themes in the Formation and Preservation of Intrinsic Porosity in Shales and Mudstones – Illustrated with Examples Across the Phanerozoic: Society of Petroleum Engineers Unconventional Gas Conference, SPE Paper 132370, p. 10.

Seah, T. H., 1990, Anisotropy of Resedimented Boston Blue Clay, ScD Thesis: Massachusetts Institute of Technology, Cambridge, MA.

Shin, H., and J. C. Santamarina, 2011, Desiccation cracks in saturated fine-grained soils: particle-level phenomena and effective-stress analysis: Géotechnique, v. 61, no. 11, p. 961–972.

Simms, P. H., and E. K. Yanful, 2001, Measurement and estimation of pore shrinkage and pore distribution in a clayey till during soil-water characteristic curve tests: Canadian Geotechnical Journal, v. 38, p. 741–754.

Simms, P. H., and E. K. Yanful, 2002, Predicting soil—water characteristic curves of compacted plastic soils from measured pore-size distributions: Géotechnique, v. 52, no. 4, p. 269–278.

Sitte, H., L. Edelmann, and K. Neumann, 1987, Cryofixation without pretreatment at ambient pressure, in R. A. Steinbrecht, and K. Zierold, eds., Cryotechniques in biological electron microscopy: Springer Berlin Heidelberg, p. 87–113.

Slatt, R. M., and N. R. O'Brien, 2011, Pore types in the Barnett and Woodford gas shales: Contribution to understanding gas storage and migration pathways in fine-grained rocks: AAPG Bulletin, v. 95, no. 12, p. 2017–2030.

Sondergeld, C. H., R. J. Ambrose, C. S. Rai, and J. Moncrieff, 2010, Micro-structural studies of gas shales: Society of Petroleum Engineers Unconventional Gas Conference, SPE Paper 131771, p. 17.

Stawinsk, J., J. Wierzchos, and M. T. Garcia-gonzalez, 1990, Influence of calcium and sodium concentration on the microstructure of bentonite and kaolin: v. 38, no. 6, p. 617–622.

Streiner, D. L., 1996, Maintaining standards: Differences between the standard deviation and standard error, and when to use each: Canadian Journal of Psychiatry, v. 41, no. October, p. 498–502.

Studer, D., W. Graber, A. Al-Amoudi, and P. Eggli, 2001, A new approach for cryofixation by high-pressure freezing.: Journal of microscopy, v. 203, no. January, p. 285–294.

Studer, D., B. M. Humbel, and M. Chiquet, 2008, Electron microscopy of high pressure frozen samples: Bridging the gap between cellular ultrastructure and atomic resolution: Histochemistry and Cell Biology, v. 130, p. 877–889.

Studer, D., M. Michel, and M. Müller, 1989, High pressure freezing comes of age.: Scanning microscopy. Supplement, v. 3, p. 253–68; discussion 268–9.

Studer, D., M. Michel, M. Wohlwend, E. B. Hunziker, and M. D. Buschmann, 1995, Vitrification of articular cartilage by high-pressure freezing: Journal of microscopy, v. 179, p. 321–332.

Stump, B. B., and P. B. Flemings, 2001, Consolidation State, Permeability, and Stress Ratio as Determined from Uniaxial Strain Experiments on Mudstone Samples from the Eugene Island 330 Area, Offshore Louisiana, in A. Huffman, and G. Bowers, eds., Pressure Regimes in Sedimentary Basins and Their Prediction: The American Association of Petroleum Geologists, p. 131–144.

Tang, C. S., B. Shi, C. Liu, W. Bin Suo, and L. Gao, 2011, Experimental characterization of shrinkage and desiccation cracking in thin clay layer: Applied Clay Science, v. 52, no. APRIL 2011, p. 69–77.

Terzaghi, T., 1925, Erdbaumechanik auf bodenphysikalischer Grundlage: Vienna, Deuticke, p. 399.

Thompson, M. L., J. F. McBride, and R. Horton, 1985, Effects of Drying Treatments on Porosity of Soil Materials1: Soil Science Society of America Journal, v. 49, no. 6, p. 1360.

Tschopp, M. a, G. B. Wilks, and J. E. Spowart, 2008, Multi-scale characterization of orthotropic microstructures: Modelling and Simulation in Materials Science and Engineering, v. 16, p. 065009.

Vali, H., and L. Bachmann, 1988, Ultrastructure and flow behavior of colloidal smectite dispersions: Journal of Colloid and Interface Science, v. 126, no. 1, p. 278–291.

Wang, Y., S. Lu, T. Ren, and B. Li, 2011, Bound Water Content of Air-Dry Soils Measured by Thermal Analysis: Soil Science Society of America Journal, v. 75, no. 2, p. 481.

Washburn, E. W., 1921, Note on a Method of Determining the Distribution of Pore Sizes in a Porous Material.: Proceedings of the National Academy of Sciences of the United States of America, v. 7, no. 4, p. 115–6.

Wei, X., M. Hattab, J. M. Fleureau, and R. Hu, 2013, Micro-macro-experimental study of two clayey materials on drying paths: Bulletin of Engineering Geology and the Environment, v. 72, p. 495–508.

Weiss, V. A., and R. Frank, 1961, Über den Bau der Gerüste in thixotropen Gelen: p. 141–142.

Wilson, M. J., 2013, Rock-forming Minerals: Sheet silicates: clay minerals. Volume 3C: Geological Society of London, p. 736.

Zbik, M. S., W. N. Martens, R. L. Frost, Y.-F. Song, Y.-M. Chen, and J.-H. Chen, 2008, Transmission X-ray microscopy (TXM) reveals the nanostructure of a smectite gel.: Langmuir : the ACS journal of surfaces and colloids, v. 24, no. 16, p. 8954–8958.

Zbik, M. S., Y.-F. Song, and R. L. Frost, 2010, Kaolinite flocculation induced by smectite addition - a transmission X-ray microscopic study.: Journal of colloid and interface science, v. 349, no. 1, p. 86–92.